crystals

Carbonates

Edited by
Linda Pastero

Printed Edition of the Special Issue Published in *Crystals*

www.mdpi.com/journal/crystals

MDPI

Carbonates

Carbonates

Special Issue Editor

Linda Pastero

MDPI • Basel • Beijing • Wuhan • Barcelona • Belgrade

Special Issue Editor
Linda Pastero
University of Torino
Italy

Editorial Office
MDPI
St. Alban-Anlage 66
4052 Basel, Switzerland

This is a reprint of articles from the Special Issue published online in the open access journal *Crystals* (ISSN 2073-4352) from 2017 to 2018 (available at: https://www.mdpi.com/journal/crystals/special_issues/Carbonates)

For citation purposes, cite each article independently as indicated on the article page online and as indicated below:

LastName, A.A.; LastName, B.B.; LastName, C.C. Article Title. *Journal Name* **Year**, *Article Number*, Page Range.

ISBN 978-3-03897-722-3 (Pbk)
ISBN 978-3-03897-723-0 (PDF)

© 2019 by the authors. Articles in this book are Open Access and distributed under the Creative Commons Attribution (CC BY) license, which allows users to download, copy and build upon published articles, as long as the author and publisher are properly credited, which ensures maximum dissemination and a wider impact of our publications.
The book as a whole is distributed by MDPI under the terms and conditions of the Creative Commons license CC BY-NC-ND.

Contents

About the Special Issue Editor . . . . . **vii**

Preface to "Carbonates" . . . . . **ix**

Cleo Kosanović, Simona Fermani, Giuseppe Falini and Damir Kralj
Crystallization of Calcium Carbonate in Alginate and Xanthan Hydrogels
Reprinted from: *Crystals* **2017**, *7*, 355, doi:10.3390/cryst7120355 . . . . . **1**

Shashi B. Atla, Yi-Hsun Huang, James Yang, How-Ji Chen, Yi-Hao Kuo, Chun-Mei Hsu, Wen-Chien Lee, Chien-Cheng Chen, Duen-Wei Hsu and Chien-Yen Chen
Hydrophobic Calcium Carbonate for Cement Surface
Reprinted from: *Crystals* **2017**, *7*, 371, doi:10.3390/cryst7120371 . . . . . **16**

Pao Chi Chen and Shun Chao Yu
CO_2 Capture and Crystallization of Ammonia Bicarbonate in a Lab-Scale Scrubber
Reprinted from: *Crystals* **2018**, *8*, 39, doi:10.3390/cryst8010039 . . . . . **25**

Marianela Sánchez, Patricio Vásquez-Quitral, Nicole Butto, Felipe Díaz-Soler, Mehrdad Yazdani-Pedram, Juan Francisco Silva and Andrónico Neira-Carrillo
Effect of Alginate from Chilean *Lessonia nigrescens* and MWCNTs on $CaCO_3$ Crystallization by Classical and Non-Classical Methods
Reprinted from: *Crystals* **2018**, *8*, 69, doi:10.3390/cryst8020069 . . . . . **38**

Nicole Butto, Gustavo Cabrera-Barjas and Andrónico Neira-Carrillo
Electrocrystallization of $CaCO_3$ Crystals Obtained through Phosphorylated Chitin
Reprinted from: *Crystals* **2018**, *8*, 82, doi:10.3390/cryst8020082 . . . . . **53**

Wenli Xu, Huaguo Wen, Rongcai Zheng, Fengjie Li, Fei Huo, Mingcai Hou and Gang Zhou
The Carbonate Platform Model and Reservoirs' Origins of the Callovian-Oxfordian Stage in the Amu Darya Basin, Turkmenistan
Reprinted from: *Crystals* **2018**, *8*, 84, doi:10.3390/cryst8020084 . . . . . **69**

Chun-Mei Hsu, Yi-Hsun Huang, Vanita Roshan Nimje, Wen-Chien Lee, How-Ji Chen, Yi-Hao Kuo, Chung-Ho Huang, Chien-Cheng Chen and Chien-Yen Chen
Comparative Study on the Sand Bioconsolidation through Calcium Carbonate Precipitation by *Sporosarcina pasteurii* and *Bacillus subtilis*
Reprinted from: *Crystals* **2018**, *8*, 189, doi:10.3390/cryst8050189 . . . . . **91**

Emanuele Costa and Dino Aquilano
Experimental Value of the Specific Surface Energy of the Cleavage {10.4} Calcite Rhombohedron in the Presence of Its Saturated Aqueous Solution
Reprinted from: *Crystals* **2018**, *8*, 238, doi:10.3390/cryst8060238 . . . . . **106**

Linda Pastero and Dino Aquilano
Calcium Carbonate Polymorphs Growing in the Presence of Sericin: A New Composite Mimicking the Hierarchic Structure of Nacre
Reprinted from: *Crystals* **2018**, *8*, 263, doi:10.3390/cryst8070263 . . . . . **114**

About the Special Issue Editor

Linda Pastero has been working as a scientist at the University of Turin since 2004. Her interests cover a wide range of topics related to crystal growth, ranging from the fundamentals to their biological, medical and environmental applications

Preface to "Carbonates"

Although the minerals belonging to the carbonate group are a widely discussed subject, their relevance remains unchanged due to their many applications in a wide range of disciplines, from mineralogy, geochemistry and geology to biology, medicine, industry and waste remediation. Furthermore, studying the interactions between carbonates and other organic or inorganic phases may disclose new opportunities for understanding of the mechanisms involved in mineralization processes.

An open, multidisciplinary approach is mandatory when dealing with the phenomena behind the crystal nucleation and growth of carbonates, applied in so many contexts.

This Special Issue gathers a multidisciplinary collection of papers on carbonates covering many fields of interest, ranging from geological applications to their industrial and environmental exploitation and biomineralization, while not disregarding the fundamental aspects of crystal growth.

Linda Pastero
Special Issue Editor

crystals

MDPI

Article

Crystallization of Calcium Carbonate in Alginate and Xanthan Hydrogels

Cleo Kosanović [1], Simona Fermani [2], Giuseppe Falini [2,*] and Damir Kralj [3,*]

[1] Meteorological and Hydrological Service, Air Quality Division, Grič 3, HR-10000 Zagreb, Croatia; kosanovic@cirus.dhz.hr
[2] Dipartimento di Chimica "Giacomo Ciamician", Alma Mater Studiorum—Università di Bologna, via Selmi 2, 40126 Bologna, Italy; simona.fermani@unibo.it
[3] Ruđer Bošković Institute, P.O. Box 180, HR-10002 Zagreb, Croatia
* Correspondence: giuseppe.falini@unibo.it (G.F.); kralj@irb.hr (D.K.); Tel.: +39-051-209-9484 (G.F.); +385-1-468-0207 (D.K.)

Academic Editor: Linda Pastero
Received: 20 September 2017; Accepted: 27 November 2017; Published: 30 November 2017

Abstract: Calcium carbonate polymorphs were crystallized in alginate and xanthan hydrogels in which a degree of entanglement was altered by the polysaccharide concentration. Both hydrogels contain functional groups (COOH and OH) attached at diverse proportions on saccharide units. In all systems, the precipitation process was initiated simultaneously with gelation, by the fast mixing of the calcium and carbonate solutions, which contain the polysaccharide molecules at respective concentrations. The initial supersaturation was adjusted to be relatively high in order to ensure the conditions suitable for nucleation of all $CaCO_3$ polymorphs and amorphous phase(s). In the model systems (no polysaccharide), a mixture of calcite, vaterite and amorphous calcium carbonate initially precipitated, but after short time only calcite remained. In the presence of xanthan hydrogels, precipitation of either, calcite single crystals, porous polyhedral aggregates, or calcite/vaterite mixtures were observed after five days of ageing, because of different degrees of gel entanglement. At the highest xanthan concentrations applied, the vaterite content was significantly higher. In the alginate hydrogels, calcite microcrystalline aggregates, rosette-like and/or stuck-like monocrystals and vaterite/calcite mixtures precipitated as well. Time resolved crystallization experiments performed in alginate hydrogels indicated the initial formation of a mixture of calcite, vaterite and amorphous calcium carbonate, which transformed to calcite after 24 h of ageing.

Keywords: calcium carbonate; crystallization; hydrogels; alginate; xanthan

1. Introduction

The formation of diverse calcium carbonate ($CaCO_3$) solid phases is one of the most investigated precipitation process among slightly soluble ionic salts. In this system, three polymorphs (vaterite, aragonite or calcite), two hydrates (monohydrocalcite, $CaCO_3 \cdot H_2O$ and ikaite, $CaCO_3 \cdot 6H_2O$) and amorphous calcium carbonate can precipitate. Therefore, their formation pathways provide suitable models for basic the investigation of mechanisms and kinetics of nucleation, crystal growth, dissolution and, particularly, transformation of precursor phases in aqueous solutions. In addition, $CaCO_3$ phases are extensively investigated because of their relevance in geological, technological and biological environments and systems [1–6].

The most important experimental parameters, which influence the precipitation of slightly soluble salts like $CaCO_3$ and their structural, chemical and morphological properties, are the initial supersaturation, temperature, presence of additives, pH and hydrodynamic conditions. Consequently, the traditional experimental protocols, like bulk precipitation, crystal seeding, constant composition or

continuous processes, are regularly applied for tuning the properties of the precipitate. Crystallization of slightly soluble salts in gelling environments is inspired by biomineralization of $CaCO_3$ in mollusks and corals, or calcium phosphates in enamel and bones and it has been recognized as an alternative strategy for synthesis of materials with desired features [7]. Hydrogels are multicomponent, solid-like systems built up by a three-dimensional network of interconnected (macro) molecular chains, with the interspace filled up with water and possibly electrolytes. The formation of gel-like structures and their physical and chemical properties are principally influenced by the concentration of the gelling molecules, temperature, pH and in some specific cases, type and concentration of counter and co-ions present in the system [7,8]. In such gelling systems, the critical parameters for precipitation are mostly determined by diffusivity and the local charge distribution (ionotropic effect) [9–11].

Biocompatible polysaccharide hydrogels have been recognized as suitable models for investigation of $CaCO_3$ precipitation (crystallization), particularly for clarifying the role of basic processes (nucleation, crystal growth, dissolution or aging) [7,10,12–14]. However, a more explicit connection between calcium carbonates and gels is related to their possible biomedical or pharmaceutical application. Thus, for example, a class of hybrid organic–inorganic drug delivery systems, constructed from porous micro particles in which active molecules are absorbed and coated with polymer multilayers has been described. In such systems, layer-by-layer adsorption of differently charged polyelectrolytes onto porous vaterite particles may form microcapsules with gel-like interior, after removing the mineral core [15–18]. Thus, size, polymorphic composition, surface texture and/or porosity, can influence their properties relevant for potential use as a drug delivery vehicles. A role of the above-mentioned parameters is intuitively understandable and can be correlated to the efficiency of delivery. However, control of the particles' shape is recognized as a future trend in preparation of drug delivery models, since it was described that anisotropic particles show higher intracellular transport [19–23].

In addition, within the field of tissue engineering, hydrogel composites with inorganic micro particles are intensively investigated as materials for bone regeneration. Since bones can be considered as a mineralized hydrogel made of collagen fibrils and calcium-deficient hydroxyapatite, a production of synthetic hydrogel–inorganic composites is supposed to mimic the nature [24–26]. In such systems, mineral phases increase the composites' bioactivity, surface roughness, mechanical properties, adhesion, proliferation and differentiation of bone-forming cells. Convenient inorganic phases used for hydrogels enrichment are calcium phosphates and bioactive glasses, but silica and $CaCO_3$ are considered as well. Typical experimental strategies for mineralization of respective hydrogels with $CaCO_3$ involved either, mixing of previously formed particles with sols before gelation (so called "internal gelation") [27–30], or their precipitation after gelation. Indeed, in the case of postponed formation of mineral particles, precipitating components have been delivered by different techniques. Thus for example, $CaCO_3$ precipitation has been initiated by alternating a soaking of poly(acrylic acid) grafted poly(ethylene) films into Ca^{2+} or CO_3^{2-} solutions. Similar protocols have been applied for agarose or chitosan gels [14,31–33]. A diffusion of one component (CO_2) into the agarose gel preloaded with Ca^{2+} and modified with self-assembled monolayer, has been investigated as a model of biomineralization of protein-based hydrogels. In such systems nucleation and growth were simultaneously controlled [34]. Double-diffusion of calcium and carbonate ions into the polyacrylamide hydrogels of different polymer content has been investigated and a correlation between morphology of precipitate and hydrogel concentration was found [35]. A similar experimental setup was also applied in the agarose hydrogel system in order to estimate the impact of porosity on the properties of mineral phase and to correlate it with supersaturation profile and presence of additives [36,37]. Besides the above-mentioned two-step protocols, simultaneous gel and $CaCO_3$ formation has also been described. Thus, stepwise addition of Na_2CO_3/alginate solution into $CaCl_2$ resulted in creation of appropriate composites and allowed the authors to recognize an active control of the gel matrix over the size and morphology of the obtained calcite crystals [13]. Similarly, simultaneous

$CaCO_3$ precipitation and gelling of carrageenan, accomplished by the fast mixing of reactants, explained the effect of the gelling status of carrageenan on properties of precipitate [12].

The objective of this work is to elaborate the protocols for production of a significant amount of $CaCO_3$/hydrogel composites and to demonstrate the possibilities to control the physical properties of mineral particles, with emphasis on their size, surface texture, porosity and shape. Since the biocompatible and degradable polysaccharides (sodium alginate and xanthan gum) and bioactive calcium carbonate polymorphs are used, the composites may be suitable for application in a field of hard tissue engineering or drug delivery. In addition, the obtained results may be used as alternative experimental strategies for preparation of porous and/or monodispersed $CaCO_3$ polymorphs, suitable for use as templates for the preparation of polyelectrolyte multilayer capsules.

2. Results and Discussion

The precipitation in gelling environment has been initiated by the fast mixing of reactants in order to enable a rapid formation of gel and apparently instantaneous establishment of supersaturation [12]. Both polysaccharides, xanthan and alginate, are anionic polyelectrolytes with similar chemical functionalities attached to molecules' backbone (carboxylate, hydroxide). Indeed, alginate contains about one COOH, while xanthan less than 0.4 COOH per sugar unit. The alginate hydrogels are formed by crosslinking their molecules with divalent cations, while the formation of xanthan gel is caused by releasing the water molecules that are attached to polysaccharide molecules and hydrogen bonding of chains [38–42]. The pore size distribution of both gels was controlled by varying the polysaccharide molecule concentration.

The results of morphological and structural analyses of $CaCO_3$ precipitated in gels were compared to referent bulk-precipitation systems. In this way the effects caused by the space confinement and charge density may be discerned from otherwise dominating factors for precipitation of slightly soluble salts, like supersaturation and hydrodynamics. Thus, the initial supersaturation was be set to be relatively high, in order to undoubtedly exceed the threshold values for onset of nucleation in both systems. In all systems the concentrations of precipitating components were identical: $c(CaCl_2) = c(Na_2CO_3) = 0.066$ mol dm^{-3}, which correspond to supersaturations expressed with respect to amorphous calcium carbonate (ACC), $S_C = 89.2$ and $S_{ACC} = 8.1$, respectively. Indeed, the addition of polysaccharides affects the concentration of unbound calcium ions and the activity of all reactants present in the system, so it is rather difficult to calculate the actual supersaturation in gelling systems. Therefore, the applied concentrations of reactants were relatively high in order to ensure that the threshold value for the onset of nucleation was exceeded in both systems and at all concentrations of hydrogels. Indeed, fast and intensive precipitation was observed in all systems.

Three types of precipitation experiments in gel were performed in order to discriminate possible hydrodynamic effects (order of addition of reactants), or the adjustment of pH, which may influence the distribution of charges of polysaccharide molecules. Thus, in the system Ca-gel, pH = 10.5, Na_2CO_3 solution was introduced into the $CaCl_2$/polysaccharide solution with respective concentration of alginate or xanthan. The pH of $CaCl_2$ was pre-adjusted to 10.5. The system Ca-gel, pH = 9.0, is identical, but the pH of the $CaCl_2$ was pre-adjusted to 9.0. The order of addition of reactants was changed in the CO_3-gel, pH = 10.5 system, in which the $CaCl_2$ solution (pH = 10.5) was rapidly introduced into the Na_2CO_3/polysaccharide solutions of the appropriate concentration of polysaccharide.

However, in the respective model systems (identical concentrations of reactants, but without presence of polysaccharide), a mixture of amorphous calcium carbonate (ACC), calcite and vaterite precipitated immediately after mixing the reactants. Transformation of unstable phases into the calcite was completed after about 24 h. Figure S10 shows typical calcite crystals isolated from the system. Similar precipitation/transformation pattern, according to which only calcite remained in the system after 24 h, was also observed in the systems of higher and lower supersaturation ($c(CaCl_2) = c(Na_2CO_3) = 0.1$ mol dm^{-3} and $c(CaCl_2) = c(Na_2CO_3) = 0.033$ mol dm^{-3}).

2.1. $CaCO_3$ Precipitation in Xanthan Gels

The concentrations of xanthan used for precipitation experiments varied in the range from 0.20–2.00 wt % with respect to water and, in all systems, the formation of precipitate occurred immediately after the addition of calcium or carbonate solution. The results of structural analyses (P-XRD) and morphological observations (SEM) of precipitates are reported in Table 1 and in Figure S1a. Typical X-ray diffractograms and respective FT-IR spectra are also shown (Figures S2, S3 and S6). Hence, it is shown that at lower gel concentrations, c_{xan} = 0.20 wt % and 0.35 wt %, the precipitate obtained five days after initiating the process, consists predominantly of calcite, with traces of vaterite. At a moderate concentration of gel, c_{xan} = 0.40 wt %, calcite is still the predominant phase unless in the system Ca-gel, pH = 10.5, about 39 wt % of vaterite is mixed with calcite. At the highest gel concentration, c_{xan} = 2.00 wt %, vaterite was found to be significantly present in all systems.

Table 1. Mineralogical composition, shape and average size (referred to the longest axis of single particle or aggregate) of precipitate (calcite and vaterite) prepared in different xanthan gels and $c_i(CaCl_2) = c_i(Na_2CO_3) = 0.066$ mol dm^{-3}, t = 5 days.

	c_{xan}/wt %	w_{calc}/wt %	Shape	L/μm #
Ca-gel pH = 9.0	0.20	99	*c*-axis elongated rhombohedra	15(5)
	0.35	95	*c*-axis elongated rhombohedra	10(5)
	0.40	99	etched rhombohedra	10(5)
	2.00	21	etched rhombohedra-spheres	10(5)–10(5)
Ca-gel pH = 10.5	0.20	100	Rhombohedra	10(5)
	0.35	99	Rhombohedra	10(5)
	0.40	61	etched rhombohedra-spheres	10(5)–10(5)
	2.00	19	etched rhombohedra-spheres	10(5)–10(5)
CO_3-gel pH = 10.5	0.20	100	rhombohedra *	15(5)
	0.35	100	rhombohedra *	10(5)
	0.40	100	rhombohedra *	10(5)
	2.00	54	Rhombohedra-spheres	10(5)–10(5)

* Indicates the presence of a high number of hemispherical cavities on the {10.4} faces. # Values in parenthesis indicates the standard deviation.

The results of morphological analyses (SEM) are consistent with structural analyses of precipitate. Thus, Figure 1 shows the typical morphologies of crystals isolated five days after initiating the precipitation in different xanthan gels. In the system Ca-gel, pH = 9.0, and lower concentrations of xanthan (c_{xan} = 0.20 wt % and 0.35 wt %) the obtained calcite single crystals were elongated along the *c* axis: Some of the latter showed hemispherical cavities. In the precipitate obtained by using, c_{xan} = 0.40 wt %, the calcite crystals are actually the assembly of subcrystals, etched on the {104} faces. At c_{xan} = 2.00 wt % the SEM showed predominantly single spheres having a smooth surface and few elongated calcite crystals showing {011} faces and {104} faces. In the Ca-gel, pH = 10.5 system and c_{xan} = 0.20 wt %, calcite appeared as {104} rhombohedra single crystals in which some {104} showed hemispherical cavities. At a c_{xan} = 0.35 wt % the calcite crystals showed aggregation and the morphology was not regular, while at increased concentration, c_{xan} = 0.40 wt %, the rhombohedral calcite crystals were elongated along the *c*-axis. At the highest concentration, c_{xan} = 2.00 wt %, the precipitate consists of spheres, having a smooth surface and sometimes joined with calcite crystal with cavities. In some cases, the spheres fill calcite crystals (Figure S8). The precipitates observed in the CO_3-gel pH = 10.5 systems, c_{xan} < 2.0 wt %, were rather similar to Ca-gel, pH = 10.5 and c_{xan} = 0.35 wt %: Calcite appeared in a form of single crystals in which some of the {104} faces showed cavities. However, when the applied xanthan concentration was the highest, c_{xan} = 2.00 wt %, the precipitate consisted of {104} rhombohedral calcite and aggregates of spheres with rough surfaces.

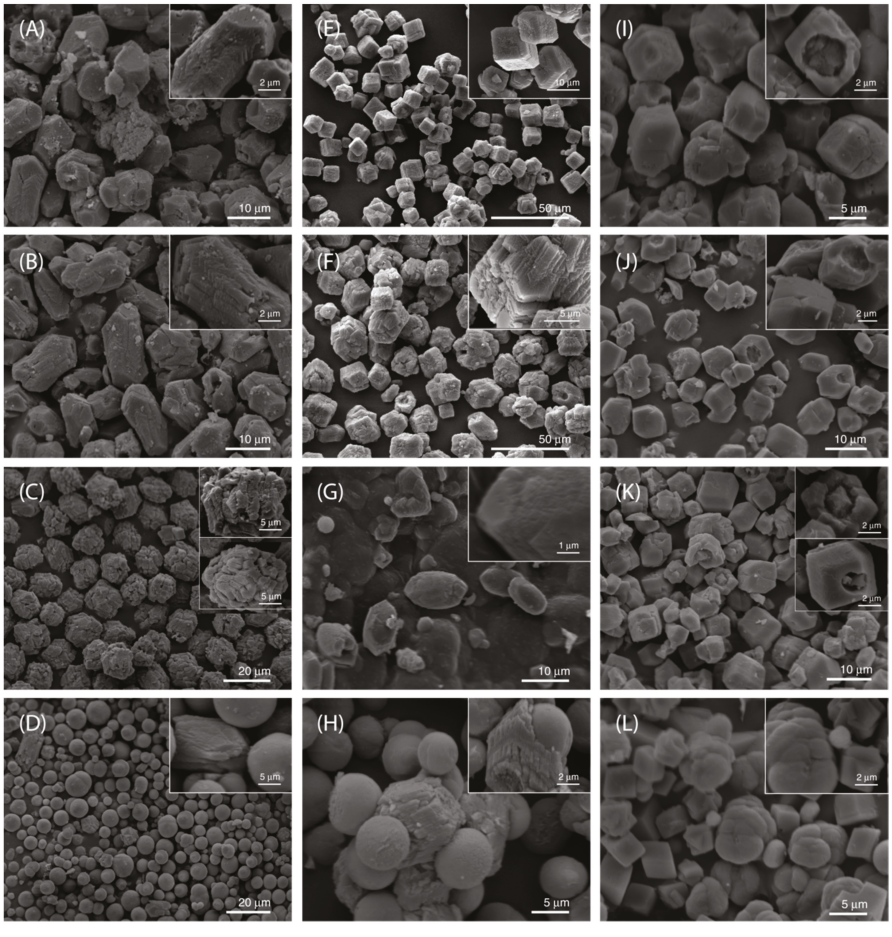

Figure 1. SEM micrographs of $CaCO_3$ precipitated in xanthan hydrogels, prepared by different procedures and concentration of polysaccharide. Precipitate was isolated 5 days after initiating the process. (**A**–**D**) sample prepared using the system Ca-gel, pH = 9.0 and c_{xan} = 0.20 wt % (**A**); c_{xan} = 0.35 wt % (**B**); c_{xan} = 0.40 wt % (**C**); c_{xan} = 2.00 wt % (**D**). (**E**–**H**) sample prepared using the system Ca-gel, pH = 10.5 and c_{xan} = 0.20 wt % (**E**); c_{xan} = 0.35% (**F**); c_{xan} = 0.40 wt % (**G**); c_{xan} = 2.00 wt % (H). (**I**–**L**) sample prepared using the system CO_3-gel, pH = 10.5 and c_{xan} = 0.20 wt % (**I**); c_{xan} = 0.35% (**J**); c_{xan} = 0.40 wt % (**K**); c_{xan} = 2.0 wt % (**L**). The images are representative of the entire populations of particles.

Similar gradual change of calcite morphology with increasing xanthan gel concentration (from compact rhombohedral crystals to spherical aggregates) has been described in the system in which crystallization was initiated in $(NH_4)_2CO_3$-$CaCl_2$ systems [43]. The authors used xanthan as a model of the exopolysaccharides excreted by soil bacteria, which are supposed to be responsible for accumulation of terrestrial carbonates. The observed formation of spherical calcite and vaterite was explained with increased diffusivity (viscosity) of the medium and the presence of carboxyl groups, which were additionally introduced into a form of acidic amino acids.

It should be emphasized that in all xanthan systems and c_{xan} = 2.00 wt %, a mixture of calcite and vaterite precipitated. Thus, spherical aggregates of vaterite, calcite rhombohedra or rhombohedral

calcite aggregates were observed. High fraction of not-transformed vaterite in these systems can be explained by assuming a simultaneous nucleation and crystal growth of metastable and stable polymorphs and subsequent transformation of metastable phases, either by solution mediated, or a solid-state mechanism. During the transformation process, dissolution of vaterite and growth of calcite crystals occur simultaneously. It was found previously that in pure aqueous systems [44] vaterite dissolution is controlled by the diffusion of constituent ions (Ca^{2+} and CO_3^{2-}) away from the crystal surfaces, while calcite growth is controlled by surface process. At conditions of high concentration of macromolecules and restricted diffusivity, vaterite dissolution becomes the rate determining step of the overall transformation process. Therefore, at the highest xanthan concentrations, the vaterite content is still high. In most of the systems, size of the particles varied in the range from 10 to 15 μm, without any systematic correlation between their sizes and xanthan concentration. In addition, in the systems of the highest gel concentration (c_{xan} = 2.0 wt %) two polymorphs could be observed: Spherical vaterite particles and prismatic calcite, which are of different size. However, the vaterite aggregates, which are trapped within a calcite crystal, indicate the initial growth of both polymorphs in a limited space (Figure S8).

In order to prove the incorporation of xanthan molecules by $CaCO_3$, the thermogravimetric analyses (TGA) of selected samples have been done. Thus, in the system Ca-gel, pH = 10.5, c_{xan} = 0.2 wt %, a mass loss of about 0.8%, in the range of temperatures between 50–150 °C was observed. This loss corresponds to water molecules, while loss of about 1.0%, obtained within the range, 150–400 °C, corresponds to the decomposition of the organic matter. In the similar system, Ca-gel, pH = 10.5, c_{xan} = 0.35 wt %, about 0.3% of water (60–150 °C) and 0.9% of organic matter (150–400 °C) detected. The results are comparable to those described in literature for calcite precipitation in the presence of relatively low content of xanthan (c = 0.05%) and different initial concentrations of Ca^{2+} and CO_3^{2-} [45]. Thus, the authors found that about 1% of xanthan could be incorporated into the calcite which grow in system [Ca^{2+}] = [CO_3^{2-}] = 16 mmol dm^{-3}, while at higher concentration, [Ca^{2+}] = [CO_3^{2-}] = 32 mmol dm^{-3}, the incorporated amount is lower, 0.27%. Similar investigations in the agarose hydrogels of different strengths and degree of entanglements [7,46] showed exactly the opposite trend of incorporation of gelling polysaccharide into the calcite structure. Thus, the increase of the Ca^{2+} concentration from 5 mmol dm^{-3} to 30 mmol dm^{-3} caused the increase of the agarose incorporation in the range from about 0.5 wt % to 0.9 wt %. The authors also proposed different models of incorporation, which assumed a competition between parameters like the strength of the gel, growth rate or specific crystal/agarose interactions.

2.2. $CaCO_3$ Precipitation in Alginate Gels

The concentrations of alginate used for precipitation experiments varied in the range from 0.20 wt % to 2.00 wt % with the respect to water and precipitation started immediately after mixing the reactants. The results of structural analyses of precipitate (P-XRD and FT-IR) are shown in Table 2 and in Figure S1, while Figures S4, S5 and S7 show the typical X-ray diffractograms and FT-IR spectra. Thus, in the Ca-gel, pH = 10.5, mixture of calcite and vaterite was observed, while predominantly calcite precipitated in the Ca-gel, pH = 9.0 and CO_3-gel, pH = 10.5 systems. In the Ca-gel, pH = 9.0 and lowest alginate concentration, vaterite was observed as well. In all gelling systems, the largest $CaCO_3$ particles were observed at the lowest alginate concentration (c_{alg} = 0.20 wt %). However, at higher gel concentrations, the average size of the particles decreased but no distinct correlation between the size distribution and gel concentration was observed.

Table 2. Mineralogical composition, shape and average size (referred to the longest axis of single particle or aggregate) of precipitate (calcite and vaterite) prepared in different alginate gels and $c_i(CaCl_2) = c_i(Na_2CO_3) = 0.066$ mol dm^{-3}, $t = 5$ days.

	c_{alg}/wt %	w_{calc}/wt %	Shape	L/μm [#]
Ca-gel pH = 9.0	0.20	78	rhombohedra */spheres	10(3)–5(1)
	0.50	100	rhombohedra	5(2)
	0.80	100	rhombohedra *	5(2)
	2.00	100	rhombohedra *	5(2)
Ca-gel pH = 10.5	0.20	63	rhombohedra *-spheres	15(5)–5(2)
	0.50	76	rhombohedra *-spheres	10(5)–5(3)
	0.80	61	rhombohedra *-spheres	10(5)–5(4)
	2.00	77	rhombohedra *-spheres	10(5)–5(3)
CO_3-gel pH = 10.5	0.20	100	rhombohedra *	15(5)
	0.50	100	rhombohedra	10(3)
	0.80	100	rhombohedra	10(5)
	2.00	100	rhombohedra	10(5)

* Indicates the presence of a high number of hemispherical cavities on the {10.4} faces. [#] Values in parenthesis indicates the standard deviation.

Typical SEM micrographs of the dried $CaCO_3$ samples, precipitated in different alginate gels are shown in Figure 2. Thus, calcite crystals precipitated in the CO_3-gel, pH = 10.5 appeared in the form of stack-like or polyhedral aggregates, built up of prismatic primary particles. On the other hand, the rosette-like aggregates are predominant calcite forms in both Ca-gels. This is in agreement with findings of some other authors that precipitated $CaCO_3$ in presence of alginate or xanthan, but at concentrations lower than critical for gel formation [45,47]. The predominant formation of rosette-like calcite was explained by its nucleation on a gelled microparticles template. However, predominant growth of stuck-like calcite morphology in the xanthan systems has been explained by its nucleation directly on ionized carboxylate groups along the backbone of polysaccharide molecules (see SI: Description of molecular gelling process) [38–42]. In comparison to literature data, the systems investigated in this work are additionally complicated by strong gel formation and initial precipitation of metastable and stable solid phases in close physical contact. Thus, Figure S9, shows vaterite and calcite particles merged in a single phase in the alginate system in which vaterite to calcite transformation was not completed (Ca-gel, pH = 10.5, c(alg) = 0.8 wt %). Contrarily, in the systems in which the solution-mediated process of transformation was completed, the cavities in the calcite crystals are visible (CO_3-gel, pH = 10.5, c_{alg} = 0.8 wt % and Ca-gel, pH = 9.0, c_{alg} = 0.8 wt %). The effect is stronger than in the xanthan gels of comparable concentration, which can be explained by difference between their gelling mechanism: Strong crosslinking between alginate molecules with divalent cations, versus the hydrogen bonding in xanthan. In addition, it should be considered that xanthan contains less COOH groups that could initially interact with solid phases (1 COOH per monosaccharide unit in alginate, versus 2/5 COOH per monosaccharide in xanthan).

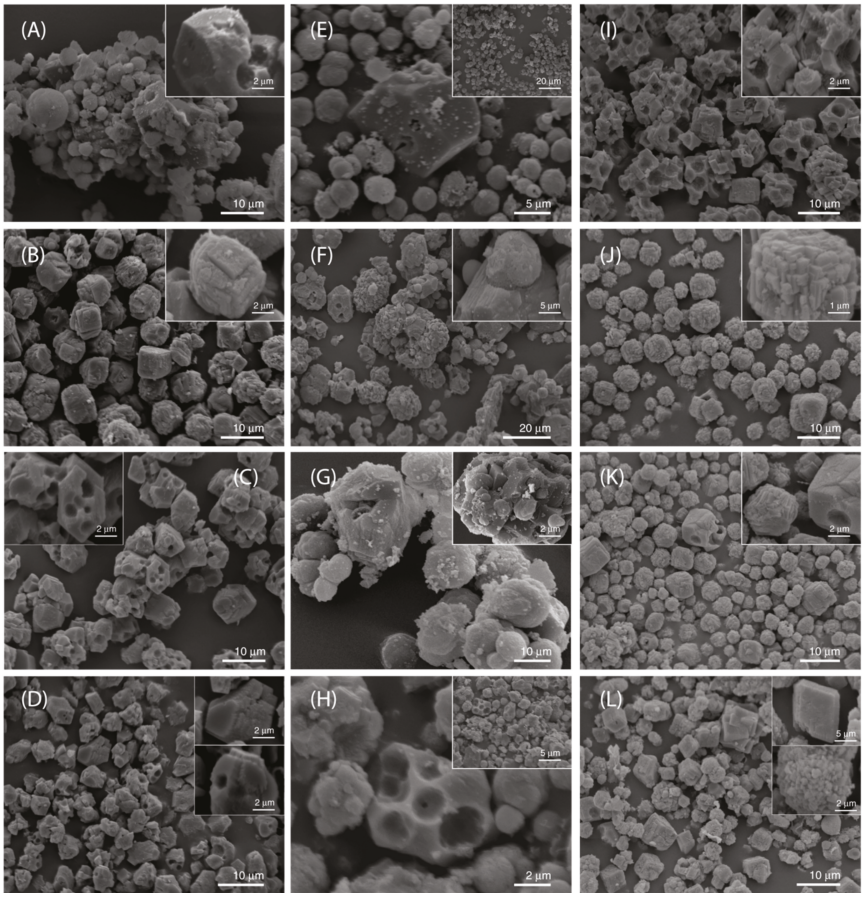

Figure 2. SEM micrographs of $CaCO_3$ precipitated in alginate hydrogels, prepared by different procedures and concentration of polysaccharide. Precipitates are isolated 5 days after initiating the process. (**A**–**D**) sample prepared using the system Ca-gel, pH = 9.0 and c_{alg} = 0.2 wt % (**A**); c_{alg} = 0.5 wt % (**B**); c_{alg} = 0.8 wt % (**C**); c_{alg} = 2.0 wt % (**D**). (**E**–**H**) sample prepared using the system Ca-gel, pH = 10.5 and c_{alg} = 0.2 wt % (**E**); c_{alg} = 0.5 wt % (**F**); c_{alg} = 0.8 wt % (**G**); c_{alg} = 2.0 wt % (**H**). (**I**–**L**) sample prepared using the system CO_3-gel, pH = 10.5 and c_{alg} = 0.2 wt % (**I**); c_{alg} = 0.5 wt % (**J**); c_{alg} = 0.8 wt % (**K**); c_{alg} = 2.0 wt % (**L**). The images are representative of the entire populations of particles.

2.3. Kinetics of $CaCO_3$ Phase Transition in the Alginate Gels

The assumed initial and simultaneous formation of several $CaCO_3$ phases in alginate gels was confirmed by time resolved precipitation experiments in a moderately strong gelling environment (Ca-gel, pH = 9.0, c_{alg} = 0.8 wt %). Figure 3A shows SEM micrographs of mineral particles isolated immediately after formation of precipitate and after termination of the process (Figure 3B). Indeed, typical vaterite spherulitic aggregates can be seen at the early stages of the process, while irregular prismatic calcite crystals with spherical imprints were found at later stages. The existence of both, metastable and stable polymorphs in alginate gelling systems are similar to findings of Dias-Dosque et al. [48], obtained by spin-coating techniques and a slow CO_2 diffusion. The semi quantitative FT-IR analysis of mineral samples [49] separated from the gel at time intervals coincide with the SEM observations (Figure 4). It is shown that vaterite content decreased from about 80 wt % at

the beginning of the process and dropped to zero after 24 h. The observed relatively fast transformation of vaterite crystals is apparently in contradiction to the results of $CaCO_3$ growth in the system in which alginate and Ca^{2+} have slowly released from respective gels [29]. In these systems, in which CO_2 diffusion technique was used, vaterite remained stabilized for 8 days, which is probably the consequence of continuous supply of Ca^{2+} and CO_3^{2-}. Their concentrations were obviously high enough to keep the supersaturation level above the vaterite solubility and, as a result, hindered the dissolution. Unfortunately, such experimental setup does not provide the information on solution composition, which is crucial for understanding the mechanisms of formation of specific phases. However, in the experimental setup applied in this work, the initial supersaturation could be estimated and the continuous sampling for the FT-IR analyses applied. The analyses indicated that, besides the crystalline polymorphs, the amorphous $CaCO_3$ also existed at the early stages of the process. It was identified according to the normal vibration frequencies of carbonate ions at about 1490 and 1430 cm^{-1} (ν_{3a}, ν_{3b}), 1080 cm^{-1} (ν_1), 866 cm^{-1} (ν_2), 725 and 690 cm^{-1} (ν_{4a}, ν_{4b}) [50–52]. Since, ν_2 and ν_4 bands cannot be detected in the mixtures with high content of polymorphs, the ratios of the intensities of ν_2 and ν_4 absorption bands of calcite were measured [53,54]. In the case of pure calcite, the ratio is about 3, while in the mixtures with ACC, it increases as a consequence of the absence of ν_4 absorption of ACC in the 713 cm^{-1} region. Thus, it was found that the ν_2/ν_4 of the sample isolated at the beginning of the crystallization was about 7.7, while after 24 h it drops to 2.3.

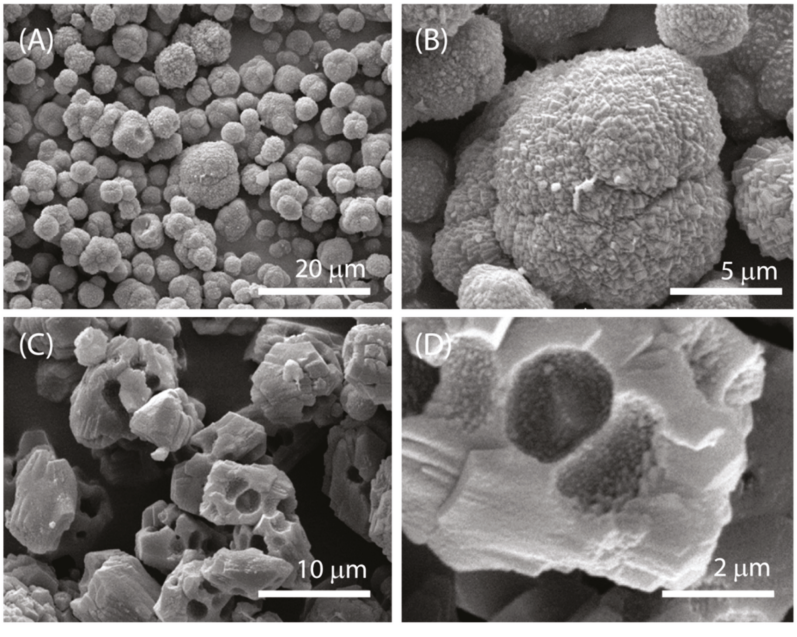

Figure 3. SEM micrographs of $CaCO_3$ precipitated in Ca-gel, pH = 9.0 and c_{alg} = 0.8 wt %, isolated from the system immediately after onset of the crystallization (**A**,**B**) and after 24 h (**C**,**D**). The higher magnification micrographs are shown on the right side. The images are representative of the entire populations of particles.

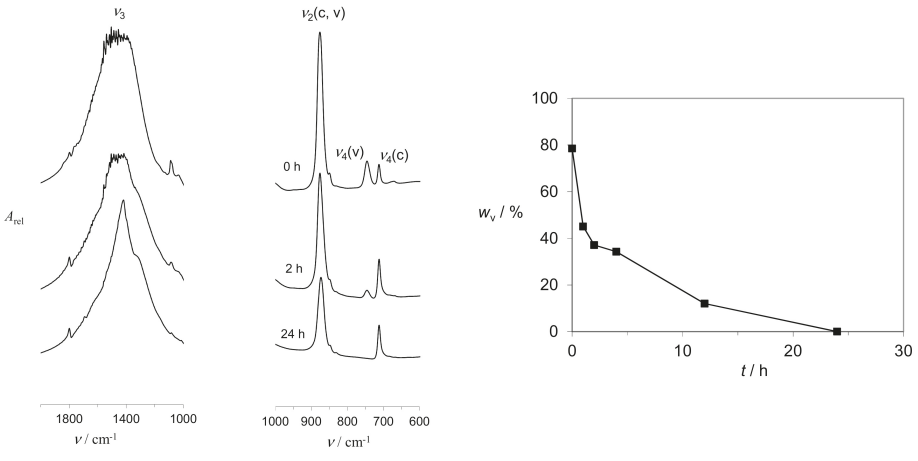

(**a**) (**b**)

Figure 4. (**a**) The FT-IR spectra of typical $CaCO_3$ samples precipitate in Ca-gel (pH = 9.0; c_{alg} = 0.8 wt %) and separated at respective time intervals. The absorption bands of calcite and vaterite at 712 cm^{-1} and 745 cm^{-1} are indicated. (**b**) The change of vaterite/calcite content with time, estimated by comparison of the intensities of ν_4 normal vibrations of carbonate ions in vaterite (v) and calcite (c).

The expected incorporation of the alginate molecules into the $CaCO_3$ precipitate was tested by TGA analyses of the samples isolated at selected time intervals. The results show (Table S1) that the precipitate which consisted of calcite (t = 24 h) incorporated significantly less organic matter and water in comparison to systems containing vaterite. However, no straightforward correlation between the TG data and the vaterite or calcite content was found, which indicates that the water and organic matter are not uniformly distributed within the gel and mineral phases. However, the correlation can be found between the vaterite content and the total amount of incorporated water and alginate macromolecules. Similar measurements were made in the system Ca-gel, pH = 10.5, c_{alg} = 0.8 wt %, in which about 39% of vaterite was found after five days of aging. It was determined that about 3.2% of water and 5.3% of organic matter are incorporated into the precipitate, which is qualitatively consistent with data obtained from kinetics.

3. Materials and Methods

The chemicals used to prepare reactant solutions, $CaCl_2$ and Na_2CO_3, were analytically pure and the deionized water was of high quality (conductivity < 0.055 μS cm^{-1}). Sodium carbonate solution, c = 0.20 mol dm^{-3}, was prepared by dissolving anhydrous Na_2CO_3 in water, while calcium chloride solution, c = 0.20 mol dm^{-3}, was made by diluting appropriate $CaCl_2$ stock.

The polysaccharides used for gel preparation were kindly supplied by Danicso. Xanthan gum was produced by a fermentation process of bacteria *Xanthomonas campestris*, while sodium alginate was produced from brown seaweed, mainly *Laminaria digitata* species. The appropriate polysaccharide stock solutions were prepared by the addition of respective amount of dry powder into deionized water at 70–80 °C and intensive stirring until complete dissolution. Three different protocols of simultaneous calcium carbonate precipitation and gel formation were employed.

3.1. CO_3-Gel, pH = 10.5

50 cm^3 of hot (70–80 °C) polysaccharide (alginate or xanthan) solution of respective concentration was mixed with 50 cm^3 of Na_2CO_3 solution (c = 0.20 mol dm^{-3}, pH = 11.5) and intensively stirred. Precipitation was initiated by rapid addition of 50 cm^3 of $CaCl_2$ solution (c = 0.20 mol dm^{-3}) into

100 cm^3 of thus prepared Na_2CO_3/polysaccharide mixture. The pH of $CaCl_2$ solution was previously adjusted by the addition of NaOH, to the value, pH = 10.5. The obtained suspension was aged for 5 days at room temperature.

3.2. C-Gel, pH = 9.0

50 cm^3 of hot (70–80 °C) polysaccharide (alginate or xanthan) solution of respective concentration was mixed with 50 cm^3 of $CaCl_2$ solution (c = 0.20 mol dm^{-3}) and intensively stirred. The pH of $CaCl_2$ solution was previously adjusted by the addition of NaOH to the value, pH = 9.0. Precipitation was initiated by rapid addition of 50 cm^3 of Na_2CO_3 solution (c = 0.20 mol dm^{-3}, pH = 11.5) into 100 cm^3 of thus prepared $CaCl_2$/polysaccharide mixture. The obtained suspension was aged for 5 days at room temperature.

3.3. Ca-Gel, pH = 10.5

50 cm^3 of hot (70–80 °C) polysaccharide (alginate or xanthan) solution of respective concentration was mixed with 50 cm^3 of $CaCl_2$ solution (c = 0.20 mol dm^{-3}) and intensively stirred. The pH of $CaCl_2$ solution was previously adjusted by the addition of NaOH to the value, pH = 10.5. Precipitation was initiated by rapid addition of 50 cm^3 of Na_2CO_3 solution (c = 0.20 mol dm^{-3}, pH = 11.5) into 100 cm^3 of thus prepared $CaCl_2$/polysaccharide mixture. The obtained suspension was aged for 5 days at room temperature.

3.4. Model System

Precipitation was initiated by rapid addition of 50 cm^3 of Na_2CO_3 solution (c = 0.20 mol dm^{-3}, pH = 11.5) into 100 cm^3 of magnetically stirred $CaCl_2$ solution, (c = 0.20 mol dm^{-3}, pH = 6.7). The progress of the reaction was followed by measuring the pH. The system was aged for 24 h.

At the end of each experiment, the suspension was centrifuged, the precipitate was washed several times with saturated calcite solution and dried at 105 °C for 3 h. Thermogravimetric analyses of precipitates were performed by means of Mettler TG 50 thermobalance, equipped with TC 10 TA processor, at rate 10 K/min. Qualitative and semi quantitative composition of the dried precipitate was determined by means of FT-IR spectroscopy (FT-IR Bruker, Tensor II) using KBr pellet technique [35] and by X-ray powder diffraction (XRD) using an automatic Philips diffractometer, model PW1820 (CuKα radiation, graphite monochromator, proportional counter) in Bragg-Brentano geometry. The diffraction intensities were measured in the angular range $10^\circ \leq 2\Theta \leq 70^\circ$. Step size was set to 0.02° of 2θ with measuring time of 2 s per step. Calcite and vaterite were identified according to the ICDD Powder Diffraction File [55]. In order to determine the mole fractions of calcite and vaterite in the samples, a calibration curve, correlating the intensity ratios of selected diffraction lines and the mole ratio of calcite and vaterite, was constructed. The morphologies of the precipitate were observed by optical microscopy (Orthoplan photographic microscope, E. Leitz, Wetzlar, Germany) and by scanning electron microscopy, SEM (Hitachi 6400) operating at 20 kV. For the SEM observations, the samples were glued by a carbon tape on the aluminum stub and gold sputtered.

Calculation of the initial solution composition (supersaturation) was based on the known total calcium chloride and sodium carbonate concentrations and the known NaOH concentration used for pH adjustment. The initial supersaturation was defined as relative supersaturation, $S = (\Pi/K_{sp})^{1/2}$, where Π is the ion activity product, $\Pi = a(Ca^{2+})\cdot a(CO_3^{2-})$, and K_{sp} is the thermodynamic solubility product of calcite ($K_{sp} = 3.313 \times 10^{-9}$), vaterite ($K_{sp} = 1.221 \times 10^{-8}$) or amorphous calcium carbonate (ACC) ($K_{sp} = 3.976 \times 10^{-7}$) [37] at 25 °C. Detailed calculation procedure, which considers the respective protolytic equilibria and equilibrium constants, as well as the charge and mass balance equations, was shown previously [56,57]. However, it should be emphasized that in the case of precipitation in gels, the presence of the respective polysaccharide was not considered so the calculated initial supersaturation is given only for comparison with bulk precipitation experiments.

4. Conclusions

Precipitation of calcium carbonate was investigated in xanthan and alginate hydrogels in which the concentration of polysaccharide molecules varied in the range from 0.2 to 2.0%.

Precipitation was performed simultaneously with the gel formation and was initiated by a fast addition of reactants (Ca^{2+} or CO_3^{2-} solutions) into hot CO_3-polysaccharid or Ca-polysaccharide solutions, respectively. Relatively high initial supersaturation was selected in order to exceed the threshold values for starting the nucleation in both gelling systems and at all concentrations of macromolecules. In addition, high initial supersaturation provided the environment for initial and simultaneous formation of different polymorphic modification of calcium carbonate. Simultaneous nucleation and growth of spherical vaterite aggregates and prismatic calcite crystals in the confined space resulted in the formation of hybrid, ingrown structures. After dissolution of vaterite, which is a result of aging of the precipitate, calcite crystals with spherical imprints remained.

In the model systems (no polysaccharide), a mixture of calcite, vaterite and amorphous calcium carbonate precipitated initially, but due to the solution-mediated process of transformation, only calcite remained in the solution after 24 h. Transformation (dissolution) of ACC typically finished after five min.

In the presence of lowest concentrations of xanthan gel, the precipitate aged for five days consisted predominantly of calcite single crystals with developed {011} faces, elongated along *c* axis and capped with {104} faces. At moderate xanthan concentrations, the porous polyhedral aggregates were found after five days of aging. At the highest xanthan gel concentration, a substantial amount of not-transformed vaterite was observed in all systems, thus pointing out to the strong inhibition of vaterite dissolution.

In the CO_3-alginate gels of all concentrations, calcite was the only calcium carbonate polymorph found after five days of aging, while in the Ca-gels the vaterite was found as well. In the CO_3-gels, calcite appeared in a form of microcrystalline aggregates, while in Ca-gels the rosette-like or stuck-like monocrystals was found.

Time resolved crystallization experiments in moderately strong Ca-alginate hydrogels, showed that a mixture of calcite, vaterite and amorphous calcium carbonate formed initially. After 24 h of aging, only calcite remained in suspension. In comparison to the model system, transformation of amorphous calcium carbonate was significantly inhibited and it was detected even after four h of aging.

Calcite samples isolated from gelling systems typically incorporate less than 1% of water molecules and about 1% of macromolecules. The incorporation of water into the samples containing vaterite is significantly higher and up to 6.8% was determined. The content of absorbed macromolecules is also much higher and more than 3% was found in all systems.

Described one-step protocols may be useful for preparation of biocompatible $CaCO_3$/alginate or $CaCO_3$/xanthan hydrogel composites, with different gel strength, mineral phase composition and adjustable micro or macro porosity. Indeed, such mixtures may be suitable for diverse applications in the hard tissue engineering and/or drug delivery.

Supplementary Materials: The following are available online at www.mdpi.com/2073-4352/7/12/355/s1.

Acknowledgments: This work was supported (Damir Kralj and Cleo Kosanović) by the Croatian Science Foundation under the project (IP-2013-11-5055). Giuseppe Falini and Simona Fermani thank the Consorzio Interuniversitario per la Chimica dei Metalli nei Sistemi Biologici for the support.

Author Contributions: The manuscript was written through contributions of all authors. All authors have given approval to the final version of the manuscript.

Conflicts of Interest: The authors declare no conflict of interest.

References

1. Brecevic, L.; Kralj, D. On calcium carbonates: From fundamental research to application. *Croat. Chem. Acta* **2007**, *80*, 467–484.

2. Sommerdijk, N.A.J.M.; de With, G. Biomimetic $CaCO_3$ mineralization using designer molecules and interfaces. *Chem. Rev.* **2008**, *108*, 4499–4550. [CrossRef] [PubMed]
3. Gebauer, D.; Völkel, A.; Cölfen, H. Stable prenucleation calcium carbonate clusters. *Science* **2008**, *322*, 1819–1822. [CrossRef] [PubMed]
4. Meldrum, F.C.; Cölfen, H. Controlling mineral morphologies and structures in biological and synthetic systems. *Chem. Rev.* **2008**, *108*, 4332–4432. [CrossRef] [PubMed]
5. Demichelis, R.; Raiteri, P.; Gale, J.D. Structure of hydrated calcium carbonates: A first-principles study. *J. Cryst. Growth* **2014**, *401*, 33–37. [CrossRef]
6. Carlson, W.D. The polymorphs of $CaCO_3$ and the aragonite-calcite transformation. *Rev. Mineral. Geochem.* **1983**, *11*, 191–225.
7. Asenath-Smith, E.; Li, H.; Keene, E.C.; Seh, Z.V.; Estroff, L.A. Crystal growth of calcium carbonate in hydrogels as a model of biomineralization. *Adv. Funct. Mater.* **2012**, *22*, 2891–2914. [CrossRef]
8. Flory, P.J. Introductory lecture. *Faraday Discuss. Chem. Soc.* **1974**, *57*, 7–18. [CrossRef]
9. Estroff, L.A.; Hamilton, A.D. Water gelation by small organic molecules. *Chem. Rev.* **2004**, *104*, 1201–1218. [CrossRef] [PubMed]
10. Nindiyasari, F.; Fernández-Díaz, L.; Griesshaber, E.; Astilleros, J.M.; Sánchez-Pastor, N.; Schmahl, W.W. Influence of gelatin hydrogel porosity on the crystallization of $CaCO_3$. *Cryst. Growth Des.* **2014**, *14*, 1531–1542. [CrossRef]
11. Max, A.; Lauffer, M.A. Theory of diffusion in gels. *Biophys. J.* **1961**, *1*, 205–213.
12. Kosanovic, C.; Falini, G.; Kralj, D. Mineralization of calcium carbonates in gelling media. *Cryst. Growth Des.* **2011**, *11*, 269–277. [CrossRef]
13. Xie, M.; Olderoy, M.O.; Andreassen, J.P.; Selbach, S.M.; Strand, B.L.; Sikorski, P. Alginate-controlled formation of nanoscale calcium carbonate and hydroxyapatite mineral phase within hydrogel networks. *Acta Biomater.* **2010**, *6*, 3665–3675. [CrossRef] [PubMed]
14. Munro, N.H.; McGrath, K.M. Biomimetic approach to forming chitin/aragonite composites. *Chem. Commun. (Camb.)* **2012**, *48*, 4716–4718. [CrossRef] [PubMed]
15. Volodkin, V.; Petrov, A.I.; Prevot, M.; Sukhorukov, G.B. Matrix polyelectrolyte microcapsules: New system for macromolecule encapsulation. *Langmuir* **2004**, *20*, 3398–3406. [CrossRef] [PubMed]
16. Trushina, D.B.; Bukreeva, T.V.; Kovalchuk, M.V.; Antipina, M.N. $CaCO_3$ vaterite microparticles for biomedical and personal care applications. *Mater. Sci. Eng. C* **2014**, *45*, 644–658. [CrossRef] [PubMed]
17. Volodkin, D.; Klitzing, R.; Möhwald, H. Pure protein microspheres by calcium carbonate templating. *Angew. Chem. Int. Ed.* **2010**, *122*, 9444–9447. [CrossRef]
18. Lengert, E.; Saveleva, M.; Abalymov, A.; Atkin, V.; Wuytens, P.C.; Kamyshinsky, R.; Vasiliev, A.L.; Gorin, D.A.; Sukhorukov, G.B.; Skirtach, A.G.; et al. Silver alginate hydrogel micro- and nanocontainers for theranostics: Synthesis, encapsulation, remote release, and detection. *ACS Appl. Mater. Interfaces* **2017**, *9*, 21949–21958. [CrossRef] [PubMed]
19. Parakhonskiy, B.V.; Yashchenok, A.M.; Konrad, M.; Skirtach, A.G. Colloidal micro- and nano-particles as templates for polyelectrolyte multilayer capsules. *Adv. Colloid Interface Sci.* **2014**, *207*, 253–264. [CrossRef] [PubMed]
20. Yashchenok, A.; Parakhonskiy, B.; Donatan, S.; Kohler, D.; Skirtachad, A.; Mohwald, H. Polyelectrolyte multilayer microcapsules templated on spherical, elliptical and square calcium carbonate particles. *J. Mater. Chem. B* **2013**, *1*, 1223–1228. [CrossRef]
21. Yi, Q.; Sukhorukov, G.B. Externally triggered dual function of complex microcapsules. *ACS Nano* **2013**, *7*, 8693–8705. [CrossRef] [PubMed]
22. Donatan, S.; Yashchenok, A.; Khan, N.; Parakhonskiy, B.; Cocquyt, M.; Pinchasik, B.; Khalenkow, D.; Möhwald, H.; Konrad, M.; Skirtach, M. Loading capacity versus enzyme activity in anisotropic and spherical calcium carbonate microparticles. *ACS Appl. Mater. Interfaces* **2016**, *8*, 14284–14292. [CrossRef] [PubMed]
23. Svenskaya, Y.I.; Fattah, H.; Zakharevich, A.M.; Gorin, D.A.; Sukhorukov, G.B.; Parakhonskiy, B.V. Ultrasonically assisted fabrication of vaterite submicron-sized carriers. *Adv. Powder Technol.* **2016**, *27*, 618–624. [CrossRef]
24. Douglas, T.E.L. *Biomimetic Mineralization of Hydrogels in Biomineralization and Biomaterials, Fundamentals and Applications*; Aparicio, C., Ginebra, M., Eds.; Woodhead Publishing: Cambridge, UK; 2015; pp. 291–313.
25. Gkioni, K.; Leeuwenburgh, S.C.; Douglas, T.E.; Mikos, A.G.; Jansen, J.A. Mineralization of hydrogels for bone regeneration. *Tissue Eng. B* **2010**, *16*, 577–585. [CrossRef] [PubMed]

26. Douglas, T.E.L.; Sobczyk, K.; Łapa, A.; Włodarczyk, K.; Brackman, G.; Vidiasheva, I.; Reczyńska, K.; Pietryga, K.; Schaubroeck, D.; Bliznuk, V.; et al. Ca:Mg:Zn:CO_3 and Ca:Mg:CO_3—tri- and bi-elemental carbonate microparticles for novel injectable self-gelling hydrogel–microparticle composites for tissue regeneration. *Biomed. Mater.* **2017**, *12*, 025015. [CrossRef] [PubMed]
27. Jang, J.; Seol, Y.J.; Kim, H.J.; Kundu, J.; Kim, S.W.; Cho, D.W. Effects of alginate hydrogel cross-linking density on mechanical and biological behaviors for tissue engineering. *J. Mech. Behav. Biomed. Mater.* **2014**, *37*, 69–77. [CrossRef] [PubMed]
28. Kuo, C.K.; Ma, P.X. Maintaining dimensions and mechanical properties of ionically crosslinked alginate hydrogel scaffolds in vitro. *J. Biomed. Mater. Res. A* **2008**, *84*, 899–907. [CrossRef] [PubMed]
29. Corni, I.; Harvey, T.J.; Wharton, J.A.; Stokes, K.R.; Walsh, F.C.; Wood, R.J.K. A review of experimental techniques to produce a nacre-like structure. *Bioinspir. Biomim.* **2012**, *7*, 031001. [CrossRef] [PubMed]
30. Bidarra, S.J.; Barrias, C.C.; Fonseca, K.B.; Barbosa, M.A.; Soares, R.A.; Granja, P.L. Injectable in situ crosslinkable RGD-modified alginate matrix for endothelial cells delivery. *Biomaterials* **2011**, *32*, 7897–7904. [CrossRef] [PubMed]
31. Ogomi, D.; Serizawa, T.; Akashi, M. Bioinspired organic–inorganic composite materialsprepared by an alternate soaking process as a tissue reconstitution matrix. *J. Biomed. Mater. Res. A* **2003**, *67*, 1360–1366. [CrossRef] [PubMed]
32. Suzawa, Y.; Funaki, T.; Watanabe, J.; Iwai, S.; Yura, Y.; Nakano, T.; Umakoshi, Y.; Akashi, M. Regenerative behavior of biomineral/agarose composite gels as bone grafting materials in rat cranial defects. *J. Biomed. Mater. Res. A* **2010**, *93*, 965–975. [CrossRef] [PubMed]
33. Munro, N.H.; McGrath, K.M. Biomimetic mineralisation of polymeric scaffolds using a combined soaking approach: Adaptation with various mineral salts. *Dalton Trans.* **2011**, *40*, 9269–9275. [CrossRef] [PubMed]
34. Li, H.; Estroff, L.A. Hydrogels coupled with self-assembled monolayers: An in vitro matrix to study calcite biomineralization. *J. Am. Chem. Soc.* **2007**, *129*, 5480–5483. [CrossRef] [PubMed]
35. Helbig, U. Growth of calcium carbonate in polyacrylamide hydrogel: Investigation of the influence of polymer content. *J. Cryst. Growth* **2008**, *310*, 2863–2870. [CrossRef]
36. Sancho-Tomas, M.; Fermani, S.; Goeffredo, S.; Dubinsky, Z.; Garcia-Ruiz, J.M.; Gomez-Morales, J.; Falini, G. Exploring coral biomineralization in gelling environment by means of a counter diffusion system. *CrystEngComm* **2014**, *16*, 1257–1267. [CrossRef]
37. Sancho-Tomas, M.; Fermani, S.; Duran-Olivencia, M.D.; Otalora, F.; Gomez-Morales, J.; Falini, G.; Garcia-Ruiz, J.M. Influence of carged polypeptides on nucleation and growth of $CaCO_3$ evaluated by counterdiffusion experiments. *Cryst. Growth Des.* **2013**, *13*, 3884–3891. [CrossRef]
38. Iijima, M.; Shinozaki, M.; Hatakeyama, T.; Takahashi, M.; Hatakeyama, H. AFM studies on gelation mechanism of xanthan gum hydrogels. *Carbohydr. Polym.* **2007**, *68*, 701–707. [CrossRef]
39. Takahashi, M.; Hatakeyama, T.; Hatakeyama, H. Phenomenological theory describing the behaviour of non-freezing water in structure formation process of polysaccharide aqueous solutions. *Carbohydr. Polym.* **2000**, *41*, 91–95. [CrossRef]
40. Smidsrød, O. Molecular basis for some physical properties of alginates in the gel state. *Faraday Discuss. Chem. Soc.* **1974**, *57*, 263–274. [CrossRef]
41. Huynh, U.T.D.; Lerbret, A.; Neiers, F.; Chambin, O.; Assifaoui, A. Binding of divalent cations to polygalacturonate: A mechanism driven by the hydration water. *J. Phys. Chem. B* **2016**, *120*, 1021–1032. [CrossRef] [PubMed]
42. Leea, K.Y.; Mooneya, D.J. Alginate: Properties and biomedical applications. *Prog. Polym. Sci.* **2012**, *37*, 106–126. [CrossRef] [PubMed]
43. Braissant, O.; Cailleau, G.; Dupraz, C.; Verrecchia, E.P. Bacterially induced mineralization of calcium carbonate in terrestrial environments: The role of exopolysaccarides and amino acids. *J. Sediment. Res.* **2003**, *73*, 485–490. [CrossRef]
44. Kralj, D.; Brečević, L.; Kontrec, J. Vaterite growth and dissolution in aqueous solutions. III. Kinetics of transformation. *J. Cryst. Growth* **1997**, *177*, 248–257. [CrossRef]
45. Yang, X.; Xu, G. The influence of xanthan on the crystallization of calcium carbonate. *J. Cryst. Growth* **2011**, *314*, 231–238. [CrossRef]
46. Li, H.; Estroff, L.A. Calcite growth in hydrogels: Assessing the mechanism of polymer-network incorporation into single crystals. *Adv. Mater.* **2009**, *21*, 470–473. [CrossRef]

47. Butler, M.F.; Glaser, N.; Weaver, A.C.; Kirkland, M.; Heppenstall-Butler, M. Calcium carbonate crystallization in the presence of biopolymers. *Cryst. Growth Des.* **2006**, *6*, 781–794. [CrossRef]
48. Diaz-Dosque, M.; Aranda, P.; Darder, M.; Retuert, J.; Yazdani-Pedrame, M.; Arias, J.L.; Ruiz-Hitzky, E. Use of biopolymers as oriented supports for the stabilization of different polymorphs of biomineralized calcium carbonate with complex shape. *J. Cryst. Growth* **2008**, *310*, 5331–5340. [CrossRef]
49. Flemming, A.A.; Kralj, D. Determination of the composition of calcite-vaterite mixtures by infrared spectrophotometry. *Appl. Spectrosc.* **1991**, *45*, 1748–1751.
50. Fleming, A.A.; Brecevic, L. Infrared spectra of amorphous and crystalline calcium carbonate. *Acta Chem. Scand.* **1991**, *45*, 1018–1024.
51. Kontrec, J.; Ukrainczyk, M.; Babic-Ivancic, V.; Kralj, D. Synthesis of calcium carbonate by semicontinuous carbonation method in the presence of dextrans. *Croat. Chem. Acta* **2011**, *84*, 25–32. [CrossRef]
52. Kralj, D.; Kontrec, J.; Brecevic, L.; Falini, G.; Nothing-Laslo, V. Effect of inorganic anions on the Morphology and structure of magnesium calcite. *Chem. Eur. J.* **2004**, *10*, 1647–1656. [CrossRef] [PubMed]
53. Raz, S.; Hamilton, P.S.; Wilt, F.H.; Weiner, S.; Addadi, L. The transient phase of amorphous calcium carbonate in sea urchin larval spicules: The involvement of proteins and magnesium ions in its formation and stabilization. *Adv. Funct. Mater.* **2003**, *13*, 480–486. [CrossRef]
54. Beniash, E.; Aizenberg, J.; Addadi, L.; Weiner, S. Amorphous calcium carbonate transforms into calcite during sea urchin larval spicule growth. *Proc. R. Soc. Lond. B* **1997**, *264*, 461–465. [CrossRef]
55. International Centre for Diffraction Data. *Powder Diffraction File, Inorganic Volume*; Table Nos. 88-1087, 86-0174, 83-0578 for Calcilte; 33-0268 for Vaterite; International Centre for Diffraction Data: Swarthmore, PA, USA, 1988.
56. Plummer, L.N.; Busenberg, E. The solubilities of calcite, aragonite and vaterite in CO_2-H_2O solutions between 0 and 90 °C, and an evaluation of the aqueous model for the system $CaCO_3$-CO_2-H_2O. *Geochim. Cosmochim. Acta* **1982**, *46*, 1011–1040. [CrossRef]
57. Kralj, D.; Brecevic, L.; Nielsen, A.E. Vaterite growth and dissolution in aqueous solutions. I. Kinetics of crystal growth. *J. Cryst. Growth* **1990**, *104*, 793–800. [CrossRef]

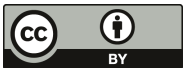

© 2017 by the authors. Licensee MDPI, Basel, Switzerland. This article is an open access article distributed under the terms and conditions of the Creative Commons Attribution (CC BY) license (http://creativecommons.org/licenses/by/4.0/).

crystals

MDPI

Article

Hydrophobic Calcium Carbonate for Cement Surface

Shashi B. Atla [1], Yi-Hsun Huang [2], James Yang [1], How-Ji Chen [2,†,*], Yi-Hao Kuo [2], Chun-Mei Hsu [3], Wen-Chien Lee [3], Chien-Cheng Chen [4], Duen-Wei Hsu [4] and Chien-Yen Chen [1,†,*]

1 Department of Earth and Environmental Sciences, National Chung Cheng University, 168 University Road, Minhsiung, Chiayi County 62102, Taiwan; shashi_org@yahoo.com (S.B.A.); chieyechen@yahoo.com (J.Y.)
2 Department of Civil Engineering, National Chung Hsing University, 250 Kuo Kuang Road, Taichung 4022, Taiwan; x699237014x@gmail.com (Y.-H.H.); yhkao31@gmail.com (Y.-H.K.)
3 Department of Chemical Engineering, National Chung Cheng University, 168 University Road, Ming-Shung, Chiayi County 62102, Taiwan; gupi_girl@livemail.tw (C.-M.H.); chmwcl@ccu.edu.tw (W.-C.L.)
4 Department of Biotechnology, National Kaohsiung Normal University, No.62 Shenjhong Road, Yanchao Township, Kaohsiung County 82444, Taiwan; cheng@nknu.edu.tw (C.-C.C.); duenwei.hsu@gmail.com (D.-W.H.)
* Correspondence: hojichen@nchu.edu.tw (H.-J.C.); chien-yen.chen@oriel.oxon.org (C.-Y.C.); Tel.: +886-5-2720411 (ext. 66220) (C.-Y.C.)
† These authors contributed equally to this work.

Academic Editor: Linda Pastero
Received: 14 November 2017; Accepted: 8 December 2017; Published: 11 December 2017

Abstract: This report describes a novel way to generate a highly effective hydrophobic cement surface via a carbonation route using sodium stearate. Carbonation reaction was carried out at different temperatures to investigate the hydrophobicity and morphology of the calcium carbonate formed with this process. With increasing temperatures, the particles changed from irregular shapes to more uniform rod-like structures and then aggregated to form a plate-like formation. The contact angle against water was found to increase with increasing temperature; after 90 °C there was no further increase. The maximum contact angle of 129° was obtained at the temperature of 60 °C. It was also found that carbonation increased the micro hardness of the cement material. The micro hardness was found to be dependent on the morphology of the $CaCO_3$ particles. The rod like structures which caused increased mineral filler produced a material with enhanced strength. The ^{13}C cross polarization magic-angle spinning NMR spectra gave plausible explanation of the interaction of organic-inorganic moieties.

Keywords: SEM; X-ray diffraction; carbonation; micromechanics; $CaCO_3$; cement

1. Introduction

Synthesis of organic-inorganic hybrids has received a great deal of attention in the field of material science [1] because it can result in the creation of multifunctional materials. The applications of hybrid organic-inorganic materials are found in various fields such as optics, electronics, energy, housing and the environment [2]. The desired function can be delivered from manipulating organic or inorganic or both components.

It is fair to say that modern civilizations have depended to a large degree on concrete material for the history of concrete usage, please see [3]. Various properties of concrete can be fabricated for specific applications. Concrete, however, is potentially vulnerable to a variety of different exposures unless some certain precautions are taken. Durability of concrete has serious economic implications in the form of maintenance and replacement costs of a structure. Therefore, in designing structures, the durability characteristics of the concrete should be evaluated as carefully as other aspects such

as mechanical properties, hardness, and initial coast. Permeability is a determinant parameter that has the largest influence on the durability of concrete; the size and continuity of the pores in hydrated cement mortar would control the coefficient of permeability [4]. To decrease the permeability of concrete, the waterproofing treatment is recognized as an effective way. For waterproofing treatments, it requires the impregnation of concrete walls with hydrophobic agents. Hydrophobic treatment prevents wetting of the concrete's porous structure. A great number of organic additives have been studied as hydrophobic reagents including alkyl-alkoxy silane [5,6], surfactants [7,8], acrylic and polyurethane [6,9]. Concrete carbonation is a process in which carbondioxide reacts with calcium hydroxide [10–12] in the cement matrix to form calcium carbonate and water and the reaction stoichiometry is: $Ca(OH)_2 + CO_2 \rightarrow CaCO_3 + H_2O$.

There are many reports on the synthesis of hydrophobic calcium carbonate via carbonation route [13]. Hydrophobic calcium carbonate leads to many industrial applications. It is used as pigment, mortar, and abrasive and in paper and plastic as a filler [14]. Chen et al. have reported carbonation of $Ca(OH)_2$ to synthesize cubic $CaCO_3$ using dodecanoic acid as modifier [13]. Several organic additives used for synthesizing hydrophobic $CaCO_3$ via carbonation of $Ca(OH)_2$ include oleic acid [15], octadecyl dihydrogen phosphate [16], sodium oleate [17], stearic acid [18], and dodecanoic acid [19]. Various hydrophobic admixtures have been examined for concrete and mortar. In many cases the admixture caused damage, e.g., greater decay of samples in the frost resistance test. Some admixtures are effective, but their selection must be confirmed by further research [20,21].

No study, however, has yet been reported on synthesis of hydrophobic cement surface material via carbonation route. For many years, metal soaps have been studied for the hydrophobic properties, but have not been used in hydrophobising building materials in practice [12]. This is because the by-products of the use of soaps are water-soluble salts that lead to increased hygroscopicity of the material [22]. In addition, it is not recommended to use soaps for the hydrophobising of building surfaces due to its low resistance to dirt, mechanical damage and salinity [23,24]. Another unfavorable factor includes interference with the cement hydration process in the presence of a hydrophobic compound that decreases the compressive strength of materials. Currently, only the organosilicon compounds are used for hydrophobisation concrete with Portland cement. However, the disadvantage of this hydrophobic cement is that it is very expensive [21,25,26].

In this report we describe a feasible single step involving in situ synthesis of hydrophobic cement surface with stearic acid. We found that the temperature of carbonation reaction has a great deal of effect on morphology of $CaCO_3$ and thus the hydrophobicity of the concrete surface. Furthermore, the carbonation and mineralization improved the surface micro hardness of the samples.

2. Experimental Section

Type I Portland cement based on ASTM C150 and Ottawa sand with the size distribution from 0.1 mm to 1 mm were used. A cement mortar was made from Portland cement with saturated surface dry sand, and tap water in the ratio of 4:11:2, and was cast into 2.5 cm cubes in an acrylic mold. The cubes were conserved at room temperature for a day and curing was done by continuous immersion in supersaturated solution of $Ca(OH)_2$ for one week. The cement blocks were then taken for carbonation reaction. Carbonation reaction was done in an autoclave (Autoclave Engineers, V = 500 cm^3) at CO_2 pressure of 2 kgf/cm^2. The organic solution was prepared by taking 1:1 molar ratio (0.004 moles) of stearic acid and sodium hydroxide in 400 mL of deionized water. The mixture was stirred at 70 °C for 5 min and was filled so as to cover cubes in the autoclave. The autoclave was sealed and pressurized with CO_2 to a desired pressure. The carbonation reaction was carried out at different temperatures (30, 60, 90, 120 and 150 °C) for a period of 24 h. After this, the reactor was allowed to attain room temperature and CO_2 gas was vented off, and the cubes were oven dried at 50 °C for one day. The cement cubes without organic solution and carbonation are referred to as "control experiments". The cement cubes with organic solution and without carbonation are referred to as "Ctrl-2 experiments".

A small quantity of the material was scrapped from the cube surface and was characterized by XRD, IR and SEM. Powder X-ray diffraction (XRD) patterns were recorded on a Shimadzu X-ray diffractometer (LabX XRD-6000, Shimadzu, Tokyo, Japan) equipped with Ni-filtered CuKα (λ = 0.1541 nm, 4 kVA, 30 mA) radiation and a graphite crystal monochromator. SEM measurements were carried out on a Leica Stereoscan-440 scanning electron microscope (SEM, Leica, Cambridge, UK) equipped with a Phoenix EDAX attachment (Mahwah, NJ, USA). The water contact angles of the samples were measured using FTA 2000 contact angle goniometer (First Ten Angstroms, Portsmouth, VA, USA) by the sessile drop method using a micro syringe at 25 °C. FTIR spectra of the samples were recorded on a Shimadzu 8300 FTIR spectrometer (Shimadzu, Tokyo, Japan). Microhardness was measured using a micro-indentation tester (Shimadzu Micro Hardness Testers HMV-2, Shimadzu Corporation, Kyoto, Japan). The spectra of solid state NMR were performed using Bruker Avance III 400 NMR Spectrometer (Bruker, Billerica, MA, USA).

3. Results and Discussion

Figure 1 shows the XRD spectrum of the control and the carbonated cement cubes at different temperatures. The major peak of the controlled experiment were comprised of crystalline SiO_2 diffraction signal value at 2θ = 26.66°. It is well known that SiO_2 is the common major constituent of the sand. On the other hand, XRD of the carbonated samples showed formation of a new peak at 2θ = 29.32°, which corresponds to that of calcite peak ($CaCO_3$). Among the polymorphs of $CaCO_3$ (calcite, aragonite, and vaterite), calcite is the thermodynamically stable phase under ambient conditions. This clearly indicates that carbonation has taken place in the materials undertaken for this study. Solid state ^{13}C CP-MAS NMR also corroborates this and is discussed in the later section. Besides the peaks of SiO_2 and $CaCO_3$, few peaks at higher carbonation temperatures (60 and 90 °C) arise, which may be attributed to the association of organic molecule with the cement matrix to form calcium stearate. Ozturk et al. have reported the synthesis and X-ray diffraction of calcium stearate [27]. As per the synthesis procedure we synthesized 50% excess calcium stearate precipitate and obtained XRD spectrum which showed a high intensity diffraction peak at 2θ value of 19.96°. We assume small peaks near 20° to be associated with calcium stearate in the cement matrix. Several typical vibrations bands of pure stearate molecules, including 2920, 2848 and 1463 cm^{-1} in the FTIR spectrum of stearate with different temperatures, are also observed (Figure S1).

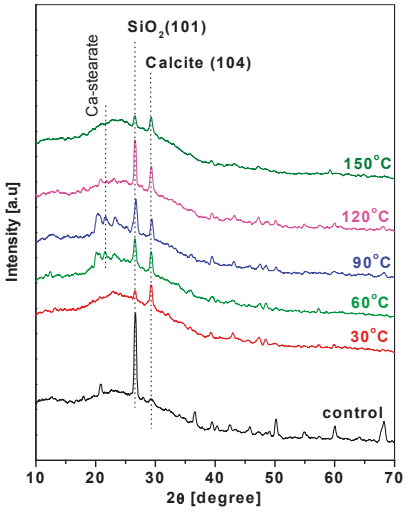

Figure 1. XRD pattern obtained from controlled and carbonated samples at different temperatures.

Figure 2 shows the SEM images of the carbonated samples, which showed differences in particle morphology that were strongly dependent on carbonation reaction temperature. At 30 °C, the product has irregular morphology (flat surfaces). At temperatures of 60 and 90 °C, these irregular particles transformed to form rod like structures and at higher temperatures of 120 and 150 °C the rod like structures transformed to aggregate particles (plate-like). The series of interactions between $Ca(OH)_2$ in the cement matrix, stearic acid and CO_2 varied with increasing carbonation reaction temperatures which gave rise to products with different morphology.

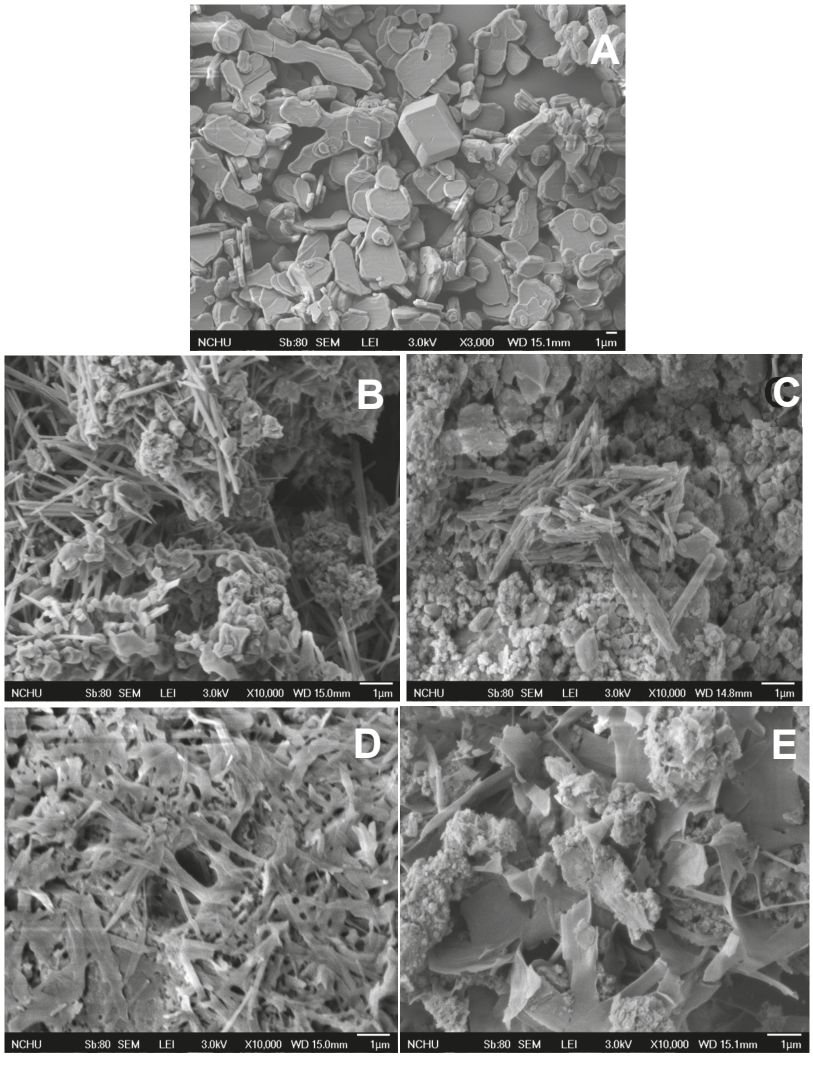

Figure 2. SEM images of the carbonated samples (**A**) 30 °C, (**B**) 60 °C, (**C**) 90 °C, (**D**) 120 °C, (**E**) 150 °C.

The FTIR spectra of the carbonated samples showed (Figure 3) the characteristic peaks of calcium stearate. The interaction of Ca^{2+} and organic substrate with COO^- functionality is already known in the literature [15]. Calcium stearate can be formed by the reaction of the $–COO^-$ of the stearic acid and Ca^{2+} ions to form a cover on the surface of $CaCO_3$ particles. The peaks at 1577 and 1541 cm^{-1}

are due to antisymmetric stretching bands for unidentate and bidentate association with calcium ions. The antisymmetric and symmetric methylene stretching were observed at 2916 and 2849 cm^{-1} respectively. These results are in agreement with functional groups present for calcium stearate [27]. The IR results showed that the intensity of CH_2 stretching band increased initially for the temperatures from 30 to 90 °C and then decreased with further increase in temperature. This suggests that the surface modification of $CaCO_3$ is reduced at higher temperatures.

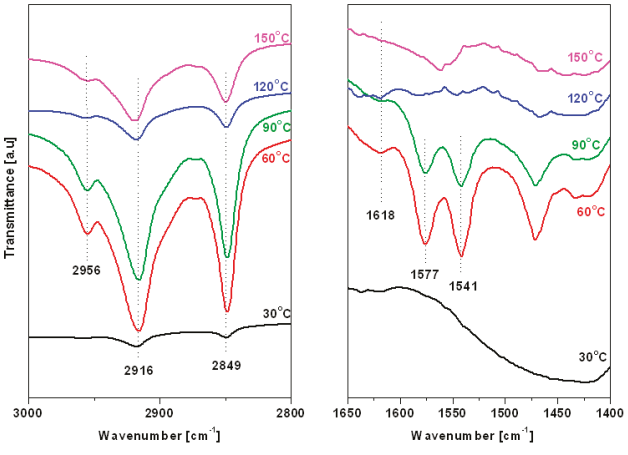

Figure 3. FTIR spectra of the carbonated samples at different temperatures.

In order to further investigate the structure elucidation of the synthesized samples, solid-state NMR spectroscopy was utilized in this study. Figure 4 presents the schematic of organic-inorganic interaction on the surface of the cement matrix. The Ca^{2+} reacts with $CH_3(CH_2)_{16}COO^-$ to form hydrophobic $Ca(CH_3(CH_2)_{16}COO)_2$, and thus formed $Ca(CH_3(CH_2)_{16}COO)_2$ are deposited on the $CaCO_3$ precipitate formed during the carbonation of $Ca(OH)_2$.

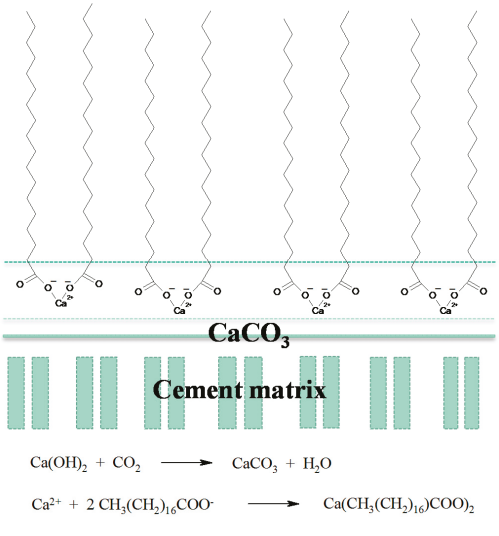

Figure 4. Schematic of the stearate molecules on $CaCO_3$ in cement matrix.

For NMR, samples obtained at 90 °C carbonation were used as a material for case study. Calcium stearate (50% excess Ca) were taken as reference material for comparing with the carbonated cement material. The solid state ^{13}C NMR spectras are presented in Figure 5. Figure 5a shows the NMR spectrum of pure calcium stearate. The carbonyl carbon (C1) signal exhibits at a resonance frequency of about 185.4 ppm (normal stearic acid C1 position is at 179 ppm [28]. The methyl (CH_3) and methylene (CH_2) group of calcium stearate resonates in the frequency range of 14.6–39.9 ppm. The high intensity peak at 33.05 ppm is due to CH_2 group (C4-C16) indicating their higher population of alkyl chain in the calcium stearate structure. The C1, C2, C3, C17, and C18 peaks are difficult to detect in the spectrum of cement block materials as compared to pure calcium stearate. Figure 5b shows the carbonation of cement block without any sodium sterate, the formation of ^{13}C peak arises due to the formation of $CaCO_3$ and its chemical shift value is 169.12. This data clearly indicates that carbonation has taken place in our samples. Figure 5c shows the carbonation in the presence of sodium stearate. The presence of signal at chemical shift value of 33.5 ppm can be attributed to the presence of stearate molecules, and the peak signal at 168.6 ppm arises from $CaCO_3$. There is slight change in peak value of CH_2 group (C4–C16) after surface modification (33.5 ppm) as compared to pure calcium stearate (33.05 ppm). There is also a change in peak value of the corresponding ^{13}C peak of $CaCO_3$ in the presence (168.6) of stearate molecules (absence 169.12). This upfield shift of $CaCO_3$ arises due to shielding effect and clearly indicates surface modifications of cement blocks in the presence of stearate molecule. These studies also suggest plausible explanation of the organic-inorganic moieties interaction as shown in Figure 4.

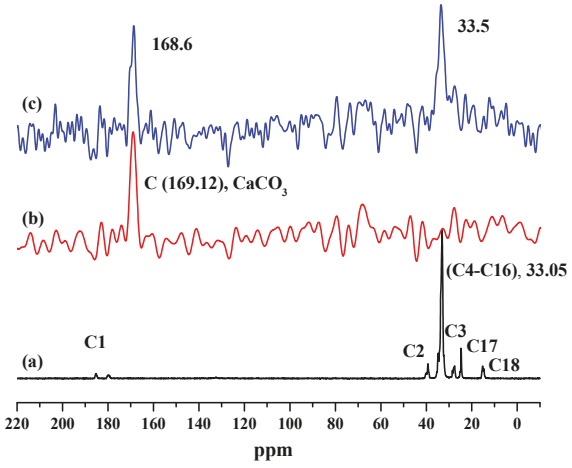

Figure 5. Solid-state ^{13}C CP-MAS NMR (**a**) calcium stearate (**b**) carbonation of cement without stearate (**c**) carbonation in the presence of stearate.

The hydrophobic function is often demonstrated with water contact angle and is sometimes referred to as "lotus effect". Hydrophobicity is controlled both by hydrophobic substrate film and the roughness of the surface. To show the lotus effect, hydrophobicity as the basis for self-cleaning mechanism, the organic interaction characteristic of cement surface was measured by contact angle. The organic additive changes the property of concrete material in situ, Figures 6 and 7a show the contact angle of the cement surfaces obtained at different carbonation reaction temperatures. At lower reaction temperature (30 °C), the contact angle against the hydrophobized cement surface was zero. The contact angle increased to 129 and 125° respectively for the temperatures 60 and 90 °C. Temperature increases the efficient interaction of stearate molecules and Ca^{2+} and CO_3^{2-} inducing hydrophobic calcite hence an increment in the contact angle. However, further increase in temperature caused

a slight decrease in the contact angle and remained constant after 90 °C. The surface roughness also seems to play an important role in enhancing or decreasing the hydrophobicity [29]. The results of IR and contact angle are in accordance with each other. On the other hand, contact angle of Ctrl-2 experiment at 90 °C was found to be ~80° (other samples were not studied); this indicates that CO_2 plays an important role in enhancing the hydrophobicity of the cement surface.

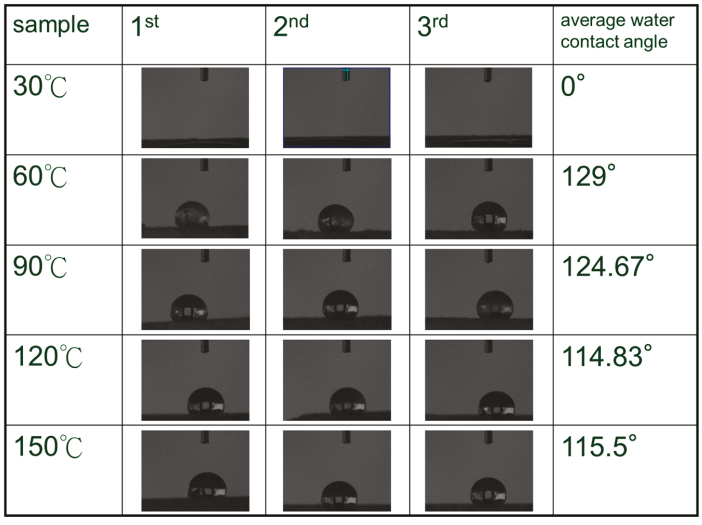

Figure 6. Water contact angle study on cement surfaces prepared by carbonation at different temperatures.

Micro structural features in cement systems such as porosity, pore structure, density, crystallinity and morphology, may affect the dependence of the fracture terms on microhardness. In our experiments, the micro hardness value first increases and then decreases with temperature as shown in Figure 7a. From SEM images, the rod like structures of $CaCO_3$ at 60 and 90 °C caused increased calcite fiber mineral filler that bridged between cement particles, and thus they enhanced micro hardness of the interface. Microhardness of the carbonated samples was compared with that of the Ctrl-2 experiments as shown in Figure 7b. The carbonated samples showed higher microhardness of the cement surface, which was found to be dependent on the morphology of the carbonated samples.

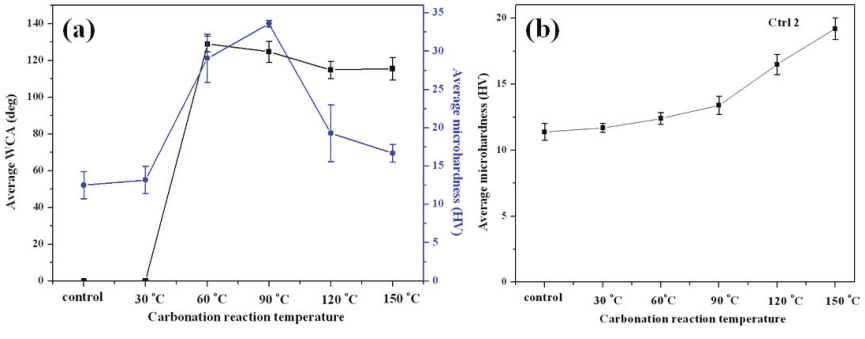

Figure 7. (**a**) Double Y axis graph showing contact angle of the cement surface against water and micro hardness of cement blocks obtained at different carbonation reaction temperature; (**b**) microhardness of cement cubes of Ctrl 2 experiments.

4. Conclusions

We have succeeded in obtaining hydrophobic cement surface via carbonation with the surface treatment with stearic acid in situ. The alkyl chain of stearic acid makes the $CaCO_3$ hydrophobic. Our study showed that at carbonation temperatures of 60 and 90 °C, maximum surface treatment with the stearic acid takes place as was seen from both the IR and contact angle. The different reaction temperature produced different morphology of the $CaCO_3$ particles, and the rod like structures enhanced the microhardness of the samples. NMR studies also suggest the presence of organic-inorganic interactions. The synthesis of the hydrophobicity does not guarantee the effectiveness of the use of cement in concrete and construction. This is because the cement grains are surrounded by a hydrophobic coating, which makes it difficult or impossible to hydrate the cement. Hence, this leads to the decrease in compressive strength and the loss of sample mass after freezing-thawing [6]. Admixture hydrophobic creates chemical bonds between the individual components of concrete, affecting the changes in the microstructure, as well as changing the strength parameters [30]. The carbonation of cement surface seems to be a promising route to synthesize hydrophobic surface and its properties can be tailored by using different organic additives.

Supplementary Materials: The following are available online at www.mdpi.com/2073-4352/7/12/371/s1, Figure S1: FTIR spectrum of pure stearate stored at different temperatures.

Acknowledgments: The authors are very grateful to the Ministry of Science and Technology in Taiwan for sponsoring this research.

Author Contributions: James Yang, Yi-Hsun Huang and Chun-Mei Hsu conceived and designed the experiments; Yi-Hao Kuo and How-Ji Chen performed the experiments; Duen-Wei Hsu and Shashi B. Atla analyzed the data; Wen-Chien Lee contributed reagents/materials/analysis tools; Shashi B. Atla, Chien-Yen Chen and Chien-Cheng Chen wrote the paper.

Conflicts of Interest: The authors declare no conflict of interest.

References

1. Naka, K.; Chujo, Y. Control of Crystal Nucleation and Growth of Calcium Carbonate by Synthetic Substrates. *Chem. Mater.* **2001**, *13*, 3245–3259. [CrossRef]
2. Sanchez, C.; Belleville, P.; Popall, M.; Nicole, L. Applications of advanced hybrid organic-inorganic nanomaterials: From laboratory to market. *Chem. Soc. Rev.* **2011**, *40*, 696–753. [CrossRef] [PubMed]
3. Mindess, S.; Young, J.F.; Darwin, D. *Concrete*; Prentice Hall: Upper Saddle River, NJ, USA, 2003.
4. Monteiro, P.J.M.; Mehta, P.K. *Concrete: Structure, Properties, and Materials*; Prentice-Hall, Inc.: Upper Saddle River, NJ, USA, 1986.
5. Basheer, P.A.M.; Basheer, L.; Cleland, D.J.; Long, A.E. Surface treatments for concrete: Assessmentmethods and reported performance. *Constr. Build. Mater.* **1997**, *11*, 413–429. [CrossRef]
6. Tkach, E.V.; Semenov, V.S.; Tkach, S.A.; Rozovskaya, T.A. Highly Effective Water-repellent Concrete with Improved Physical and Technical Properties. *Procedia Eng.* **2015**, *111*, 763–769. [CrossRef]
7. Zhang, T.; Shang, S.; Yin, F.; Aishah, A.; Salmiah, A.; Ooi, T.L. Adsorptive behavior of surfactants on surface of Portland cement. *Cem. Concr. Res.* **2001**, *31*, 1009–1015. [CrossRef]
8. Maryoto, A. Resistance of Concrete with Calcium Stearate Due to Chloride Attack Tested by Accelerated Corrosion. *Procedia Eng.* **2017**, *171*, 511–516. [CrossRef]
9. Medeiros, M.H.F.; Helene, P. Surface treatment of reinforced concrete in marine environment: Influence on chloride diffusion coefficient and capillary water absorption. *Constr. Build. Mater.* **2009**, *23*, 1476–1484. [CrossRef]
10. Park, D.C. Carbonation of concrete in relation to CO_2 permeability and degradation of coatings. *Constr. Build. Mater.* **2008**, *22*, 2260–2268. [CrossRef]
11. Izaguirre, A.; Lanas, J.; Álvarez, J.I. Effect of water-repellent admixtures on the behaviour of aerial lime-based mortars. *Cem. Concr. Res.* **2009**, *39*, 1095–1104. [CrossRef]
12. Maryoto, A. Improving Microstructures of Concrete Using $Ca(C_{18}H_{35}O_2)_2$. *Procedia Eng.* **2015**, *125*, 631–637. [CrossRef]

13. Chen, Y.; Ji, X.; Zhao, G.; Wang, X. Facile preparation of cubic calcium carbonate nanoparticles with hydrophobic properties via a carbonation route. *Powder Technol.* **2010**, *200*, 144–148. [CrossRef]
14. Keum, D.-K.; Kim, K.-M.; Naka, K.; Chujo, Y. Preparation of hydrophobic $CaCO_3$ composite particles by mineralization with sodium trisilanolate in a methanol solution. *J. Mater. Chem.* **2002**, *12*, 2449–2452. [CrossRef]
15. Wang, C.; Sheng, Y.; Hari, B.; Zhao, X.; Zhao, J.; Ma, X.; Wang, Z. A novel aqueous-phase route to synthesize hydrophobic $CaCO_3$ particles in situ. *Mater. Sci. Eng. C* **2007**, *27*, 42–45. [CrossRef]
16. Wang, C.; Xiao, P.; Zhao, J.; Zhao, X.; Liu, Y.; Wang, Z. Biomimetic synthesis of hydrophobic calcium carbonate nanoparticles via a carbonation route. *Powder Technol.* **2006**, *170*, 31–35. [CrossRef]
17. Sheng, Y.; Zhou, B.; Wang, C.; Zhao, X.; Deng, Y.; Wang, Z. In situ preparation of hydrophobic $CaCO_3$ in the presence of sodium oleate. *Appl. Surf. Sci.* **2006**, *253*, 1983–1987. [CrossRef]
18. Wang, C.; Sheng, Y.; Zhao, X.; Pan, Y.; Hari, B.; Wang, Z. Synthesis of hydrophobic $CaCO_3$ nanoparticles. *Mater. Lett.* **2006**, *60*, 854–857. [CrossRef]
19. Wang, C.; Piao, C.; Zhai, X.; Hickman, F.N.; Li, J. Synthesis and characterization of hydrophobic calcium carbonate particles via a dodecanoic acid inducing process. *Powder Technol.* **2010**, *198*, 131–134. [CrossRef]
20. Jumate, E.; Manea, D.L.; Moldovan, D.; Fechete, R. The Effects of Hydrophobic Redispersibele Powder Polymer in Portland Cement Based Mortars. *Procedia Eng.* **2017**, *181*, 316–323. [CrossRef]
21. Falchi, L.; Zendri, E.; Müller, U.; Fontana, P. The influence of water-repellent admixtures on the behaviour and the effectiveness of Portland limestone cement mortars. *Cem. Concr. Compos.* **2015**, *59*, 107–118. [CrossRef]
22. Izaguirre, A.; Lanas, J.; Álvarez, J.I. Ageing of lime mortars with admixtures: Durability and strength assessment. *Cem. Concr. Res.* **2010**, *40*, 1081–1095. [CrossRef]
23. Maranhao, F.; John, V.; Loh, K.; Pileggi, R. The influence of silicone based water repellents as admixtures on the rheological properties of cement slurry. In Proceedings of the Hydrophobe V, 5th International Conference on Water Repellent Treatment of Building Materials, Brussels, Belgium, 15–16 April 2008; pp. 255–258.
24. Klisińska-Kopacz, A.; Tišlova, R. Effect of hydrophobization treatment on the hydration of repair Roman cement mortars. *Constr. Build. Mater.* **2012**, *35*, 735–740. [CrossRef]
25. Falchi, L.; Müller, U.; Fontana, P.; Izzo, F.C.; Zendri, E. Influence and effectiveness of water-repellent admixtures on pozzolana–lime mortars for restoration application. *Constr. Build. Mater.* **2013**, *49*, 272–280. [CrossRef]
26. Xue, X.; Li, Y.; Yang, Z.; He, Z.; Dai, J.-G.; Xu, L.; Zhang, W. A systematic investigation of the waterproofing performance and chloride resistance of a self-developed waterborne silane-based hydrophobic agent for mortar and concrete. *Constr. Build. Mater.* **2017**, *155*, 939–946. [CrossRef]
27. Gönen, M.; Öztürk, S.; Balköse, D.; Okur, S.; Ülkü, S. Preparation and Characterization of Calcium Stearate Powders and Films Prepared by Precipitation and Langmuir–Blodgett Techniques. *Ind. Eng. Chem. Res.* **2010**, *49*, 1732–1736. [CrossRef]
28. Cunningham, I.D.; Courtois, J.-P.; Danks, T.N.; Heyes, D.M.; Moreton, D.J.; Taylor, S.E. Synthesis and characterisation of calixarene-stabilised calcium carbonate overbased detergents. *Colloids Surf. A Physicochem. Eng. Asp.* **2003**, *229*, 137–147. [CrossRef]
29. Bhushan, B.; Jung, Y.C. Natural and biomimetic artificial surfaces for superhydrophobicity, self-cleaning, low adhesion, and drag reduction. *Prog. Mater. Sci.* **2011**, *56*, 1–108. [CrossRef]
30. Corinaldesi, V. Combined effect of expansive, shrinkage reducing and hydrophobic admixtures for durable self compacting concrete. *Constr. Build. Mater.* **2012**, *36*, 758–764. [CrossRef]

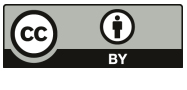

© 2017 by the authors. Licensee MDPI, Basel, Switzerland. This article is an open access article distributed under the terms and conditions of the Creative Commons Attribution (CC BY) license (http://creativecommons.org/licenses/by/4.0/).

crystals

MDPI

Article

CO_2 Capture and Crystallization of Ammonia Bicarbonate in a Lab-Scale Scrubber

Pao Chi Chen * and Shun Chao Yu

Department of Chemical and Materials Engineering, Lunghwa University of Science and Technology, Taoyuan 33306, Taiwan; sc.yu@eink.com

* Correspondence: chenpc@mail2000.com.tw

Received: 21 November 2017; Accepted: 12 January 2018; Published: 16 January 2018

Abstract: A lab-scale bubble-column scrubber is used to capture CO_2 gas and produce ammonia bicarbonate (ABC) using aqueous ammonia as an absorbent under a constant pH and temperature. The CO_2 concentration is adjusted by mixing N_2 and CO_2 in the range of 15–60 vol % at 55 °C. The process variables are the pH of the solution, temperature, gas-flow rate and the concentration of gas. The effects of the process variables on the removal efficiency (E), absorption rate (R_A) and overall mass-transfer coefficient (K_Ga) were explored. A multiple-tube mass balance model was used to determine R_A and K_Ga, in which R_A and K_Ga were in the range of 2.14×10^{-4}–1.09×10^{-3} mol/(s·L) and 0.0136–0.5669 1/s, respectively. Results found that, R_A showed an obvious increase with the increase in pH, inlet gas concentration and gas temperature, while K_Ga decreased with an increase in inlet gas concentration. Using linear regression, an empirical expression for K_Ga/E was obtained. On the other hand, ammonia bicarbonate crystals could be produced at a pH of 9.5 when the gas concentration was higher than 30% and γ ($=F_g/F_A$, the gas-liquid molar flow rate ratio) $\geq$ 1.5.

Keywords: ammonia bicarbonate; carbon dioxide; mass-transfer coefficient; capture; bubble-column scrubber

1. Introduction

The total global carbon dioxide emissions are increasing by the day, which causes the temperature to rise rapidly, thus, creating severe impacts on the global ecology. Therefore, the issues of CO_2 have attracted great attention with the most attention on the CO_2 emission of coal fired power plants and steel plants [1]. There are two main kinds of CO_2 capturing methods currently under study, namely, pre-combustion and post-combustion [2]. The technology of the pre-combustion method is to primary treat fossil fuels with steam and air or oxygen, in order to separate the fossil fuel into carbon dioxide and hydrogen and then, to store the carbon dioxide and use the hydrogen for combustion meaning no carbon dioxide would be produced. In the post-combustion method, the emitted CO_2 is about 15% which is mainly captured by chemical absorption.

The absorbents used for chemical absorption include the alkaline solutions of all levels, such as amine, ammonia, sodium hydroxide and hot potassium carbonate [3–6]. Among numerous absorption technologies and absorbents, the monoethanolamine (MEA) process is the most popular and already operates in more than a thousand units which is comparable with 700 plants for potassium carbonate solution [6]. However, the MEA process still has some disadvantages including low absorption efficiency, low CO_2 loading, high regeneration energy requirements and the container corrosion issue [3,7]. In the case of using MEA as the absorbent, the absorbed carbon dioxide is stored in the liquid phase in a liquid state, which might be released again due to the influence of the pH value and the huge volume. Therefore, in some studies, MEA is changed to aqueous ammonia as the absorbent, which is used to absorb the carbon dioxide as reported in the literature [1,3,8].

The advantages of using aqueous ammonia as the absorbent are high absorption load, low regeneration energy requirement, low corrosiveness, lower cost and higher removal efficiency [9–11]. Another advantage is that an aqueous ammonia solution can be used to simultaneously remove CO_2, SO_2 and NO_x [12]. Moreover, the other reasons for using aqueous ammonia as an absorbent solution are due to its high CO_2 loading capacity, low regeneration energy at a relatively low temperature (~8 °C) and reuse of ammonia and stripped water vapor for the distillation of aqueous carbonated ammonia [1,4,13]. The CO_2 absorption process using aqueous ammonia solution depends on the temperature, ion concentration and pH value of the solution where more carbon dioxide is absorbed at a higher pH value and more ammonia is created [3,14]. Moreover, a higher aqueous ammonia concentration or lower CO_2 concentration would cause the absorption efficiency to decline, which would affect the absorption of carbon dioxide. The carbonate dissociation degree in the aqueous phase is shown in Figure 1 [15,16]. Within a pH range of pH = 7–9, as shown by α1, the solution mainly contains bicarbonate; when the pH value is above 10, as shown by α2, the solution mainly contains carbonate; and when the pH value is less than 6, the solution mainly contains carbonic acid (H_2CO_3*).

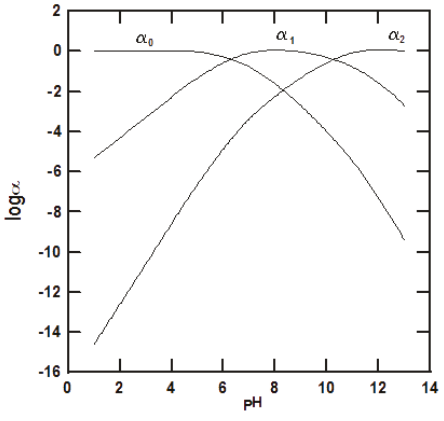

Figure 1. Influence of pH values on carbonate dissociation, re-plotted in here [15,16].

More carbon dioxide is absorbed by aqueous ammonia at a higher pH value; in addition, more ammonia is created at a higher pH value. Therefore, the best pH value will facilitate the absorption process, as shown in Figure 2. Equations (1)–(3) are the formulas for ammonia dissociation in water. As ammonia will be separated due to the effect of the pH value and a higher pH value can help the formation of NH3(aq), NH3 can be separated out of the solution [16]. As shown in Figure 2, it is known that, when pH = 9.5 the mole fraction of NH3 is about 0.8, which could be a very good operating condition in terms of ammonium bicarbonate generation.

$$NH_4^+ + OH^- = NH_3(aq) + H_2O \quad (1)$$

$$NH_3(aq) = NH_3(q) \quad (2)$$

$$H_2O = H^+ + OH^- \quad (3)$$

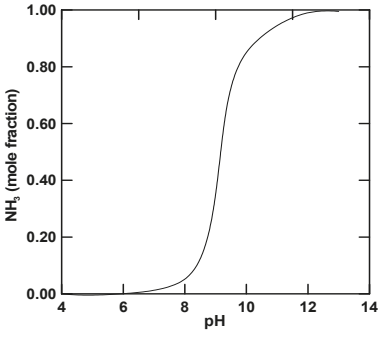

Figure 2. Dissociation of ammonium hydroxide varies with pH, re-plotted in here [16].

Many scholars have studied the absorption of CO_2 using an aqueous ammonia solution and have adopted different scrubbers for their studies, such as the stirred cell [4,17], sieve plate column [9], falling film [18], absorption column [19] and spray tower [20] scrubbers. In literature, the suitability of an absorber is determined by the level of the mass transfer coefficient. However, we can also use the absorption factor (φ) to make the comparison, which is the moles of CO_2 that are able to be absorbed per mole per unit volume and is defined, as follows:

$$\varphi = \frac{F_g E}{F_A V_B} \tag{4}$$

where Fg (mol/s) represents the molar flow rate of the feed gas, E is the absorption efficiency, FA (mol/s) is the molar flow rate of the solvent and VB (L)is the volume of the absorber.

Regarding the bubble column, the absorption factor is 5 to 10 times that of the packed column of high-efficiency structured packing material, which indicates that under the same conditions, in order to obtain the same absorption factor, the volume of the packed column of high-efficiency structured packing material should be 5 to 10 times that of the bubble column; and while the volume of a conventional packed column, needs to be 130 times that of the bubble column to have the same absorption factor as the bubble column [21]. The above results show that the bubble column shows superior performance and many scholars use the bubble column as the absorber and object of study to this end [5,22–24]. To summarize, using aqueous ammonia as the absorbent requires high load and low energy for regeneration. In addition, according to the absorption factor comparison, the absorption factor of the bubble column is higher than other types of absorbers.

From literature survey, capturing CO_2 using aqueous ammonia has two possible: one is absorption without precipitation and the other is absorption with precipitation, depending on the pH of the solution. In addition, precipitation of ABC in the bubble-column scrubber is feasible as compared packed column and sieve tray. However, the research regarding to the capture of CO_2 using aqueous ammonia in a bubble-column scrubber is scare. This indicates that no technique data, including precipitation rate of ABC, absorption rate and overall mass-transfer coefficient, can be found in the literature. Due to this, a study of capturing CO_2 using aqueous ammonia solution in a bubble-column scrubber is required, including absorption without precipitation and absorption with precipitation. Therefore, the purposes of this research are to understand the phenomena in the absorption of CO_2 in the bubble-column scrubber; to find the effect of process variables on the absorption rate, overall mass-transfer coefficient, precipitation of ABC; and to search for the better process in the capture of CO_2 using aqueous ammonia as absorbent.

2. Absorption Model and Solution Chemistry

In a bubble-column scrubber, a gas mixture containing carbon dioxide (A) and nitrogen (B) flows into a bubble column from the bottom and continues through the distributor, thus, coming into continuous contact with the aqueous ammonia solution flowing into the column from the top. The two streams come into contact within the column's countercurrent simultaneously. The diffusing of CO_2 gas inside a gas bubble in the solution can be described by a Two-film model, as shown in Figure 3. The CO_2 gas at pressure P diffuses from the left side to the gas-liquid interface and enters into the liquid side, where it is absorbed by the aqueous ammonia solution. At the interface, the relationship between the partial pressure of the CO_2 and the dissolution of the CO_2 in the liquid can be expressed by Harry's Law ($P_A = HC_A$). According to this model, the absorption rate and overall mass transfer coefficient can be determined using measurable quantities [21].

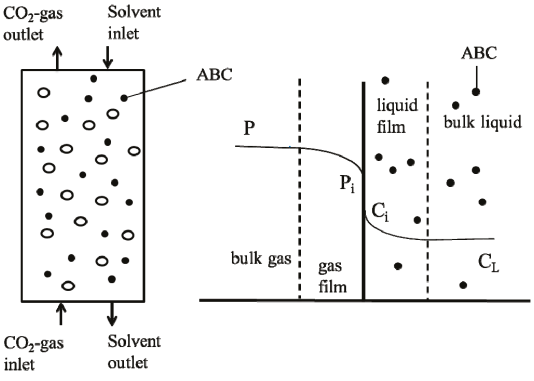

Figure 3. A two-film model showing the absorption of CO_2 in an aqueous ammonia solution.

The solution's chemistry for the NH_3-CO_2-H_2O system is presented in Table 1 [25]. Ionization of each component after the absorption of the CO_2 into the aqueous ammonia solution can be expressed by six equations, as shown in Table 1. Equations (6) and (7) show the carbonation of CO_2 dissolved in an aqueous solution. Equations (8)–(10) show that NH_3 as a weak base will cause the chemical absorption of the weak acid CO_2. In the absorbed solution, the various species include CO_2 and bicarbonate, carbonate, carbamate anions and ammonium cation. In addition, Table 1 and Equation (10) include the formation of ammonia bicarbonate (ABC) and NH_4HCO_3(s), as this solid can precipitate in the scrubber depending on the operating conditions. However, the concentrations of chemical species can vary when the solution pH, CO_2 concentration, temperature and ammonia concentration are changed. Thus, how to control the process variables becomes significant in the ammonia capture study. The absorption rate and overall mass transfer coefficient can be determined when CO_2 is captured by an aqueous ammonia solution [5]. Therefore, once the inlet and outlet concentrations of CO_2 can be measured at a steady state; the absorption rate, Equation (11) and overall mass transfer coefficient, Equation (13), can be evaluated, as shown in Table 2. Alternatively, the K_Ga can be estimated using Equation (14) when the outlet CO_2 concentration is near zero. In Equation (14), $(C_A - HC_L)_{av}$ is the arithmetic mean between the inlet and outlet.

Table 1. Solution chemistry for NH_3-CO_2-H_2O system [25].

$H_2O \leftrightarrow H^+ + OH^-$	(5)
$CO_2 + H_2O \leftrightarrow H^+ + HCO_3^-$	(6)
$HCO_3^- \leftrightarrow H^+ + CO_3^{2-}$	(7)
$NH_3 + H_2O \leftrightarrow NH_4^+ + OH^-$	(8)
$NH_3 + HCO_3^- \leftrightarrow NH_2COO^- + H_2O$	(9)
$NH_4^+ + HCO_3^- \leftrightarrow NH_4HCO_3(s)$	(10)

Table 2. Absorption rate and overall mass-transfer coefficient used in this work.

$R_A = \frac{F_{A1}}{V_L}\left[1 - \left(\frac{1-y_{A1}}{y_{A1}}\right)\left(\frac{y_{A2}}{1-y_{A2}}\right)\right]$	(11)
$F_{A1} = Q_g \times \frac{P_{A1}}{RT} \times \frac{1}{60}$	(12)
$K_G a = \left(\frac{Q_g}{V_L}\right) \times \ln\left(\frac{C_{A1}}{C_{A2}}\right)$	(13)
$K_G a = \frac{R_A}{(C_A - HC_L)_{av}}$	(14)
$R_p = \frac{M_T}{\tau}$	(15)
$\tau = \frac{V_L}{Q_L}$	(16)

3. Experimental Procedure

The experimental device used is shown in Figure 4. The inside diameter of the column is 5 cm and the gas distributor is a perforated plate designed with four holes per square centimeter and each hole is 1 mm in diameter. Initially, a known amount of aqueous ammonia solution (14%) is introduced into the column, into which a pH electrode is inserted. The solution is adjusted to the desired pH value by adding a known concentration of aqueous solution (28%). The experiment starts when the mixed N_2–CO_2 gas, in the range of 15–60% CO_2 gas, begins bubbling through the column. The gas flow rates are in the range of 3 to 5 L/min. A gas heater and circulating cooling water tank are used to control the gas and solution temperatures. The mixed gas is delivered to the heater, which maintains the inlet gas temperature at 55 °C. The operating pH value is in the range of 9.5–11.5. The temperature in the bubble column is maintained at 25–60 °C by a water cooling system (Deng Yng, D-620, New Taipei, Taiwan). The operating time is 5–7 h, depending on the operating conditions. During the operation, the pH of the solution is decreased due to absorption in the scrubber. In order to hold the pH value of the solution at a desired value during operation, an aqueous ammonia solution is introduced into the column through the action of a pH controller (Suntex, PC-310, New Taipei, Taiwan). The overflow solution automatically flows out to the reservoir. The volume of added solution is recorded every ten minutes during the operation. A digital gauge pressure meter measures the inlet gas pressure. A CO_2 gas meter (Guardian Plus, D600, Hartford, USA) is used to measure the concentration of the CO_2 gas at the outlet of the bubble column (y_2). When the concentration of CO_2 gas changes to a steady state, the solutions are withdrawn using a syringe to measure the total dissolved CO_2 in the solution. At the end of the operation, the solution is poured into a vessel and the volume of the solution (V_L) is measured. In addition, the slurry solution is separated using a filter. The crystal size distribution is measured by a particle size analyzer (Galai, CIS-50, Or Akiva, Israel). The crystals obtained are characterized by X-ray (Rigaku, D/MAX-2200/PC, Tokyo, Japan), FESEM (Jeol, JSM-6500F, Tokyo, Japan) and EA (Thermo, Flash EA1112, Cambridge, UK), respectively. A total of twenty runs are carried out in this work. The operating conditions and physical properties of ABC are, as shown in Table 3.

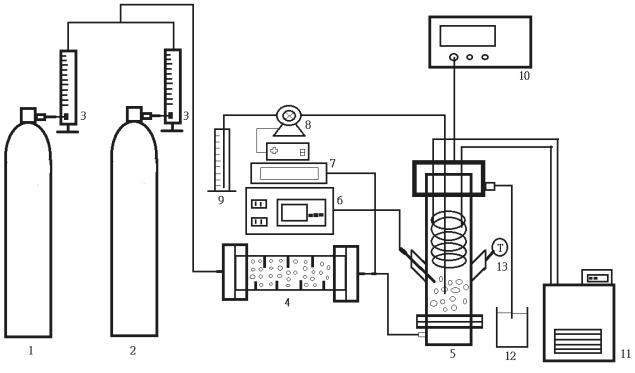

Figure 4. Capture of CO_2 using a lab-scale bubble-column scrubber. 1. CO_2 gas tank; 2. N_2 gas tank; 3. Gas-flow meter; 4. Gas-flow meter; 5. Bubble-column scrubber; 6. pH control; 7. Digital Pressure Gauge; 8. Tubing pump; 9. Solvent; 10. CO_2 meter; 11. Cooling machine; 12. Reservoir; Digital thermometer.

Table 3. Operating conditions and physical properties of ABC crystals.

Operating Condition	
Gas-flow rate (L/min)	3–5
Concentration of CO_2	15–60%
pH	9.5
Operating time (h)	5–7
Gas inlet temperature (°C)	55
Working temperature in the scrubber (°C)	25–60
Physical Property of ABC	
Density (kg/m^3)	1.58
Molecular weight	79.06
Solubility (g/L-H_2O) (20 (°C))	220
Decomposition temperature (°C)	35–60

4. Results and Discussion

The results listed in Table 4 include the R_A, K_Ga and E. It is found that, the removal efficiency E obtained here is in the range of 10.9–100%; the R_A was in the range of 3.2122 $\times$ 10^{-4}–10.999 $\times$ 10^{-4} mol/(s·L) and the K_Ga is in the range of 0.0136–0.3302 L/s. In addition, the ABC crystals are formed at a pH of 9.5, such as Nos. 3, 4, 6, 7, 8, 10, 11 and 12. For other pH values, no ABC crystals could be obtained.

Table 4. Operating conditions and experimental data obtained in this work.

No.	pH	Q_g (L/min)	y_1 (%)	y_2 (%)	T (°C)	Q_L (mL/min)	γ (-)	$R_A \times 10^4$ (mol/(s·L))	K_Ga (1/s)	E (%)
1	9.5	3	15	7.95	25	3.66	0.58	3.9178	0.0794	47.0
2	9.5	3	30	17.7	25	3.30	1.33	5.1831	0.0447	41.3
3	9.5	3	50	38.8	25	4.90	1.50	5.7170	0.0194	22.4
4	9.5	3	60	53.5	25	4.96	1.75	7.1506	0.0143	10.9
5	9.5	4	15	8.7	25	2.22	1.33	3.5858	0.0692	42.1
6	9.5	4	30	22	25	3.51	1.71	5.0876	0.0327	26.7
7	9.5	4	50	39.3	25	4.73	2.05	7.0207	0.0136	21.4
8	9.5	4	60	51.7	25	6.63	1.77	9.3765	0.0199	13.8
9	9.5	5	15	7.56	25	3.30	1.11	5.4895	0.1142	49.6
10	9.5	5	30	22.9	25	0.60	12.24	7.0572	0.0506	23.6

Table 4. *Cont.*

No.	pH	Q_g (L/min)	y_1 (%)	y_2 (%)	T (°C)	Q_L (mL/min)	γ (-)	$R_A \times 10^4$ (mol/(s·L))	$K_G a$ (1/s)	E (%)
11	9.5	5	50	39.6	25	7.28	1.69	9.0338	0.0299	20.8
12	9.5	5	60	50.6	25	7.10	2.07	10.999	0.0241	15.8
13	10.0	3	15	10.0	25	2.96	0.75	3.2122	0.0608	33.3
14	10.5	3	15	5.3	25	8.89	0.24	4.1095	0.1020	64.6
15	11.0	3	15	3.7	25	9.73	0.22	4.8295	0.1573	75.3
16	11.5	3	15	0	25	37.63	0.058	6.3943	0.2083	100
17	10.0	4	15	5.5	25	7.08	0.41	7.4126	0.1808	63.3
18	10.0	4	15	0	40	4.14	0.67	5.9145	0.1963	96.7
19	10.0	4	15	0	50	8.71	0.31	6.7421	0.2381	100
20	10.0	4	15	0	60	46.13	0.053	9.0425	0.3302	100

4.1. Effect of Process Variables on E

Figure 5a shows the effect of the CO_2 inlet concentrations at various gas-flow rates on the removal efficiency of CO_2. It is found that E decreases with the increase in CO_2 gas concentration, while the effect of the gas flow rate was not obvious. On the other hand, the effects of the pH level and gas inlet temperature of E are significant, as shown in Figure 5b,c. The results show that E increases with the increase in the pH level and gas flow rate at the gas inlet. The analysis of the gas-liquid molar flow rate ratio, γ, as listed in Table 4, finds that the removal efficiency is higher than 60% when γ is lower than 0.5, indicating the influence of γ on E.

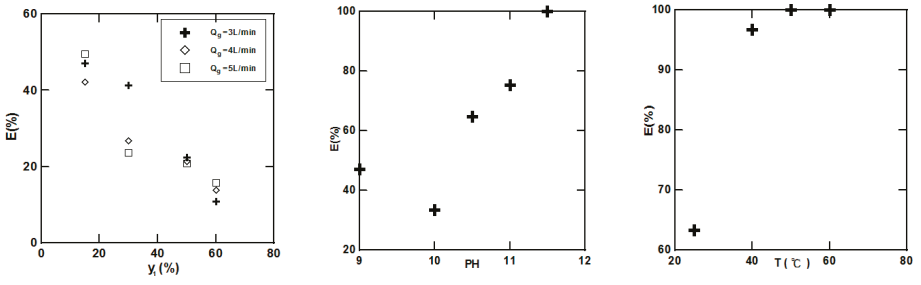

(**a**) pH = 9.5 (**b**) T = 25 °C (**c**) pH = 10.0

Figure 5. Effects of process parameters on the removal efficiency of CO_2: (**a**) effect of y_1 on E at pH = 9.5; (**b**) effect of pH on E at T = 25 °C; (**c**) effect of T on E at pH = 10.0.

4.2. Effect of Process Variables on the R_A and $K_G a$

A plot of R_A versus y_1 at various gas-flow rate absorption rates is shown in Figure 6a. The results show that R_A increases with an increase in y_1, while R_A is higher at higher gas flow rates. In addition, the results find that the R_A increases with the pH and gas input concentrations, as shown in Figure 6b,c. Alternatively, a wetted-wall column for CO_2 absorption test is reported in literatures by different scholars, who obtain R_A in the range of 2.15×10^{-4}–4.48×10^{-3} mol/(L·s) [13] and 2.05×10^{-4}–5.53×10^{-3} mol/(L·s) [26], respectively. Some of these values are higher than that reported in here, 3.21×10^{-4}–1.10×10^{-3} mol/(L·s). In addition, the higher R_A (2.07×10^{-3}–7.24×10^{-3} mol/(L·s)) can be obtained when aqueous hydrazine is used as a solvent for CO_2 capture [27].

The effects of y_1, Q_g, pH and T on the overall mass transfer are also investigated. Figure 7a shows that the effect of y_1 on $K_G a$ at various Q_g is obvious. It also shows that $K_G a$ decreases with an increase in y_1 indicating a higher mass resistance at higher gas concentrations. In addition, $K_G a$ increases with the increase in Q_g, which indicates that increasing the gas-liquid contact surface area and turbulence mixing results in a more effective contact. The effects of pH levels and gas inlet

temperatures on K_Ga are expressed in Figure 7b,c. The effects of the pH level and temperature on K_Ga are obvious, indicating the significance of pH and temperature. However, the K_Ga, as obtained here, is in the range of 0.0136–0.3302 1/s, which is comparable with other solvents, such as MEA solvent which is in the range of 0.0342–0.881 1/s [28] and $NaOH/BaCl_2/H_2O$, which is in the ranges of 0.0651–0.3396 1/s [5] and 0.015–0.14 1/s for a stirred-tank scrubber using an aqueous ammonia solution as the scrubbing solution [4]. On the other hand, from data reported in literatures [8,13,26,27], the K_Ga can be recalculated for comparison. The recalculated values of wetted-wall column tests are 0.03469–0.2658 1/s [13] and 0.02551–0.4336 1/s [26], respectively; while the recalculated values for packed column are in the range of 0.486–2.43 1/s [8] when a specific area of packings, 500 m^2/m^3, is available. Moreover, the K_Ga is 2.21 1/s when using aqueous hydrazine solvent [27].

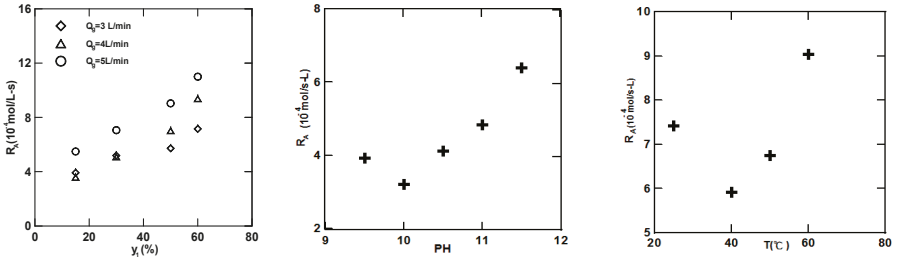

(**a**) pH = 9.5 (**b**) T = 25 °C (**c**) pH = 10.0

Figure 6. Effects of process variables on the absorption rate: (**a**) effect of y_1 on R_A at pH = 9.5; (**b**) effect of pH on R_A at T = 25 °C; (**c**) effect of T on R_A at pH = 10.0.

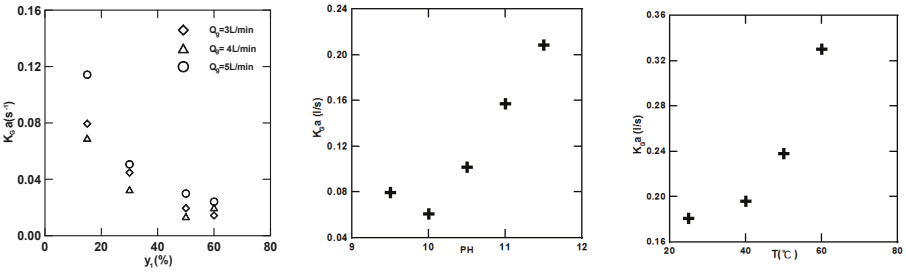

(**a**) pH = 9.5 (**b**) T = 25 °C (**c**) pH = 10.0

Figure 7. Effects of process variables on K_Ga showing the significant parameters: (**a**) effect of y_1 on K_Ga at pH = 9.5; (**b**) effect of pH on K_Ga at T = 25 °C; (**c**) effect of T on K_Ga at pH = 10.0.

4.3. Characterization of ABC Crystals

While the formation of ABC is found here, it is not found under all conditions, such as Nos. 3, 4, 6, 7, 8, 10, 11 and 12 at a pH level of 9.5. Figure 8 for No. 12 shows the crystal size distribution measured using a CIS-1 particle size analyzer. The major distribution is in the size range of 30–100 μm. On the other hand, when the crystals are examined by SEM, as also shown in Figure 8, small irregular crystals are observed indicating the fracture property of ABC crystals.

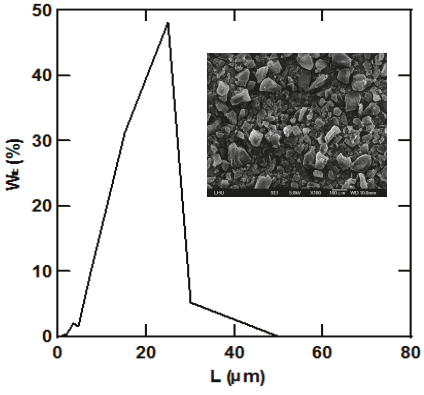

Figure 8. A plot of wt % vs. L showing the crystal size distribution of ABC (No. 12).

Figure 9 shows the XRD spectra for the three runs, as compared with the standard ABC crystals bought at the market. The major peaks for a standard sample are 29.7 (131), 16.6 (020), 21.9 (012) and 24.5 (200), which are the major peaks for ABC crystals, as reported by Meng [29]. However, the peaks of the three samples exhibit the same peaks as the standard sample, thus, confirming the formation of ABC crystals in this work. Alternatively, EA analyses according to N, H, O and C for ABC crystals are shown in Figure 10. Analysis finds that all elements are close to that of a standard sample, indicating that the precipitates obtained here are confirmed to be ABC crystals.

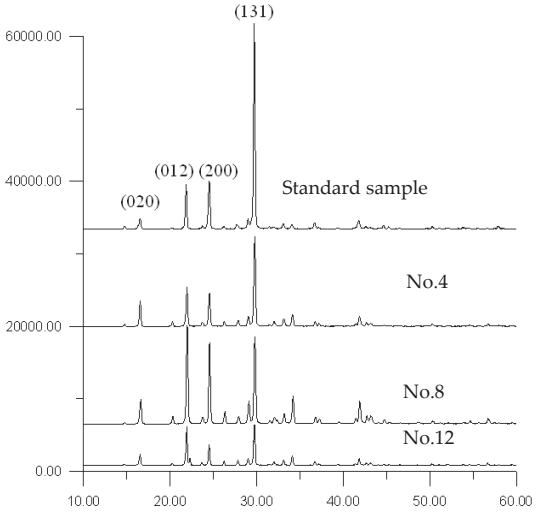

Figure 9. XRD spectra for ABC crystals.

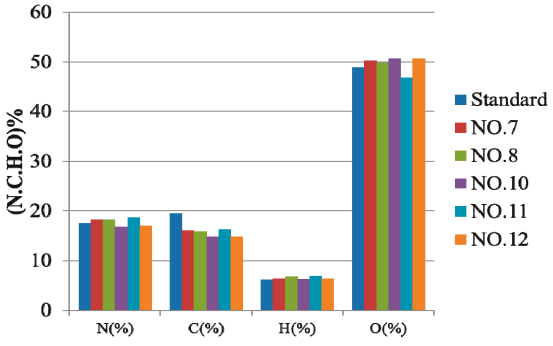

Figure 10. EA analysis for ABC crystals compared with a standard sample.

Finally, the precipitation rate for ABC crystals could be evaluated using Equations (15) and (16) when the slurry density (M_T) and mean residence time (T) are obtained. Figure 11 shows that R_p is increased with an increase in y_1 at various rates of Q_g. The results show that, the gas concentration has significant effect on the R_p value as compared with Q_g. Alternatively, analysis of γ finds that the precipitates of ABC can be obtained when γ is higher than 1.5; however, no precipitates are observed when γ is lower than 1.5, regardless of the pH level.

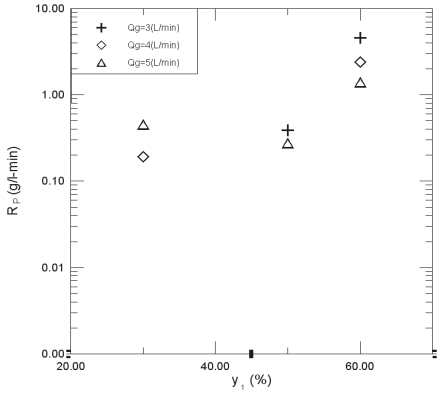

Figure 11. A plot of R_p vs. y_1 at various values of Q_g showing the influence of y_1 and Q_g.

4.4. Strategy of CO_2 Capture Using Aqueous Ammonia Solution

The K_Ga obtained here can be used to calculate the scrubber size [16]. Generally speaking, a larger K_Ga means that a smaller scrubber size is required, while a higher E shows an effective reduction in CO_2 emissions. Thus, obtaining a larger K_Ga and E is the major focus in process design. Figure 12 shows that K_Ga increased with an increase in E, showing a linear relationship. In order to clarify, the target of K_Ga and E are set at 0.2 L/s and 80%, respectively. Therefore, the figure can be divided into four areas, i.e., A, B, C and D, in which C shows a higher K_Ga and E. On the contrary, B shows a lower K_Ga and E, especially in the case of the formation of ABC. Excluding the formation of ABC data, K_Ga/E can only be correlated with the pH of the solution and γ, as parameters T, the concentration and flow-rate are included in γ. The regression results are shown, as follows:

$$\frac{K_Ga}{E} = 0.8826\gamma^{-0.206}\exp(-0.1681pH) \quad (17)$$

The regression error in Equation (17) is 12.68%. This equation can be used to predict $K_G a$ when E, pH and γ are given. In this way, the size of the scrubber can be estimated. In addition, in order to obtain the ABC at a higher E value, a two-scrubber in series is required. Figure 13 shows a possible process for CO_2 capture using an aqueous ammonia solution in a bubble column.

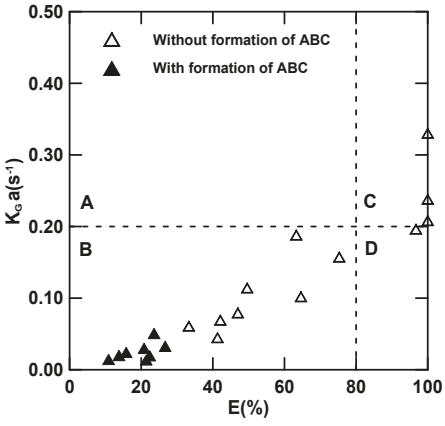

Figure 12. A plot of $K_G a$ vs. E showing the performance of the scrubbing process.

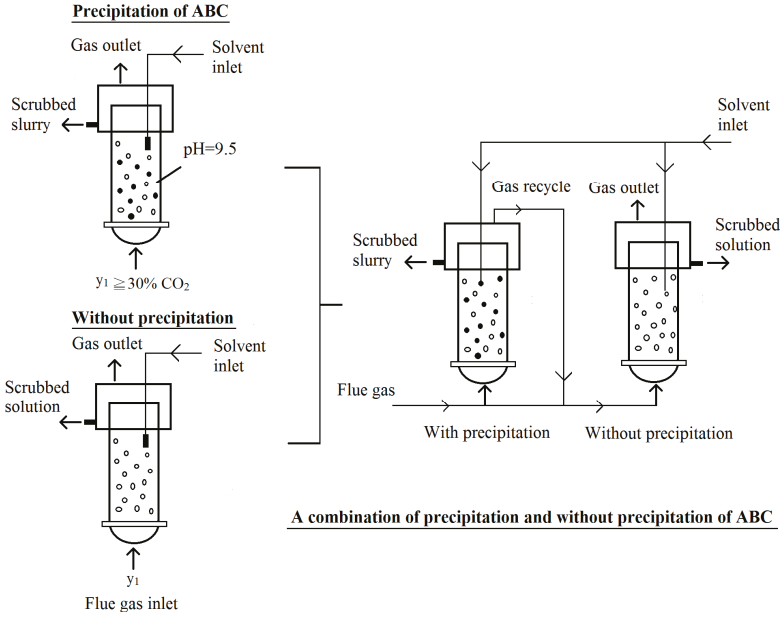

Figure 13. A combination of the crystallization and non-crystallization of ABC in CO_2 capture process using an aqueous ammonia solution.

5. Conclusions

A bubble-column scrubber was successfully used to explore the capture of CO_2 and the precipitation of ABC crystals. ABC crystals can be generated at a pH level of 9.5 in the concentration

range of 30–60% and $\gamma \geq 1.5$. The removal efficiency can be controlled to a desired level when the pH of the solution and inlet gas temperature were effectively adjusted. The absorption rates and overall mass-transfer coefficient obtained were comparable with other solvents, resulting in positive development for the capture of CO_2 using an aqueous ammonia solution. Data showed that $K_G a/E$ can be correlated with pH and γ to obtain an empirical equation for $K_G a/E$. Finally, reducing the emission of CO_2 from flue gas using an aqueous ammonia solution is found to be flexible both with and without precipitation depending on the requirement of CO_2 capture technology.

Acknowledgments: The authors acknowledge the financial support of the MOST in Taiwan ROC (MOST-106-2221-E-262-015).

Author Contributions: Pao Chi Chen conceived and designed the experiments and wrote the paper, while Shun Chao Yu performed the experiments and analyzed the data.

Conflicts of Interest: The authors declare no conflict of interest.

References

1. Han, K.; Ahn, C.K.; Lee, M.S. Performance of an ammonia-based CO_2 capture pilot facility in iron and steel industry. *Int. J. Greenh. Gas Control* **2014**, *27*, 239–246. [CrossRef]
2. Leung, D.Y.C.; Caramanna, C.; Maroto-Valer, M.M. An overview of current status of carbon dioxide capture and storage technologies. *Renew. Sustain. Energy Rev.* **2014**, *39*, 426–443. [CrossRef]
3. Yeh, A.C.; Bai, H. Comparison of ammonia and monoethanolamine solvents to reduce CO_2 greenhouse gas emissions. *Sci. Total Environ.* **1999**, *228*, 121–133. [CrossRef]
4. Chen, P.C.; Lin, L.C. Capture of carbon dioxide using aqueous ammonia in a lab-scale stirred-tank scrubber. *Adv. Mater. Res.* **2014**, *955–959*, 1927–1934. [CrossRef]
5. Chen, P.C.; Shi, W.; Du, R.; Chen, V. Scrubbing of CO_2 greenhouse gases, accompanied by precipitation in a continuous bubble-column scrubber. *Ind. Eng. Chem. Res.* **2008**, *47*, 6336–6343. [CrossRef]
6. Borhani, T.N.G.; Azarpour, A.; Akbari, V.; Wan Alwi, S.R.; Manan, Z.A. CO_2 capture with potassium carbonate solutions: A state-of-the-art review. *Int. J. Greenh. Gas Control* **2015**, *41*, 142–162. [CrossRef]
7. Bai, H.; Yeh, A.C. Removal of CO_2 greenhouse gas by ammonia scrubbing. *Ind. Eng. Chem. Res.* **1997**, *36*, 2490–2493. [CrossRef]
8. Dave, N.; Do, T.; Puxty, G.; Rowland, R.; Feron, P.H.M.; Attalla, M.I. CO_2 capture by aqueous amines and aqueous ammonia—A Comparison. *Energy Procedia* **2009**, *1*, 949–954. [CrossRef]
9. Diao, Y.F.; Zheng, X.Y.; He, B.S.; Chen, C.H.; Xu, X.C. Experimental study on capuring CO_2 greenhouse gas by ammonia scrubbing. *Energy Convers. Manag.* **2004**, *45*, 2283–2296. [CrossRef]
10. Huang, H.; Chang, S.G. Method to regenerate ammonia for the capture of carbon dioxide. *Energy Fuels* **2002**, *16*, 904–910. [CrossRef]
11. Darde, V.; Thomsen, K.; van Well, W.J.M.; Stenby, E.H. Chilled ammonia process for CO_2 capture. *Energy Procedia* **2009**, *1*, 1035–1042. [CrossRef]
12. Resnik, K.P.; Yeh, J.T.; Pennline, H.W. Aqua ammonia process for simultaneous removal of CO_2, SO_2 and NO_x. *Int. J. Environ. Technonl. Manag.* **2004**, *4*, 89–104. [CrossRef]
13. Liu, J.; Wang, S.; Zhao, B.; Tong, H.; Chen, C. Absorption of carbon dioxide in aqueous ammonia. *Energy Procedia* **2009**, *1*, 933–940. [CrossRef]
14. Yeh, J.T.; Resnik, K.P.; Rygle, K.; Pennline, H.W. Semi-batch absorption and regeneration studies for CO_2 capture by aqueous ammonia. *Fuel Process. Technol.* **2005**, *86*, 1533–1546. [CrossRef]
15. Chen, P.C.; Liu, S.M.; Jang, C.J.; Hwang, R.C.; Yang, Y.L.; Lee, J.S.; Jang, J.S. Interpretation of gas-liquid reactive crystallization data using a size-independent agglomeration model. *J. Cryst. Growth* **2003**, *257*, 333–343. [CrossRef]
16. Morel, F.M.M. *Principles of Aqueous Chemistry*; John Wiley & Sons: New York, NY, USA, 1983; Chapter 4; pp. 127–177. ISBN 0-471-08683-5.
17. Shen, J.F.; Yang, Y.M.; Ma, J.R. Promotion mechanism for CO_2 absorption into partially carbonated ammonia solutions. *J. Chem. Eng. Jpn.* **1999**, *32*, 378–381. [CrossRef]
18. Xiao, J.; Li, C.C.; Li, M.H. Kinetics of absorption of carbon dioxide into aqueous solutions of 2-amino-2-methyl-1-propanol + monoethanolamin. *Chem. Eng. Sci.* **2000**, *55*, 161–175. [CrossRef]

19. Meng, L.; Burris, S.; Bui, H.; Pan, W.P. Development of an analytical method for distinguishing ammonia bicarbonate form the products of an aqueous ammonia CO_2 scrubber. *Anal. Chem.* **2005**, *77*, 5947–5952. [CrossRef] [PubMed]
20. Ma, S.; Zang, B.; Song, H.; Chen, G.; Yang, J. Research on mass transfer of CO_2 absorption using ammonia solution in spray tower. *Int. J. Heat Mass Transf.* **2013**, *67*, 696–703. [CrossRef]
21. Chen, P.C. *Absorption of Carbon Dioxide in a Bubble Column Scrubber. Greenhouse Gases*; Liu, G., Ed.; InTech: Rijeka, Croatia, 2012; Chapter 5; pp. 95–116.
22. Petrov, P.; Ewert, G.; Rohm, H.J. Chemisorptive removal of carbon dioxide from process streams using a reactive bubble column with simultaneous production of usable materials. *Chem. Eng. Technol.* **2006**, *29*, 1084–1089. [CrossRef]
23. Sánchez, O.; Michaud, S.; Escudié, R.; Delgenès, J.-P.; Bernet, N. Liquid mixing and gas–liquid mass transfer in a three-phase inverse turbulent bed reactor. *Chem. Eng. J.* **2005**, *114*, 1–7. [CrossRef]
24. Zhao, B.; Su, Y.; Peng, Y.C. Effect of reactor geometry on aqueous ammonia-based carbon dioxide capture in bubble column reactors. *Int. J. Greenh. Gas Control* **2013**, *17*, 481–487. [CrossRef]
25. Mathias, P.M.; Reddy, S.; Connell, J.P.O. Quantitative evaluation of the aqueous-ammonia process for CO_2 capture using fundamental data and thermodynamic analysis. *Energy Procedia* **2009**, *1*, 1227–1234. [CrossRef]
26. Puxty, G.; Rowland, R.; Attalla, M. Comparison of the rate of CO_2 absorption into ammonia and manoethanolamine. *Chem. Eng. Sci.* **2010**, *65*, 915–922. [CrossRef]
27. Lee, K.H.; Lee, B.; Lee, J.H.; You, J.K.; Park, K.T.; Baek, I.H.; Hur, N.H. Aqueous hydrazine as a promising candidate for capyuring carbon dioxide. *Int. J. Greenh. Gas Control* **2014**, *29*, 256–262. [CrossRef]
28. Chen, P.C.; Luo, Y.X.; Cai, P.W. CO_2 Capture using monoethanolamine in a bubble-column scrubber. *Chem. Eng. Technol.* **2015**, *38*, 274–282. [CrossRef]
29. Meng, L. Development of an Analytical Method for Distinguishing Ammonium Bicarbonate from the Products of an Aqueous Ammonia CO_2 Scrubber and the Characterization of Ammonium Bicarbonate. Master's Thesis, Western Kentucky University, Bowling Green, KY, USA, December 2004.

© 2018 by the authors. Licensee MDPI, Basel, Switzerland. This article is an open access article distributed under the terms and conditions of the Creative Commons Attribution (CC BY) license (http://creativecommons.org/licenses/by/4.0/).

crystals

MDPI

Article

Effect of Alginate from Chilean *Lessonia nigrescens* and MWCNTs on $CaCO_3$ Crystallization by Classical and Non-Classical Methods

Marianela Sánchez [1], Patricio Vásquez-Quitral [1], Nicole Butto [1], Felipe Díaz-Soler [1], Mehrdad Yazdani-Pedram [2], Juan Francisco Silva [3] and Andrónico Neira-Carrillo [1,*]

1 Department of Biological and Animal Sciences, Faculty of Veterinary and Animal Sciences, University of Chile, Santiago, P.O. Box 2-15, Chile; m.sanchez@ciq.uchile.cl (M.S.); pvasquitral@yahoo.com (P.V.-Q.); nbutto@veterinaria.uchile.cl (N.B.); fdiazsoler@gmail.com (F.D.-S.)

2 Faculty of Chemical and Pharmaceutical Sciences, University of Chile, Santiago, S. Livingstone 1007, Chile; myazdani@ciq.uchile.cl

3 Department of Material Chemistry, Electrocatalysis Laboratory, Faculty of Chemistry and Biology, University of Santiago de Chile, Santiago, P.O. Box 40-33, Chile; juan.silva.r@usach.cl

* Correspondence: aneira@uchile.cl; Tel.: +56-22-978-5642

Received: 23 December 2017; Accepted: 29 January 2018; Published: 31 January 2018

Abstract: In our crystallization experiments, the influence of alginate from Chilean *Lessonia nigrescens* and functionalized multi-walled carbon nanotubes (MWCNTs) was tested through electrocrystallization (EC) and gas diffusion (GD) methods on the crystal growth of calcium carbonate ($CaCO_3$) and their possible stabilization of proto-structures in amorphous $CaCO_3$ (ACC) state through pre-nucleation clusters (PNC) essays with automatic potentiometric titrations were performed. $CaCO_3$ crystals obtained in the in vitro above-mentioned crystallization systems were characterized by scanning electron microscope (SEM), energy-dispersive X-ray spectrometry (EDS) and powder X-ray diffractometer (XRD). Our experimental findings showed that ALG and functionalized MWCNTs stabilized truncated and agglomerated vaterite-like particles through GD and EC methods. While, on the other hand, we obtained qualitative information about induction or inhibition of $CaCO_3$ nucleation that was provided by potentiometric titrations.

Keywords: calcium carbonate; alginate; *Lessonia nigrescens*; electrocrystallization; multi-wall carbon nanotubes; potentiometric titration

1. Introduction

It is well known that living organisms produce advanced functional biogenic materials with precise control of morphology, size, polymorphism and crystal growth orientation. That control is governed by a diverse variety of biomolecules, including proteins and polysaccharides [1,2]. The effect of proteins and polysaccharides (PS) on biomineralization has been studied; however few studies have evaluated the mechanistic effect of PS on crystallization. For example, polycarboxylated PS regulate calcite growth and morphology in coccoliths [3,4]. Calcium carbonate ($CaCO_3$) is the most abundant inorganic biomineral in nature and has considerable industrial interest [5]. In order to achieve control over this biomineral, it is important to understand the mechanisms by which crystals are formed and the interaction between organic and inorganic components, as it occurs in nature. In the last decade, the role of inorganic precursor species (IPS), such as amorphous phases and pre-nucleation clusters (PNCs) has become relevant [6]. PNCs of $CaCO_3$ occur before the formation of metastable solid nucleus of amorphous $CaCO_3$ (ACC) and this was initially seen with measurements with a calcium ion-selective electrode and pH-titration during the early stages of precipitation (pre- and post-nucleation) [7]. The

existence of PNCs in homogeneous solutions has been evidenced for the most important biominerals, calcium phosphates and carbonates, iron oxides, silica and organic compounds such as amino acids [8]. Thus, potentiometric titration has become an excellent technique to study the influence of additives in the overall process of precipitation [9]. $CaCO_3$ has more than one amorphous phase (polyamorphism) identified as proto-calcite (pc-ACC), proto-aragonite (pa-ACC) and proto-vaterite (pv-ACC) by the local arrangement of atoms [10,11].

In an attempt to understand the effect of PS on the early stages of crystallization, short chain sugars have been tested by using automatic potentiometric titrations [12]. In this regard, it is demonstrated that the nature of glycosidic linkages, polarity, ion binding sites and stereochemistry has strong influence on $CaCO_3$ crystallization [13]. With this in mind and following our previous results, here we used an alginate (ALG) sample obtained from Chilean brown algae *Lessonia nigrescens* (ALG *Les*) in order to add more experimental evidence to the relationship between PS and IPS [12,14–16]. In this work, we investigated the direct effect of ALG *Les*, extracted from a natural brown algae located in north of Chile, on early stages of $CaCO_3$ mineralization. ALG is a linear copolymer composed of two monomeric units: β-D-mannuronic acid (M) and α-L-guluronic acid (G), where the M and G units are $1 \rightarrow 4$ linked by glycosidic bonds. The M and G homopolymeric blocks are distributed along the copolymeric chain and region of MG blocks. The ratio and location of M and G units are critical factors for their physicochemical properties such as affinity to cations, gelification and hydrogel behaviors and chain rigidity. ALGs are relevant to crystallization because G units can interact with divalent cations through binding sites [17]. On the other hand, it is known that organic hydrogels play an important role in $CaCO_3$ biomineralization in corals and mollusks [18]. Therefore, the investigation of the influence of PS hydrogels such as ALG on $CaCO_3$ crystallization through classical and non-classical methods is necessary. Rounded calcite crystals have been obtained through gas diffusion (GD) method by using ALG [19]. ALG does not alter the typical rhombohedral calcite form on $CaCO_3$ crystallization [20] and it has shown inhibiting capacity by adsorption onto the active growth sites of the crystal surface [21]. Also, "rosette-like" $CaCO_3$ aggregates have been obtained by direct mixing of Ca^{2+} and $CO_3{}^{2-}$ ions in the presence of sodium ALG [22]. Ma and Feng used Ca-ALG beads as a slow and continuous source of Ca^{2+} ions into Na_2CO_3 solution. Crystal size, morphology and surface roughness were influenced by the type of ALG used in the crystallization experiments, which could be accounted by the length of the G blocks [22]. Our group extracted and purified ALG from Chilean algae. The purified ALG was used for microencapsulation of parathyroid gland cells from human patients showing good viability and sustained release of PTH hormones [23]. To our knowledge, most of the investigations have addressed the effect of ALG on $CaCO_3$ mineralization in terms of morphology and polymorphism of the resulting crystals by using only GD as a classical method. In general, the structure and stability of IPS and chemical nature of the additives influence the characteristics of inorganic minerals, including the formation of superstructures, inhibition of the nucleation, and stabilization of different polymorphs, among others [24].

Additionally, carbon-based materials have been investigated as nanomaterials-controlled crystallization [25]. Carbon nanotubes (CNTs) have become an attractive material due to: large energy absorbing capacity, electrical conductivity, chemical stability, low density, high aspect ratio, stiffness, etc. [26]. CNTs have been proved an efficient heterogeneous nucleating agents that can accelerate the crystallization of several inorganic materials, including cement, silicon nitride and zirconium oxide [27–29]. The effect of pristine and functionalized single-walled CNT (SWCNT) and multi-walled CNT (MWCNT) on $CaCO_3$ mineralization has been also investigated. Typical calcite and spherical or ellipsoidal $CaCO_3$ crystals were obtained when pristine CNTs and modified CNTs were utilized as templates [30]. In other work, CNT favored the formation and stabilization of vaterite crystals [31]. Therefore, it is very important to introduce alternative classical methods such as electrocrystallization (EC) for in vitro $CaCO_3$ mineralization. For instance, very few studies have reported the effect of commercial ALGs on crystal growth of $CaCO_3$ by using an electrochemical approach [32]. In addition,

for a better understanding of the events of PNCs on $CaCO_3$ mineralization in the presence of ALG as natural PS and carbon nanomaterials, quantitative techniques are necessary.

Herein, we evaluated the effect of ALG *Les* from *Lessonia nigrescens*, and pristine MWCNT and functionalized MWCNT and their combination, on the different stages of $CaCO_3$ crystallization using EC and GD techniques and automatic potentiometric titrations as classical and non-classical crystallizations, respectively.

2. Materials and Methods

2.1. Reactants

Calcium chloride dihydrate ($CaCl_2 \cdot 2H_2O$), sodium bicarbonate ($NaHCO_3$), sodium hydroxide (NaOH), sodium chloride (NaCl) and potassium nitrate (KNO_3) were obtained from Merck. Sodium alginate extracted from *Lessonia nigrescens* (ALG *Les*) was purified in ethanol by using soxhlet purification protocol [23]. MWCNTs were purchased from Bayer (Bayer, Germany). According to the manufacturer's specifications, the average diameter and length of MWCNTs were 30 nm and tens micrometer, respectively, with 95% purity. Indium tin oxide (ITO) conductive glass electrodes used as conductive material on EC of $CaCO_3$ were purchased from Delta Technologies (Dallas, TX, USA). In case of MWCNT-COOH and MWCNT-OX materials were gently provided by the laboratory of electrocatalysis of the University of Santiago de Chile (Dr. J.F. Silva) and laboratory of polymer chemistry of the University of Chile (Dr. M. Yazdani-Pedram), respectively.

2.2. In Vitro Gas Diffusion (GD) Crystallization of $CaCO_3$.

GD crystallization of $CaCO_3$ crystals in the presence of ALG *Les* and MWCNTs derivatives as polymeric additives was carried out at room temperature for 24 h. GD method was performed as we described in our previous works [33–36].

2.3. Electrodeposition of Alginate/MWCNTs.

For the preparation of ALG-MWCNTs/ITO electrodes, $CaCO_3$ powder (0.25%) was blended into ALG *Les* solution (12.5 g/L), and sonicated during 30 min. After, 1.6 mg of MWCNTs were added to the above solution (ALG/MWCNT/$CaCO_3$), and this new mixture was ultrasonicated for 5 min at room temperature in order to obtain a black and homogeneous suspension, containing 0.08 mg mL^{-1} MWCNTs. Then, an ITO coated glass slide was partially immersed (1.25 cm × 1.0 cm) into this deposition solution, and an anodic voltage was applied to achieve a current density of 3 $A \cdot m^{-2}$ during 2 min. After electrodeposition, ITOs electrodes were removed from the solution, rinsed with nanopure water and air dried prior to electrochemical measurements [37].

2.4. Electrocrystallization (EC) Experiments of $CaCO_3$.

EC essays were performed onto ITO glass surface into the glass electrochemical cell using a galvanostat/potentiostat BASi Epsilon (USA) instrument. Chronoamperometry was used during the $CaCO_3$ electrocrystallization. ITO working electrodes from Corning® aluminosilicate glass, 25 × 25 × 1.1 mm, coated with one surface of RS = 5–15 Ω was used. ITO were washed with methanol and Milli Q water, obtained from a water purification system LaboStar 4-DI/UV and sonicated them during 5 min. The electrochemical measurements were conducted in pieces of ITO as working electrodes (WE), a coiled platinum (Pt) wire was used as auxiliary electrode (AE) and a silver chloride electrode (Ag/AgCl) as reference electrode (RE). For the electrochemical reaction we used an electrolyte solution with dissolved O_2, at a basic pH and at room temperature. The electrolytic solution consisted of 0.2 mM $CaCl_2$, 6 mM $NaHCO_3$ and 10 mM NaCl. For the EC of $CaCO_3$, a linear sweep voltammetry was also performed in order to determine first the potential maximal value where O_2 reduction reaches the maximum voltage activity, that is, −890 mV. This potential value was fixed and further used for the chronoamperometry technique performed on $CaCO_3$ coating for 120 min [32,38].

2.5. Prenucleation Clusters (PNC) Assay of $CaCO_3$

PNC essays were conducted by direct automatic potentiometric titrations using a titration system (Titrando 907) from Metrohm (Herisau, Switzerland), with two dosing units (Dosino 800), controlled by software (Tiamo v2.2). 10 mM $CaCl_2$ was added at a rate of 0.01 mL/min into 20 mL sample solution in a 50 mL beaker while stirring at 900 r.p.m. Then, pH was kept constant at 9.00 by automatic counter-titration of 0.01 M NaOH. The pH and free Ca^{2+} concentration in the samples were monitored by a glass electrode (Metrohm, No. 6.0256.100) and a Ca^{2+} ion-selective electrode (ISE, Metrohm, No. 6.0508.110), respectively. Between experiments, beaker and electrodes were cleaned with acetic acid to remove precipitated $CaCO_3$ particles, followed by multiple rinsing with water. The Ca^{2+}-ISE was calibrated regularly by titrating $CaCl_2$ into 20 mL water (adjusted to pH 9.00 by addition of NaOH) using the above-mentioned procedure. All titrations were performed at room temperature with a minimum of three repetitions [6,12,13].

2.6. Characterization

The surface morphology of the resultant $CaCO_3$ crystals was characterized by scanning electron microscopy (SEM) using a JEOL JSM-6390LV (Tokyo, Japan) and HITACHI TM3000 (Hong Kong, China) instruments. The XRD diffraction spectra were taken from a powdered $CaCO_3$ sample using a Siemens D-5000 X-ray diffractometer (Siemens, Munich, Germany).

3. Results and Discussion

EC and GD classical methods were utilized in order to evaluate the morphogenetic effect of Chilean ALG *Les*, pristine MWCNT and oxidized MWCNT (MWCNT-OX) on $CaCO_3$ crystal growth. In addition, non-classical PNCs essays through automatic potentiometric titrations showed a possible mechanism of early action of these additive compounds. GD crystallization was carried out for 24 h at room temperature. Figure 1 shows SEM images of $CaCO_3$ crystals grown without additive as control (Figure 1A), and in the presence of additives at 2 mg/mL ALG *Les* (Figure 1B), 1 mg/mL MWCNT (Figure 1C), 1 mg/mL MWCNT-OX (Figure 1D), mixtures of ALG *Les*/MWCNT (Figure 1E) and ALG *Les*/MWCNT-OX (Figure 1F). Figure 1A shows typical rhombohedral calcite crystals of size 20–50 μm, while Figure 1B shows individual and aggregated calcite crystals in the presence of ALG *Les* as additive. These experimental results are in agreement with the non-modified calcite form already reported by several authors who used commercial ALGs [39]. However, when spin coated ALG was used as oriented support for $CaCO_3$ GD method, abundant calcite and vaterite particles were obtained [40]. Figure 1C shows that when MWCNT was used as additive for $CaCO_3$ mineralization, mainly single calcite crystals were formed. We found that at increasing concentration of MWCNTs, higher quantity of small calcite crystals appeared (see Supplementary Material, Figure S1). In consequence, MWCNT induced large quantity of small calcite crystals in comparison to control experiment. Furthermore, experimental set up under agitation causes the production of smaller crystals (see, Figure S2). These indicate that MWCNT may act as nucleation sites in the above-described assays, favoring larger amount of $CaCO_3$ crystals. On the other hand, numerous calcite crystals and agglomerated vaterite-like particles were stabilized in the presence of MWCNT-OX (Figure 1D). Resultant $CaCO_3$ crystals of 30–50 μm were formed with ALG *Les* combined with MWCNT or MWCNT-OX. The overall results with MWCNTs are in agreement with Tasis et al. who utilized GD method for $CaCO_3$ mineralization with non-modified MWCNT and non-covalently modified MWCNT with amphiphilic isoprene-*b*-acrylate copolymer [30]. $CaCO_3$ crystals grown on non-modified MWCNT substrate showed similar rhombohedral calcites, while modified MWCNT substrate induced ellipsoidal or spherical crystals. These morphological changes can be attributed to the interactions between the carboxylic and hydroxyl groups and specific faces of the growing $CaCO_3$ crystals. Moreover, Li et al. proved the influence of carboxylated SWCNT and MWCNT on spherical vaterite stabilization [31]. Herein, we evaluated the effect of the combination of ALG *Les*/MWCNT and ALG *Les*/MWCNT-OX

as additive on $CaCO_3$ crystallization. Our findings showed a synergic effect when ALG *Les*/MWCNT mixture was used, indicating an effective stabilization capacity. In this case, isolated calcite crystals of 10–30 μm with well-defined edges were observed (Figure 1E). Moreover, when ALG *Les*/MWCNT-OX mixture was used, small truncated calcites of 5–10 μm with rounded edges were obtained due to the active surface of combined additives. These rounded edges can be due to the deposition of a thin organic layer underneath, evidenced by the bright background, causing differences in conductivity and brightness of the image (Figure 1F).

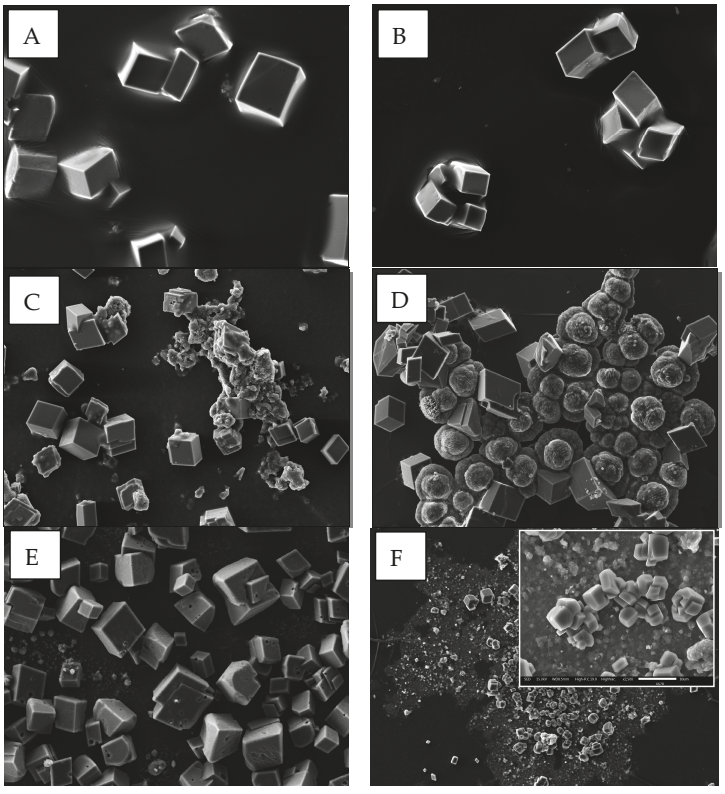

Figure 1. SEM images of $CaCO_3$ crystals obtained by using GD crystallization. Control (**A**), ALG *Les* (**B**) MWCNT (**C**), MWCNT-OX (**D**), ALG *Les*/MWCNT (**E**) and ALG *Les*/MWCNT-OX (**F**). Scale bar = 50 μm. Inset scale bar = 10 μm.

In order to determine the internal lattice of crystalline $CaCO_3$ products, X-ray diffraction (XRD) technique was performed. Figure 2 shows XRD pattern of $CaCO_3$ crystals obtained by GD method without an additive as control (Figure 2A), and in the presence of ALG *Les* (Figure 2B), MWCNT (Figure 2C), MWCNT-OX (Figure 2D), mixtures of ALG *Les*/MWCNT (Figure 2E), and ALG *Les*/MWCNT-OX (Figure 2F). In general the XRD spectra shows crystalline peaks with slight difference in the intensity of the main reflections from calcite (104) and vaterite (101), suggesting that the obtained inorganic product mainly consisted of mixed phases of calcite and vaterite particles. Although the integrate intensity of the (104) reflections from calcite at ca. $2\theta = 30°$ and vaterite at ca. $2\theta = 25°$ were not used to determine the relative amount of the calcite and vaterite, the calcite polymorphism in the resultant inorganic deposition was higher as observed by SEM analysis. It is interesting to note that the XRD analysis clearly showed a new diffraction peaks at $2\theta = 56.7°$, which is ascribed to (202)

crystallographic face of vaterite when ALG *Les* (Figure 2B) and MWCNT-OX (Figure 2D) and their respective mixtures of ALG *Les*/MWCNT (Figure 2E) and ALG *Les*/MWCNT-OX (Figure 2F) were used as additives.

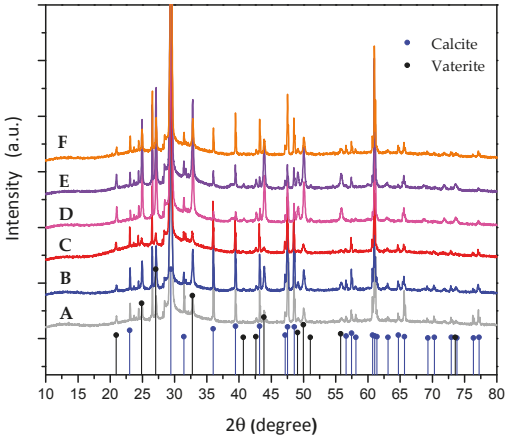

Figure 2. XRD pattern of $CaCO_3$ crystals obtained by GD crystallization: Control (**A**), ALG *Les* (**B**), MWCNT (**C**), MWCNT-OX (**D**), ALG *Les*/MWCNT (**E**) and ALG *Les*/MWCNT OX (**F**). Vertical blue line and black line designation in graph indicate calcite and vaterite standard peaks, respectively.

We believe that different complementary crystallization methods can be used to address the effect of ALG *Les* and MWCNT on the in vitro $CaCO_3$ mineralization. With this in mind, a second in vitro crystallization method by an electrochemical approach was carried out. The EC method corresponds to a heterogeneous system, in which abundant and uniform $CaCO_3$ crystals on ITO electrode were formed. The general scheme of EC of $CaCO_3$ onto ITO substrate is illustrated in the supplementary material (see Figure S3). The electrolyte solution composed of $Ca(NO_3)_2$, $NaHCO_3$ and NaCl with dissolved molecular oxygen (O_2) was used at alkaline pH solution media and the electrochemical reduction of O_2 is promoted by applying a sufficiently negative potential. The electro-reduction produces a local increment of pH, which in turn induces the bicarbonate (HCO_3^-) ions present at the interface to become carbonate (CO_3^{-2}), thus the precipitation of $CaCO_3$ is achieved [32]. Deposited $CaCO_3$ crystals onto ITO surface are not conductive, reducing the active area of the ITO electrode. Consequently, the total cathodic current decreases, which can be measured by chronoamperometry [41]. Therefore, a set of ITO substrates with ALG and MWCNTs separately and mixed through EC of $CaCO_3$ by electrodeposition was carried out. The resultant crystals were then analyzed by scanning electron microscopy SEM (Figure 3) and chronoamperometry. The chronoamperometric curves of EC of $CaCO_3$ in the absence of additive (control; Figure S4A) and in the presence of ALG *Les* (Figure S4B) can be seen in the Supplementary Material, Figure S4. SEM analysis showed that when EC essays were performed on bare ITO (Figure 3A) rhombohedral calcite and circular vaterite were formed in a similar proportion. When the EC was performed on ALG *Les* on modified ITO, isolated rhombohedral calcite and spherical $CaCO_3$ superstructures composed of small and aggregated calcite were observed (Figure 3B). Similar "rosette-like" calcite was obtained in the presence of pectin as additive on $CaCO_3$ crystallization [42]. Moreover, when EC of $CaCO_3$ was performed on modified ALG *Les*/MWCNT-ITO, a great quantity of agglomerated small calcite and spherical metastable vaterite particles were produced (Figure 3C). Surprisingly, in the presence of ALG *Les*/MWCNT-OX mixture on modified ITO, agglomerated vaterite and calcite crystals were stabilized (Figure 3D). In this case, the presence of chemical moieties e.g., hydroxyl group in MWCNT-OX could influence the $CaCO_3$ mineralization explaining the huge amount and size of the metastable form of vaterite particles.

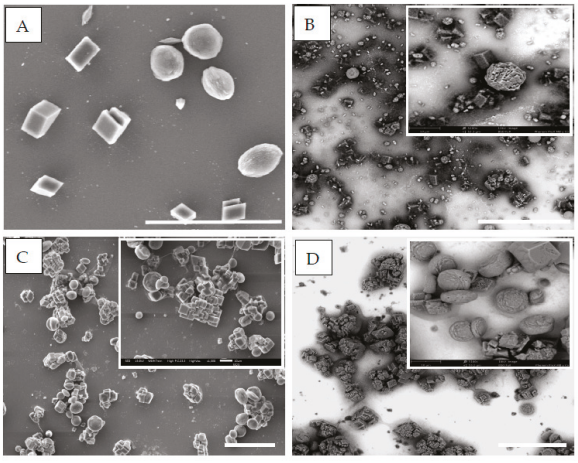

Figure 3. SEM images of $CaCO_3$ crystals obtained through EC on modified ITO electrodes: control (bare ITO) (**A**), ALG *Les* modified ITO (**B**), ALG *Les*/MWCNT modified ITO (**C**), ALG *Les*/MWCNT-OX modified ITO (**D**). Scale bar = 50 μm. Inset scale bar = 10 μm.

Moreover, grazing incidence X-ray diffraction (XRD) measurements of the bare ITO glass substrate and $CaCO_3$ particles obtained on modified ITOs through EC is shown in Figure 4. Grazing incidence XRD analysis was performed on ITO electrode because of strong ITO interference and low quantity deposited inorganic mineral. The principal crystalline peaks of bare ITO substrate (green line) at 2θ = 31.7° (Figure 4A), and $CaCO_3$ particles on bare ITO (black line) (Figure 4B) and in the presence of MWCNT-OX and ALG *Les* at 2θ = 30° suggested that the calcite polymorph was the principal product. Although all crystalline peaks ascribed to the diffraction of calcite, less thermodynamically vaterite polymorphs was also observed (Figure 4D). A broad peak in the range of 2θ = 8–18° was observed only when ALG *Les*, ALG *Les*/MWCNT or ALG *Les*/MWCNT-OX were used as additive. This fact is due to semi-crystalline nature of sodium ALG, showing peaks at 2θ = 12.81°, 21.83°, 23.25°, 35.9° and 39.92° [43,44].

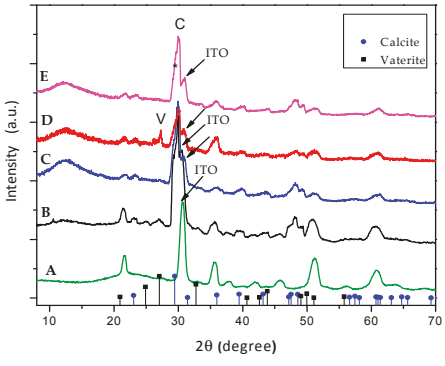

Figure 4. XRD pattern of ITO substrate (**A**) and $CaCO_3$ crystals obtained through EC in the presence on bare ITO as control (**B**), ALG *Les* modified ITO (**C**), ALG *Les*/MWCNT modified ITO (**D**), ALG *Les*/MWCNT-OX modified ITO (**E**), Vertical blue line and black line designation in graph indicate calcite and vaterite standard peaks, respectively. Meanwhile, designation C, V and * correspond to (104) face of calcite and ITO signal, respectively.

To gain a better understanding of the effect of ALG *Les* and MWCNTs on in vitro $CaCO_3$ obtained through GD and EC methods, a non-classical technique was conducted by direct automatic potentiometric titrations using PNCs essays at pH 9.0. The advantage of PNCs methods lies in the fact that is possible to obtain information regarding the changes of slope before nucleation, nucleation time and solubility product after nucleation, among others directly from the $CaCO_3$ crystallization kinetic curves. Therefore, induction or inhibition effect of additives on pre-nucleation of $CaCO_3$ species and the additives according to their effect on titration essays can be classified as follows. Type I, complexation of Ca^{2+} ions (delayed initial increase in free Ca^{2+}), type II, influence on the PNC equilibriums in solution (change in the slope of the curve before nucleation), type III, effect on nucleation, inhibition (IIIa) or promotion (IIb) of nucleation, type IV, adsorption onto nucleated particles, and type V, modification of the structure and stability of the initially precipitated phase, giving liquid-like, amorphous or crystalline polymorphs (after nucleation) [13,24].

With this in mind, we studied the control assay of $CaCO_3$ nucleation time, that was 6.300 s and the ion product measured as 3.21×10^{-8} M^2 after nucleation (Figure 5), which is slightly higher but in concordance with the solubility values reported for the proto-calcite (ACC I or pc-ACC) formed at pH 9.0 [6]. When the titration experiments were performed in the presence of ALG *Les* at two concentrations, a direct relationship between nucleation time and the concentration of ALG *Les* was found (Figure 5). There was a slight decrease in the pre-nucleation slope observed with ALG *Les* at 5 mg/L, indicating an increase in the complexed Ca^{2+} ions during mineralization. These results suggest the stabilization of amorphous PNC species. Moreover, the solubility product observed was close to the value obtained for the control assay. However, when ALG *Les* at 10 mg/L was utilized, the value of the solubility product reaches that of ACC species representing the more soluble initial stages of unstable amorphous entities (Figure 5). These results are in agreement with the previous $CaCO_3$ mineralization by classical methods using ALG *Les*, where proto-structures are stabilized. This behavior has been previously documented, where ALG favors the formation of ACC state. Leng et al. proposed a mechanism for the formation of saucer-like structures in which Ca^{2+}-ALG interactions stabilizes aggregated proto-structures of ACC particles [45]. According to our PNC essays, lower concentration of ALG *Les* selectively controls the in vitro $CaCO_3$ mineralization by direct interaction of ACC surfaces through PNC essays. The possible mechanisms of ALG *Les* on $CaCO_3$ nucleation could be explained by PNC equilibriums in solution (type II), inhibition of nucleation (type IIIa) and by the solubility product changes (type V).

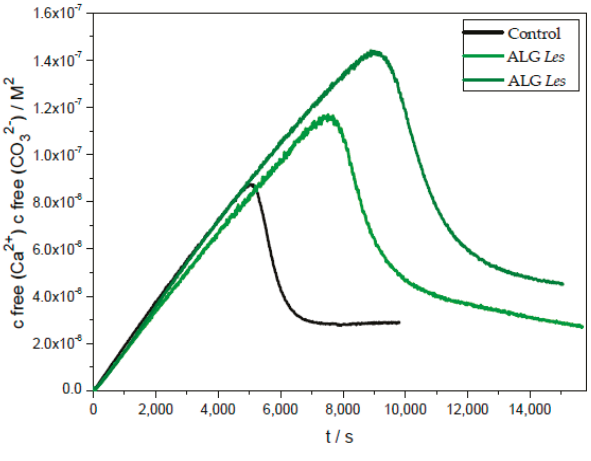

Figure 5. Time development of $CaCO_3$ solubility products using two concentrations of ALG *Les* at pH 9.0: blank (**black line**), 5 mg/L ALG *Les* (**green line**) and 10 mg/L ALG *Les* (**olive line**).

Moreover, evolution of the solubility product was studied in the presence of MWCNT at 2.5 and 7.5 mg/L concentrations as is shown in Figure 6. Both concentrations were selected since previous studies indicated an observable effect on the $CaCO_3$ crystallization by this method [46]. As seen in Figure 6 no difference in the slopes of the curves and solubility products was noticed, however a notorious decrease of nucleation time was observed. Specifically, nucleation time decreased to 5.000 s for both concentrations in comparison to the control essay registered at 6.250 s. Therefore, this additive at this concentration acted as strong promoter of $CaCO_3$ crystallization. We also found that the concentration MWCNT does not affect the nucleation time. This is a characteristic of heterogeneous nucleation, where $CaCO_3$ crystals are in contact with MWCNT. No chemical interaction between $CaCO_3$ and pristine MWCNT exists due to the absence of polar functional groups on the surface of MWCNT, thus the final solubility product value remains unaltered. These results can be related to preliminary empirical observations, in which pristine MWCNTs induced the formation of small $CaCO_3$ particles that may randomly contact each other, therefore the crystals can grow on MWCNTs [31]. Other studies have shown similar nucleating activity as this current study. Some examples included nucleation and growth of hydroxyapatite crystals on functionalized SWCNT [47]. They found that SWCNT accelerate the rate of the hydration reaction of tricalcium silicate in the ordinary Portland cement acting as a nucleating site [27]. According to our PNC essays, the influence of pristine MWCNT on the $CaCO_3$ mineralization showed an induction capacity on the nucleation time (type IIIb), however this did not affected the pre-nucleation slope and the solubility product of nucleated phase.

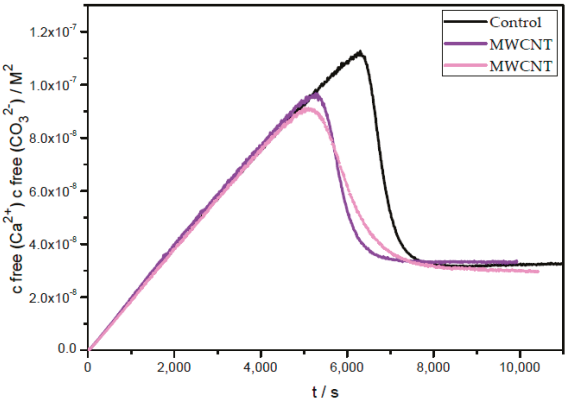

Figure 6. Time development of $CaCO_3$ solubility products using two concentration of MWCNT at pH 9.0: blank (**black line**), 2.5 mg/L MWCNT (**purple line**) and 7.5 mg/L MWCNT (**magenta line**).

In order to evaluate the effect of functionalized MWCNT-COOH on the PNCs experiments, MWCNT containing predominantly carboxylic groups was used as additive at 2.5 mg/L (Figure 7). Our findings showed a notorious decrease in the slope of the free Ca^{2+} curve before nucleation, indicating a strong interaction of the MWCNT-COOH with Ca^{2+} ions and suggesting the PNCs stabilization. The nucleation time is ca. 2.5 times greater than the control experiment, indicating that functionalized MWCNT act as an effective inhibitor of the nucleation of $CaCO_3$ and stabilizing the proto-structure of ACC entities. Accordingly, the influence of MWCNT-COOH on the $CaCO_3$ mineralization obeys the following mechanism: PNC equilibriums in solution (type II) and inhibits nucleation (type IIIa). These findings are in agreement with previous studies, which showed that MWCNT-OX can alter the nucleation, growth and aggregation of $CaCO_3$ crystals under classical crystallization conditions.

With the above-mentioned results obtained with ALG *Les* at lowest concentration (5 mg/L), the evolution of the solubility product was studied in mixture with two concentrations of MWCNT at

2.5 mg/L (Figure 8A) and at 7.5 mg/L (Figure 8B). Figure 8A (orange line) shows a similar decrease in the slope of the free Ca^{2+} curve before nucleation, indicating interaction of the additive surface with Ca^{2+} ions and inhibition of the nucleation similarly to ALG *Les*. Moreover, the solubility product observed here was close to the value obtained for the control assay. However, when the evolution of the solubility product was evaluated in mixture but with the higher concentration of MWCNT (7.5 mg/L), the slope of the free Ca^{2+} curve before nucleation was similar to ALG *Les*, but the presence of MWCNT 7.5 mg/L affected the overall results (Figure 8B). In this manner, a decrease of the nucleation time was observed, showing a less powerful inhibition of the nucleation time than with ALG *Les* as additive. At the end, the solubility product obtained with this mixture had a lower value than the control assay indicating stabilization of ACC proto-structures.

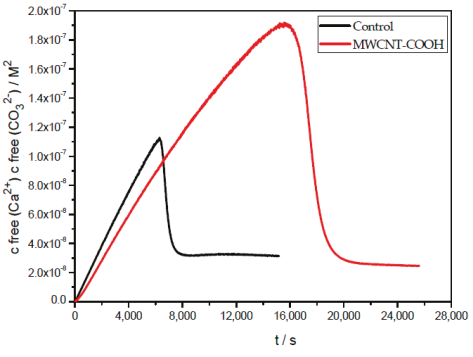

Figure 7. Time development of $CaCO_3$ solubility products using 2.5 mg/L MWCNT-COOH at pH 9.0: control (**black line**) and 2.5 mg/L (**red line**).

Figure 9 shows the evolution of the solubility product using the ALG *Les* with functionalized MWCNT-COOH. Our experimental curves showed a decrease in the slope of the free Ca^{2+} curve before nucleation indicating the strongest interaction of additive surface with Ca^{2+} ions, and inhibition of the nucleation here was similar to MWCNT-COOH and the solubility product value is higher than those of control and MWCNT-COOH. These results indicate that the optimum additive for inhibiting the nucleation of $CaCO_3$ is the mixture of ALG *Les* with MWCNT-COOH, in which the evolution of the solubility product shows almost the same effect of MWCNT-COOH alone. It is concluded the best synergetic effect is achieved when a strong interaction exists between components of additives with inhibiting activity.

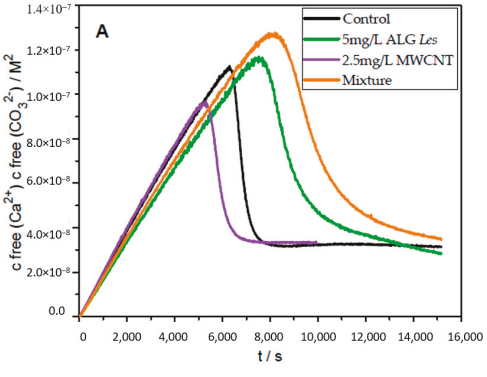

Figure 8. *Cont.*

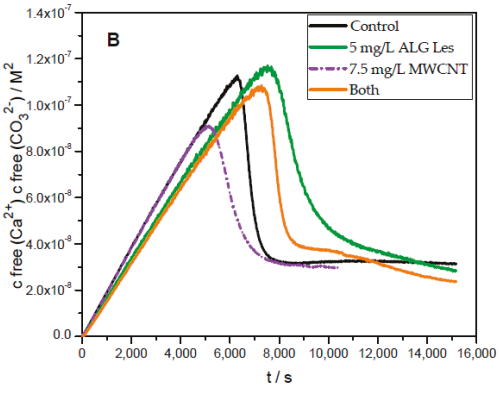

Figure 8. Time development of $CaCO_3$ solubility products using 5 mg/L ALG *Les* and MWCNT of 2.5 mg/L (**A**) and 7.5 mg/L (**B**) concentrations at pH 9.0: Blank (black line), 5 mg/L ALG *Les* (green line), 2.5 mg/L MWCNT (purple straight line) and 7.5 mg/L MWCNT (purple dash dot line), and both in mixture (orange line).

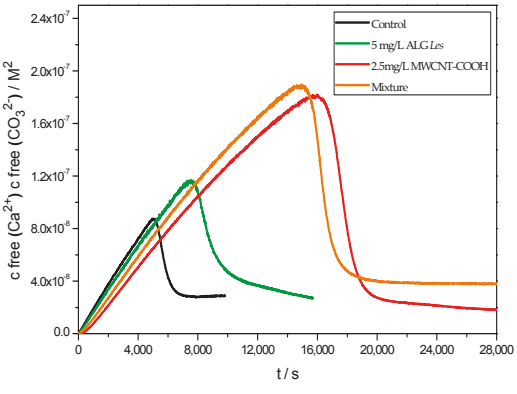

Figure 9. Time development of $CaCO_3$ solubility products using ALG Les and MWCNT-OH at pH 9.0: blank (**black line**), 5 mg/L ALG *Les* (**green line**), 2.5 mg/L MWCNT-COOH (**red line**), and both in mixture (**orange line**).

4. Conclusions

We demonstrated that by using classical methods such as GD and EC, a synergic effect of the mixture of ALG *Les* and MWCNT on the in vitro $CaCO_3$ mineralization was obtained indicating an effective stabilization. Moreover, the XRD analysis showed the main reflections from calcite and the less thermodynamically stable polymorph vaterite particles as the main inorganic products. On the other hand, non-classical methods through automatic potentiometric titrations essays clearly demonstrated the direct relationship between nucleation time and the concentration of additives. The pre-nucleation slope indicated complexed Ca^{2+} ions with additive surface during mineralization, stabilization of amorphous proto-structure of ACC, etc. showing a quantitative data of the entire crystallization process of additives at pre-and post-nucleation state. Therefore, by using simultaneously both crystallization approaches, we can further understand how biomacromolecules act as inductor or inhibitor and selectively control the crystal growth, size and polymorphism of biogenic mineral in a similar manner that occurs in nature.

Supplementary Materials: The following are available online at http://www.mdpi.com/2073-4352/8/2/69/s1. Figure S1: SEM images of $CaCO_3$ obtained through GD showing the effect of MWCNT concentration on number and size of calcite particles. Figure S2: Effect of agitation on the resultant $CaCO_3$ crystals. Figure S3: Scheme of EC of $CaCO_3$ onto ITO. Figure S4: Chronoamperometric curves of EC of $CaCO_3$ in absence of additive (control) and additives such as pristine MWCNT, ALG Les, MWCNT-OX and mixed of ALG *Les*/MWCNT and ALG *Les*/MWCNT-OX.

Acknowledgments: This research was supported by FONDECYT 1171520, ACCDiS 15130011 granted by the Chilean Council for Science and technology (CONICYT), and funded by the Program U-Redes, Vice-presidency of Research and Development, University of Chile. Marianela Sánchez thanks CONICYT scholarship 21120326.

Author Contributions: Marianela Sánchez, Patricio Vásquez-Quitral, Nicole Butto, Felipe Díaz-Soler conceived, designed and performed the experiments; Marianela Sánchez and Andrónico Neira-Carrillo wrote the paper. Mehrdad Yazdani-Pedram and Juan Francisco Silva contributed with manuscript supervision. Andrónico Neira-Carrillo contributes with reagents/materials/analysis tools and represents the senior author, and he is principal investigator of the 1171520 FONDECYT project and Program U-Redes, Vice-presidency of Research and Development, University of Chile, in which the current research work were realized. Therefore, Andrónico Neira-Carrillo gives the first author the intellectual input, designs and approves the reported protocols of this study. Andrónico Neira-Carrillo and Mehrdad Yazdani-Pedram have been responsible for the manuscript correction, proof reading during all paper submission, handling the revisions and re-submission process of the revised manuscript.

Conflicts of Interest: The authors declare no conflict of interest.

Appendix A

Appendix A.1 ALG Extraction from L. nigrescens

ALG extraction from algae was conducted using a modified extraction method described in literature [48]. Resultant ALG sample of various ALG particle sizes were obtained from dried *L. nigrescens* by mechanical crushing and screening were obtained. Briefly, 10 g of algae were ground on a Thomas-Wiley laboratory mill, model 4, wetted with 400 mL of distilled water under vigorous stirring and acidified with HCl 0.1 M solution to pH 4. This mixture was stirred for 15 min at room temperature and then the supernatant was removed. This pre-treatment was repeated three times on each sample, each time using 40, 25 and 20 mL of HCl solution, respectively. Then wet-algae was mixed with 250 mL of a 1.0 N Na_2CO_3 solution at pH 11.5 in a beaker and mechanically stirred for 2 h at 60 °C. Sodium alginate was removed from starting material and diluted with 800 mL of distilled water and then treated with 1 g of diatomaceous earth or activated charcoal. The resulting mixture was stirred for 15 min and the insoluble material removed by centrifugation, giving sodium ALG as product in the supernatant.

Appendix A.2 Purifying of ALG Extracted from L. nigrescens

A sodium ALG solution with 1M HCl (250 mL) was mixed until reaching a pH value of 2, and then kept at room temperature under stirring for 1 h. Further, the precipitated alginic acid was removed by centrifugation, and distilled water (100 mL) and 1.0 M Na_2CO_3 (150 mL) were added. The total mixture was left under stirring at room temperature for 1 h until soluble sodium ALG was obtained. After that, ALG was precipitated from this solution by slow addition of ethanol (volume 1/1). The resultant precipitate was purified by washing with ethanol through soxhlet extractor for 100 h, and dried under vacuum at room temperature, until reaching a constant mass [25,48].

References

1. Mann, S. *Biomineralization: Principles and Concepts in Bioinorganic Materials Chemistry*, 1st ed.; Oxford University Press: New York, NY, USA, 2001; pp. 1–30. ISBN 0198508824.
2. Arias, J.L.; Neira-Carrillo, A.; Arias, J.I.; Escobar, C.; Bodero, M.; David, M.; Fernández, M.S. Sulfated polymers in biological mineralization: A plausible source for bio-inspired engineering. *J. Mater. Chem.* **2004**, *14*, 2154–2160. [CrossRef]
3. Arias, J.L.; Fernández, M.S. Polysaccharides and proteoglycans in calcium carbonate-based biomineralization. *Chem. Rev.* **2008**, *108*, 4475–4482. [CrossRef] [PubMed]

4. Young, J.R.; Henriksen, K. Biomineralization within vesicles: The calcite of coccoliths. *Rev. Mineral. Geochem.* **2003**, *54*, 189–215. [CrossRef]
5. Boyjoo, Y.; Pareek, V.K.; Liu, J. Synthesis of micro and nano-sized calcium carbonate particles and their applications. *J. Mater. Chem. A* **2014**, *2*, 14270–14288. [CrossRef]
6. Gebauer, D.; Völkel, A.; Cölfen, H. Stable prenucleation calcium carbonate clusters. *Science* **2008**, *322*, 1819–1822. [CrossRef] [PubMed]
7. Gebauer, D.; Cölfen, H. Prenucleation clusters and non-classical nucleation. *Nano Today* **2011**, *6*, 564–584. [CrossRef]
8. Gebauer, D.; Kellermeier, M.; Gale, J.D.; Bergström, L.; Cölfen, H. Pre-nucleation clusters as solute precursors in crystallisation. *Chem. Soc. Rev.* **2014**, *43*, 2348–2371. [CrossRef] [PubMed]
9. Kellermeier, M.; Cölfen, H.; Gebauer, D. Investigating the early stages of mineral precipitation by potentiometric titration and analytical ultracentrifugation. *Methods Enzymol.* **2013**, *532*, 45–69. [PubMed]
10. Cartwright, J.H.; Checa, A.G.; Gale, J.D.; Gebauer, D.; Sainz-Díaz, C.I. Calcium carbonate polyamorphism and its role in biomineralization: How many amorphous calcium carbonates are there? *Angew. Chem. Int. Ed.* **2012**, *51*, 11960–11970. [CrossRef] [PubMed]
11. Chen, S.-F.; Cölfen, H.; Antonietti, M.; Yu, S.-H. Ethanol assisted synthesis of pure and stable amorphous calcium carbonate nanoparticles. *ChemComm* **2013**, *49*, 9564–9566. [CrossRef] [PubMed]
12. Rao, A.; Berg, J.K.; Kellermeier, M.; Gebauer, D. Sweet on biomineralization: Effects of carbohydrates on the early stages of calcium carbonate crystallization. *Eur. J. Miner.* **2014**, *26*, 537–552. [CrossRef]
13. Rao, A.; Vásquez-Quitral, P.; Fernández, M.S.; Berg, J.K.; Sánchez, M.; Drechsler, M.; Neira-Carrillo, A.; Arias J., L.; Gebauer, D.; Cölfen, H. pH-dependent schemes of calcium carbonate formation in the presence of alginates. *Cryst. Growth Des.* **2016**, *16*, 1349–1359. [CrossRef]
14. Neira-Carrillo, A.; Krishna Pai, R.; Fernández, M.S.; Carreño, E.; Vásquez-Quitral, P.; Arias, J.L. Synthesis and characterization of sulfonated polymethylsiloxane polymer as template for crystal growth of $CaCO_3$. *Colloid Polym. Sci.* **2009**, *287*, 385–393. [CrossRef]
15. Neira-Carrillo, A.; Vásquez-Quitral, P.; Díaz, M.P.; Fernández, M.S.; Arias, J.L.; Yazdani-Pedram, M. Control of calcium carbonate crystallization by using anionic polymethylsiloxanes as templates. *J. Solid State Chem.* **2012**, *194*, 400–408. [CrossRef]
16. Neira-Carrillo, A.; Vásquez Quitral, P.; Yazdani-Pedram, M.; Arias, J.L. Crystal growth of $CaCO_3$ induced by new carboxylated monomethylitaconate grafted polymethylsiloxane. *Eur. Polym. J.* **2010**, *46*, 1184–1193. [CrossRef]
17. Lee, K.Y.; Mooney, D.J. Alginate: Properties and biomedical applications. *Prog. Polym. Sci.* **2012**, *37*, 106–126. [CrossRef] [PubMed]
18. Asenath-Smith, E.; Li, H.; Keene, E.C.; Seh, Z.W.; Estroff, L.A. Crystal growth of calcium carbonate in hydrogels as a model of biomineralization. *Adv. Funct. Mater.* **2012**, *22*, 2891–2914. [CrossRef]
19. Salgado, L.T.; Amado Filho, G.M.; Fernández, M.S.; Arias, J.L.; Farina, M. The effect of alginates, fucans and phenolic substances from the brown seaweed *Padina gymnospora* in calcium carbonate mineralization in vitro. *J. Cryst. Growth* **2011**, *321*, 65–71. [CrossRef]
20. Manoli, F.; Dalas, E. The effect of sodium alginate on the crystal growth of calcium carbonate. *J. Mater. Sci. Mater. Med.* **2002**, *13*, 155–158. [CrossRef] [PubMed]
21. Olderøy, M.Ø.; Xie, M.; Strand, B.L.; Flaten, E.M.; Sikorski, P.; Andreassen, J.P. Growth and nucleation of calcium carbonate vaterite crystals in presence of alginate. *Cryst. Growth Des.* **2009**, *9*, 5176–5183. [CrossRef]
22. Ma, Y.; Feng, Q. Alginate hydrogel-mediated crystallization of calcium carbonate. *J. Solid State Chem.* **2011**, *184*, 1008–1015. [CrossRef]
23. Egaña Palma, R. Preparación de Esferas de Alginato Purificado de Origen Comercial y Desde Algas Chilenas *Lessonia nigrescens* Como Implante Para Terapia Celular. MVD Thesis, Facultad de Ciencias Veterinarias y Pecuarias, Universidad de Chile, Santiago, Chile, 2013.
24. Gebauer, D.; Cölfen, H.; Verch, A.; Antonietti, M. The multiple roles of additives in $CaCO_3$ crystallization: A quantitative case study. *Adv. Mater.* **2009**, *21*, 435–439. [CrossRef]
25. Xu, J.Z.; Zhong, G.J.; Hsiao, B.S.; Fu, Q.; Li, Z.M. Low-dimensional carbonaceous nanofiller induced polymer crystallization. *Prog. Polym. Sci.* **2014**, *39*, 555–593. [CrossRef]

26. Tasis, D.; Tagmatarchis, N.; Bianco, A.; Prato, M. Chemistry of carbon nanotubes. *Chem. Rev.* **2006**, *106*, 1105–1136. [CrossRef] [PubMed]
27. Makar, J.M.; Chan, G.W. Growth of cement hydration products on single-walled carbon nanotubes. *J. Am. Ceram. Soc.* **2009**, *92*, 1303–1310. [CrossRef]
28. Balázsi, C.; Wéber, F.; Kövér, Z.; Shen, Z.; Konya, Z.; Kasztovszky, Z.; Vértesy, Z.; Biró, L.P.; Kiricsi, I.; Arato, P. Application of carbon nanotubes to silicon nitride matrix reinforcements. *Curr. Appl. Phys.* **2006**, *6*, 124–130. [CrossRef]
29. Lupo, F.; Kamalakaran, R.; Scheu, C.; Grobert, N.; Rühle, M. Microstructural investigations on zirconium oxide–carbon nanotube composites synthesized by hydrothermal crystallization. *Carbon* **2004**, *42*, 1995–1999. [CrossRef]
30. Tasis, D.; Pispas, S.; Galiotis, C.; Bouropoulos, N. Growth of calcium carbonate on non-covalently modified carbon nanotubes. *Mater. Lett.* **2007**, *61*, 5044–5046. [CrossRef]
31. Li, W.; Gao, C. Efficiently stabilized spherical vaterite $CaCO_3$ crystals by carbon nanotubes in biomimetic mineralization. *Langmuir* **2007**, *23*, 4575–4582. [CrossRef] [PubMed]
32. Pavez, J.; Silva, J.F.; Melo, F. Effects of alginic acid from marine algae on calcium carbonate electrodeposited coating. *J. Cryst. Growth* **2005**, *282*, 438–447. [CrossRef]
33. Neira-Carrillo, A.; Acevedo, D.F.; Miras, M.C.; Barbero, C.A.; Gebauer, D.; Cölfen, H.; Arias, J.L. Influence of Conducting Polymers Based on Carboxylated Polyaniline on in vitro $CaCO_3$ Crystallization. *Langmuir* **2008**, *24*, 12496–12507. [CrossRef] [PubMed]
34. Neira-Carrillo, A.; Yazdani-Pedram, M.; Retuert, J.; Díaz-Dosque, M.; Gallois, S.; Arias, J.L. Selective crystallization of calcium salts by poly(acrylate)-grafted chitosan. *J. Colloid Interface Sci* **2005**, *286*, 134–141. [CrossRef] [PubMed]
35. Neira-Carrillo, A.; Retuert, J.; Martinez, F.; Arias, J.L. Effect of crosslinked chitosan as a constrained volume on the in vitro calcium carbonate crystallization. *J. Chil. Chem. Soc.* **2008**, *53*, 1367–1372. [CrossRef]
36. Neira-Carrillo, A.; Pai, R.; Fuenzalida, V.; Fernandez, M.S.; Retuert, J.; Arias, J.L. Calcium carbonate growth modification by constituents releases from porous cellulose filter membranes. *J. Chil. Chem. Soc.* **2008**, *53*, 1469–1473. [CrossRef]
37. Yang, X.; Kim, E.; Liu, Y.; Shi, X.W.; Rubloff, G.W.; Ghodssi, R.; Payne, G.F. In-film bioprocessing and immunoanalysis with electroaddressable stimuli-responsive polysaccharides. *Adv. Funct. Mater.* **2010**, *20*, 1645–1652. [CrossRef]
38. Lédion, J.; Leroy, P.; Labbé, J.-P. Détermination du caractère incrustant d'une eau par un essai d'entartrage accéléré. *Tech. Sci. Munic. (1971)* **1985**, *7–8*, 323–328.
39. Butler, M.F.; Glaser, N.; Weaver, A.C.; Kirkland, M.; Heppenstall-Butler, M. Calcium carbonate crystallization in the presence of biopolymers. *Cryst. Growth Des.* **2006**, *6*, 781–794. [CrossRef]
40. Díaz-Dosque, M.; Aranda, P.; Darder, M.; Retuert, J.; Yazdani-Pedram, M.; Arias, J.L.; Ruiz-Hitzky, E. Use of biopolymers as oriented supports for the stabilization of different polymorphs of biomineralized calcium carbonate with complex shape. *J. Cryst. Growth* **2008**, *310*, 5331–5340. [CrossRef]
41. Ketrane, R.; Saidani, B.; Gil, O.; Leleyter, L.; Baraud, F. Efficiency of five scale inhibitors on calcium carbonate precipitation from hard water: Effect of temperature and concentration. *Desalination* **2009**, *249*, 1397–1404. [CrossRef]
42. Butler, M.F.; Frith, W.J.; Rawlins, C.; Weaver, A.C.; Heppenstall-Butler, M. Hollow calcium carbonate microsphere formation in the presence of biopolymers and additives. *Cryst. Growth Des.* **2008**, *9*, 534–545. [CrossRef]
43. Qi, Y.; Jiang, M.; Cui, Y.L.; Zhao, L.; Zhou, X. Synthesis of quercetin loaded nanoparticles based on alginate for Pb (II) adsorption in aqueous solution. *Nanoscale Res. Lett.* **2015**, *10*, 408. [CrossRef] [PubMed]
44. Lakouraj, M.M.; Mojerlou, F.; Zare, E.N. Nanogel and superparamagnetic nanocomposite based on sodium alginate for sorption of heavy metal ions. *Carbohydr. Polym.* **2014**, *106*, 34–41. [CrossRef] [PubMed]
45. Leng, B.; Jiang, F.; Lu, K.; Ming, W.; Shao, Z. Growth of calcium carbonate mediated by slowly released alginate. *CrystEngComm* **2010**, *12*, 730–736. [CrossRef]
46. Neira-Carrillo, A.; Vásquez-Quitral, P.; Sánchez, M.; Farhadi-Khouzani, M.; Aguilar-Bolados, H.; Yazdani-Pedram, M.; Cölfen, H. Evaluation of functionalized multi-walled CNTs as template for classical and non-classical $CaCO_3$ crystallization. Unpublished work. 2018.

47. Zhao, B.; Hu, H.; Mandal, S.K.; Haddon, R.C. A Bone mimic based on the self-assembly of hydroxyapatite on chemically functionalized single-walled carbon nanotubes. *Chem. Mater.* **2005**, *17*, 3235–3241. [CrossRef]
48. Gomez, C.G.; Lambrecht, M.V.P.; Lozano, J.E.; Rinaudo, M.; Villar, M.A. Influence of the extraction–purification conditions on final properties of alginates obtained from brown algae (*Macrocystis pyrifera*). *Int. J. Biol. Macromol.* **2009**, *44*, 365–371. [CrossRef] [PubMed]

© 2018 by the authors. Licensee MDPI, Basel, Switzerland. This article is an open access article distributed under the terms and conditions of the Creative Commons Attribution (CC BY) license (http://creativecommons.org/licenses/by/4.0/).

crystals

MDPI

Article

Electrocrystallization of $CaCO_3$ Crystals Obtained through Phosphorylated Chitin

Nicole Butto [1], Gustavo Cabrera-Barjas [2,*] and Andrónico Neira-Carrillo [1,*]

[1] Department of Biological and Animal Sciences, Faculty of Veterinary and Animal Sciences, University of Chile, P.O. Box 2-15, 832000 Santiago, Chile; nbutto@veterinaria.uchile.cl

[2] Unit for Technology Development (UDT), University of Concepción, Av. Cordillera 2634, Parque Industrial Coronel, P.O. Box 4051 mail 3, Concepción, Chile

* Correspondence: gcabrerab@gmail.com (G.C.-B.); aneira@uchile.cl (A.N.-C.); Tel.: +56-41-2661-819 (G.C.-B.); +56-22-978-5642 (A.N.-C.)

Received: 22 December 2017; Accepted: 2 February 2018; Published: 3 February 2018

Abstract: A phosphorylated chitin (Chi-P) derivative was synthesized and its chemical structure was verified with Fourier-transform infrared spectroscopy (FTIR), elemental analysis, and thermogravimetric techniques (TGA). The influence of Chi-P used as a solid template through in vitro electrocrystallization (EC) supported on an indium zinc oxide (ITO) surface on the growth of calcium carbonate ($CaCO_3$) was studied. $CaCO_3$ crystals through EC essays were also compared with crystals obtained with the gas diffusion (GD) method. Scanning electron microscopy (SEM), energy dispersive X-ray spectrometry (EDS), chronopotentiometry, Raman, and powder X-ray diffractometry (XRD) characterized all resultant inorganic particles. Our findings revealed that the EC method selectively controlled the coexistence of truncate calcite and the metastable phase of vaterite. The crystals' morphology reflects the electrostatic interaction of phosphate moieties from Chi-P onto $CaCO_3$ crystals through both EC and GD crystallization methods. We believe that the EC method represents a viable electrochemical approach for studying different inorganic minerals and could be useful as an in vitro classical crystallization method for the design of advanced inorganic materials with desirable shapes and properties.

Keywords: calcium carbonate; phosphorylated chitin; electrocrystallization; potentiometric titration; gas diffusion method

1. Introduction

Biological crystallization is the process by which living organisms produce hybrid biogenic composites and exert accurate control over the minerals they deposit, creating advanced materials with uniform particle size, novel morphology, and myriad shapes or sizes that often exhibit high strength and remarkable properties [1–4]. It is known that the inorganic crystallization mechanism is altered by specific interactions between chemical groups, such as $–CO_2H$, $–PO_3H$, $–SO_3H$ containing insoluble additives or functionalized networks as solid templates [5–10]. In this sense, calcium carbonate ($CaCO_3$) represents the most abundant biomineral in nature and it has considerable industrial interest. It nucleates in three known crystalline polymorphs: calcite, aragonite and vaterite [11–13]. For understanding the biological control of $CaCO_3$ crystallization many studies regarding the effect of natural and synthetic polymers, copolymers, functionalized biopolymers, and adsorption surface phenomena involved in this process have been reported [14–20]. In order to achieve control over this biomineral it is important to understand the mechanisms of how crystals interacts between organic and inorganic components using different classical crystallization setup in a similar manner that they occur in nature. Such selective control is governed by different functionalized biomolecules, including proteins, polysaccharides, glycosaminoglycan, etc. Therefore, control of

polymorphs of $CaCO_3$ is strongly affected by additives chemical groups (e.g., carboxylic, phosphate), crystallization method, and precipitation conditions (e.g., pH, concentration, temperature, etc.) [21–25]. Sulfate groups in biopolymers and phosphate groups of proteins have been known as active groups on biomineralization of hard bioceramic exoskeletons and eggshell calcified layer [8,26]. We expected that functionalized biopolymers like phosphorylated chitin (Chi-P) used as a solid template could be an efficient crystallization modifier acting by adsorption onto the active growth sites of the $CaCO_3$ surface under the biopolymer-controlled crystallization concept. It is well known that chitinous and collagenous components represent the main structural skeletal system, which support the cellular structure of abundant animal tissues with active roles on biological mineralization [27,28]. Moreover, non-functionalized chitin (Chi) in the structural and shell formation at in vitro level has been described as a non-mineralized laminar substrate or framework, which compartmentalizes a microenvironment where mineralization take place [29].

On the other hand, gas diffusion (GD) crystallization has been widely employed to study the effect of a number of ionic macromolecules (proteins, polysaccharides, surfactants) and biological organic support (egg-shell matrix, gastrolith) on $CaCO_3$ crystallization [30–37]. Meanwhile, the electrocrystallization (EC) method, as an electrochemical concept approach, represents a novel crystallization technique of inorganic materials, such as calcium salts (carbonate, sulfate, oxalate, etc.). It is important to note that the EC method has some technical advantages, e.g., control of applied voltage and current, concentration of additives, times that are precisely controlled inducing selective control of the type of crystals grown onto the indium zinc oxide (ITO) substrate [38–41], etc. In this regard, our group has recently extracted and purified alginate from Chilean algae (*Lessonia nigrescens)*, and tested the plant extract from *Dendroligotrichum dendroide polytrichaceae* (Chilean family) as an additive on $CaCO_3$ and calcium oxalate (CaOx) through EC on electrospun polycaprolactone fibers [42].

The aim of this work was to study the influence of phosphorylated chitin (Chi-P) on $CaCO_3$ particles through EC method supported onto a conductive ITO glass surface, and the obtained crystals were compared to those obtained with the gas diffusion (GD) method. This study was supported and performed in the context of the active anionic groups on biomineralization, low solubility of Chi-P in acid form, and the scarce knowing effect of Chi derivatives on in vitro $CaCO_3$ crystallization.

2. Materials and Methods

2.1. Reactants

Calcium chloride dihydrate ($CaCl_2 \cdot 2H_2O$), sodium bicarbonate ($NaHCO_3$), sodium hydroxide (NaOH), sodium chloride (NaCl) and potassium nitrate (KNO_3), methanesulfonic acid and phosphorous pentoxide were obtained from Merck (Kenilworth, NJ, USA). All solvents and other reagents were of the highest available purity. Indium zinc oxide (ITO) conductive glass electrodes were used as the conductive material for electrocrystallization of $CaCO_3$ and were purchased from Delta Technologies (Dallas, TX, USA). ITO working electrodes were purchased from Corning® and aluminosilicate glass, 25 × 25 × 1.1 mm, coated with one surface of RS = 5–15 Ω was used. The chitin sample was obtained in the laboratory by standard demineralization and deproteinization processes of Chilean red prawn (*Pleuroncodes monodon*) exoskeletons [43]. The synthesis of P-Chi is described as is shown in Appendix A (please see Appendix A.1).

2.2. Gas Diffusion (GD) Method

GD crystallization of $CaCO_3$ particles was carried out in the presence of Chi-P as polymeric solid template and compared in the absence of Chi-P as negative control at room temperature for 24 h. GD method was performed as we described in our previous works [37,44–48].

2.3. Electrocrystallization (EC) Method

In vitro EC of $CaCO_3$ particles were produced in the presence of Chi-P onto the ITO glass surface at room temperature using a galvanostat/potentiostat BASi Epsilon (West Lafayette, IN, USA) instrument. The chronopotentiometry technique was used during the EC of $CaCO_3$. ITO were washed with methanol and Milli Q water, obtained from a water purification system LaboStar 4-DI/UV and sonicated for 5 min. $CaCO_3$ crystallization by using electrolyte solution with dissolved O_2 in alkaline media was carried out through an electrochemical reaction. The electrolytic solution consisted of 0.2 mM $CaCl_2$, 6 mM $NaHCO_3$, and 10 mM NaCl. The EC equations of EC of $CaCO_3$ has been as previously described [39]. The utilized reactants concentrations of the EC of $CaCO_3$ demonstrated clearly the production of $CaCO_3$ particles on ITO substrate. Before the EC of $CaCO_3$ essays, a linear sweep voltammetry was performed in order to determine first the maximal potential value where the reduction of molecular O_2 is reached. The maximum voltage activity established was at −890 mV [49]. Therefore, the use of this potential value generate a basic pH media allowing efficient conversion of bicarbonate to carbonate ions favoring the $CaCO_3$ particle formation. Before the EC of $CaCO_3$ essays was performed, the electrochemical cell was saturated with molecular O_2 for 40 min. After the above potential was fixed, a set of chronoamperometry tests on $CaCO_3$ coating for 120 min was carried out.

2.4. Characterization

The surface morphology of the resultant $CaCO_3$ crystals was characterized by scanning electron microscopy (SEM) using JEOL JSM-6390LV and HITACHI TM3000 instruments. Fourier transform infrared spectroscopy (FTIR), and attenuated total reflectance in conjunction with FTIR (FTIR-ATR) analysis were performed by using FTIR Nicolet Magna 5PC spectrophotometer coupled to a PC with OMNIC software to data analysis and a Interspectrum Interspec p/n 200-X spectrometer (Toravere, Estonia) was used. TGA of Chi and Chi-P was carried out using a Netzsch (Selb, Germany), model STA 409 PC, system. The sample in a platinum crucible was heated from 25 °C to 800 °C at 10 °C/min in air atmosphere (70 mL/min). The XRD diffraction spectra were taken from a powdered resultant $CaCO_3$ sample using a Siemens D-5000 X-ray diffractometer.

3. Results

In order to evaluate the Chi-P effect as a solid template on in vitro $CaCO_3$ mineralization, a set of $CaCO_3$ crystallization essays using the EC method were performed and the morphology of the resultant $CaCO_3$ particles deposited onto the Chi-P surface were compared with the crystals obtained through GD method. The illustration of the EC of $CaCO_3$ on the Chi-P and experimental conditions can be observed in Figure 1.

The EC of $CaCO_3$ method is an electrochemical electrodeposition technique of inorganic material based on the use of a specific voltage in an electrochemical solution media that induces the formation of crystals in a controlled manner. The EC method consists of two stages: first, the particles suspended in a solution are forced to move towards an electrode by the application of a certain electric field, and then inorganic particles accumulate and deposit on the conductive ITO glass surface as a working electrode (WE). Once the EC tests were carried out, it was determined that $CaCO_3$ crystals can be generated on ITO substrates in the absence and presence of Chi-P. This is due to the highly conductive capacity of the ITO substrate, which conducts the current previously established in the program at −890 mV in the electrochemical solution, allowing the reduction of oxygen, which generates an increase in the pH value that favors the conversion of bicarbonate to carbonate [39]. It is well known that the ITO substrate represents a conductive material with optoelectronic applications due to its good optical transparency, high conductivity, and electrochemical stability [40]. $CaCO_3$ crystals obtained with EC method in the presence and absence of Chi-P onto ITO substrate were compared and evaluated through the measurement of current (mA) at different times (min). For this purpose, an electrolytic solution was placed into an electrochemical cell and the EC essays were performed in a galvanostat/potentiostat

BASi Epsilon instrument. Figure 2 shows the chroamperometric curves related to crystalline deposits of $CaCO_3$ onto the ITO surface during the EC performed on the ITO by using −890 mV for 120 min.

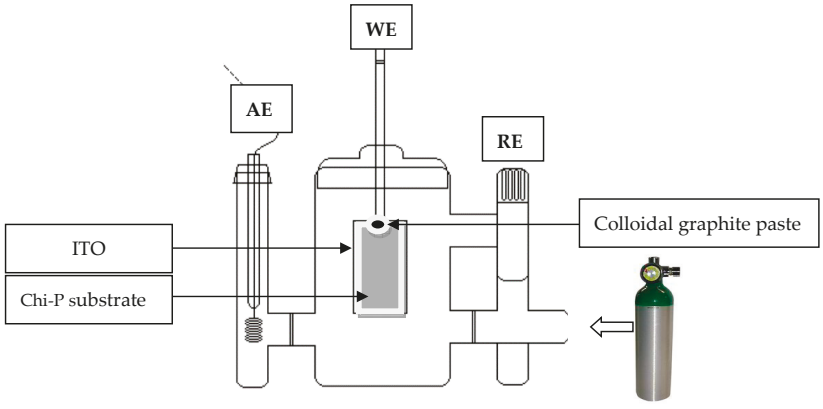

Figure 1. Experimental setup for the EC experiments of $CaCO_3$ onto ITO in the presence of Chi-P. WE, AE, and RE are the working electrode, auxiliary reference, and working electrode, respectively.

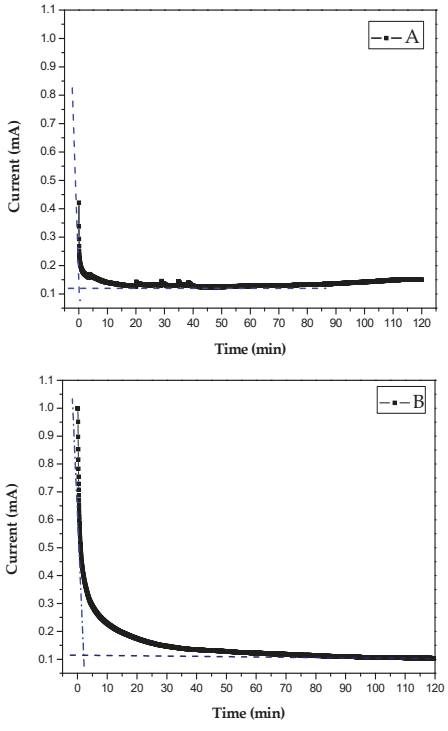

Figure 2. Chronamperometry curves for EC of $CaCO_3$ crystals. Without additive (**A**) and in the presence of Chi-P as a solid template (**B**).

Figure 2 shows a notorious decrease in the electrochemical current curve during the EC of $CaCO_3$ when Chi-P was used as a template (Figure 2B), in a similar manner than the control experiment

without Chi-P (Figure 2A). However, the initial induced current was higher in Chi-P (ca. 1.0 mA) than control (ca. 0.42 mA). Moreover, we found the generated current stabilization for Chi-P begin ca. of 2.10 min at 0.11 mA instead of ca. 0.12 min at 0.17 mA in the absence of the additive. In both cases, the applied current became asymptotic until the end of the EC experiment at 0.035 mA and 2.15 min, respectively.

In order to evaluate the morphogenetic effect of Chi-P template on $CaCO_3$ crystals growth onto ITO surface a scanning electron microscopy (SEM) was performed. Figure 3 shows the SEM images of $CaCO_3$ crystals obtained on Chi-P surface. In general, Figure 3A shows the typical rhombohedral calcite crystals growth on ITO in absence of additive (control) of size ca. 10 μm. Figure 3B–D shows abundant truncate and rounded calcite particles growth in the presence of Chi-P as solid template of size ca. 8–20 μm. In addition, swollen and extended Chi-P sample embedded into the electrolytic solution and the starting rigid Chi-P film sample before the EC essays was observed in the Figure 3E,F, respectively. Then, diffusion of Chi-P molecules at the local ITO surface may have tremendous influence on the local nucleation of $CaCO_3$ crystals, or alter the process of crystal formation as we observed by energy dispersive X-ray spectrometry (EDS) analysis.

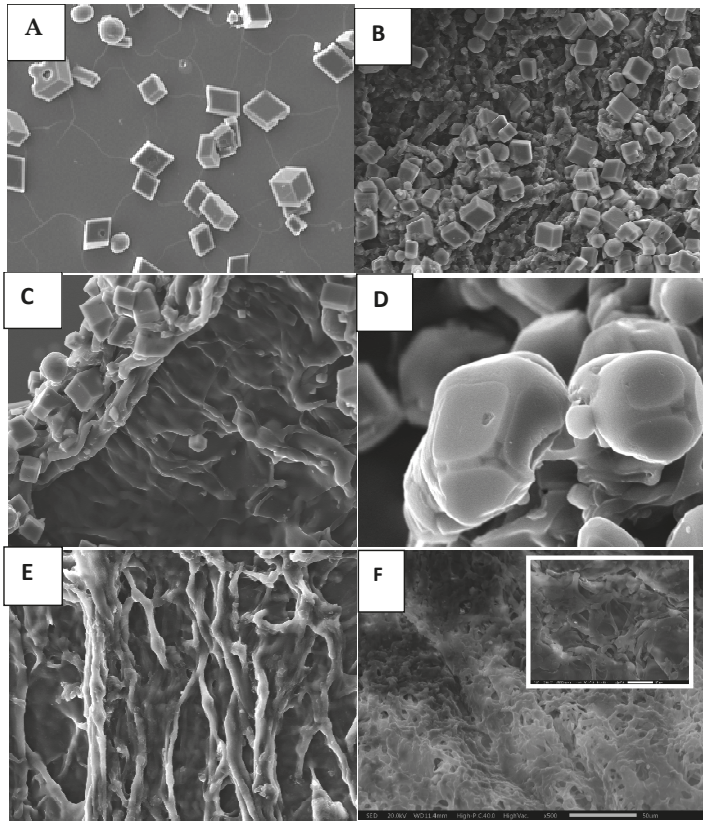

Figure 3. SEM images of $CaCO_3$ crystals obtained through the EC method on Chi-P onto the ITO surface. Control calcite on ITO (**A**); truncate and rounded calcites on Chi-P (**B**–**D**); swollen and extended Chi-P sample embedded into the electrolytic solution (**E**); and the starting Chi-P sample before the EC (**F**). The size of Chi-P sample attached to ITO was ca. 3 mm × 3 mm. The insert in (**F**) shows compact matrix of Chi-P at high magnification.

It is well known that scanning electron microscopy/energy dispersive X-ray spectrometry (SEM/EDS) is a widely applied elemental microanalysis technique capable of identifying and quantifying almost all elements in the periodic table. With this in mind, SEM-EDS measurements of the resultant modified $CaCO_3$ particles' growth onto the ITO surface in the presence of Chi-P, Chi-P and ITO surfaces were conducted and all results are shown in Figure 4.

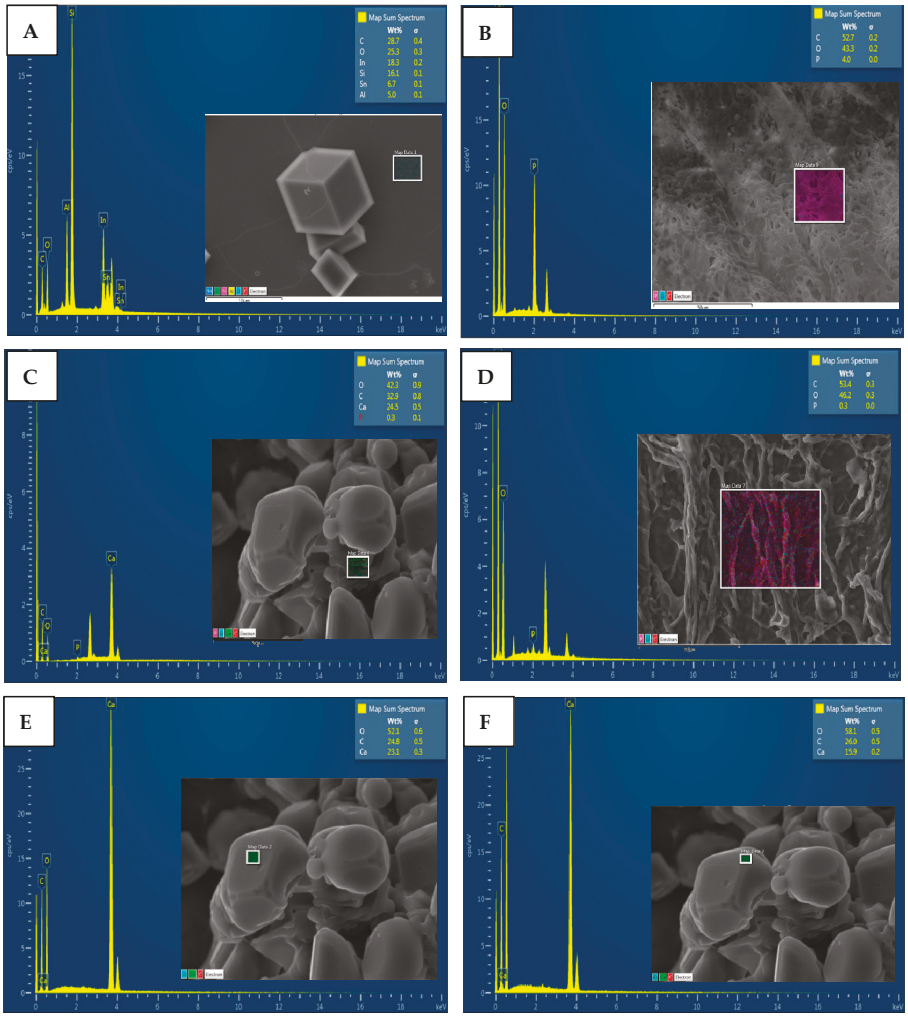

Figure 4. SEM-EDS measurements of $CaCO_3$ crystals obtained through EC in the presence of Chi-P at 24 °C for 2 h. EDS data of ITO surface (**A**), starting Chi-P sample (**B**), combined area of the Chi-P sample and crystal (**C**), swollen Chi-P embedded into the electrolytic solution (**D**), flat plane (**E**), and rounded plane (**F**) of crystal. The color assigned to each element were arbitrarily selected in the EDS measurements.

The ATR/FTIR technique allows that samples, in liquid or solid matter state, be examined directly without further preparation. In order to determine the chemical composition of Chi-P film (starting sample) and the resultant $CaCO_3$ crystals precipitated through EC on Chi-P surface we

used attenuated total reflectance (ATR) and Fourier-transform infrared spectroscopy (FTIR) as a sampling technique to provide excellent quality data in conjunction. The FTIR analysis is described in Appendix A (please see Appendix A.2). Figure 5 shows the FTIR spectra of Chi-P film, commercial $CaCO_3$ and deposited $CaCO_3$ particles. The spectra of Chi derivative plus $CaCO_3$ crystals is slightly different to the original Chi-P spectrum showing new absorption bands at 1390 cm^{-1} and 871 cm^{-1}, respectively. They are coincident with the broad band that appears in commercial $CaCO_3$ samples at 1394 cm^{-1} (υ_3 asymmetric CO_3^{2-}) and with the sharp band at 871 cm^{-1} (υ_2 asymmetric CO_3^{2-}). Those bands confirmed the presence of deposited $CaCO_3$ crystals.

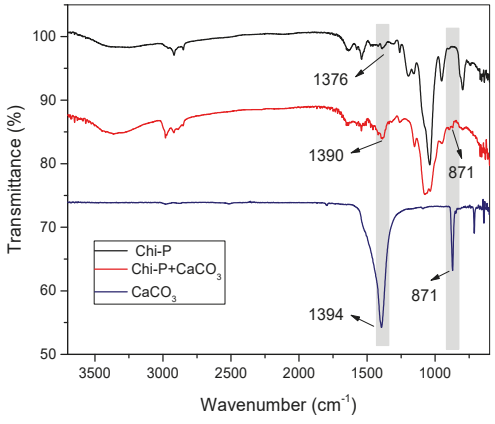

Figure 5. FTIR spectra of Chi-P, $CaCO_3$ and $CaCO_3$ crystals obtained through EC in the presence of Chi-P at 24 °C for 2 h.

In addition, the ATR/FTIR analysis was based on the presence of new absorption bands associated to $CaCO_3$ deposition on the Chi-P surface. The inorganic particles depositions was confirmed through the absorption bands representing the main vibrations of the carbonate ions (CO_3^{2-}). For a more detailed analysis of samples, the ATR/FTIR spectra for Chi-P and Chi-P + $CaCO_3$ in different spectral regions are obtained (Figure 6).

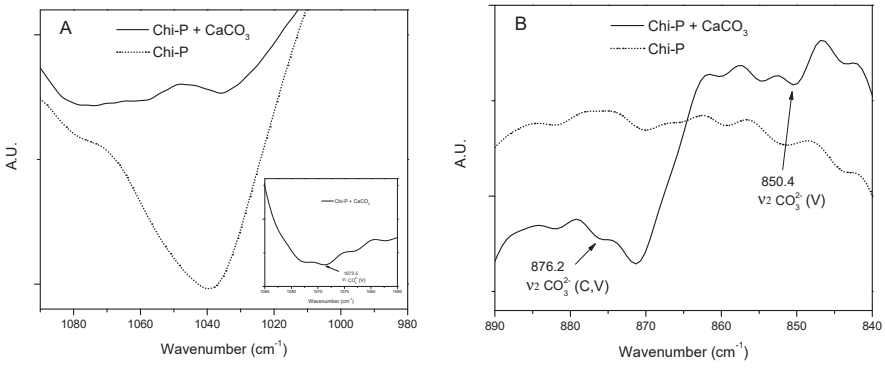

Figure 6. *Cont.*

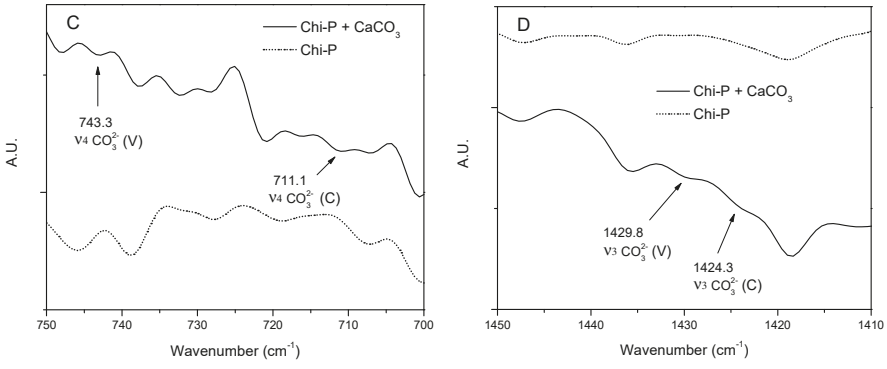

Figure 6. ATR/FTIR spectra for Chi-P membrane and Chi-P + $CaCO_3$ deposited salt analyzed in different spectral regions from 700 cm^{-1} to 1450 cm^{-1} (A–D). The presence of bands associated with different $CaCO_3$ polymorphs (V = vaterite, C = calcite) are indicated.

In Figure 6 the FT-IR spectra of Chi-P and Chi-P + $CaCO_3$ were shown. The main absorptions of CO_3^{2-} ions were analyzed and it is important to note that most of its characteristics vibration bands appear only in the Chi-P + $CaCO_3$ spectra. This suggests that spectral changes for this sample are associated with salt deposition on the Chi-P surface. In Figure 6A the weak vibrational band observed at 1073.5 cm^{-1} in Chi-P + $CaCO_3$ spectra only was assigned to CO_3^{2-} (symmetric stretching, ν_1) from vaterite crystalline polymorph. Figure 6B shows two carbonate bands seen at 876.2 cm^{-1} that are common to both calcite and vaterite (asymmetric deformation, ν_2) and at 850.4 cm^{-1} (ν_2, vaterite), respectively. The absorption band at 711.1 cm^{-1} is characteristic for calcite, whereas in vaterite the same band (symmetric deformation, ν_4) is shifted to 743.3 cm^{-1} (Figure 6C) [50]. Previous research found that latter vibrations are characteristic of crystalline $CaCO_3$ phases only [51,52]. In Figure 6D the main CO_3^{2-} bands at 1429.8 cm^{-1} and 1424.3 cm^{-1} (asymmetric stretching, ν_3) for vaterite and calcite polymorphs are presented, respectively. From previous analysis it could be concluded that a mixture of two $CaCO_3$ crystalline polymorphs, vaterite and calcite, were crystallized on the surface of the Chi-P membrane. Those results are consistent with XRD analysis.

In order to further study the relationship between $CaCO_3$ and Chi-P, a detailed FTIR analysis of Chi-P and Chi-P + $CaCO_3$ spectra in the PO_4^{3-} absorption regions are presented in Figure 7.

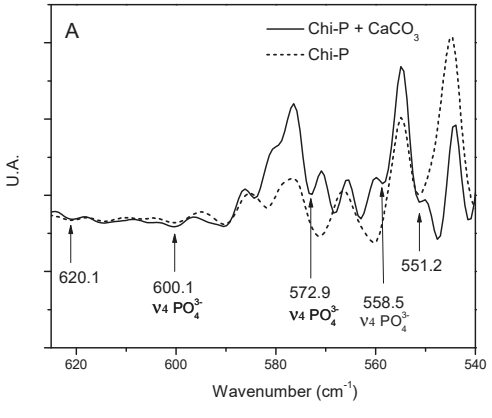

Figure 7. *Cont.*

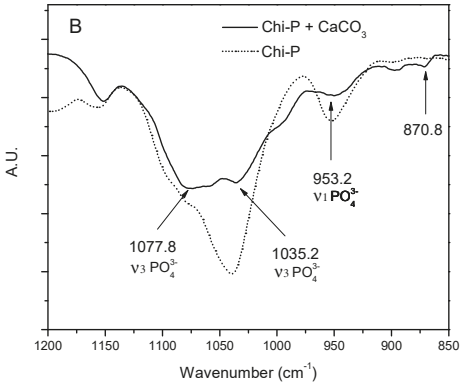

Figure 7. ATR/FTIR spectra of Chi-P membrane and Chi-P + $CaCO_3$ deposited inorganic minerals in different spectral regions.

From Figure 7 it could be observed that the presence of deposited $CaCO_3$ salt changes the shape of some bands in FTIR spectra, producing phosphate bands that are more resolved than in the original Chi-P spectra. This fact could be due to different chemical environments for those PO_4^{3-} groups from the Chi-P membrane surface involved in the interaction with Ca^{2+} ions at deposition sites to form calcium phosphate or its hydrogen phosphate salts. This is supported by the presence of O-P-O bending bands v_4 PO_4^{3-} (572.9 cm^{-1}, 558.5 cm^{-1}, 600.1 cm^{-1}) and HPO_4^{2-} (551.2 cm^{-1}) (Figure 7A). Other corresponding characteristic bands (P-O stretching of P-OH) are v_1 PO_4^{3-} (953.2 cm^{-1}), v_3 PO_4^{3-} (1035.28 cm^{-1}, 1077.8 cm^{-1}) (Figure 7B). All those bands are coincident with those previously reported for calcium phosphate salts, demonstrating its formation on the surface of the Chi-P membrane [53–56].

In order to determine the internal lattice of crystalline $CaCO_3$ products obtained through EC method and to determine the polymorphism of resultant $CaCO_3$ crystals growth on Chi-P onto ITO substrate, X-ray diffraction (XRD) technique was performed as we can observe in Figure 8. Figure 8 shows the XRD pattern of $CaCO_3$ crystals obtained by the EC method (Figure 8A), compared to the spectrum of the starting Chi-P sample (Figure 8B).

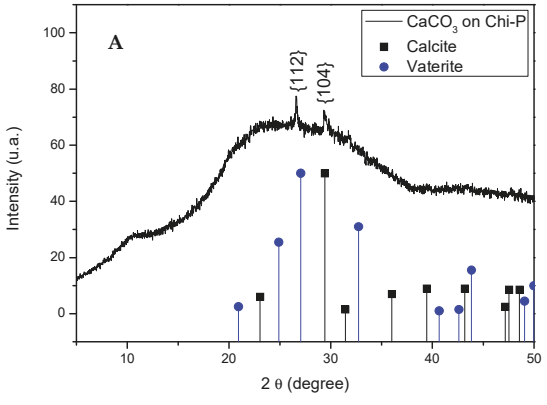

Figure 8. *Cont.*

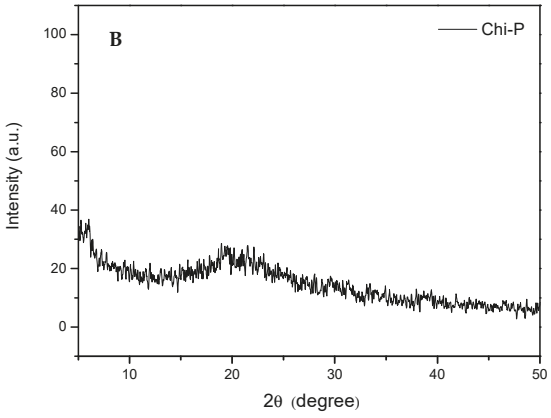

Figure 8. XRD spectra of $CaCO_3$ crystals obtained through EC on Chi-P onto ITO substrate (**A**) and the Chi-P sample (**B**). The vertical black and blue lines, and the blue line designations in the graph, indicate calcite and vaterite standard peaks, respectively.

4. Discussion

4.1. Chemical Characterization of Chitin (Chi) and Chitin Phosphate (Chi-P)

The ATR spectra of starting Chi and functionalized Chi-P samples can be observed in the Supplementary Materials Figure S1. The typical amide I band at about 1655 cm^{-1} and amide II band at about 1555 cm^{-1} that gives the acetyl content in Chi are present. A broad 3000–3200 cm^{-1} band due to N–H and O–H stretching with small shoulders at about 3106 cm^{-1} band is observed for this biopolymer. From the spectrum of Chi-P several differences are apparent when compared with the spectrum of former lobster Chi. The peak at 1380 cm^{-1} was attributed to P=O stretching and the peak at 1042.7 cm^{-1} was due to –P–OH groups from Chi-P. The presence of a small peak at 956.1 cm^{-1} may also be attributed to the P–O stretching of P–OH, overlap with CH_3 rocking band after Chi phosphorylation [57]. Furthermore, the Chi peak from O–H deformation of $–CH_2–OH$ at 1378 cm^{-1} almost disappears. It seems that Chi primary hydroxyl groups are involved in the substitution reaction as expected.

The thermal properties of lobster Chi and Chi-P were also investigated by TGA and results are given in Figures S2 and S3. It is important to clarify that the TGA was used only to demonstrate the phosphorylation reaction of chitin as supporting material. The resultant inorganic mineral on Chi-P was not considered in the current work by TGA due to the hybrid $CaCO_3$-Chi-P material was demonstrated by using spectroscopic techniques (FTIR, Raman), X-ray diffraction (XRD), chronoamperometric curves and SEM analyses. The thermogravimetric (TG) curves from both compounds shown a first mass loss in the range of 55–110 °C due to water evaporation. The TG curve of Chi shows two maximum decomposition rates peaking at 316.4 °C and 384.1 °C, which are associated to weight losses of 12.1 and 60.2%, respectively. The first effect was attributed to a complex process corresponding to the initial biopolymer pyrolysis stage. During this process, simultaneous ring dehydration, depolymerization, and decomposition of deacetylated units of the polysaccharide occurs. In the second and larger process decomposition of acetylated units occurs, including polymer deacetylation. The Chi decomposition temperature range observed was in agreement with previously reported for other Chi sources between 300–460 °C [58]. On the contrary, it could be observed that Chi-P shown a complex decomposition process having three weight losses, which is a typical behavior of block copolymers. The maximum decomposition rates for each stage was peaking at 243.5 °C, 316.4 °C, and 480.1 °C and were associated to weight losses of 20.8, 18.3, and 3.1%, respectively. The first decomposition stage could be related to thermal decomposition of phosphorylated units where the hydrolysis of phosphate groups linked

to Chi backbone occurs provoking a polymer backbone hydrolysis and dehydration. The second stage is assigned to Chi units decomposition processes, taking in count the coincidence in maximum decomposition rate temperature among both samples. It is of interest to note that the third stage occurs at 96 °C higher temperature than in Chi. It could be due to thermal degradation of residual compounds resulting from previous thermal stages (e.g., crosslinked chains) or formation of new type of phosphate species but this subject will deserve further investigation. In general, Chi-P was less thermal stable than Chi, which is in agreement with previous report for other Chi phosphate derivatives [57]. Finally, the elemental analysis allows us to determine the Chi-P degree of substitution that was 0.38 from the P/N mol ratio. The Elemental analysis is described in Appendix A (please see Appendix A.3).

4.2. Study of $CaCO_3$ Crystals Deposition by EC and GD Methods

The GD method of $CaCO_3$ as in vitro crystallization has been widely employed using different biomacromolecules, instead of the EC method, which uses an electrochemical approach, can be realized in a short time and the resistant inorganic material selectively growth on the ITO substrate can be also directly monitored by using chronoamperometry or chronopotentiometry analysis. One of the aim of this work was to use both crystallization methods for knowing the effect of the same biomolecule using as additive or electrodeposited on the ITO conductive support as a solid template. It is well known that anionic functionalization, e.g., carboxylic, sulfate, or phosphate groups attach to the main chain of macromolecules has been reported as active group on biomineralization. Therefore, the EC method was selected to study the effect of Chi-P on $CaCO_3$ and the resultant crystals compared to the classical GD method.

4.3. Characterization of $CaCO_3$ Crystals through Amperometry, FTIR, SEM-EDS, and XRD Analyses

Amperometrical curves, as with all pulsed techniques, chronoamperometry generates high charging currents at the beginning of the EC essays, which decay exponentially with time. Since the current is integrated over relatively longer time intervals, chronoamperometry gives a better signal to noise ratio in comparison to other amperometric techniques. Here, we observe a strong influence of the electrochemical current curve during the EC when Chi-P, as a solid template on the ITO substrate, was used (see Figure 2B). This behavior can be rationalized by increasing the amount of inorganic resistant material when the EC was performed at a constant voltage, then the applied current through the WE decayed until the stabilization of the crystallized $CaCO_3$ particles, which occurred in a very short time of 0.12 min at 0.17 mA. In this context, Chi-P induced the EC of $CaCO_3$ as a promoter effect, although, in both cases, the current became asymptotic until the end of the EC test was reached at 0.035 mA.

The FTIR results clearly demonstrated that although small amounts of inorganic materials were deposited onto the Chi-P film through the EC method, as supported by SEM analysis, all absorption bands of calcite polymorphism of $CaCO_3$ crystals can be identified by comparison with typical absorption bands of commercial $CaCO_3$ samples. As the Chi-P film could present a low surface chemical salt deposition, it is very likely that the resulting spectrum will mainly show bands corresponding to this derivative. However, the resulting $CaCO_3$ crystals' bands (vaterite and calcite bands), as well as PO_4^{3-} salts, were clearly identified in the spectra from those of Chi-P, proving ATR/FTIR usefulness for material surface characterization (Figures 6 and 7). In a complementary analysis, Raman spectroscopy was performed on the low amounts of $CaCO_3$ crystals grown on Chi-P surface, as was provided in supplementary material (please see Figure S4). Figure S4 shows the Raman spectra of ITO surface, starting Chi-P powder sample and $CaCO_3$ crystals as calcite polymorphism grown on Chi-P (Figure S4C) after EC experiments. The Raman spectra allowed us to also identify the deposited layer of $CaCO_3$ salt as calcite polymorphism confirming previous spectroscopic analysis.

In order to determine the elemental chemical information of all organic and inorganic components, that is, ITO substrate and the presence of Chi-P adsorbed on the crystal surface, energy dispersive X-ray spectroscopy (EDS) was also used. For the ITO substrate and Chi-P surface, the EDS measurements confirmed the presence of typical elemental composition of In, Sn, Al, and O for ITO (Figure 4A) and

the C, O, and P for Chi-P (Figure 4B), respectively. The percentage of phosphorous content of the starting Chi-P sample was slightly higher of 4.0 wt% (Figure 4B). In Figure 4C, truncated crystals were found, suggesting an efficient modifier capacity of Chi-P during the EC of $CaCO_3$, although with a low concentration of phosphate groups on the film surface and low amounts of deposited crystals. EDS analysis determined a phosphorous content of 0.3 wt% of Chi-P immediately at the interface from $CaCO_3$ crystals and swollen Chi-P film (Figure 4D) (see Figure 4). Furthermore, EDS showed that theoretical calcium/oxygen ratio (Ca/O = 1/3) of the resultant $CaCO_3$ crystals in both flat and rounded analyzed area (symbol in the image) changed. In order to confirm these results in a broad area from spherical $CaCO_3$ particles, a flat and rounded area was selected and EDS was performed (Supplementary Materials Figure S5). This observation suggests that the adsorption of crystal particles onto Chi-P film does not occur preferentially on the Chi-P surface and the additive effect on the nucleation of $CaCO_3$ may occur due to the diffusion or more expanded (or soluble) chains of Chi-P, which can alter the process of crystal growth formation in order to favor a selective morphogenetic effect on $CaCO_3$. This effect could be due to the presence of small amount of phosphorylated Chi oligomers with higher water solubility than the original Chi-P polymer. Such oligomers could be solubilized and diffused from solid matrix to the aqueous media once the Chi-P film is swollen. It is known that Chi with phosphate derivatization in strong acid media may produce polymer degradation. With this in mind, SEM-EDS measurements of the resultant modified $CaCO_3$ particle growth onto the ITO surface in the presence of Chi-P, the Chi-P and ITO surface performed as we observed in Figure 4. On the other hand, similar truncate calcite and aggregated spherical particles of $CaCO_3$ were obtained when the GD method was performed. The morphological aspect of $CaCO_3$ crystals obtained in the absence and presence of Chi-P through the GD method and aggregated truncate calcite crystals are shown in Supplementary Material Figure S6.

Finally, SEM-EDS results are in qualitative agreement with all inorganic $CaCO_3$ particles obtained from both crystallization methods. It is important to mention that inspected $CaCO_3$ particles on the Chi-P surface were difficult to determine by spectroscopic analysis despite the large number of $CaCO_3$ particles layered on the Chi-P surface. Furthermore, an X-ray diffraction (XRD) analysis of the truncate calcite and spherical $CaCO_3$ particles obtained with the EC method was performed as shown in Figure 8A. Here, the XRD analysis clearly demonstrates the coexistence of calcite and vaterite polymorphs. It can be seen that the only two diffraction peaks appear at $2\theta = 29.4^\circ$ and at $2\theta = 26.7^\circ$, which are ascribed to the most intense (104) and (112) crystallographic faces of calcite and vaterite, respectively. The diffraction peaks for calcite and vaterite for crystallographic planes and 2θ degree are in agreement with both crystals designations as was recently published using the ultrasound technique [59]. In the case of the XRD spectrum of Chi-P sample (Figure 8B), it shows a typical non-crystalline XRD curve, suggesting an amorphous nature of Chi-P biopolymer. The present data strongly suggest the ability of anionic functionalize Chi-P template for modifying the morphological aspect of $CaCO_3$ crystals and the stabilization capacity of the metastable form of vaterite. Consequently, the EC method offers a viable alternative for polymer-controlled crystallization of different inorganic minerals, such as Ca-salts, CaOx, hydroxyapatite, and silica, among others.

5. Conclusions

Phosphate moieties of Chi-P act showed inhibitor capability on the in vitro mineralization of $CaCO_3$ as we demonstrated in both crystallization methods and by using chronoamperometric curves of $CaCO_3$ obtained by the EC method. Since the phosphorous content of Chi-P was to be at ca. 3–4 wt% and $CaCO_3$ surface interaction is driven by anionic surface charge, we suggest that in vitro EC and GD methods are influenced by parameters such as current, voltage, phosphorous content, purity, pH, and topography surface of Chi-P, etc. The resultant $CaCO_3$ crystals obtained by EC method represents an advanced and fast in vitro mineralization system for studying different aspect of nucleation, crystal growth, size, and polymorphism of inorganic materials. For instance, Chi-P regulates the selectively precipitation of truncate and spherical aggregate $CaCO_3$ crystals in both mineralization systems. Here, ATR-FTIR and

XRD analysis determined clearly the coexistence of calcite and the metastable form of vaterite as the unique polymorphism when EC method was performed. In summary, anionic Chi-P biopolymer acted as an efficient modifier of $CaCO_3$ crystallization using EC and GD methods and the EC demonstrated the viable capacity to control the polymorphism of $CaCO_3$. Therefore, the classical EC method offers a great chance for understanding the crucial role of functionalized biomacromolecules on the stabilization of metastable forms of crystals in the biomineralization field.

Supplementary Materials: The following are available online at www.mdpi.com/2073-4352/8/2/82/s1. Figure S1. FTIR spectra of chitin (Chi) and phosphorylated chitin (Chi-P). Figure S2. SEM images of $CaCO_3$ crystals obtained through the GD method. Figure S3. TGA analysis of chitin (Chi) and phosphorylated chitin (Chi-P). Figure S4. Thermogravimetric data of chitin (Chi) and phosphorylated chitin (Chi-P). Figure S5. X-ray diffraction of phosphorylated chitin (Chi-P). Figure S6. SEM-EDS of spherical calcite particles grown on an ITO surface.

Acknowledgments: This research was supported by FONDECYT 1171520, ACCDiS 15130011 granted by the Chilean Council for Science and Technology (CONICYT), and funded by the Program U-Redes, Vice-Presidency of Research and Development, University of Chile. GC would like to thanks to Proyecto Basal PFB-27 granted by the Chilean Council for Science and Technology (CONICYT), Unidad de Desarrollo Tecnológico (UDT), University of Concepción.

Author Contributions: Nicole Butto and Andronico Neira-Carrillo conceived, designed, and performed the experiments; Gustavo Cabrera-Barjas synthesized and characterized the chitin phosphate derivative and related material together with Andrónico Neira-Carrillo, and wrote the paper. Andrónico Neira-Carrillo contributed with reagents/materials/analysis tools and represents the senior author; he is also principal investigator of the 1171520 FONDECYT' project and Program U-Redes, Vice-Presidency of Research and Development, University of Chile, in which the current research work was done. Therefore, Andrónico Neira-Carrillo is the first author of the intellectual input, designs, and approves the reported protocols of this study. Andrónico Neira-Carrillo and Gustavo Cabrera-Barjas was responsible for the manuscript correction, proofreading during all paper submissions, and handling the revisions and re-submission process of the revised manuscript.

Conflicts of Interest: The authors declare no conflict of interest.

Appendix A

Appendix A.1. Synthesis of Phosphorylated Chitin

The synthesis of Chi-P was carried out following the procedure reported by Nishi et al. [60] where 35 mL of concentrated methanesulfonic acid was placed in a round bottom flask submerged in an ice bath with magnetic stirring (500 r.p.m). To this media 5 g of prawn Chi was slowly added to complete dissolution. Phosphorus pentoxide was then added to the Chi solution at 1 equivalent mol to the Chi residues. The phosphorylation reaction was allowed to proceed for 4 h at 0–5 °C. The mixture of Chi solution with phosphorus pentoxide was poured into a large amount of ether and the white solid was centrifuged and washed with ethanol several times up to complete acid removal. The Chi-P derivative was suspended in water, dialyzed for three days using distilled water, and lyophilized.

Appendix A.2. FTIR Analysis

The FTIR spectra were measured using FTIR Nicolet Magna 5PC spectrophotometer coupled to a PC with OMNIC software to data analysis. The KBr disks were prepared by well blending KBr with dried polymer at 2% concentration.

Appendix A.3. Elemental Analysis

Elemental analysis of nitrogen (N) was carried out with a Perkin Elmer 2100 automatic analyzer and phosphorus content was determined by the modified molybdenum blue method [61]. The degree of Chi phosphoric substitution (DS) was calculated using the following equation:

$$DS = P\ (mol\%)/N\ (mol\%),$$

where %P phosphorus content of phosphoric groups, %N nitrogen content in chitin molecules.

References

1. Lowenstam, H.A. Minerals formed by organisms. *Science* **1981**, *211*, 1126–1131. [CrossRef] [PubMed]
2. Lowenstam, H.A.; Weiner, S. *On Biomineralization*; Oxford University Press: Oxford, UK, 1989; p. 336. ISBN 0-19-504977-2.
3. Sanchez, C.; Arribart, H.; Giraud Guille, M.M. Biomimetism and bioinspiration as tools for the design of innovative materials and systems. *Nat. Mater.* **2005**, *4*, 277–288. [CrossRef] [PubMed]
4. Simkiss, K.; Wilbur, K.M. *Biomineralization: Cell Biology and Mineral Deposition*; Academic Press: San Diego, CA, USA, 1989; p. 337. ISBN 0-12-643830-7.
5. Addadi, L.; Weiner, S. Control and design principles in biological mineralization. *Angew. Chem. Int. Ed. Engl.* **1992**, *31*, 153–169. [CrossRef]
6. Cölfen, H.; Mann, S. Higher-order organization by mesoscale self-assembly and transformation of hybrid nanostructures. *Angew. Chem. Int. Ed.* **2003**, *42*, 2350–2365. [CrossRef] [PubMed]
7. Feng, J.; Wu, G.; Qing, C. Biomimetic synthesis of hollow calcium carbonate with the existence of the agar matrix and bovine serum albumin. *Mater. Sci. Eng. C* **2016**, *58*, 409–411. [CrossRef] [PubMed]
8. Arias, J.L.; Neira-Carrillo, A.; Arias, J.I.; Escobar, C.; Bodero, M.; David, M.; Fernández, M.S. Sulfated polymers in biological mineralization: A plausible source for bio-inspired engineering. *J. Mater. Chem.* **2004**, *14*, 2154–2160. [CrossRef]
9. Addadi, L.; Raz, S.; Weiner, S. Taking advantage of disorder: Amorphous calcium carbonate and its roles in biomineralization. *Adv. Mater.* **2003**, *15*, 959–970. [CrossRef]
10. Gower, L.B. Biomimetic model systems for investigating the amorphous precursor pathway and its role in biomineralization. *Chem. Rev.* **2008**, *108*, 4551–4627. [CrossRef] [PubMed]
11. Meldrum, F.C. Calcium carbonate in biomineralisation and biomimetic chemistry. *Int. Mater. Rev.* **2003**, *48*, 187–224. [CrossRef]
12. Cartwright, J.H.E.; Checa, A.G.; Gale, J.D.; Gebauer, D.; Sainz-Díaz, C.I. Calcium carbonate polyamorphism and its role in biomineralization: How many amorphous calcium carbonates are there? *Angew. Chem. Int. Ed.* **2012**, *51*, 11960–11970. [CrossRef] [PubMed]
13. Chen, X.; Qian, X.; An, X. Using calcium carbonate whiskers as papermaking filler. *Bioresources* **2011**, *6*, 2435–2447.
14. Falini, G.; Fermani, S. The strategic role of adsorption phenomena in biomineralization. *Cryst. Res. Technol.* **2013**, *48*, 864–876. [CrossRef]
15. Neira-Carrillo, A.; Yazdani-Pedram, M.; Retuert, J.; Díaz-Dosque, M.; Gallois, S.; Arias, J.L. Selective crystallization of calcium salts by poly(acrylate)-grafted chitosan. *J. Colloid Interface Sci.* **2005**, *286*, 134–141. [CrossRef] [PubMed]
16. Gebauer, D.; Cölfen, H.; Verch, A.; Antonietti, M. The multiple roles of additives in $CaCO_3$ crystallization: A quantitative case study. *Adv. Mater.* **2009**, *21*, 435–439. [CrossRef]
17. Gao, Y.X.; Yu, S.H.; Guo, X.H. Double hydrophilic block copolymer controlled growth and self-assembly of $CaCO_3$ multilayered structures at the air/water interface. *Langmuir* **2006**, *22*, 6125–6129. [CrossRef] [PubMed]
18. Zhao, L.N.; Feng, J.D.; Wang, X.Y.; Wang, Z.C. Synthesis of self-assembled needle-shaped calcium carbonate superstructures. *Chin. Sci. Bull.* **2010**, *55*, 2131–2135. [CrossRef]
19. Laskshminarayanan, R.; Valiyaveettil, S.; Loy, G.L. Selective nucleation of calcium carbonate polymorphs: Role of surface functionalization and poly (vinyl alcohol) additive. *Cryst. Growth Des.* **2003**, *3*, 953–958. [CrossRef]
20. Butler, M.F.; Glaser, N.; Weaver, A.C.; Kirkland, M.; Heppenstall-Butler, M. Calcium carbonate crystallization in the presence of biopolymers. *Cryst. Growth Des.* **2006**, *6*, 781–794. [CrossRef]
21. Neira, A.C.; Fernandez, M.S.; Retuert, J.; Arias, J.L. Effect of the crystallization chamber design on the polymorphs of calcium carbonate using the sitting-drop method. In *Architecture and Application of Biomaterials and Biomolecular Materials*; EXS-1:321-326; Barron, A.E., Klok, H.-A., Deming, T.J., Eds.; Materials Research Society: Warrendale, PA, USA, 2004.
22. Ma, Y.F.; Gao, Y.H.; Feng, Q.L. Effects of pH and temperature on $CaCO_3$ crystallization in aqueous solution with water soluble matrix of pearls. *J. Cryst. Growth* **2010**, *312*, 3165–3170. [CrossRef]

23. Pai, R.K.; Pillai, S. Nanoparticles of amorphous calcium carbonate by miniemulsion: Synthesis and mechanism. *CrystEngComm* **2008**, *10*, 865–872. [CrossRef]
24. Gomez-Morales, J.; Hernández-Hernández, A.; Sazaki, S.; García-Ruiz, J.M. Nucleation and Polymorphism of calcium carbonate by a vapor diffusion sitting drop crystallization technique. *Cryst. Growth Des.* **2010**, *10*, 963–969. [CrossRef]
25. Song, R.-Q.; Colfen, H. Additive controlled crystallization. *CrystEngComm* **2011**, *13*, 1249–1276. [CrossRef]
26. Mann, K.; Olsen, J.V.; Macek, B.; Gnad, F.; Mann, M. Phosphoproteins of the chicken eggshell calcified layer. *Proteomics* **2007**, *7*, 106–115. [CrossRef] [PubMed]
27. Falini, G.; Fermani, S. Chitin mineralization. *Tissue Eng.* **2004**, *10*, 1–6. [CrossRef] [PubMed]
28. Ehrlich, H. Chitin and collagen as universal and alternative templates in biomineralization. *Int. Geol. Rev.* **2010**, *52*, 661–669. [CrossRef]
29. Arias, J.L.; Fernández, M.S. Biomimetic processes through the study of mineralized shells. *Mater. Charact.* **2003**, *50*, 189–195. [CrossRef]
30. Jimenez-Lopez, C.; Rodríguez-Navarro, A.; Domínguez-Vera, J.M.; Garcia-Ruiz, J.M. Influence of lysozyme on the precipitation of calcium carbonate: A kinetic and morphologic study. *Geochim. Cosmochim. Acta* **2003**, *67*, 1667–1676. [CrossRef]
31. Fernández, M.S.; Passalacqua, K.; Arias, J.I.; Arias, J.L. Partial biomimetic reconstitution of avian eggshell formation. *J. Struct. Biol.* **2004**, *148*, 1–10. [CrossRef] [PubMed]
32. Hernández-Hernández, A.; Rodríguez-Navarro, A.B.; Gomez-Morales, J.; Jiménez-Lopez, C.; Nys, Y.; García-Ruiz, J.M. Influence of model globular proteins with different isoelectric points on the precipitation of calcium carbonate. *Cryst. Growth Des.* **2008**, *8*, 1495–1502. [CrossRef]
33. Hernández-Hernández, A.; Vidal, M.L.; Gomez-Morales, J.; Rodríguez-Navarro, A.B.; Labas, V.; Gautron, J.; Nys, Y.; García Ruiz, J.M. Influence of eggshell matrix proteins on the precipitation of calcium carbonate ($CaCO_3$). *J. Cryst. Growth* **2008**, *310*, 1754–1759. [CrossRef]
34. Hernández-Hernández, A.; Gomez-Morales, J.; Rodríguez-Navarro, A.B.; Gautron, J.; Nys, Y.; García-Ruiz, J.M. Identification of some active proteins in the process of hen eggshell formation. *Cryst. Growth Des.* **2008**, *8*, 4330–4339. [CrossRef]
35. Rao, A.; Vásquez-Quitral, P.; Drechsler, M.; Fernández, M.S.; Neira-Carrillo, A.; Arias, J.L.; Berg, J.K.; Sánchez, M.; Gebauer, D.; Cölfen, H. pH-dependent schemes of calcium carbonate formation in the presence of alginates. *Cryst. Growth Des.* **2016**, *16*, 1349–1359. [CrossRef]
36. Neira-Carrillo, A.; Retuert, J.; Martínez, F.; Arias, J.L. Effect of crosslinked chitosan as a constrained volume on the in vitro calcium carbonate crystallization. *J. Chil. Chem. Soc.* **2008**, *53*, 1367–1372. [CrossRef]
37. Neira-Carrillo, A.; Fernández, M.S.; Poblete Hevia, G.; Gebauer, D.; Cölfen, H.; Arias, J.L. Retrosynthesis of $CaCO_3$ via amorphous precursor particles using gastroliths of the Red Claw lobster (Cherax quadricarinatus). *J. Struct. Biol.* **2017**, *199*, 46–56. [CrossRef] [PubMed]
38. Lédion, J.; Leroy, J.P.; Labbé, J.P. Détermination du caractère incrustant D'une eau par un essai D'entartrage accélère. *TSM L'eau* **1985**, *80*, 323–328.
39. Pavez, J.; Silva, J.; Melo, F. Homogeneous calcium carbonate coating obtained by electrodeposition: In Situ atomic force microscope observations. *Electrochim. Acta* **2005**, *50*, 3488–3494. [CrossRef]
40. Neira-Carrillo, A.; Sánchez, M.; Vásquez-Quitral, P.; Vargas-Fernández, A.; Silva, J.F. Control of calcium oxalate morphology through electrocrystallization as an electrochemical approach for preventing pathological disease. *Ionics* **2015**, *21*, 3141–3149. [CrossRef]
41. Hau, N.; Chang, Y.; Feng, C. Kinetics study of silver Electrocrystallization on (3-mercaptopropyl) trimethoxysilane-grafted indium tin oxide plastic substrate. *Electrochim. Acta* **2015**, *158*, 121–128. [CrossRef]
42. Gozalvo, R. Efecto de un Extracto de Origen Vegetal en la Mineralizacion Patologica de Oxalato de Calcio Sobre Fibras Polimericas Electrohiladas. Bachelor´s Thesis, Facultad de Ciencias de la Salud, Universidad San Sebastián, Santiago, Chile, 2017.
43. Cardenas, G.; Cabrera, G.; Taboada, E.; Miranda, S.P. Chitin characterization by SEM, FTIR, XRD, and ^{13}C cross polarization/mass angle spinning NMR. *J. Appl. Polym. Sci.* **2004**, *93*, 1876–1885. [CrossRef]
44. Neira-Carrillo, A.; Retuert, J.; Martínez, F.; Arias, J.L. Calcium carbonate growth modification by constituents released from porous filter membranes. *J. Chil. Chem. Soc.* **2008**, *53*, 1469–1473. [CrossRef]

45. Neira-Carrillo, A.; Vásquez-Quitral, P.; Díaz, M.P.; Fernández, M.S.; Arias, J.L.; Yazdani-Pedram, M. Control of calcium carbonate crystallization by using anionic polymethylsiloxanes as templates. *J. Solid State Chem.* **2012**, *194*, 400–408. [CrossRef]
46. Neira-Carrillo, A.; Krishna Pai, R.; Fernández, M.S.; Carreño, E.; Vásquez-Quitral, P.; Arias, J.L. Synthesis and characterization of sulfonated polymethylsiloxane polymer as template for Crystal growth of $CaCO_3$. *Colloid Polym. Sci.* **2009**, *287*, 385–393. [CrossRef]
47. Neira-Carrillo, A.; Vásquez Quitral, P.; Yazdani-Pedram, M.; Arias, J.L. Crystal growth of $CaCO_3$ induced by new carboxylated monomethylitaconate grafted polymethylsiloxane. *Eur. Polym. J.* **2010**, *46*, 1184–1193. [CrossRef]
48. Neira-Carrillo, A.; Acevedo, D.F.; Miras, M.C.; Barbero, C.A.; Gebauer, D.; Cölfen, H.; Arias, J.L. Influence of conducting polymers based on carboxylated polyaniline on in vitro $CaCO_3$ crystallization. *Langmuir* **2008**, *24*, 12496–12507. [CrossRef] [PubMed]
49. Castañeda, E. Efecto de los Ácidos Poliacrílico y Fítico y de Quitosano Sobre la Electrocristalización de Carbonato Cálcico. Bachelor´s Thesis, Facultad de Ciencias Veterinarias y Pecuarias, Universidad de Chile, Santiago, Chile, 2015.
50. Vagenas, N.V.; Gatsouli, A.; Kontoyannis, C.G. Quantitative analysis of synthetic calcium carbonate polymorphs using FT-IR spectroscopy. *Talanta* **2003**, *59*, 831–836. [CrossRef]
51. Rodriguez-Blanco, J.D.; Shaw, S.; Benning, L.G. The kinetics and mechanisms of amorphous calcium carbonate (ACC) crystallization to calcite, *via* vaterite. *Nanoscale* **2011**, *3*, 265–271. [CrossRef] [PubMed]
52. Chen, J.; Xiang, L. Controllable synthesis of calcium carbonate polymorphs at different temperatures. *Powder Technol.* **2009**, *189*, 64–69. [CrossRef]
53. Destainville, A.; Champion, E.; Bernache-Assollante, D.; Laborde, E. Synthesis, characterization and thermal behavior of apatite tricalcium phosphate. *Mater. Chem. Phys.* **2003**, *80*, 269–277. [CrossRef]
54. Han, J.-K.; Song, H.-Y.; Saito, F.; Lee, B.-T. Synthesis of height purity nano-sized hydroxyapatite powder by microwave-hydrothermal method. *Mater. Chem. Phys.* **2006**, *99*, 235–239. [CrossRef]
55. Berzina-Cimdina, L.; Borodajenko, N. Research of calcium phosphates using Fourier transform infrared spectroscopy. In *Infrared Spectroscopy-Materials Science, Engineering and Technology*; InTech: London, UK, 2012; ISBN 978-953-51-0537-4.
56. Jastrzębski, W.; Sitarz, M.; Rokita, M.; Bułat, K. Infrared spectroscopy of different phosphates structures. *Spectroc. Acta A Mol. Biomol. Spectrosc.* **2011**, *79*, 722–727. [CrossRef] [PubMed]
57. Jayakumar, R.; Egawa, T.; Furuike, T.; Nair, S.V.; Tamur, H. Synthesis, characterization, and thermal properties of phosphorylated chitin for biomedical applications. *Polym. Eng. Sci.* **2009**, *49*, 844–849. [CrossRef]
58. Stawski, D.; Rabiej, S.; Herczynska, L.; Draczynski, Z. Thermogravimetric analysis of chitins of different origin. *J. Therm. Anal. Calorim.* **2008**, *93*, 489–494. [CrossRef]
59. Juhasz-Bortuzzo, J.A.; Myszka, B.; Silva, R.; Boccaccini, A.R. Sonosynthesis of vaterite-Type calcium carbonate. *Cryst. Growth Des.* **2017**, *17*, 2351–2356. [CrossRef]
60. Nishi, N.; Ebina, A.; Nishimura, S.; Tsutsumi, A.; Hasegawa, O.; Tokura, S. Highly phosphorylated derivatives of chitin, partially deacetylated chitin and chitosan as new functional polymers: Preparation and characterization. *Int. J. Biol. Macromol.* **1986**, *8*, 311–317. [CrossRef]
61. He, Z.; Honeycutt, C.W. A modified molybdenum blue method for orthophosphate determination suitable for investigating enzymatic hydrolysis of organic phosphates. *Commun. Soil Sci. Plant Anal.* **2005**, *36*, 1373–1383. [CrossRef]

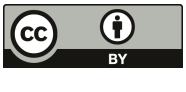

© 2018 by the authors. Licensee MDPI, Basel, Switzerland. This article is an open access article distributed under the terms and conditions of the Creative Commons Attribution (CC BY) license (http://creativecommons.org/licenses/by/4.0/).

crystals

MDPI

Article

The Carbonate Platform Model and Reservoirs' Origins of the Callovian-Oxfordian Stage in the Amu Darya Basin, Turkmenistan

Wenli Xu [1,*], Huaguo Wen [1,*], Rongcai Zheng [1], Fengjie Li [1], Fei Huo [2], Mingcai Hou [1] and Gang Zhou [3]

[1] Institute of Sedimentary Geology, Chengdu University of Technology, Chengdu 610059, China; zhengrc@cdut.edu.cn (R.Z.); lifengjie72@163.com (F.L.); houmc@cdut.edu.cn (M.H.)
[2] School of Geosciences and Technology, Southwest Petroleum University, Chengdu 610500, China; huofei342099206@163.com
[3] Exploration and Development Research Institute of PetroChina Southwest Oil & Gasfield Company, Chengdu 610051, China; zhougang29@126.com
* Correspondence: xuwenli5@163.com (W.X.); wenhuaguo08@cdut.cn (H.W.); Tel.: +86-159-2800-2838 (W.X.); +86-028-8407-9807 (H.W.); Fax: +86-028-8407-9807 (H.W.)

Received: 21 November 2017; Accepted: 29 January 2018; Published: 4 February 2018

Abstract: The Calloviane-Oxfordian carbonates in the northeastern Amu Darya Basin of southeastern Turkmenistan are composed of medium- to thick-bedded, mostly grainy limestones with various skeletal (bivalves, brachiopods, echinoderms, foraminifera, corals, and sponge) and non-skeletal grains (intraclasts, ooids and peloids). Two facies zones, six standard facies belts and some microfacies types were recognized, and sedimentary model "carbonate ramp-rimmed platform" was proposed and established that can be compared with the classical carbonate sedimentary models. In this model, favorable reservoirs not only developed in the intraplatform shoal of open platform, or reef and shoal on the platform margin, but also in the patch reefs, shoal and mound facies on the upper slope. The reservoir's pore space is dominated by intergranular and intragranular pores and fissure-pore reservoirs exist with medium porosity and medium to low permeability. Sedimentary facies and diagenetic dissolution are the key controlling factors for the development of high-quality reservoirs.

Keywords: sedimentary model; Callovian-Oxfordian; Amu Darya Basin; reservoir; main controlling factors

1. Introduction

With the constant increase of China's demand on energy resources and theory advancement in oil and gas exploration, some major discoveries of oil and gas exploration have been made in marine carbonates of the Tarim, Sichuan and Ordos basins. Subsequently, marine carbonate has become an important domain of exploration in China, and petroleum geological characteristics of carbonate platform have become a new hotspot of research [1]. High-efficiency oil and gas exploration in marine carbonates requires the guidance of the sedimentary model. Studies on carbonate sedimentary evolution and models commenced in the 1960s. Shaw (1964) [2] first introduced the concepts of epicontinental sea and marginal sea and laid the foundation for the carbonate sedimentary model. Since then, many scholars have come up with new ideas on controlling factors and depositional models of carbonate sedimentation from the aspects of sea level variation, marine environment, climatic conditions and structural settings [3–18], which enriched and developed the research contents of the carbonate sedimentary model. As oil and gas exploration progressed, in practice, it is still difficult to characterize the carbonate platform in detail with a certain model, although achievements have been made in analogy study with the application of existing models. Therefore, the only method applicable

is to build a carbonate sedimentary model suitable for the study area through analysis, correlation and summarization of real data, to guide oil and gas exploration practices. Based on existing carbonate sedimentary models proposed by researchers before [19–21] and the author's understandings of the Callovian-Oxfordian marine carbonates in the Amu Darya Basin, Turkmenistan, a new carbonate sedimentary model applicable to this basin has been proposed. The development conditions and distribution law of reservoirs in this basin have been analyzed by using this model, in the hope of providing the basis for oil and gas exploration of the Middle-Upper Permian and Middle-Lower Triassic strata in the Middle-Upper Yangtze region that share similar carbonate sedimentary model and reservoir origin in the Callovian-Oxfordian strata in the Amu Darya Basin.

2. Geological Setting

Located in the northeastern part of Turkmenistan, southern part of Uzbekistan and northwestern part of Afghanistan, the Amu Darya Basin is one of the most important hydrocarbon basins in the Central Asia region [22], as well as the source of China's West-East gas transmission project. Structurally, it is a large-scale Mesozoic superimposed basin situated in the southeastern part of the Turan Platform on the Sino-Korea-Tarim Plates, within the Tethys structural domain in the central-western parts of the Central Asian structural belt (Figure 1) [23–26]. The Amu Darya Basin has experienced three stages of evolution: the rifting stage during the Permian to Triassic periods, the steady subsidence stage from the Jurassic to Cretaceous periods, and the uplifting and reforming stage during the Paleogene-Quaternary periods. From the Late Permian to Triassic periods, the subduction of Tethys Ocean into the Eurasian plate enabled the formation of the back-arc extensional rift and, under the extensional tectonic setting, fault terrace belt was formed in the basin, thereby laying the foundation for steady subsidence of the basin. From the Jurassic to Cretaceous periods, a critical period for the formation of the basin, the basin subsided steadily, with relatively weak tectonic movements and absence of faults, and the thickness of the strata deposited increased from west to east, but the variation is small. Tectonic movements occurred during this period have a strong control on the formation and development of source rocks, reservoirs and caprocks in the basin (Figure 2a–c). From the Paleogene to Quaternary periods, in response to the Alpine movement and the neotectonics, folds in the eastern and northeastern parts of the basin were uplifted, the basin was divided into the north and south two depression zones by a salt dome structural belt in the middle. In addition, tectonic framework of the fault terrace belt surrounding the basin and the placanticline uplift belt within the basin was eventually formed (Figure 2d) [27,28]. On the whole, the Amu Darya Basin is surrounded by fold mountain systems and deep-large faults. It is bordered to the northeast by the Kyzylkum High Belt, to the southeast by the southwest branch range of the Gissar mountains and the Bande Turkestan Foldbelt, and to the southwest by the Kopet-Dag Foldbelt. With a series of uplifts, depressions and paleo-anticlines in the middle, and the margin plunging towards the hinterland in a ladder-like mode, the basin generally takes on a NW-SE trending dustpan shape that is narrow and steep in the south and west wings and wide and gentle in the north and east wings (Figure 1). The basin is divided into three first-order structural units, according to structural morphology of the basement and the sedimentary strata: the Kopet-Dag piedmont depression belt in the southwestern part, the Karakum High in the central part and the Amu Darya Depression belt in the northeastern part [29,30]. Regional tectonic-sedimentary framework and distribution of reservoirs, caprocks and gas pools are controlled by the NW- and NE-trending faults developed in the basin [31].

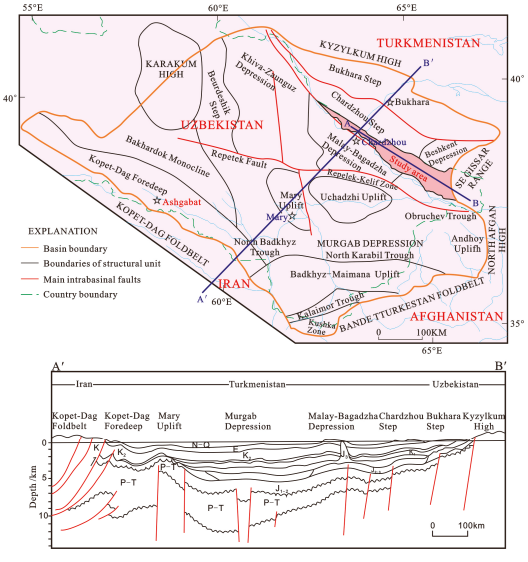

Figure 1. Overview of regional structure in the Amu Darya right bank area.

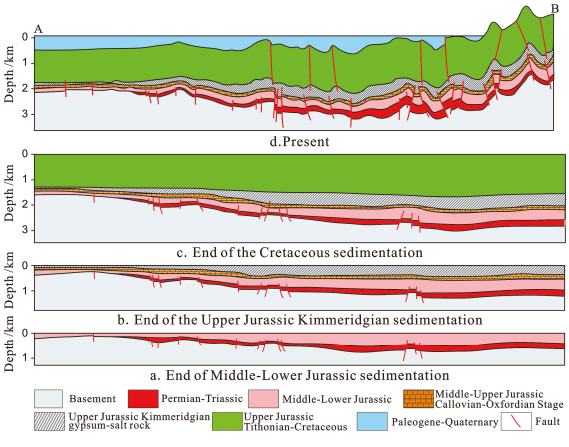

Figure 2. Palinspastic sections in Amu Darya Basin, location of profile is shown in Figure 1 (Reference [27,28]).

The study area is located in the right bank of the Amu Darya, Turkmenistan (Figure 3), and structurally is part of the Chardzhou terrace in the Amu Darya Basin. The Amu Darya basin contains three structural bed series with different structural and sedimentary characteristics: i.e., the basement, transition bed and sedimentary bed. The basement is composed of the Paleozoic volcanic and metamorphic rocks and its burial depth varies greatly. The transition bed consists of the Permian-Triassic terrigenous clastic rocks, with thickness increasing from north to south. The sedimentary bed is comprised of the Jurassic, Cretaceous and Paleogene carbonates, evaporites and interbedded sandstone, mudstone and coal bed [32–34]. The Middle-Upper Jurassic Callovian-Oxfordian stratum, consisting of a carbonate sedimentary assemblage [34–37], is the most important hydrocarbon-bearing formation in the basin. It is in unconformable contact with the

underlying the Middle-Lower Jurassic coal-bearing clastic rock that can act as source rock, and in conformable contact with the overlying Upper Jurassic Kimmeridgian gypsum-salt rock that can act as tight caprock. The Callovian-Oxfordian stratum can be divided into eight layers according to lithologies XVI, XVa2, Z, XVa1, XVhp, XVm, XVp, XVac and three sedimentary sequences with a complete regional transgressive-regressive cycle (SQ1, SQ2, SQ3) (Figure 4). Of these sequences, SQ1 is composed of four lithologic layers (XVI, XVa2, Z, XVa1) that are equivalent to the Callovian, SQ2 consists of three lithologic layers (XVhp, XVm) that are equivalent to the early-stage of the Oxfordian, and SQ3 is comprised of two lithologic layers (XVp, XVac) that are equivalent to the later-stage of the Oxfordian. Basically, lithological layers of these three integral sequences correspond well with the sedimentary system tracts that span various sedimentary facies belts and hence can be correlated on a regional scale, although these sequences differ in regional lithology, lithofacies and thickness (Figure 5).

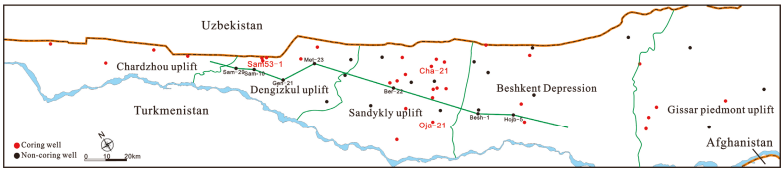

Figure 3. Distribution of wells in Amu Darya right bank area.

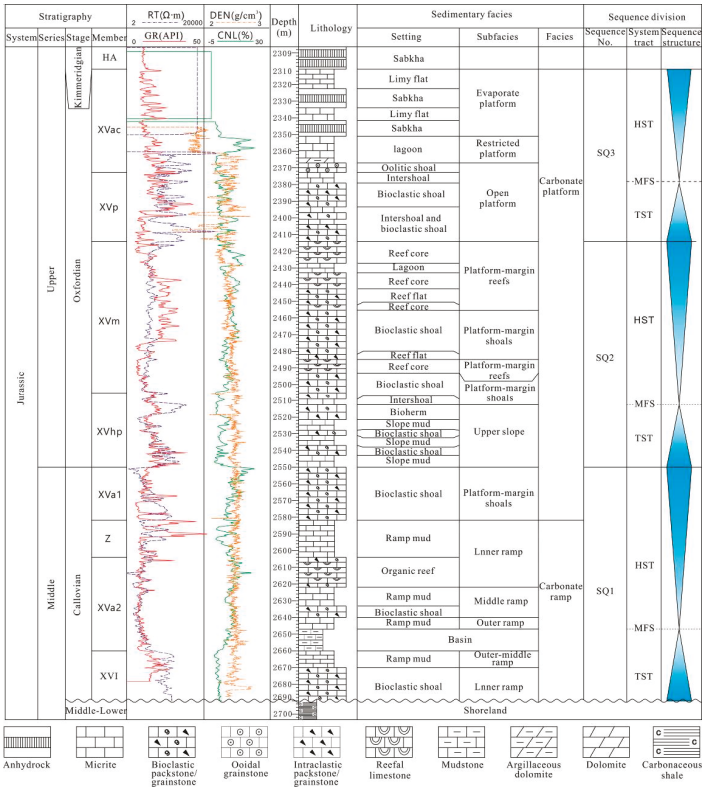

Figure 4. Lithological, chronostratigraphy and stratigraphic sequence of Callovian-Oxfordian Stage in Amu Darya Basin.

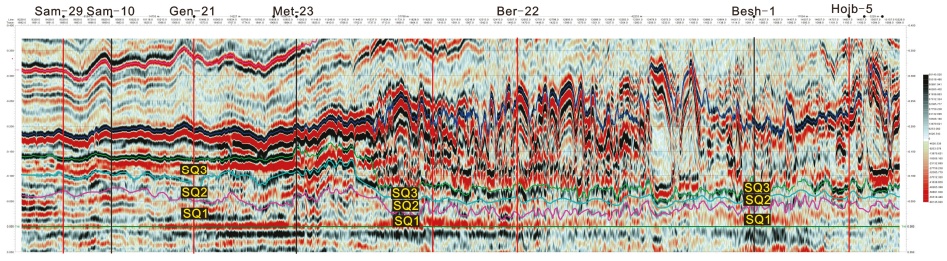

Figure 5. Sequence stratigraphy and seismic characteristics of Callovian-Oxfordian Stage, location of profile is shown in Figure 3 (Reference [38]).

3. Samples and Method

Detailed petrographic studies were based on approximately 800 thin sections (Figure 1) stained with Alizarin Red S and potassium ferricyanide solution [39]. Carbonate rocks were classified by following the nomenclature of carbonate rocks by Dunham (1962) [40]. Depositional sequences and inferred relative sea level changes were interpreted based on the Carrozi method [41]. Facies identification and stacking patterns of facies followed the classification of Tucker and Wright (1990) [42], Flügel (2010) [43]. Sedimentary system tracts were defined based on facies trends, stacking pattern, lithological changes, and nomenclature by following Vail (1977a, 1977b) [44,45] and Wang (2014) [38]. These sequence-stratigraphic tracts were then correlated with each other based on facies and depositional environments and finally related to the global sea level curves of Haq (1988) [46]. In this paper, division of sedimentary facies was based primarily on the carbonate sedimentary model proposed by Wilson (1975) [5], Tucke (1981) [7], Basilone (2016) [16], and secondly on the model proposed by Mcllreath and James (1979) [6], and Read (1985) [9]. Core samples used in this study were recovered from the Callovian-Oxfordian in the right bank of the Amu Darya, Turkmenistan. These carbonate samples were utilized for thin section, porosity-permeability and mercury injection analyses.

Physical properties and mercury injection tests were conducted on cylinder shape samples (25 mm long and 25 mm in diameter), with CMS-300 tester (Core Lab, Houston, State of Texas, USA) for testing porosity and permeability under overburden pressure and AutoPore IV 9500 mercury injection apparatus (MICROMERITICS INSTRUMENT CORP, Atlanta, GA, USA), in accordance with SY/T6385-1999 and SY/T 5346-1994, and undertaken by Key National Lab of Oil and Gas Reservoir Geology and Development Engineering, Chengdu University of Technology. The detail data were presented in Supplementary Table S1.

X-ray diffraction analysis was conducted by using D/MAX-IIIC diffractometer (Rigaku Corporation, Tokyo, Japan), in accordance with JCPDS-ICDD, and was undertaken by Key National Lab of Oil and Gas Reservoir Geology and Development Engineering, Chengdu University of Technology. The detail data were presented in Supplementary Table S2.

Electron probe X-ray microanalysis was conducted by using EPMA-1720 H Series Probe microregion analyzer (SHIMADZU, Kyoto, Japan) and INCA Energy 250 X-Max20 energy disperse spectroscopy (SHIMADZU, Kyoto, Japan), and was undertaken by Key National Lab of Oil and Gas Reservoir Geology and Development Engineering, Chengdu University of Technology.

4. Sedimentary Characteristics and Models of Carbonates

4.1. Sedimentary Characteristics

By observing and characterizing cores recovered from 33 wells and conducting well log interpretation of several non-coring wells, in combination with preexisting research data of sedimentary sequence, lithofacies paleo-geography and petroleum geological characteristics [33–38,47–54], it is

found that, under the control of the paleo-geomorphology high in northwest and low in southeast, a set of carbonate rock with distinct features of deep- and shallow-marine facies was deposited in the study area. The distribution framework of facies belt and basic characteristics of each facies belt are as follows.

Shallowwater platform facies zone in the northwest of the study area contains platform evaporitic, restricted platform, open platform and platform margin. Platform evaporitic is present in the XVac layer only, the lithology is dominated by massive anhydrock with crystal grain structure (Figure 6a), intercalated with anhydrite-carbonate dolostone and mudstone. Restricted platform is present primarily in the XVac and XVp layers, and is dominated by interbedded grey to dark grey thin-bedded micrite (Figure 6b) and microbioclastic, intraclastic wackestone. Open platform is present broadly in various layers, consisting of platform interior restricted and shoal with alternating sequences, and is dominated by grainstone deposited in high-energy shoal environment, such as well-sorted micrite, ooidal grainstone (Figure 6c) and bioclastic grainstone, and alternatively developed micrite and bioclastic wackestone deposited in low-energy environment. In this facies belt, a large variety of biotypes were present, including the actinozoan, echinodermata, bryozoan, foraminifer, gastropods, bivalve and algae. Platform margin zone depositing in strong hydrodynamic force include two types, marginal reef and shoal, and is dominated by the assemblage of well-sorted grainstone (Figure 6d), bioclastic and ooidal–grainstone with isopachous rimmed cementing structure, and rudist bivalve framestone and boundstone (Figure 6e), with the rudist bivalve being the primary reef-building organism, as well as a small amount of sponge boundstone (Figure 6f), Ceriocava boundstone (Figure 6g), stromatoporoids boundstone, coral boundstone and coral-rudist bivalve framestone, intercalated with a little bioclastic packstone/wackestone. Some typical accessory reef organisms present commonly in this facies belt include benthic foraminifera, brachiopoda, gastropods, algae, Echinodermata and bivalve. In seismic profile, marginal shoal body is represented by the wavily changed events, with amplitude, frequency and phase changed accordingly; reef body is represented by the mound-like inclined reflection of moderate to high amplitude, with high amplitude on top, and low frequency, weak amplitude, and disordered and lenticular reflection inside, and is relatively steep towards the sea and flat-gentle towards the land; and the shoal facies is generally represented by worm-like and wavy-like reflections (Figure 7).

Deepwater front slope and basin facies zones are situated in the southeast of the study area. In the slope facies zone, intraclastic packstone (Figure 6h), bioclastic packstone, organic boundstone and micrite occur in the upper slope, while micrite, intercalated with a small amount of microbioclastic wackestone and mudstone, deposited on the lower slope. Bioclasts are dominated by sponge spicule and radiolarian. On seismic section, slope facies is commonly represented by the parallel continuous reflection with low frequency, and is thinner than the platform and platform margin facies. Interestingly, mound-like or amygdaloidal or irregular reef-shoal anomalies are commonly seen under the strong amplitude and disorder reflection background on the upper slope (Figure 7), leading to considerable increase of formation thickness. The basin facies zone is dominated by micrite and mudstone, intercalated with dark shale.

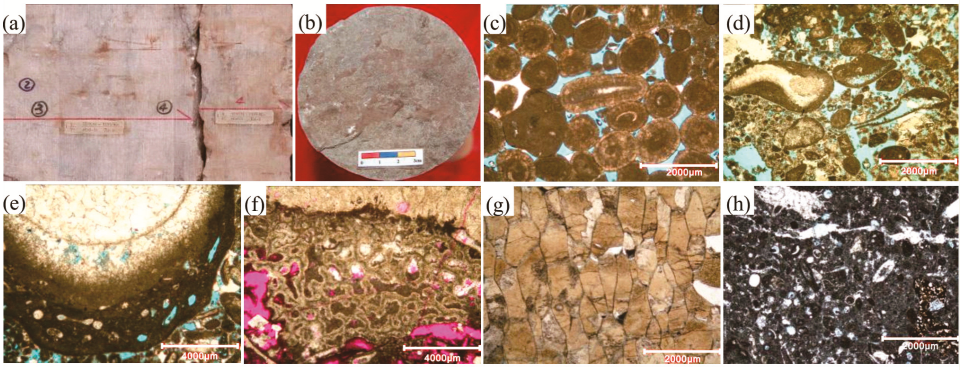

Figure 6. Paleontologic characteristics and various carbonate rock types of Callovian-Oxfordian Stage. (**a**) Grey white gypsum rock, 2247.45–2247.92 m, XVac, Well NFar-21, platform interior evaporitic; (**b**) Micrite, 2377.06–2377.29 m, XVp, Well Sam53-1, restricted platform; (**c**) Ooidal grainstone, 2372.69 m, XVac, Well Sam53-1, open platform interior oolitic shoal, casting thin section (-); (**d**) Bioclastic grainstone, with bioclasts dominated by rudist bivalve, foraminifer, metacrinus, brachiopoda, bryozoan and red alga, 2447.92 m, XVm, Well Sam45-1, platform marginal shoal, casting thin section (-); (**e**) Rudist bivalve framestone, 2454.76 m, XVm, Well Sam53-1, platform marginal reef, casting thin section (-); (**f**) Sponge boundstone, 2459.42 m, XVm, Well Sam53-1, platform marginal reef, casting thin section (-); (**g**) Bryozoan boundstone, bryozoan is istulipora, 2439.85 m, XVm, Well Sam53-1, platform marginal reef, casting thin section (-); (**h**) Intraclastic packstone, with a little ostracoda, foraminifer, bryozoan and echinodermata, XVhp, 3557.4 m, Well Shi-21, upper slope, casting thin section (-).

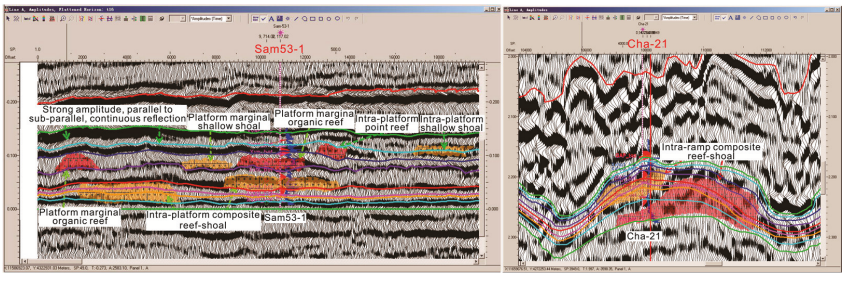

Figure 7. Interpretation of facies types based on seismic profiles in Samendepe and Chashgui areas, well sites are in Figure 3 (Reference [37]).

4.2. Sedimentary-Sequence Evolution Characteristics of Callovian-Oxfordian

It is indicated from the feature of basin margin that the basement of the Amu-Darya Basin is a Hercynian accreted terrane composed of two large Precambrian continental massifs (micro- continents in pre-collisional structure) expanding northwardly and southwardly and Paleozoic metamorphosed rocks [29,55]. In Late Permian-Triassic (possibly Late Triassic/Early Jurassic [56]) the Iranian Block collided with the southern margin of Eurasia, and the Paleotethys Ocean was closed [29,57,58]. A series of structural faults formed in the collision event separate the basement of the basin into numerous paleo-uplifts and graben structures [59–62]. Hereafter, the Amu-Darya Basin entered the development stage of rift basin [63] and a period of stable settlement. In Lower-Middle Jurassic, there were the clastic sediments with greater thickness [64], which were unconformably contacted with the underlying stratum [65]. In Middle Jurassic Bathonian Stage/Callovian Stage, there was large-scale transgression,

and the successive paleo-uplifts (e.g., Chardzhou, Dengizkul, Sandykly) and basement faults in the basin controlled the deposition of carbonates in this period [14–18]. During the deposition of Callovian stage, affected by the basement and Permian to Triassic tectonic movements, paleo-geomorphology of the study area remained high in the northwest and low in the southeast, and the water depth increased gradually from the northwest to southeast, the paleo-uplifts were situated within the relatively deepwater zone, while a broad area to the west of the Chardzhou uplift was the shallowwater zone, slope-break belt was absent, the paleo-geomorphology was relatively gentle and flat, and carbonate sedimentation exhibited the ramp model. During the Oxfordian sedimentation, the overall water depth was shallower than that during the Callovian sedimentation, paleo-uplifts exhibited differential sedimentary characteristics due to the influence of water depth; the water depth increased successively from northwest to southeast, that is, Chardzhou paleo-uplift → Dengizkul paleo-uplift → Sandykly paleo-uplift → Beshkent depression (Figure 3). The Dengizkul paleo-uplift was located in the transition zone from the shallowwater to deepwater, was the conjunction between the transfer zone in the central Sandykly and the weak tectonic deformation belt in the western Sandykly, and was uplifted higher than other paleo-uplifts. At that period, the Dengizkul paleo-uplift had high hydrodynamic energy and abundant nutriments, enabling large-scale growth of organic reef, and carbonate sediments were characterized by the rimmed platform model. Sedimentary-sequence evolution characteristics of the Callovian-Oxfordian are as follows.

4.2.1. Sedimentary-Sequence Evolution Characteristics of Callovian

The Callovian is an integral sedimentary sequence 80 to 330 m thick made up of a transgressive system tract and a highstand system tract, exhibiting an asymmetric structure of rapid transgressive and slow regression (SQ1 in Figure 4). The transgressive system tract is mainly in the XVI layer. Affected by the paleo-geomorphology of the study area high in the northwest and low in the southeast and a rapid transgression over a broad range, marine carbonate rocks retrograded from southeast to northwest and onlapped the Middle-Lower Jurassic clastic continental shelf, the difference between the primary form of the carbonate ramp and the sedimentary framework of the inner ramp, mid-ramp, outer ramp and basin facies began to emerge. The lithology is dominated by interbedded dark grey thin-medium micrite and bioclastic wackestone. Aggradation during the maximum flooding period (or condensed member) is present in the lower part of XVa2, and the lithology is grey black thin-bedded marlstone intercalated with dark shale of mid-outer ramp and basin facies. Early-stage sediments of highstand system tract are in the middle and upper parts of XVa2 and Z, which retain the differential sedimentary frameworks of inner ramp, mid-ramp, outer ramp and basin facies, but relatively large-scale progradational shallow shoal and organic reef began to form at the front of the inner ramp (Figures 4 and 8a), and the lithology is dominated by non-isopachous assemblage of bioclastic wackestone, bioclastic packstone and reefal packstone. Later-stage sediments of highstand system tract deposited in XVa1, as the sea level fell, carbonate ramp break began to transform into the carbonate platform, forming a sedimentary framework with obvious differentiation from the shallowwater facies zone to deepwater facies zone, that is, from the margin to the center of the basin, open platform → platform margin → front ramp → basin facies (Figures 4 and 8b). It is noteworthy that the platform marginal organic reef and shoal facies belts with intensive progradation effect were developed within the border of Uzbekistan north in the study area, and the main part of the study area was situated in the platform marginal ramp → deepwater facies belts of the basin at this period. The event of great significance is the commencement of the formation of shoal and organic reef with intensive progradation effect in the upper part of the shallowwater ramp in relatively shallowwater, and the lithology is dominated by the assemblage of grey medium to thick-bedded sparry bioclastic grainstone and massive reefal packstone intercalated with medium to thin-bedded bioclastic wackestone.

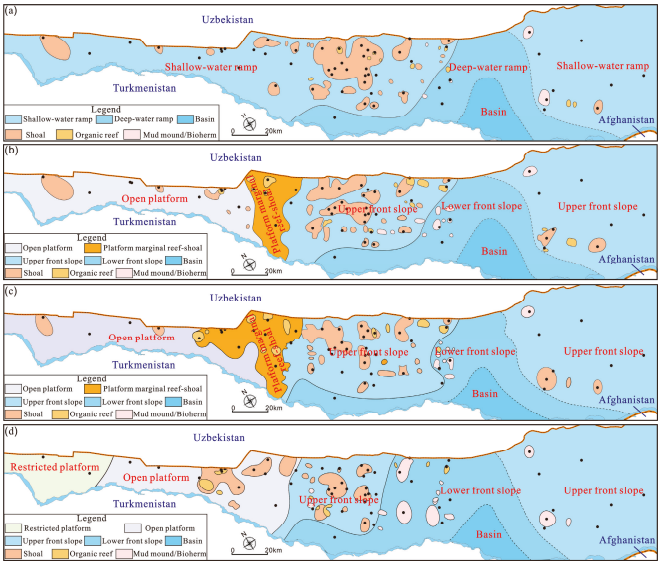

Figure 8. Sketch map showing distribution of sedimentary facies and paleogeography of Callovian-Oxfordian Stage in Amu Darya Basin ((**a**) layer XVa2; (**b**) layer XVa1; (**c**) layer XVm; (**d**) layer XVp)).

4.2.2. Sedimentary-Sequence Evolution Characteristics of Oxfordian

Two integral sedimentary sequences were formed in the Oxfordian, each of which consists of transgression and highstand system tract and possesses the asymmetric structure of rapid transgression-slow retrogression (SQ2 and SQ3 in Figure 4). The first sedimentary sequence (SQ2) includes the XVhp-XVm layers, with the thickness of 10 to 180 m. Under the control of the global "Oxfordian transgression", sea level rose rapidly during the early stage of Oxfordian, transgressive system tract was formed in the XVhp layer, which kept the rimmed platform sedimentary framework of SQ1 highstand system tract at late stage, i.e., open platform → platform margin → front ramp → basin facies, and the lithology is dominated by the non-isopachous interlayer assemblage of grey, medium to thick-bedded bioclastic grainstone, massive reefal packstone and medium to thin-bedded bioclastic wackestone. Sediments deposited during the maximum transgression period (or condensed member) are present in the upper part of the XVhp layer, and the lithology is dominated by grey thin-bedded micrite of front ramp facies. Highstand system tract was formed in the XVm layer, the sedimentary framework retained the previous open platform → platform margin → front ramp → basin facies (Figure 8c). In addition, as sea level fell slowly and reefs and shoals commonly grew and accumulated rapidly, the growth of reefs and shoals reached the largest scale in the whole Callovian-Oxfordian. As a result, reefs and shoals were widespread at the platform margin, and large-scale aggradational shallow shoals and point reefs were commonly present on the upper front ramp, and the lithology is dominated by non-isopachous interlayer assemblage of micrite, bioclastic wackestone/packstone, intraclastic packstone and reefal packstone.

The third sedimentary sequence (SQ3) consists of the XVp-XVac layers, with a thickness of 10–140m. The transgressive system tract was formed mainly in the XVp layer. The sea level remained low in the study area due to the shallow depth and relatively closed water body, although transgression occurred rapidly; sediments of platform marginal reef and shoal facies didn't develop any more, and the sedimentary framework was restricted platform → open platform → front slope → basin facies, from the margin to the center of the basin (Figure 8d). Large-scale shallow shoal with intensive aggradation → progradation still developed in the upper part of platform front slope, and the lithology

is dominated by the assemblage of grey medium to thick-bedded bioclastic grainstone and intraclastic grainstone intercalated with medium to thin-bedded bioclastic wackestone. Aggradation of the maximum flooding period (or condensed member) occurred in the upper part of the XVp layer, and the lithology is grey thin-bedded micrite of open platform facies. Highstand system tract sediments were developed in the XVac layer. As sea level fell considerably, the sedimentary framework of platform interior evaporitic → restricted platform → open platform → front slope → basin facies was formed gradually from the margin to the center of basin. It is noteworthy that, the so-called basin facies sediments in this framework refer to the deep lagoon with closed bay, of which the lithology is dominated by thin-bedded high-gamma mudstone intercalated with a few thin-bedded grey black marlite. Its origin is related to the direct transition of deepwater basin into deep lagoon driven by the intensive limitation to seawater circulation resulted from the rapid and considerable sea level fall occurred at the end of the Oxfordian.

4.2.3. Sedimentary Model

Since the epicontinental sea fresh-water carbonate sedimentary model was first proposed by Shaw (1964) in the 1960s, the research related to the carbonate sedimentary model has been enriched and developed constantly [1–18] over the past 50 years, but the current available models are inapplicable to lithofacies paleo-geography research of the Callovian-Oxfordian in the Amu Darya Basin. Similar situation happened in the Upper Paleozoic and Mesozoic marine carbonates in the Sichuan Basin too. Therefore, based on the carbonate sedimentary models proposed by Wilson (1975) [5], Mcllreath and James (1979) [6], Tucker (1985) [8], Read (1985) [9], Gu (2007) [1], Basilone (2016) [16], in combination with the sedimentary characteristics of the Callovian-Oxfordian in the Amu Darya Basin, the sedimentary model of "carbonate ramp-rimmed platform" has been proposed (Figure 9).

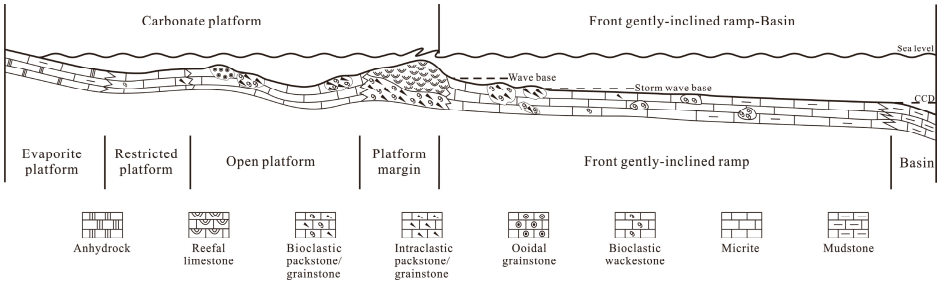

Figure 9. A sedimentary model of carbonate ramp (gently inclined slope) and rimmed platform of Callovian-Oxfordian Stage in Amu Darya Basin (Reference [8,16]).

1 Concept of sedimentary model of "carbonate ramp-rimmed platform"

In this study, this sedimentary model of "carbonate ramp-rimmed platform" is defined as open shallow shelf marine domain, where the sedimentation is dominated by carbonate, carbonate shelf is rimmed with reef and shoal facies, and wide and gentle slope is present in the transition zone between shelf and deepwater basin. In general, the domain can be subdivided into two sedimentary facies provinces, including six facies belts and several microfacies (Figure 9). According to the model proposed by "Tucker (1985) [8]", these two sedimentary facies provinces are named the carbonate shallowwater platform sedimentary province and the front ramp-basin deepwater province, and the six standard facies belts include the platform evaporitic, restricted platform, platform margin, front ramp and basin.

2 Characteristics and evidence of the sedimentary model of "carbonate ramp-rimmed platform"

Original version of this model was first proposed by Gu (2009) [1] based on development characteristics of Great Barrier Reef in Australia, which is named the "open ramp-rimmed platform". The sedimentary model of "carbonate ramp-rimmed platform" proposed by the authors [29] on the basis of the development characteristics of the Callovian-Oxfordian carbonates has two evident sedimentary characteristics and evidences.

(1) Width and dip of slope

Of over 140 wells penetrating the Callovian-Oxfordian in the study area, around 90 encountered the front slope facies belt in the XVa1-XVm layers. Based on core data and well log data of the coring interval, as well as seismic data, the carbonate rimmed platform commenced broad development during the XVa1-XVm sedimentation, and the width of the front slope commonly exceeded 350 km, much greater than the average width (70 km) of the modern marine slope. Within a distance of 60 km from the Tan wellblock to Besh wellblock on the upper front slope, thickness of the XVa1-XVm increases from 60 to 90 m, indicating a relatively small variation in slope inclination, which is consistent with the tectonic evolution characteristics of Callovian-Oxfordian obtained by Zhang [27] through the analysis based on the principle of balanced section (Figure 2b). Therefore, it is speculated that the front slope belt in the study is different from normal platform in two aspects: (1). the front slope belt is quite wide and gentle; (2). although slope break belt with gradually deepening water body is present between platform margins, the sedimentary characteristics of slope break belt, particularly the landform-controlled gravity flow sediments, are absent.

(2) Development scale of reefs and shoals

In the study area, other than platform margin facies belt, large-scale and continuously distributed shoals were developed in the upper part of front slope belt, with point reefs and bioherm groups locally, and the lithology is dominated by bioclastic packstone/grainstone and intraclastic packstone/grainstone, intercalated organic boundstone and reefal packstone. Similar features are described from the seaward front of marine sand belt adjacent to the reef environment of NW Sicily, Florida and Bahamas modern carbonate platform [16,66–68]. The Sicily Island and other platform margin reef front-upper slope mainly contain the deposition of oolitic limestone and bioclastic limestone, and shoal bodies show obvious lateral distribution and slightly narrower longitudinally [16]. It can be seen from lithologic characteristics and development scale of reefs and shoals that the formation of reef-shoal assemblage in front slope over 350 km wide, with the scale ranking second only to those formed in platform margin, is possible only when waves and ocean currents having a certain energy occur. From another perspective, it demonstrates that the formation of shallow shoals, point shoals and bioherm groups with good reservoir performance within the range of the front slope of over 350 km wide requires a quite low inclination of slope.

3 Sedimentary characteristics of each facies belt

(1) Platform evaporite facies

The poor connectivity between the platform and open sea, coupled with the hot and dry climate, all add up to the intense evaporation in this facies belt. The anhydrite gypsum microcrystalline dolomite and marl are widely developed (Figures 4 and 9). It is similar to the sedimentary environment of sabkha and salina in the "Tucker (1985) [8]" model and the evaporate platform in the arid climate in the "Wilson (1975) [5]" model.

(2) Restricted platform

It is a relatively closed shallow water body with lower hydrodynamic energy and a water depth of less than one meter to tens of meters. The lithology is dominated by the interbedding assemblages of thin-layered gray-dark gray micrite and granular wackestone (Figures 4 and 9). It is similar to the restricted platform in the "Wilson (1975) [5]" model, post-shoal lagoon and carbonate mud

in the "Tucker (1985) [8]" model, and the tidal flat and lagoon in the isoclinal slope in the "Read (1985) [9]" model.

(3) Open platform

The water depth in this facies belt is several meters to tens of meters, the water here is actively circulated and the salinity is normal. It contains rich biological types, including gastropods, lamellibranchia, echinoderms, foraminifers and a variety of algae. It is mainly composed of subtidal low-energy environment and high-energy shoal environment (Figures 4 and 9). Among them, the subtidal low-energy environment is similar to the lagoon in open sea platform in the "Wilson (1975) [5]" model, and the sedimentary environment of euxinic lime in the "Tucker (1985) [8]" model. It mainly contains micrite and bioclastic wackestone; the high-energy shoal environment is similar to the shallow carbonate sand shoal in the "Tucker (1985) [8]" model. In addition, it is similar to the combined shallow environment of shoals or ooids (aggregates) in the isoclinal slope in the "Read (1985) [9]" model. The lithologies consist of intraclastic grainstone, ooidal grainstone and bioclastic grainstone.

(4) Platform margin facies

The sedimentary characteristics in this facies belt is similar to the platform margin shoal+ platform margin reefs in the "Wilson (1975) [5]" model, to the carbonate shoals and/or continent shelf reefs in the "Tucker (1985) [8]" model, to the sedimentary-type continent shelf margin facies belt in the "Mcllreath and James (1979) [6]", to the continent margin in the "Basilone (2016) [16]"model.

The high-energy position in this facies belt is different from that in the nearshore continental slope break (the so-called first slope break of onshore) in the isoclinal slope in the "Read (1985) [9]" model. It is located in the slope break of rimmed platform distant to the continent (the so-called second slope break of the shelf margin). It is the strongest hydrodynamic sedimentary environment with a depth of several meters to tens of meters. There is a strong reworking under this hydrodynamic condition and it is the transformation zone of deepwater and shallow water sedimentations. There are the developments of two facies types, the platform margin reefs and platform margin shoal.

(1) Platform margin shoal: jointly controlled by wave and tidal action, it shows extremely strong hydrodynamic conditions, good circulation of seawater, adequate oxygen and normal salinity. However, it is not suitable for the dwelling and propagation of marine benthonic organisms because the substrate is in a mobile state. Therefore, it is not adaptable to marine benthonic organisms. Mainly, there are the developments of bioclastic grainstone, intraclastic grainstone and ooidal grainstone. In addition, it develops a small amount of wackestone and micrite in intra-shoal low-energy belt.

(2) Platform margin reefs: it is distributed along the platform margin in groups. Vertically, the reefs often co-exist with the biological debris shoals, forming reefs and shoal complexes or using the platform margin shoal as the growth base. This is different from development relationship in platform reef and in shoal front in the "Wilson (1975) [5]" model. The lithology is mainly composed of thick rudist bivalve framestone and boundstone, with a small amount of coral boundstone and coral-rudist bivalve framestone. In addition, the biological framework components include thick-shelled clams, coral, moss, algae and the likes, and there are filled by micritic calcite.

(5) Gentle ramp facies belt in platform front

The location is equivalent to the platform front ramp + deep shelf margin + shelf in the "Wilson (1975) [5]" model, front ramp in the "Mcllreath and James (1979) [6]" model and "Tucker (1985) [8]" model, relatively deep ramp facies belt in isoclinal slope in "Read (1985) [9]".

In the study area, this facies belt is evidently characterized by the development of extremely wide and gentle slope in deep continent shelf. The slope break zone is not obvious. However, based on

the large-scale sedimentary assemblage of reefs and shoals, the gravitational flow is not developed. The depositional environment extends from near wave base of rimmed platform margin to the deeper waters or the one below maximum storm wave base. It is different from the sedimentary models proposed by previous scholars; the platform front slope belt is an obvious narrow facies belt with common development of calcareous gravity flow deposition controlled by steep terrain in the "Wilson (1975) [5]", "Mcllreath and James (1979) [6]", "Tucker (1985) [8]", and "Basilone (2016) [16]" models. There is no development of slope break and only the existence of lagoon-tidal flat facies sedimentary facies equivalent to restricted platform after the assemblage of reef and shoal facies in the isoclinal slope in the "Read (1985) [9]" model. In addition, the "front slope" in the "gentle slope-rimmed carbonate platform" model includes two depositional environments, the upper slope and the lower slope. The upper slope is located near the wave base or slightly deeper. There are the developments of shoal and point reefs, which are representatives of highlands in the slope, even large-scale independent platform (or atoll). The water depth of the lower slope is up to several hundred meters, and it is mainly composed of micrite, with a small amount of wackestone and mudstone.

(6) Basin facies

There are two types of sedimentary facies in the basin. One is an early deepwater basin with deep water and low energy. It is similar to the sedimentary features of basin mentioned in the "Wilson (1975) [5]", "Tucker (1985) [8]", and "Read (1985) [9]" models. The lithology is mainly composed of dark micrite and mudstone, which is rich in organic matter and mud lamina. The second is the occluded gulf basin in late period, and this type is different to abyssal basin. Its genesis is related to the occluded gulf basin with lagoonal character directly transformed from the strongly occluded seawater in the basin resulted from large-scale sea level decline at the end of the Oxford stage. The water body energy is extremely low, and the biological fossils are rare. It is a thin high gamma mudstone with a thickness of only 10–20 m, with a few thin layers of gray black micrite and mudstone.

5. Origin of "Carbonate Ramp-Rimmed Platform" Reservoir

In the "carbonate reef-rimmed platform" model, reservoirs develop broadly over the open platform, platform margin and upper front ramp facies belt. In particular, open platform and platform margin facies share similar reservoir characteristics with other carbonate sedimentary models. The major differences between them are the presence of a variety of grain banks, point reefs and bioherms formed in relatively strong hydrodynamic condition in the upper front ramp, which enables the formation of reservoirs with good physical properties. Hence, an outstanding feature of the "carbonate ramp-rimmed platform" model, which makes it different from the classic platform model, is the possibility of the formation of reservoirs in the upper front ramp in marine carbonate sedimentary province. A discussion on the genesis and major controlling factors of high-quality reservoirs in the upper front ramp is presented in the following section with a case study from the Callovian-Oxfordian in the Amu Darya Basin.

5.1. Favorable Sedimentary Microfacies for Reservoir Formation

Water body energy in the upper part of the Callovian-Oxfordian front ramp in the Amu Darya Basin was sufficient enough for sedimentation of porous carbonates with particular structure and reef structure, thereby laying a material basis for formation of reservoirs. Reservoir space of point reef, shallow shoal and bioherm limestones in the upper part of the front ramp predominately consists of residual primary intergranular pores, organic framework pores and intergranular enlarged dissolved pores (Figure 10a–c), and intergranular and intragranular dissolved pores present locally (Figure 10a–c), molded pores (Figure 10b) and fractures (Figure 10d). The reservoirs here have good physical property: with the porosity ranging from 1.1% to 19.0%, averaging 7.9%, (6% to 12%, accounting for 59% of total samples); with permeability from $<0.1 \times 10^{-3}$ μm^2 to 10×10^{-3} μm^2. In addition, local maximum reached up to 74.7×10^{-3} μm^2, averaging 3.0×10^{-3} μm^2.Relative index of porosity to

permeability is 0.48 (Figure 11). Capillary pressure curve exhibits a platform-shaped segment that is slightly concave to the left (Figure 12), median radius of throat is 0.22 μm, sorting coefficient is 2.13, indicating a relatively poor sorting, skewness coefficient is 0.16, implying unimodal skewness with small slanting degree, and pore-throat structure is the combination of moderate pore and small throat. The reservoir type is therefore classified as fractured to porous type with moderate porosity and moderate to low permeability.

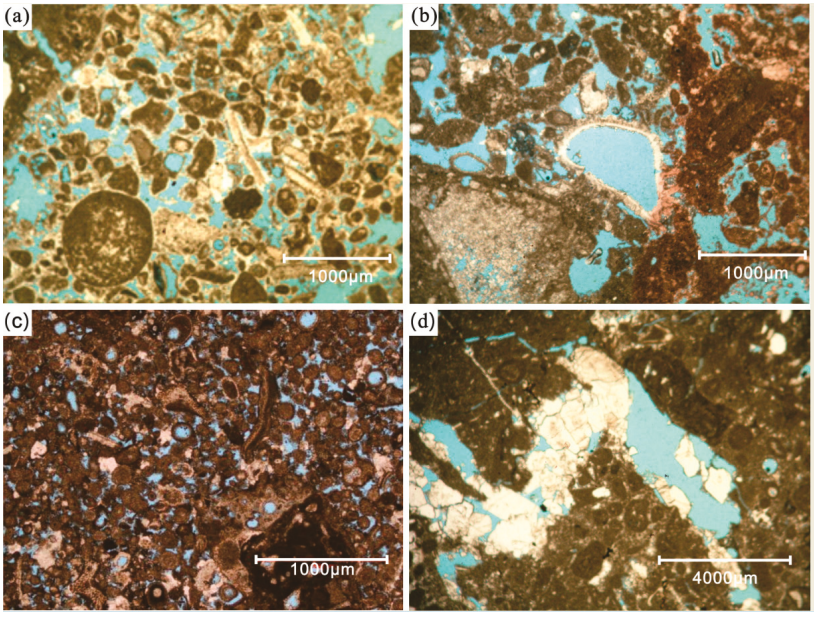

Figure 10. Types of reservoir space in the fore ramp of Callovian-Oxfordian Stage. (**a**) Intraclastic bioclastic grainstone, with residual primary intergranular pores, intergranular dissolved pores, intragranular dissolved pores and mold pores, XVa1, 3158.61 m, Well Pir-21, front ramp bioclastic shoal, casting thin section (-); (**b**) Intraclastic bioclastic grainstone, with intergranular dissolved pores, intragranular dissolved pores and molded pores, XVa1, 3158.6 m, Well Pir-21, front ramp bioclastic shoal, casting thin section (-); (**c**) Ooidal grainstone, with residual primary intergranular pores, intergranular dissolved pores, intragranular pores and mold pores, XVm, 3791.0 m, Well Oja-21, front ramp ooidal shoal, casting thin section (-); (**d**) Lump packstone, with framework dissolved pores and dissolved fractures, XVa1, 3552.17 m, Well Cha-21, front ramp mound, casting thin section (-).

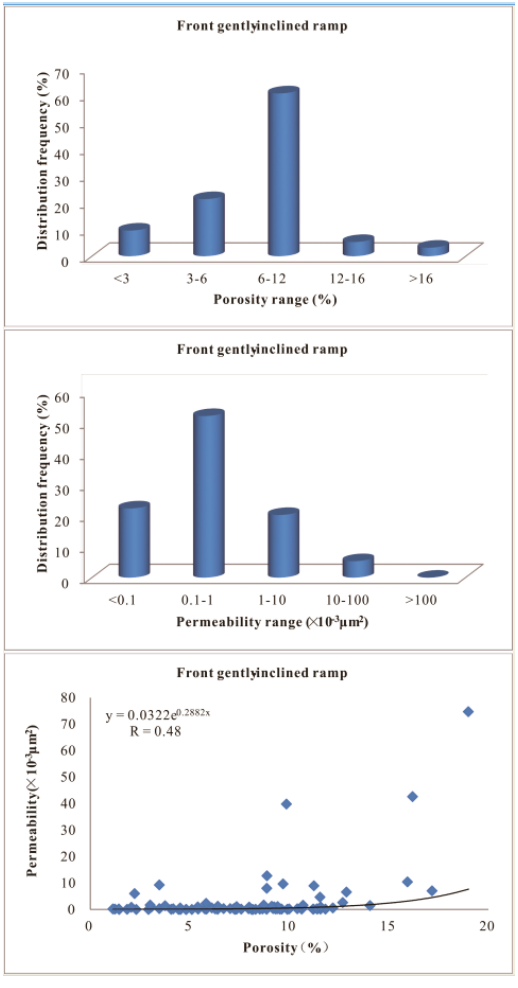

Figure 11. Physical properties of reservoirs and correlation plot between porosity permeability of Callovian-Oxfordian Stage.

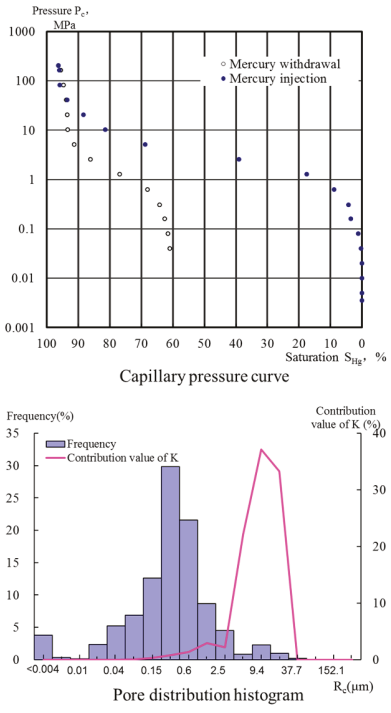

Figure 12. Plot showing capillary pressure curve of Callovian-Oxfordian Stage.

5.2. Dissolution Role is Reservoir Formation

In addition to abundant residual primary intergranular porosity, reef and shoal reservoirs facies in the upper part of the Callovian-Oxfordian front ramp in the Amu Darya Basin contain numerous dissolution-formed secondary pores resulted from dissolution. According to the analysis of thin sections, electron probe, and X-ray diffraction data of interstitial substance, the morphology and filling sequence of minerals can indicate the sequence of dissolution. In addition, the dissolution can be divided into three stages.

5.2.1. Early Diagenesis Dissolution

Early diagenesis dissolution occurred mainly in the near-surface environment and, due to the effect of fresh water, the reservoir space of composite reef-shoal was dominated by intragranular porosity, i.e., dissolved and mold pores formed by selective dissolution. Pores formed by this dissolution are mostly filled at later-stage diagenesis and hence contributed very little to effective reservoir space. However, some residual pores could provide dissolution pathway for late dissolution and hence could accelerate the occurrence of dissolution, thereby laying the basis for the formation of good-quality reservoir space during the later-stage dissolution and superimposed reformation of preexisting pores. The reservoir volumes space formed at this stage consists of predominately residual primary intergranular pores and organic framework pores.

5.2.2. Middle Diagenesis Early-Stage Dissolution

Middle diagenesis dissolution occurred in a relatively closed to semi-closed system. Intensive diagenetic fracturing, dissolution and burial dolomitization began to occur in localized areas at this period, which enabled the formation of new pore, vug and fracture system. The effects of diagenetic

fracturing and burial dolomitization were limited, and the dissolution was predominately non-selective type, forming numerous irregular late pores. Although rendering formation and enlargement of some reservoir space, this dissolution also reduced some reservoir space by filling pores with secondary minerals including calcite (0.3–2 mm) (Figure 13a–c), dolomite (Figure 13d–e), anhydrite (Figure 13f), fluorite (Figure 13g) and celestite (Figure 13h). During this period, reservoir space type was dominated by residual primary intergranular pores and organic framework pores, and reservoir property was improved significantly as a result of superimposition of a large variety of secondary pores.

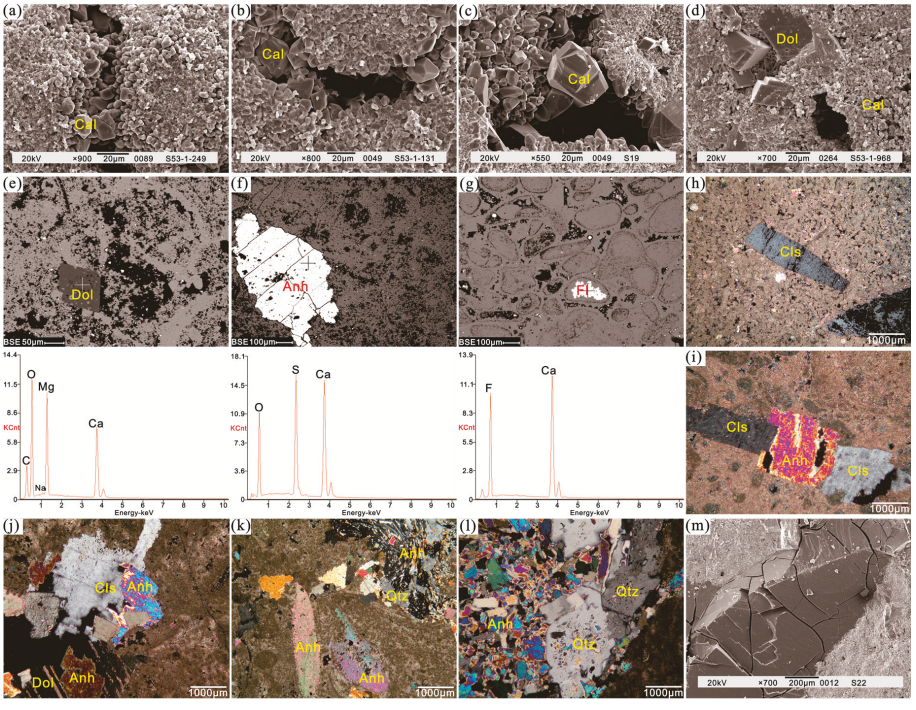

Figure 13. Typical microscopic photographs of mineral types and their syngenetic sequence. (**a**) Intergranular pores filled with calcite crystals, peloid packstone, 2404.23 m, XVp, SEM; (**b**) Intergranular pores partially filled with secondary calcite crystals, bioclastic packstone, 2384.35 m, XVp, SEM; (**c**) Primary skeletal pores partially filled with secondary calcite crystals, and the horse—tooth—shaped secondary calcite crystals grew along the pore walls, bioclastic wackestone, 2491.79 m, XVm, SEM; (**d**) Secondary rhombic dolomite shows intact crystal shape, micrite, 2519.92 m, XVhp, SEM; (**e**) Dolomite, Surrounding rocks are bioclastic wackestone, 2492.37 m, XVhp, EPMA; (**f**) Anhydrite, Surrounding rocks are bioclastic grainstone, 2410.08 m, XVp, EPMA; (**g**) Fluorite, Surrounding rocks are bioclastic packstone, 2445.35 m, XVm, EPMA; (**h**) Celestite, peloid packstone, 2399.3 m, XVp, casting thin section (+); (**i**) The syngenetic sequence of minerals is the follows: anhydrite → celestite, peloid packstone, 2399.3 m, XVp, casting thin section (+); (**j**) The syngenetic sequence of minerals is the follows: dolomite → anhydrite → celestite, bioclastic wackestone, 2518.05 m, XVhp, casting thin section (+); (**k**) The syngenetic sequence of minerals is the follows: anhydrite → quartz, bioclastic wackestone, 2518.27 m, XVp, casting thin section (+); (**l**) The syngenetic sequence of minerals is the follows: anhydrite → quartz, bioclastic wackestone, 2518.27 m, XVp, casting thin section (+); (**m**) Fractures filled with bitumen, bioclastic wackestone, 2492.685 m, XVm, SEM.

5.2.3. Middle Diagenesis Late-Stage Dissolution

The strata have been consolidated in this period, and thus, consolidation, pressure dissolution and cementation were weakened greatly and had little influence on the reservoir. However, reformation of reservoirs resulted from dissolution and tectonic disruption was strengthened, which, together with the tectonic disruption and dissolution, diagenetic alteration (e.g., the formation of anhydrite, celestite and silicification (Figure 13i–l), precipitation and filling of secondary minerals, and the continually strengthening of filling of late-stage bitumen (Figure 13m), caused reduction of partial reservoir space. In general, however, physical properties of reservoirs became better at this period, since new structural fractures were formed and preexisting pores, vugs and fractures continued to be dissolved and enlarged, providing effective space for hydrocarbon migration and accumulation. As a result, good to excellent reservoir properties could be formed in a certain scope.

5.3. Case Study of Reef and Shoal in the Upper Ramp

Well Oja-21 is in the central-southern part of the study area (Figure 3), in which SQ2 sequence includes shoal, mound and slope mud of the upper ramp subfacies. The shoal includes the bioclastic shoal, oolitic shoal and intraclastic shoal. Grainstone depositing in relatively high-energy environment contains abundant reservoir space: i.e., primary intergranular pores, intergranular enlarged dissolved pores, intragranular dissolved pores, molded pores and fractures (Figure 10c). Intraclastic shoal has the best reservoir properties: with a porosity range from 5.9% to 16.2%, averaging 10.2%, and the permeability range from 0.37 to 42.6 $\times$ 10^{-3} μm^2, averaging 22.69 $\times$ 10^{-3} μm^2. Bioclastic shoal and oolitic shoal have fairly good physical properties and the reservoirs formed are predominately porous-type (Table 1). Physical property of mound is worse than those shoals: with the porosity ranging from 4.8% to 12.2%, averaging 9.5%, and the permeability ranging from <0.01 to 1.59 $\times$ 10^{-3} μm^2, averaging 0.44 $\times$ 10^{-3} μm^2, and the reservoirs formed are predominately porous- and fractured-type. Inter-shoal and slope mud deposited in low-energy environment commonly have poor physical properties, and the reservoir in this facies with hydrocarbon shows is fractured-type reservoir with few pores.

Table 1. Values of porosity and permeability from different environment of the front gently inclined ramp in Well Oja-21.

Facies Belt		**Front Gently-Inclined Ramp**					
Microfacies		**Oolitic Shoal**	**Intraclastic Shoal**	**Bioclastic Shoal**	**Mound**	**Intershoal**	**Slope Mud**
		(*n* = 8)	**(*n* = 19)**	**(*n* = 14)**	**(*n* = 28)**	**(*n* = 9)**	**(*n* = 13)**
Porosity (%)	Range	5.8–14.1	5.9–16.2	6.4–19.0	4.8–12.2	2.9–10.7	1.5–11.6
	Mean	9.4	10.2	12.2	9.5	6.3	5.9
Permeability ($\times 10^{-3}$ μm^2)	Range	0.07–12.7	0.37–42.6	0.15–74.7	<0.01–1.59	<0.01–0.55	<0.01–0.55
	Mean	4.28	22.69	12.04	0.44	0.16	0.08

6. Conclusions

(1) Based on petrological, paleontological and seismic studies of the Callovian and Oxfordian, in combination with regional geological characteristics and sedimentary setting, an appropriate sedimentary model of "carbonate ramp-rimmed platform" has been proposed and established, and detailed demonstration, description and comparison of concept, evidence and feature of this model with other classic models are presented.

(2) In addition to intra-platform shoals and point reefs in open platform, and reefs and shoals in platform margin, according to the sedimentary model of "carbonate ramp-rimmed platform", the upper slope shoals, point reefs and mound groups in front ramp allow for the formation of reservoirs with good physical properties too. The reservoir space is dominated by primary intergranular pores, organic framework pores and intergranular enlarged dissolved pores, and the reservoirs are fractured and porous type.

(3) Sedimentary microfacies and diagenesis are the main factors controlling the formation of high-quality reservoirs. Upper slope shoals, point reefs and mound of front ramp are deemed to be the material basis for the formation of high-quality reservoirs, while dissolution and fracture mainly occurred at different periods are critical to the formation of high-quality reservoirs.

Supplementary Materials: The following are available online at http://www.mdpi.com/2073-4352/8/2/84/s1, Table S1: Results of porosity and permeability from different microfacies of the front gently-inclined ramp in Amu Darya Basin, Table S2: XRD analytical results of the front gently-inclined ramp in Amu Darya Basin.

Acknowledgments: The support of The National Natural Science Foundation of China (project 41572097), and National Major Science and Technology specific project of China (2016ZX05032-001-003).

Author Contributions: Wenli Xu and Huaguo Wen conceived and designed; Wenli Xu, Rongcai Zheng, Fei Huo, Mingcai Hou and Gang Zhou analyzed the data; Wenli Xu, Huaguo Wen and Fengjie Li contributed materials; Wenli Xu wrote the paper and led research.

Conflicts of Interest: The authors declare no conflict of interest.

References

1. Gu, J.Y.; Ma, F.; Ji, L.D. Types, characteristics and main controlling factors of carbonate platform. *J. Palaeogeogr.* **2007**, *11*, 21–27.
2. Shaw, A.B. *Time in Stratigraphy*; McGraw-Hill: New York, NY, USA, 1964; p. 365.
3. Irwin, M.L. General theory of epeiric clear water sedimentation. *Bull. AAPG* **1965**, *49*, 445–459.
4. Laporte, L.F. Recognition of a transgressive carbonate sequence within an epeiric sea: Helderberg Group (Lower Devonian) of New York State. *AAPG Bull.* **1967**, *14*, 98–119. [CrossRef]
5. Wilson, J.L. *Carbonate Facies in Geologic History*; Springer: New York, NY, USA, 1975; pp. 229–233.
6. Mcllreath, I.A.; James, N.P. Facies models Carbonate slopes. *Geosci. Can.* **1979**, *5*, 184–199.
7. Tucker, M.E. *Sedimentary Petrology: An Introduction*; Blackwell Scientific Publications: Oxford, UK, 1981; pp. 19–27.
8. Tucker, M.E. *Shallow-Marine Carbonate Facies and Facies Models*; Blackwell Scientific Publications: Oxford, UK, 1985; pp. 147–169.
9. Guan, S.C. *The Change of Sea and Land, Sedimentary Facies in Sea Area and Oil & Gas in China*; Science Press: Beijing, China, 1984; pp. 1–104.
10. Read, J.F. Carbonate platform facies models. *AAPG Bull.* **1985**, *69*, 1–21.
11. Santantonio, M. Facies associations and evolution of pelagic carbonate platform/basin systems: Examples from the Italian Jurassic. *Sedimentology* **1993**, *40*, 139–1067. [CrossRef]
12. Bosence, D.; Cross, N.; Hardy, S. Architecture and depositional sequences of Tertiary fault-block carbonate platforms; an analysis from outcrop (Miocene, Gulf of Suez) and computer modeling. *Mar. Pet. Geol.* **1998**, *15*, 203–221. [CrossRef]
13. Bosence, D. A genetic classification of carbonate platforms based on their basinal and tectonic settings in the Cenozoic. *Sediment. Geol.* **2005**, *175*, 49–72. [CrossRef]
14. Basilone, L. Mesozoic tectono-sedimentary evolution of Rocca Busambra in western Sicily. *Facies* **2009**, *55*, 115–135. [CrossRef]
15. Basilone, L.; Morticelli, G.M.; Lena, G. Mesozoic tectonics and volcanism from Tethyan rifted continental margins in western Sicily. *Sediment. Geol.* **2010**, *226*, 54–70. [CrossRef]
16. Basilone, L.; Sulli, A. A facies distribution model controlled by a tectonically inherited sea bottom topography in the carbonate rimmed shelf of the Upper Tithonian-Valanginian Southern Tethyan continental margin (NW Sicily, Italy). *Sediment. Geol.* **2016**, *342*, 91–105. [CrossRef]
17. Basilone, L.; Sulli, A.; Gasparo Morticelli, M. Integrating facies and structural analyses with subsidence history in a Jurassic-Cretaceous intraplatform basin: Outcome for paleogeography of the Panormide Southern Tethyan margin (NW Sicily, Italy). *Sediment. Geol.* **2016**, *339*, 258–272. [CrossRef]
18. Basilone, L.; Perri, F.; Sulli, A.; Critelli, S. Paleoclimate and extensional tectonics of short-lived lacustrine environments. Lower Cretaceous of the Panormide Southern Tethyan carbonate platform (NW Sicily). *Mar. Pet. Geol.* **2017**, *88*, 428–439. [CrossRef]

19. Chen, J.S.; Wang, Z.Y.; Dai, Z.Y. Study of the Middle and Upper Ordovician rimmed barbonate platform system in the Tazhong area, Tarim basin. *J. Palaeogeogr.* **1999**, *1*, 8–17.
20. Chen, M.; Xu, X.S.; Wan, F. Study on outcrop sequence stratigraphy of the Lower-Middle Ordovician strata in Keping, Tarim basin. *Acta Sedimentol. Sin.* **2004**, *22*, 110–116.
21. Guo, Y.Q.; Liu, L.F.; Zhu, S.L. Classification and assessment of petroleum system in Amu-Daria Basin. *Pet. Explor. Dev.* **2006**, *33*, 515–520.
22. An, Z.X.; Hu, Z.Q. *Oil and Gas Area of Mid-Aisa*; Petroleum Industry Press: Beijing, China, 1993; pp. 41–216.
23. Che, Z.C.; Luo, J.H.; Liu, L. The Basic Structure Classification and Genetic Analyses of Oil and Gas-bearing Basins in Central Asia and Northwestern China. *Acta Geosci. Sin.* **1997**, *18*, 113–121.
24. Jia, C.Z.; Yang, S.F.; Chen, H.L. *Structural Geology and Natural Gas in the Northern Magin Basin Group*; Petroleum Industry Press: Beijing, China, 2001; pp. 136–143.
25. Qiu, D.Z.; Xie, Y.; Li, X.Q. Geological Characteristics of Lithofacies Paleogeography and Hydrocarbon Accumulation in Asian Tethyan Tectonic Domain. *Mar. Pet. Geol.* **2009**, *14*, 41–50.
26. Xu, W.S.; Liu, X.L.; Yu, Z.Q. Geological Structure of Amu-Darya Basin in Central Asia. *Nat. Gas Geosci.* **2009**, *20*, 744–748.
27. Zhang, X.Y. *Optimization of Exploration Targets and Study on Hydrocarbon Accumulation Rules for CNPC Cooperative Blocks of the Amu Darya Basin*; Petroleum Exploration and Development Research Institute: Beijing, China, 2012.
28. Nie, M.L.; Wu, L.; Xu, S.B. Genetic mechanism and exploration significance of tectonic action in the Bieshikent Depression and its adjacent area in the Amu-Darya Basin. *Nat. Gas Ind.* **2013**, *33*, 45–50.
29. Ulmishek, G.F. *Petroleum Geology and Resources of the Amu-Darya Basin, Turkmenistan, Uzbekistan, Afghanistan and Iran*; U.S. Geological Survey Bulletin 2201–H, 2004; pp. 1–38.
30. Zhang, Z.W.; He, Y.Y.; Wang, C.S. Structural Characteristics and Evolution of Chardzhou and Bukhara Terraces in Amu-Darya Basin, Middle Asia. *Mar. Pet. Geol.* **2010**, *15*, 48–56.
31. Meisel, T.; Krahenbuhl, U.; Michael, A.N. Combined osmium and strontium isotopic study of the Cretaceous-Tertiary boundary at Sumbar, Turkmenistan: Atest for an impact vs. a volcanic hypothesis. *Geology* **1995**, *5*, 313–316. [CrossRef]
32. Qi, B.Q.; Ran, Z.B.; Wang, X.Q. Identification of limestone reservoirs and prediction of their fluid properties in the Amu Darya Right Bank Block, Turkmenistan. *Nat. Gas Ind.* **2011**, *30*, 21–25.
33. Zhang, B.; Zheng, R.C.; Liu, H.N. Characteristics of Carbonate Reservoir in Callovian-Oxfordian of Samandepe Gasfield, Turkmenistan. *Acta Geol. Sin.* **2010**, *84*, 117–125. [CrossRef]
34. Dong, X.; Zheng, R.C.; Wu, L. Diagenesis and porosity evolution of carbonate reservoirs in Samandepe Gas Field, Turkmenistan. *Lithol. Reserv.* **2010**, *22*, 54–61.
35. Li, H.W.; Tong, X.G.; Wang, S.H. An analysis of geological characteristics and exploration potential of the Jurassic play, Amu Darya Basin. *Nat. Gas Ind.* **2011**, *30*, 6–12.
36. Zheng, R.C.; Zhao, C.; Liu, H.N. Cathodoluminescence and its significance of the Callovian-Oxfordian carbonate rocks in Amu Darya basin, Turkmenistan. *J. Chengdu Univ. Technol. (Sci. Technol. Ed.)* **2010**, *37*, 377–385.
37. Xu, W.L.; Zheng, R.C.; Fei, H.Y. The sedimentary facies of Callovian-Oxfordian Stage in Amu Darya basin, Turkmenistan. *Geol. China* **2012**, *39*, 954–964.
38. Wang, Q.; Yan, X.; Xu, W.L. Sequence-Paleogeographic Characteristics and Evolution of Callovian- Oxfordian in Amu Darya Basin, Turkmenistan. *Geol. Explor.* **2014**, *50*, 795–804.
39. Dickson, J.A.D. Carbonate identification and genesis as revealed by staining. *J. Sediment. Petrol.* **1966**, *36*, 441–505.
40. Dunham, R.H. *Classification of Carbonate Rocks, According to Depositional Texture*; Ham, W.E., Ed.; Classification of Carbonate Rocks; AAPG Memoir: Tulsa, OK, USA, 1962; pp. 108–121.
41. Carozzi, A.V. *Sedimentary Petrology*; Prentice Hall: Englewood Cliffs, NJ, USA, 1993; p. 263.
42. Tucker, M.E.; Wright, V.P. *Carbonate Sedimentology*; Blackwell: Oxford, UK, 1990; p. 482.
43. Flügel, E. *Microfacies of Carbonate Rocks: Analysis, Interpretation and Application*, 2nd ed.; Springer: Berlin, Germany, 2010; p. 984.
44. Vail, P.R.; Mitchum, R.M., Jr.; Thompson, S., III. *Seismic Stratigraphy and Global Changes of Sea Level, Part 4: Global Cycles of Relative Changes of Sea Level*; Payton, C.E., Ed.; Seismic Stratigraphy-Applications to Hydrocarbon Exploration; AAPG Memoir: Tulsa, OK, USA, 1977; pp. 83–98.

45. Vail, P.R.; Mitchum, R.M., Jr. *Seismic Stratigraphy and Global Changes of Sea Level, Part 3: Relative Changes of Sea Level from Coastal Onlap*; Clayton, C.E., Ed.; Seismic Stratigraphy-Applications to Hydrocarbon Exploration; AAPG Memoir: Tulsa, OK, USA, 1977; pp. 63–81.
46. Haq, B.U.; Hardenbol, J.; Vail, P.R. *Mesozoic and Cenozoic Chronostratigraphy and Cycles of Sea-Level Change*; Wilgus, C.K., Hastings, B.S., Kendall, C.G., Posamentier, H.W., Ross, C.A., Van Wagoner, J.C., Eds.; Sea-Level Changes—An Integrated Approach; SEPM Special Publications: Tulsa, OK, USA, 1988; Volume 42, pp. 71–108.
47. Zheng, R.C.; Liu, H.N.; Wu, L. Geochemical characteristics and diagenetic fluid of the Callovian-Oxfordian carbonate reservoirs in Amu Darya basin. *Acta Petrol. Sin.* **2012**, *28*, 961–970.
48. Wen, H.G.; Gong, B.S.; Zheng, R.C. Deposition and diagentic system of carbonate in Callovian-Oxfordian of Samandepe Gasfield, Turkmenistan. *J. Jilin Univ. (Earth Sci. Ed.)* **2010**, *42*, 991–1002.
49. Xu, W.L. Sedimentary mode of glacis carbonate platform-taking Callovian-Oxfordian of Upper-Middle Jurassic in Amu-Darya basin of Turkmenistan as an example. Ph.D. Dissertation, Chengdu University of Technology, Chengdu, China, 2013; pp. 20–46.
50. Cao, J.; Xu, M.; He, Z.H. An analysis of pore fluid sensitivity parameters in reef limestone reservoirs: An example from Callovian-Oxfordian carbonate reef reservoirs in the Amu Darya Right Bank Block, Turkmenistan. *Nat. Gas Ind.* **2010**, *30*, 37–40.
51. Lu, B.X.; Zheng, R.C.; Chen, S.C. Characteristics of carbonate reservoir in Oxfordian of Odjarly Gasfield, Amu Darya Basin. *J. Guilin Univ. Technol.* **2011**, *31*, 504–510.
52. Liu, S.L.; Zheng, R.C.; Yan, W.Q. Characteristics of Oxfordian carbonate reservoir in Agayry area, Amu Darya Basin. *Lithol. Reserv.* **2012**, *24*, 57–63.
53. Zheng, R.C.; Chen, H.R.; Wang, Q. The reservoir characteristics and their controlling factors of Callovian-Oxfordian carbonates in Amu Darya Basin. *Acta Petrol. Sin.* **2014**, *30*, 779–788.
54. Xu, W.L.; Zheng, R.C.; Fei, H.Y. Characteristics and timing of fractures in the Callovian-Oxfordian boundary of the right bank of the Amu Darya River, Turkmenistan. *Nat. Gas Ind.* **2012**, *32*, 33–38.
55. Zonenshayn, L.P.; Kuzmin, M.I.; Natapov, L.M. *Tectonics of Lithospheric Plates of the USSR (Tektonika Litosfernykh Plit Territorii SSSR), Volumes I and II*; Nedra: Moscow, Russia, 1990; pp. 328–336.
56. Sheikholeslami, M.; Kouhpeym, M. Structurale analysis and tectonic evolution of the eastern Binalud Mountains, NE Iran. *J. Geodyn.* **2012**, *61*, 23–46. [CrossRef]
57. Sengor, A.M.C. *A New Model for the Late PalaeozoiceMesozoic Tectonic Evolution of Iran and Implications for Oman*; Geological Society of London, Special Publications: London, UK, 1990; Volume 49, pp. 797–831.
58. Muttoni, G.; Mattei, M.; Balini, M.; Zanchi, A.; Gaetani, A.; Berra, F. The drift history of Iran from the Ordovician to the Triassic. In *South Caspian to Central Iran Basins*; Geological Society of London, Special Publication: London, UK, 2009; Volume 312, pp. 7–29.
59. Maksimov, S.P. *Sedimentary Cover of Central Asia and South Kazakhstan (Osadochnyi Chekhol Sredney Azii i Yuzhnogo Kazakhstana)*; Nedra: Moscow, Russia, 1992; p. 148.
60. Lyberis, N.; Manby, G. Oblique to orthogonal convergence across the Turan Block in the post-Miocene. *AAPG Bull.* **1999**, *83*, 1135–1160.
61. Thomas, J.; Cobbold, P.; Shein, V.; Douaran, S.L. Sedimentary record of Late Palaeozoic to recent tectonism in Central Asiaeanalysis of subsurface data from the Turan and South Kazakh domains. *Tectonophysics* **1999**, *313*, 243–263. [CrossRef]
62. Brookfield, M.E.; Hashmat, A. The geology and petroleum potential of the North Afghan platform and adjacent areas (northern Afghanistan, with parts of southern Turkmenistan, Uzbekistan, and Tajikistan). *Earth Sci. Rev.* **2001**, *55*, 41–71. [CrossRef]
63. Khain, V.E.; Sokolov, B.A.; Kleshchev, K.A.; Shein, V.S. Tectonic and geodynamic setting of oil and gas basins of the Soviet Union. *Am. Assoc. Petrol. Geol. Bull.* **1991**, *75*, 313–325.
64. Kavoosi, M.; Lasemi, Y.; Sherkati, S.; Moussavi-Harami, R. Facies analysis and depositional sequences of the Upper Jurassic Mozduran Formation, a reservoir in the Kopet Dagh Basin, NE iran. *J. Pet. Geol.* **2009**, *32*, 235–260. [CrossRef]
65. Taheri, J.; Fürsich, F.; Wilmsen, M. Stratigraphy, depositional environments and geodynamic significance of the Upper Bajocian Bathonian Kashafrud Formation, NE Iran. In *South Caspian to Central Iran Basins*; Geological Society of London, Special Publication: London, UK, 2009; pp. 205–218.
66. Ball, M.M. Carbonate sand bodies of Florida and the Bahamas. *J. Sediment. Petrol.* **1967**, *37*, 556–591.

67. Hine, A.C.; Wilber, R.J.; Bane, J.M.; Neumann, A.C.; Lorenson, K.R. Offbank transport of carbonate sands along open, leewardmargins; Northern Bahamas. *Mar. Geol.* **1981**, *42*, 327–348. [CrossRef]
68. Harris, P.M.; Purkis, S.; Ellis, J.; Swart, P.K.; Reijmer, J.J.G. Mapping bathymetry and depositional facies on great Bahama Bank. *Sedimentology* **2015**, *62*, 566–589. [CrossRef]

© 2018 by the authors. Licensee MDPI, Basel, Switzerland. This article is an open access article distributed under the terms and conditions of the Creative Commons Attribution (CC BY) license (http://creativecommons.org/licenses/by/4.0/).

crystals

MDPI

Article

Comparative Study on the Sand Bioconsolidation through Calcium Carbonate Precipitation by *Sporosarcina pasteurii* and *Bacillus subtilis*

Chun-Mei Hsu [1], Yi-Hsun Huang [2], Vanita Roshan Nimje [3], Wen-Chien Lee [1], How-Ji Chen [2], Yi-Hao Kuo [2], Chung-Ho Huang [4], Chien-Cheng Chen [5] and Chien-Yen Chen [6,7,*]

1 Department of Chemical Engineering, National Chung Cheng University, Chiayi 62102, Taiwan; gupi_girl@livemail.tw (C.-M.H.); chmwcl@ccu.edu.tw (W.-C.L.)
2 Department of Civil Engineering, National Chung-Hsing University, Taichung 40227, Taiwan; x699237014x@gmail.com (Y.-H.H.); hojichen@nchu.edu.tw (H.-J.C.); yhkao31@gmail.com (Y.-H.K.)
3 Department of Biomedical Sciences, National Chung Cheng University, Chiayi 62102, Taiwan; vanita.nimje@gmail.com
4 Department of Civil Engineering, National Taipei University of Technology, Taipei 10655, Taiwan; cdewsx.hch@gmail.com
5 Department of Biotechnology, National Kaohsiung Normal University, Kaohsiung 82444, Taiwan; cheng@nknu.edu.tw
6 Department of Earth and Environmental Sciences, National Chung Cheng University, Chiayi 62102, Taiwan
7 Center for Innovative Research on Aging Society, National Chung Cheng University, Chiayi 62102, Taiwan
* Correspondence: chien-yen.chen@oriel.oxon.org or yen@eq.ccu.edu.tw; Tel.: +886-5-2720411 (ext. 66503)

Received: 11 November 2017; Accepted: 21 April 2018; Published: 27 April 2018

Abstract: To investigate potential implications of microbial activity on sand bioconsolidation and subsurface environments, two ureolytic strains, *Sporosarcina pasteurii* and *Bacillus subtilis* were tested for the production of calcium carbonate ($CaCO_3$). Laboratory experiments with monoculture *S. pasteurii* (column 1) and coculture *S. pasteurii-B. subtilis* (column 2) were conducted to determine urea and calcium chloride reactivity and volumetric carbonate formation. Both columns were able to consolidate sand, whereas, column 1 induced greater $CaCO_3$ precipitation. X-ray diffraction (XRD) and scanning electron microscopy (SEM) showed two columns with different mineralogy with calcite, and vaterite formation. Column 1 showed rhombohedral and trigonal crystals morphology, whereas column 2 developed the prismatic calcite and the spherulite vaterite crystals might be due to the differences of the micro-environment caused by the urease expression of these bacterial species. These results indicate the possibility of using those crystals to cement loose sand whereas, highlighted the importance of combining these techniques to understand the geomicrobiology found in the subsurface environments.

Keywords: MICP; *Sporosarcina pasteurii*; *Bacillus subtilis*; bacterial extracellular secretion; urease

1. Introduction

Calcium carbonate ($CaCO_3$) biogenic precipitation is considered as an important process in nature with respect to its role in early diagenesis of marine sediments, hydrochemical evolution of karst streams, application of Geological and Civil Engineering and environmental treatments [1]. From a geotechnical point of view, the potential of microbial carbonate precipitation (MCP) has been identified as a means of adapting soil properties to suit desired land-uses [2]. The reaction is widely distributed in soil, freshwater, marine and subsurface environments. MCP can occur via a variety of processes whereby microbial activities results in the generation of carbonate in a calcium rich environment. The urea hydrolysis by the enzyme urease of microorganisms in a calcium-rich environment is the

most commonly MCP studied. The CO_3^{2-} and NH_4^+ from the hydrolysis of urea increase of the pH and carbonates concentration, which lead to the precipitation of calcium carbonate.

$$CO(NH_2)_2 + 2H_2O \rightarrow 2NH_4^+ + CO_3^{2-} \quad ()$$

$$Ca^{2+} + CO_3^{2-} \rightarrow CaCO_3 \quad ()$$

Through MCP, microbes play an important role in promoting calcite precipitation. Some mechanisms studied by researchers that can induce $CaCO_3$ deposition are: (1) the depositing particles are captured or adhered to by microbial mat or biofilm; (2) extracellular polymeric substances (EPS) can absorb Ca^{2+} so that carbonate microcrystals form on the surface of the biofilm and result in $CaCO_3$ formation; (3) in the environment with higher content of dissolved inorganic carbon (DIC), EPS degradation will release the Ca^{2+} ions that are chelated inside it, so that the supersaturation degree of Ca^{2+} in the environment will be continuously enhanced, resulting in promoting the precipitation of $CaCO_3$; (4) Some bacteria can induce precipitation of $CaCO_3$ extracellularly through such processes as photosynthesis, ammonification, denitrification, sulfate reduction and anaerobic sulfide oxidation; (5) degradation of urea by urea-decomposing bacteria increases pH and alkalinity of the environment, leading to $CaCO_3$ precipitation [3–9]. Mechanisms 1, 2 and 3 are defined as passive forms of precipitation in the presence of organic matter and mechanisms 4 and 5 involve indirect modifications of chemical conditions [4,6]

Considerable research on MCP has been performed using ureolytic bacteria, which influence the precipitation of $CaCO_3$, by the production of the enzyme urease. Urease catalyzes the hydrolysis of urea to CO_2 and ammonia. The resulting $CaCO_3$ precipitation is governed by (1) calcium concentration; (2) carbonate concentration; (3) pH and (4) the use of nucleation sites [10]. The fact that hydrolysis of urea is a straightforward common microbial process and that a wide variety of microorganisms produce the urease enzyme makes it ideally suited for biotechnological applications. Urease activity is widespread among bacteria and this has been the approach most often applied for MCP for the production of calcite [11,12]. Urease-producing bacteria can be grouped into two categories according to their urease response to ammonium; those whose urease activity is not repressed (*S. pasteurii*, *Helicobacter pyroli*) and those whose urease activity is repressed (*Psuedomonas aeruginosa*, *Klensiella aerogenes*) [13,14]. Because high concentrations of urea are hydrolyzed during biocementation, only those microorganisms whose urease activity is not repressed by ammonium are useful. As well as meeting the needs for biocementation, the organism must also meet the needs for safe environmental application. In order to maintain the microbial ecological system in the environment, it will be suitable to apply and release those strains with non-pathogenic, non-genetically modified and non-transferable elements.

S. pasteurii has been widely used as a model organism for the MCP process because this strain is non-pathogenic with significantly high level of urease activity [15]. Calcium carbonate precipitation, a widespread phenomenon among bacteria, has been investigated due to its wide range of scientific and technological implications. Calcite formation by *B. subtilis* (which is a model laboratory bacterium that can produce calcite precipitates on suitable media supplemented with a calcium source) has also been studied [16]. It is also well known that *B. subtilis* was used to produce the varieties of exopolymeric substances, for example, biosurfactants of surfactin. At present, some studies have been done on the role of *B. subtilis* in calcite precipitation. However, there are no adequate studies on the role of calcite precipitation by *B. subtilis* in coculture environments for sand bioconsolidation. We selected *B. subtilis* to study the influence of growth and metabolism of *S. pasteurii* for biocementation processes. In order to clarify the contribution and influence of *B. subtilis*, the monoculture *S. pasteurii* and the coculture *S. pasteurii*-*B. subtilis* were studied in two different experimental systems. A main part of this research focuses on studying coculture environment for sand bioconsolidation through carbonate precipitation and geomicrobiology in the subsurface environment.

2. Results and Discussion

The effect of two types of microbial systems were evaluated to study the distribution of their activity and calcium carbonate precipitation in sand column through a number of steps elaborated in Table 1.

Table 1. Overview of the column injections for determining microbial carbonate precipitation under monoculture experiment and coculture experiment.

Phase		Description	Duration (h)	Effluent Flow Rate (L/h)	Details
Rinse		Water flush	24	0.2	Tap water
Immobilization of bacteria by two-phase injection	Bacterial injection	1. *S. pasteurii*	24	0.2	OD_{600}: 4.1; Act: 2.13 mS/cm/min
		2. *S. pasteurii* + *B. subtilis*	24	0.2	OD_{600}: 3.2; Act: 1.67 mS/cm/min
	$CaCl_2$ injection	1. *S. pasteurii*	24	0.2	0.05 M $CaCl_2$
		2. *S. pasteurii* + *B. subtilis*	24	0.2	0.05 M $CaCl_2$
Cementation		Reaction fluid injection	24	No flow for 24 h- after 24 h, with 0.2 L/h flow rate, samples were collected	1.1 M Urea and $CaCl_2$
Rinse		Water flush	24	0.2	Tap water

1 and 2 are the column number with specific bacteria. Optical density (OD) and the enzyme activity of the bacterial suspension were measured immediately before injection. For column 2, *S. pasteurii* and *B. subtilis* cultures were taken as 50 *v*/*v* %. Column 3 is not mentioned in the table. Column 3 is the control experiment consisted of uninoculated culture medium along with experimental samples.

Initially, immobilization of bacteria in the column was achieved by a two-phase injection. In order to fill the column volume, bacteria were injected. When bacteria were visualized in the outlet as seen by turbidity, 300 mL of 50 mM calcium chloride solution was injected into the column to immobilize the bacteria in a moving reaction front in the column. To start the cementation, 1.1 M equimolar urea and calcium chloride was injected. Samples were collected at regular intervals to measure OD, pH, urease activity, calcium ammonium concentration measurement [2].

2.1. Optical Density and Urease Activity

Column 1 and column 2 with monoculture and coculture bacteria were studied to elucidate the distribution of urease activity and optical density over the column length. While flushing 300 mL of bacterial suspension, immediately followed by 300 mL fixation fluid of 50 mM $CaCl_2$ solution, measurement of both optical density and urease activity in the effluent of the sand column showed that a large proportion of the injected bacteria was retained in the column (Figure 1a). Further, after injecting the cementation solution, no noticeable activity or bacteria were observed in the effluent (Figure 1b). The effluent measurements showed that bacteria in the monoculture experiment resulted in more wash-out of cells and activity corresponding to that of coculture. This retainment of more urease activity and optical density in coculture may be attributed to the synergistic relationship between *S. pasteurii* and *B. subtilis*, where, in the environment with nutrient limiting conditions or microbes living in deep subsurface, majority of the populations can thrive without any input from the earth's surface. This might be due to the symbiotic association for their survival where organic compounds or metabolites produced by one bacterial species may be utilized by the other to adapt to the harsh environment.

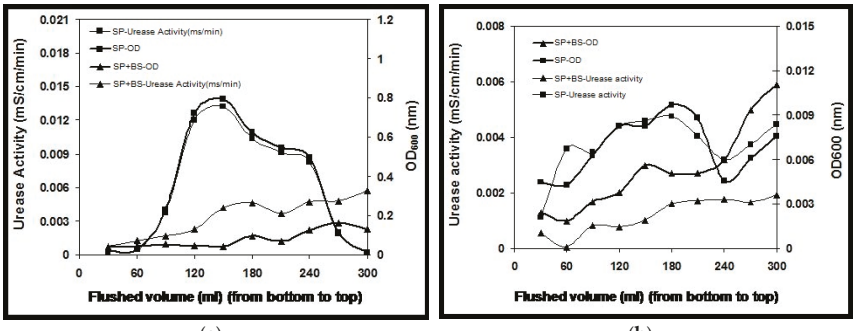

(**a**) (**b**)

Figure 1. (**a**): Effluent measurements for two columns, i.e., monoculture *S. pasteurii* and coculture *S. pasteurii* and *B. subtilis* after flushing 0.05 M $CaCl_2$; (**b**): Effluent measurements for two columns, i.e., monoculture *S. pasteurii* and coculture *S. pasteurii* and *B. subtilis* after flushing cementation solution of 1.1 M Urea and $CaCl_2$.

2.2. Solution Chemistry

The experiments conducted with monoculture and coculture ureolytic bacterial species were monitored for the measurements of pH and NH_4^+ after the column flush. Monoculture *S. pasteurii* and coculture *S. pasteurii-B. subtilis* show almost similar trend in pH over time. During the first batch flush of cementation fluid, the higher pH for column 1 (around 8.6 $\pm$ 1) and only a small pH increase (around 8.3 $\pm$ 1) in coculture experiments for column 2 were observed. Results obtained for the second and third batch flush also correspond to first batch flush with a slight increase of one-two unit pH, which indicates that *S. pasteurii* alone have a strong ureolytic capability to break down the urea while releasing NH_4^+ ions and increasing the solution pH. Similarly, an increase in solution pH for the coculture experiment also shows the strong urease activity in column 2. The control experiment evidenced no change in pH without any bacterial species.

The change in NH_4^+ concentration over time caused by urea hydrolysis for *S. pasteurii* is shown in Figure 2. These values of urea hydrolysis are calculated from measured ammonium concentrations using the stoichiometric equation by Whiffin et al. [2]. One mole of urea is assumed to hydrolyze into two moles of ammonium, and therefore, the amount of urea hydrolyzed at any given time is assumed to be equal to half the amount of ammonia produced. During the first batch flush of cementation, i.e., after 24 h, the maximum NH_4^+ ions produced by *S. pasteurii* in monoculture experiment was 398 mM which further increased to 1160 mM during the second batch flush after 48 h and 1921 mM during the third batch flush after 72 h respectively (Figure 2a). However, the NH_4^+ concentration increased linearly with flushed volume for the entire three-batch flush. To determine the urea hydrolysis under the influence of *B. subtilis* in column 2, a detailed analysis of NH_4^+ ion production was performed. Figure 2b presents the corresponding NH_4^+ concentration values determined during a period of 24, 48 and 72 h. The NH_4^+ concentration does not increase above 157 mM until 24 h during the first batch flush. During the second batch flush with this experiment, NH_4^+ concentration was found to increase to 953 mM, still lower than column 1, whereas, the third batch flush was shown to convert the urea to almost equimolar proportion with a further increase up to 1929 mM. This conclusively shows that urea hydrolysis is occurring for this system and that mono as well as coculture systems can convert the total urea with almost the same rate at the end of the experiment of around 72 h. The NH_4^+ profiles shown in Figure 2a demonstrate that bacterial growth was at its peak in the center of the column where the highest NH_4^+ concentration was measured. In contrast to this, column 2 where no significant bacterial wash out was observed, showed higher NH_4^+ concentrations at the top of the column and was lowest at the bottom.

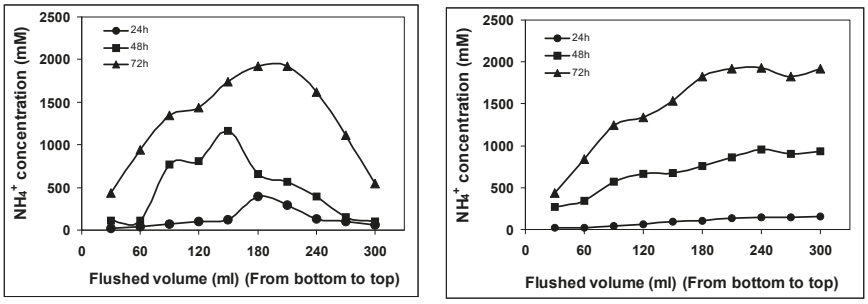

Figure 2. (**a**) Ammonium concentration measurements in the effluent for monoculture *S. pasteurii*, which was flushed out after 24 h, 48 h and 72 h respectively; (**b**) Ammonium concentration measurements in the effluent for coculture of *S. pasteurii* and *B. subtilis*, which was flushed out after 24 h, 48 h and 72 h, respectively.

The trend seen in the calcium precipitation rates mimicked those of NH_4^+ production, i.e., the monoculture of *S. pasteurii* exhibited a faster precipitation rate than coculture over first and second batch flush. Whereas, after a period of 72 h, soluble calcium was detected in the column 1 and column 2 were almost the same which shows that monoculture *S. pasteurii* and coculture *S. pasteurii-B. subtilis* have almost the same ureolytic activity to precipitate $CaCO_3$. The dissolved calcium concentrations over time for monoculture and biculture experiments are shown in Figure 3a,b. Whereas, residual calcium concentrations in the control experiments were higher and remain unreacted corresponding to that of other two systems. This decrease in calcium ion concentration for both the monoculture and biculture experiments could be due to passive precipitation of calcite, with *S. pasteurii* cells acting as nucleation points, or due to sorption of calcium to the cells. Simultaneously, it can be seen from the data that the rate of calcite precipitation was directly proportional to the rate of urea hydrolysis or NH_4^+ production. This results contrasts with that of Stocks-Fischer et al. [17] who stated that calcite precipitation was directly linked to cell growth and indirectly linked to ammonia production. We assume that the results obtained in their study relates to pH where Stocks-Fischer et al. started their experiments at a pH of 8 which is related to the supersaturation degree of the solution for calcite; whereas in the present study, experiments were initiated at a pH of 7.

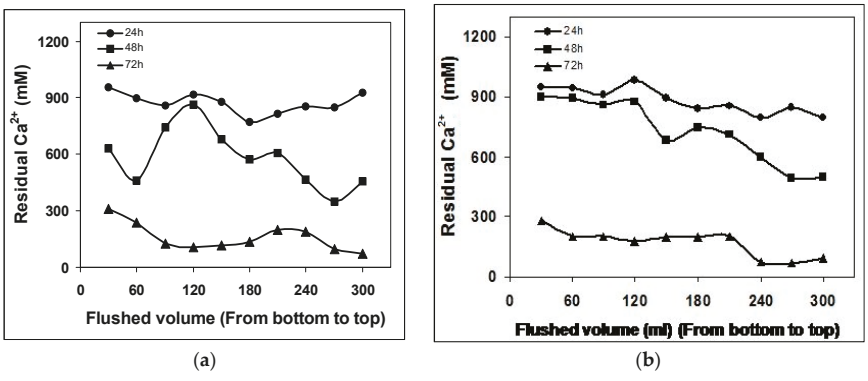

Figure 3. (**a**) Calcium concentration in the effluent for monoculture *S. pasteurii*, which was flushed out after 24 h, 48 h and 72 h respectively; (**b**) Calcium concentration in the effluent for coculture of *S. pasteurii* and *B. subtilis*, which was flushed out after 24 h, 48 h and 72 h, respectively.

2.3. $CaCO_3$ Profile along the Column

After completion of the experiment, all the three columns were flushed for 24 h with tap water and allowed to dry. Samples along the column length were scraped for evaluation of the $CaCO_3$ content. An average $CaCO_3$ content was determined from at least three samples from each column section and results were correlated with the NH_4^+ production of each of the tested samples. For both the columns with monoculture of *S. pasteurii* and coculture *S. pasteurii-B. subtilis* were almost shown to exhibit the same $CaCO_3$ precipitation at the bottom of the column as shown in Figure 4. Whereas the highest strength of $CaCO_3$ formation measured were significantly highest in the middle of the column for monoculture and for biculture highest strength was obtained at the top of the column where maximum $CaCO_3$ precipitation occurred. Hence, by correlating both of these columns for $CaCO_3$ and NH_4^+ concentration, it can be seen that the highest $CaCO_3$ precipitation was measured approximately at the same location where maximum NH_4^+ production was observed with a $CaCO_3$ content of 1.5 kg/m^3 and 1.29 kg/m^3 for monoculture column 1 and coculture column 2, respectively.

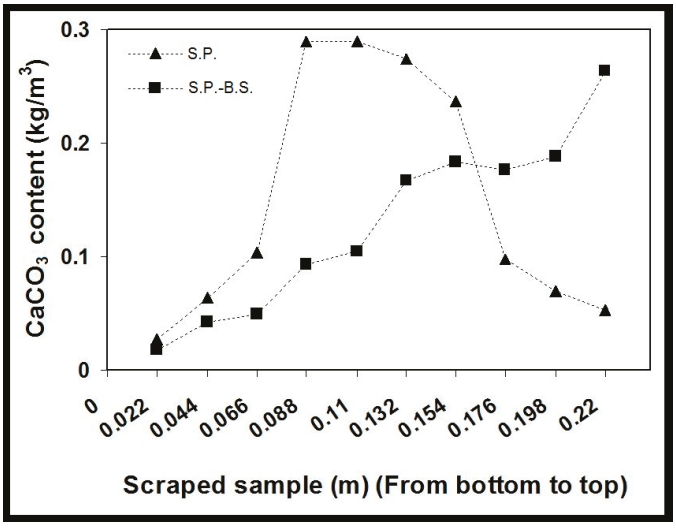

Figure 4. Calcium carbonate profiles along the column length from bottom to top.

2.4. Comparison of XRD Patterns among Monoculture and Biculture Experiments

Figure 5 indicates the results of XRD analyses of $CaCO_3$ precipitation in the sand columns. Sands were carefully removed from $CaCO_3$ precipitates with tweezers before XRD measurements. However, the peaks with strong intensity of 26.62° at the 2θ value that attributed to the Miller indices of (101) of quartz for all the samples were obtained. This is because the Ottawa sand with the size distribution of from 0.1 mm to 1 mm were used. The 2θ values at 20.85°, 26.62° and 40.28° were attributed to the tiny sand quartz particles that remained in $CaCO_3$ precipitates. The XRD peaks located at 2θ values of 29.39°, 36.0°, 39.41°, and 43.10°, which could be assigned to be due to those of calcite, were precipitated by monoculture and coculture bacteria in glass columns. This is coincides with the main characteristic peaks for quartz, and vaterite 26.63 and 26.99, respectively. Those peaks at 2θ of 24.92°, 26.99° and 32.78° might correspond to the vaterite. Aragonite was not detected with XRD and Raman analyses (Supplementary Figures S1 and S2). The Raman active bands at 714 cm^{-1} confirmed the main product of calcite from the MICP process (Supplementary Figure S1). Vaterite is a metastable polymorph of calcium carbonate and is rare in natural environments. It is unstable and rapidly transforms into calcite at room temperature in an aqueous solution [18]. Whereas, bacteria and its secretion (mainly organic

matrix) may facilitate calcium carbonate precipitation. The results showed that both the monoculture *S. pasteurii* and coculture *S. pasteurii-B. subtilis* could induce not only stable calcite crystals but also unstable vaterite crystals. The vaterite crystals have been lasting for more than two years without phase transformation.

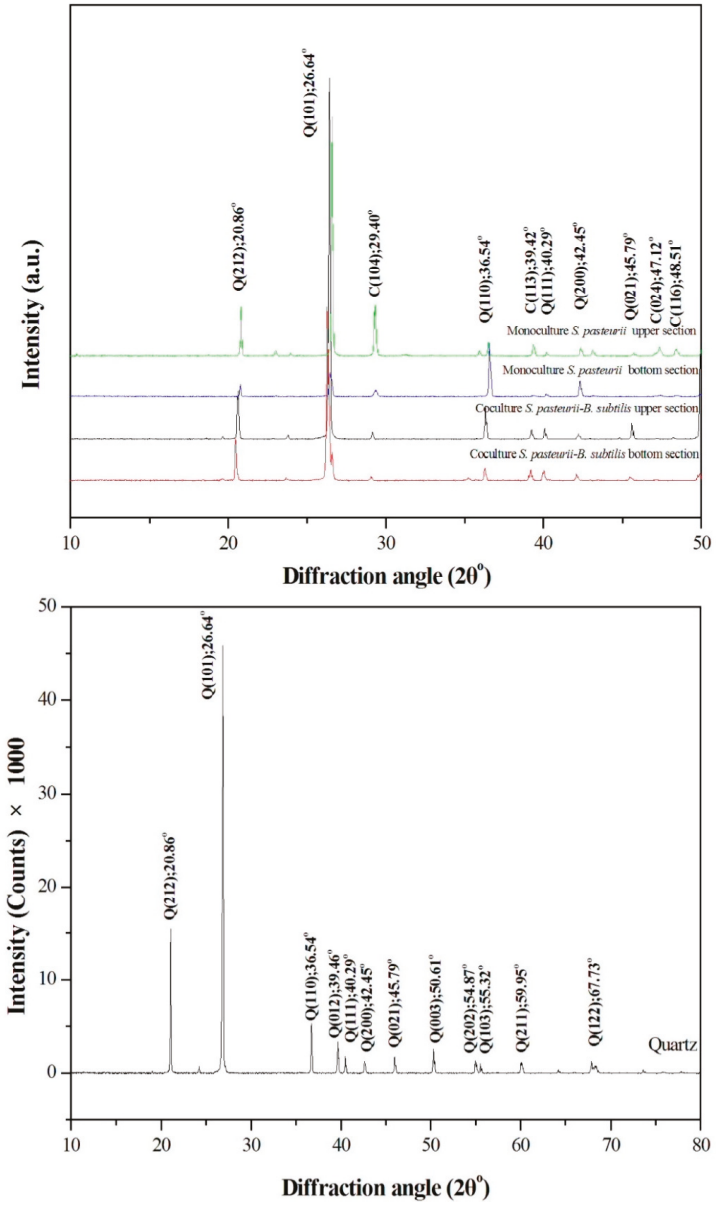

Figure 5. X-ray diffraction of upper and bottom sections for monoculture, coculture. The XRD of quartz only was measured for comparison.

2.5. Comparison of $CaCO_3$ Crystal Morphology Induced by Biological Factors

The $CaCO_3$ crystal morphologies induced by monoculture and biculture experiments are shown in Figure 6. There were obvious differences in the size and morphology of $CaCO_3$ crystals induced in both the experiments as seen in SEM. The column with monoculture *S. pasteurii* exhibited that large amount of $CaCO_3$ particles formed on the top of the column with trigonal prism $CaCO_3$ (about 3 μm) and rod-shaped calcite (25 μm) in Figure 6A, which were accumulated on the sand surface. Furthermore, it was observed that $CaCO_3$ particles were accumulated by compact calcite with irregular flakes of $CaCO_3$ crystals at the bottom of the column (Figure 6A). Those $CaCO_3$ crystals were confirmed by the XRD spectrum in Figure 5. This SEM result evidenced that the action of *S. pasteurii* on specific $CaCO_3$ morphology increased with the increasing depth of the column. However, specific morphology of crystals disappeared at the bottom of the column and irregular compact plate like flakes of $CaCO_3$ appeared probably because the control action of *S. pasteurii* weakened with the gradual bigger and denser crystal size at the top (Figure 6B). Despite the same reaction conditions, coculture bacterial sand columns induced the $CaCO_3$ crystals formation, which were of regular shape; the granular calcite as well as rod-shaped calcite on the top of the column whereas at the bottom of the column compact and lamellar shaped crystals and spherulitic vaterite crystals were induced (Figure 6B). The length/thickness ratio of the rod-shaped crystals in biculture is completely different from monoculture. The main characteristic peaks of calcite can be found from the XRD peaks located at 2θ values of 29.40 in Figure 5. Vaterite was confirmed from the peaks at 2θ of 24.92°, 26.99° and 32.78° (Figure 5). The appearance of vaterite is probably related to the local higher supersaturation of a metastable phase.

The observed carbonate formation under the influence of two bacteria indicates that both the microbes directly participate in crystallization process. In addition, SEM investigation also shows that $CaCO_3$ crystals precipitate in this experimental condition and are approximately of same size of 2–30 μm diameter. However, compared with monoculture, biculture experiments exhibited the three different crystal morphologies, i.e., lamellar, spherulitic and rod. It has been demonstrated that specific biofilm-forming bacteria which could produce exopolysaccharides (EPS) and amino acids play an essential role in the morphology and mineralogy of bacterially induced carbonate precipitation. In a review article, Marvasi et al. [19] described the production of sorptive EPS, poly-γ-glutamate that is anionic, nontoxic and biodegradable viscous polymer produced mainly by wild type *B. subtilis*. In addition, the glutamic acid solution was also shown to induce trigonal prism crystal morphology of $CaCO_3$ precipitate studied by Li et al. [1]. We hypothesize that this is why this crystal morphology was selected in the biculture microbial environment, where the EPS might have been produced by *B. subtilis* which acts as glue to specifically binds Ca^{2+} ions. However, due to its viscous nature, EPS binds more Ca^{2+} ions on the top of the column and it flows slowly down towards the bottom of the column where the $CaCO_3$ precipitation was less. Research conducted by Buczynski and Chafetz [20] showed that EPS plays an important role in the formation of carbonate crystals by providing nucleation sites and by attaching small crystals to each other to increase the size of the bioliths. In accordance with Le Me'tayer-Levrel et al. [21], *B. subtilis* can be applied as biocalcifiers producing carbonates, whereas this activity did not allow the establishment of other bacterial species to function.

Although the present hypothesis that *B. subtilis* EPS/EPS like chemical might release into the environment and influence the $CaCO_3$ formation is from the laboratory experiment, there are wide implications for natural carbonate precipitation, since bacteria are ubiquitous in nature. Thus, this needs to be examined in detail to study the role of *S. pasteurii* and *B. subtilis* monoculture and coculture environment for $CaCO_3$ precipitation and its morphology. Further studies are needed to determine whether the mineralogical biosignatures found in nutrient-rich media can also be found in the subsurface environments.

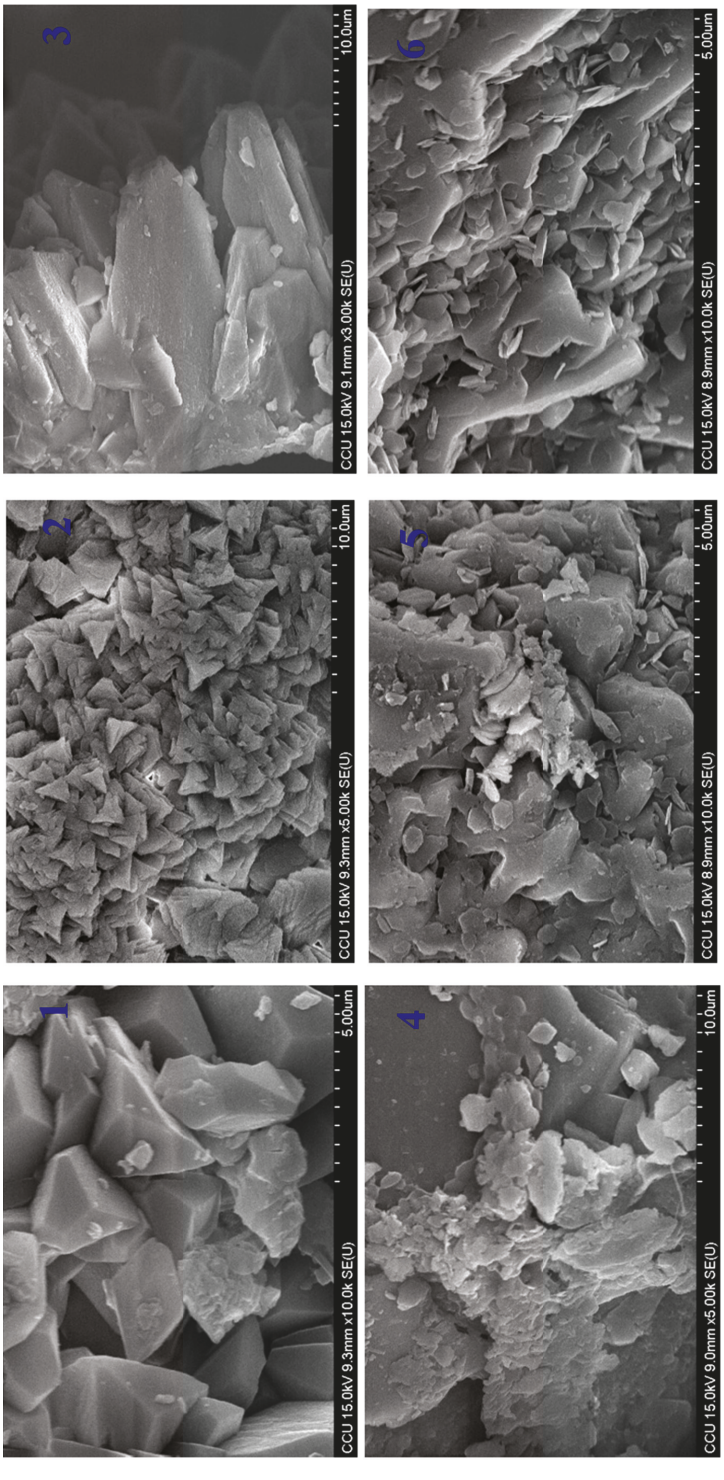

(A)

Figure 6. *Cont.*

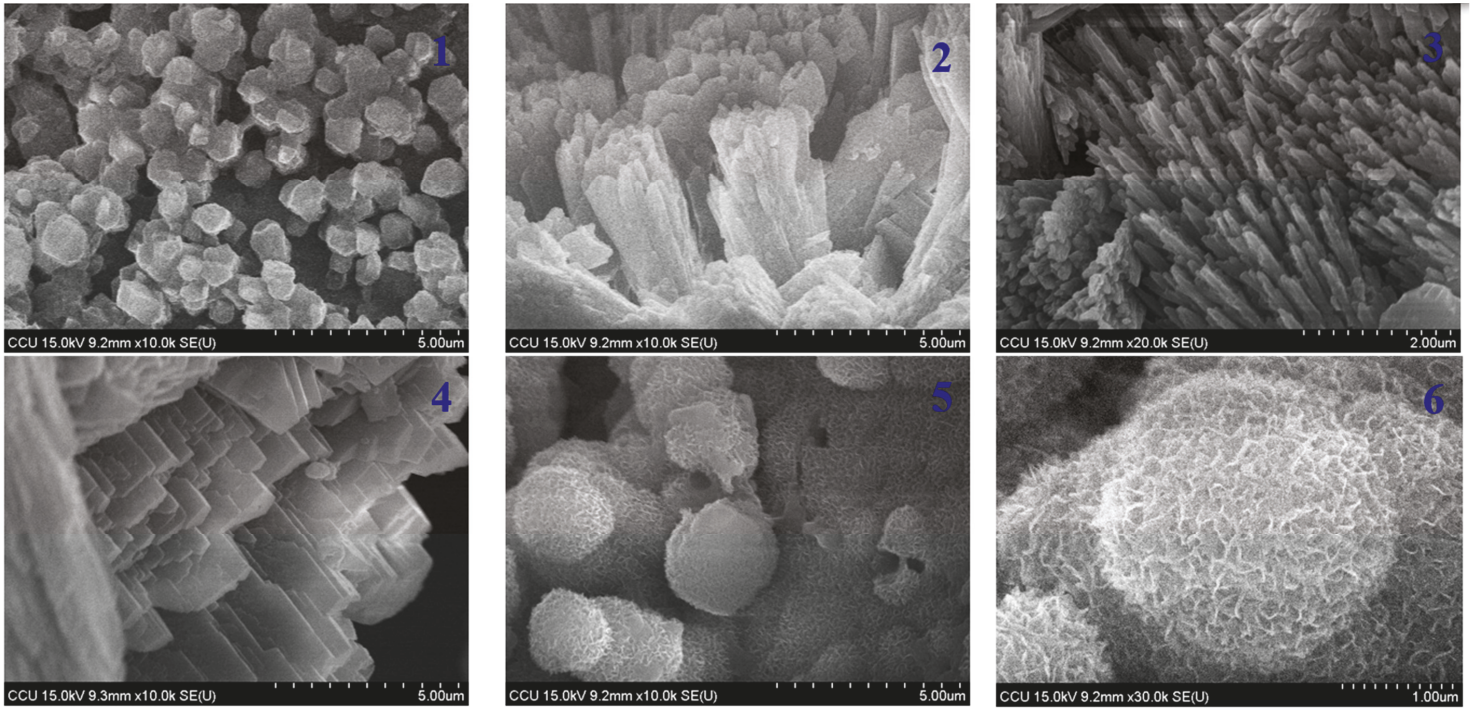

(**B**)

Figure 6. (**A**): SEM imagines of calcium carbonate precipitated by monoculture bacterial experiments. **Top** row (for upper part of column) showed the trigonal prism $CaCO_3$ (1 and 2) and rod-shaped calcite (3). **Down** row (for down part of column) showed the large and compact calcite with the irregular flakes of $CaCO_3$ (4, 5 and 6). (**B**): SEM imagines of calcium carbonate precipitated by coculture bacterial experiments. **Top** raw (for down part of column) showed the granular calcite (1) and rod-shaped calcite (2 and 3). **Down** raw (for upper part of column) showed compact and lamellar calcite (4), and spherulitic vaterite. (5 and 6).

2.6. Engineering Assessment of the Effect of Consolidation

In addition, to verify the effectiveness in consolidation of sand with the two ureolytic stains, *S. pasteurii* and *B. subtilis*, an engineering experiment of mixing standard sand, Portland cement, and bacterial solution into porous cement binder, casting 5 cm cube mortar specimen for testing of compressive strength was carried out.

Figure 7 shows the results of the mortar's compressive strength with different bacterial solutions. The average compressive strength of control specimen without bacteria is 18.2 MPa at 14 days. The mortars incorporated monoculture *S. pasteurii* (SP group) and coculture *S. pasteurii-B subtilis* (SP + BS group) and present the compressive strength of 27.7 MPa and 26.9 MPa, respectively. This indicates that both the monoculture *S. pasteurii* and coculture *S. pasteurii-B subtilis* can greatly enhance the strength of the mortars. It is significant for geotechnical engineering to improve the mechanical property of soil by the invented consolidation method.

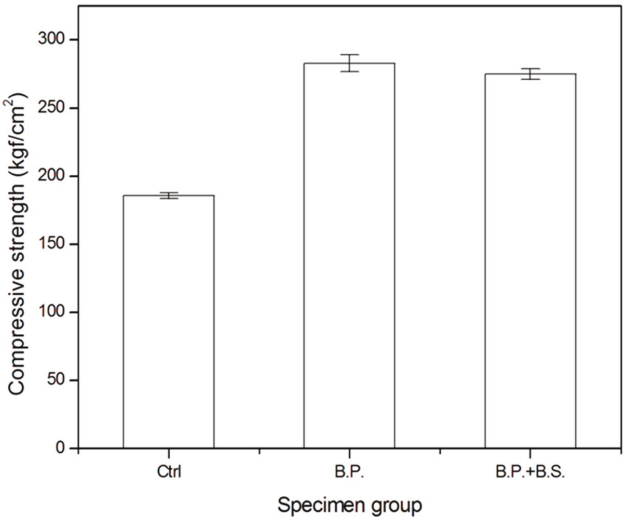

Figure 7. Test results of the compressive strength for the control, SP and SP + BS group specimen at 14 days.

3. Materials and Methods

3.1. Microorganism

The experiments were designed with two aerobically grown bacteria; *S. pasteurii* (DSMZ33) and *B. subtilis* (BBK006). *S. pasteurii* was cultivated under aerobic batch conditions in a medium containing 20 g L^{-1} yeast extract and 10 g L^{-1} NH_4Cl, at a pH of 7. The organism was grown to early stationary phase before harvest. *B. subtilis* was also grown under aerobic batch conditions in M9 medium. The composition of M9 medium was given by Miller as 0.2% glucose in mineral salts (1 g L^{-1} NH_4Cl, 3 g L^{-1} KH_2PO_4, 6 g L^{-1} Na_2HPO_4, 5 g L^{-1} NaCl, 1 mmol L^{-1} $MgSO_4$, and 0.1 mmol L^{-1} $CaCl_2$). Before sterilization, the medium pH was adjusted to 7.0 with 0.5 mol L^{-1} NaOH. The medium was sterilized at 121 °C for 20 min (without glucose for M9 medium, which was filter sterilized (Millipore membrane PVDF, 0.22 μm filter unit; Millipore, Watford, UK) and added afterwards) [22]. Control consisted of uninoculated culture medium along with experimental samples.

3.2. Column Parameters and Sampling

Three cylindrical glass columns (height—0.22 m; internal diameter—0.07 m) were used for this study. The schematic illustration of the setup and sampling positions along the columns were indicated at which the samples were analysed by SEM and XRD as shown in Figure 8. The column was positioned vertically with downward flow direction to avoid any settling of the packing material and generation of preferential flow paths that may occur if the column was positioned horizontally. Each end of the column was fitted with filter material consisting of 1 layers of scouring pad (Scotch Brite) at the outside and approximately 2 cm of filter gravel on the inside, next to the sand. Ottawa sand with the size distribution from 0.1 mm to 1 mm were used. Packing of the sand column was conducted under water to the required density to avoid the inclusion of air pockets. After column packing with sand, the column capacity to hold solution approached to 310 ± 10 mL. A pump was installed at the bottom of the column to regulate the outflow rate of 0.2 L/h. All experiments were performed at ambient temperature of 25 ± 2 °C. During the course of the experiment, samples were taken from the outlet of the column. Immediately after collection, the samples were frozen at −18 °C awaiting analysis. To study, optical density (OD_{600}), pH, urease activity and ammonium concentration samples were centrifuged and the supernatant transferred to a clean tube, which was tested for as required.

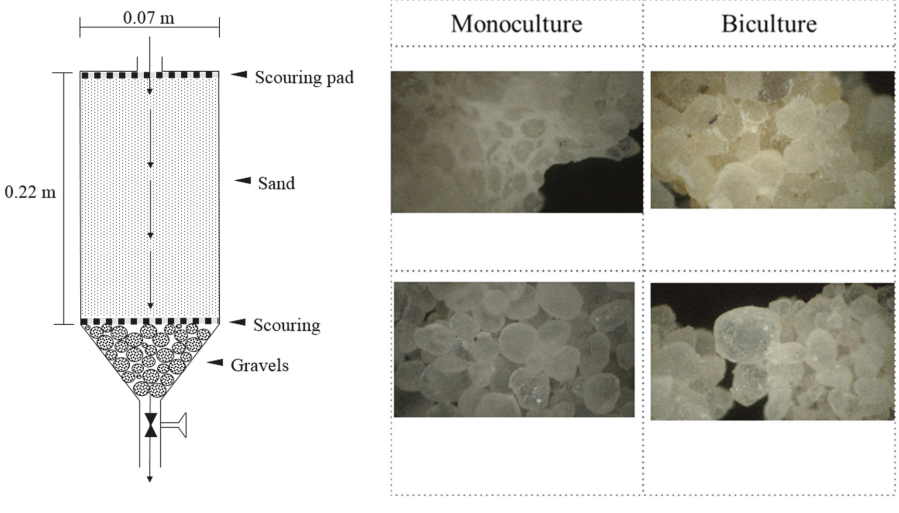

Figure 8. The schematic illustration of the setup and Sampling positions along the columns were indicated at which the samples were analysed by SEM and XRD. The imagines of optical microscopy showed the cemented sands with $CaCO_3$ precipitates for the scraped samples (Magnification = 0.28 × 20 = 5.6).

3.3. Monitoring Methods

Urease activity and NH_4^+ concentration measurements are based upon the work by Whiffin et al. [2].

3.4. Optical Density (OD_{600})

OD was determined using a spectrophotometer and recorded at 600 nm.

3.5. Urease Activity

In the absence of calcium ions, urease activity was determined by a conductivity method. This method was not suitable for determining urease activity in the presence of calcium ions (due to precipitation of calcium carbonate particles and the dampening effect of the counter ion on the solution

conductivity), thus in these cases urease activity was determined from the ammonium production rate. Both methods for determining urease activity were independently calibrated and correlated with each other.

3.6. Ammonium Concentration

Ammonium concentration was determined by a modified Nessler method of Greenburg et al. [23]. The sample was diluted with deionized water to be in the range of 0–0.5 mM. The 2 mL of sample was added to a cuvette and mixed with 100 μL of Nessler reagent (Merck, Kenilworth, NJ, USA), and allowed to react for exactly 1 min. The sample was then read in a spectrophotometer at 425 nm. Absorbance readings were calibrated with several NH_4Cl standards measured under the same conditions.

3.7. Calcium Concentration

Calcium concentration was determined by colorimetric method of Peaslee [24].

3.8. Calcium Carbonate Content

Calcium carbonate content was determined by Loeppert [25]. After drying, the 10 samples were scraped from the top (inlet) to bottom (outlet) of the column. At each sampling point, 3 samples were scraped and averages of them were calculated.

3.9. Flushed Volume

The overall column flow rate was calculated from the total flushed volume (liquid in container plus effluent and port samples) versus time.

3.10. Analysis of Crystal Properties

After drying, the samples were prepared for SEM, XRD and Raman to analyze the crystal properties and minerology. SEM measurements were carried out on a FE-SEM TOPCON field-emission scanning electron microscope (FE-SEM, TOPCON ABT-150S, Singapore). The acceleration voltage of 15 K was used for imaging. Powder X-ray diffraction (XRD) patterns were recorded on a Shimadzu X-ray diffractometer (LabX XRD-6000, Shimadzu, Tokyo, Japan) equipped with Ni-filtered CuKα (λ = 0.1541 nm, 4 kVA, 30 mA) radiation and a graphite crystal monochromator. Raman analysis were performed using inVia reflex Raman Microscopy (Renishaw Plc, Gloucestershire, UK) with the exciting source of He-Cd laser operating at 442 nm with a power of about 80 mW. The measurements were performed for all the three columns and samples for analysis were scraped from the top (inlet) and bottom (outlet) of the column as shown in Figure 8. The scraped samples with sands with $CaCO_3$ precipitates were directly observed using optical microscopy (MEIJI MS-40DR SAM1-P, Saitama, Japan) as shown in Figure 8. The precipitated carbonates were carefully separated from sands with tweezers prior to the XRD and SEM measurements.

3.11. Strength Test of Sand Consolidation

The sample for the strength test of sand consolidation was prepared with mixing standard sand, Portland cement, and bacterial solution into porous mortar. The bacterial solution is SP and SB + BS solution with the OD value of 1.23 and 1.28 respectively. Table 1 gives the mix proportion of the mortars. 3cubes in size of 50 × 50 × 50 mm^3 were cast for each specimen group and cured for 24 h at T = 25 °C and 95% ± 3% relative humidity, then demoulded and cured for 6 days at the same condition as initial. After 7 days, MICP treatments were carried out by the procedures as below:

Samples were immersed in urea solution of 1.1 M for 24 h.

(1) Removing all samples and drying naturally for 24 h.
(2) SB samples were immersed in SP bacterial solution for 24 h, the same procedure as SP + BS.

(3) Removed all samples and dried naturally for 24 h.
(4) All samples were immersed in the mixing solution of 1.1 M urea and 1.1 M calcium acetate for 24 h.
(5) Removed all samples and dried naturally for 48 h. The control group samples were the same procedure as MICP treatments except the procedure of immersed bacterial solution.

The compressive strength test was performed according to ASTM C 109 on 50 mm × 50 mm × 50 mm motar cube at age of 14 days. For each specimen group the compressive strength was the average of three specimens.

4. Conclusions

Microbiological activities that occur in bioconsolidation and subsurface environments are largely unknown. This study documented the impact of carbonate precipitation, mineral/crystal alteration and environmental implication on bioconsolidation of loose sand and subsurface environments. Comparative studies were conducted on the $CaCO_3$ precipitation induced by microbes and other biological factors. The results showed that the precipitation rate of Ca^{2+} in the presence of *S. pasteurii* was faster than that in the presence of *S. pasteurii-B. subtilis*, respectively, but at the end of the experiment, both studies were shown to induce the same precipitation rate. The mineralogical examination and experiments documented the importance of *S. pasteurii* and *B. subtilis* in promoting the formation of calcium carbonate minerals. Our research has extended the understanding of the composition of bacterially precipitated carbonate crystals and evaluated both monoculture and biculture bacteria as a sand bioconsolidant.

Supplementary Materials: The following are available online at http://www.mdpi.com/2073-4352/8/5/189/s1.

Author Contributions: C.-M.H., V.R.N. and C.-C.C. conceived and designed the experiments; C.-M.H., V.R.N. and Y.-H.H. performed the experiments; C.-M.H. and V.R.N., analyzed the data; W.-C.L., Y.-H.K. and C.-H.H. contributed reagents/materials/analysis tools; H.-J.C., C.-Y.C., C.-M.H. and V.R.N. wrote the paper.

Funding: This research was funded by Ministry of Science and Technology Taiwan, grant number [MOST 106-2116-M-194-014].

Acknowledgments: The authors are very grateful to the science council of Taiwan for sponsoring this research.

Conflicts of Interest: The authors declare no conflict of interest.

Abbreviations

$CaCl_2$	Calcium chloride
$CaCO_3$	Calcium carbonate
NH_4^+	ammonium ion
NH_4Cl	Ammonium chloride
Ca^{2+}	calcium ion
XRD	X-ray diffraction

References

1. Li, W.; Liu, L.; Chen, W.; Yua, L.; Li, W.; Yu, H. Calcium carbonate precipitation and crystal morphology induced by microbial carbonic anhydrase and other biological factors. *Proc. Biochem.* **2010**, *45*, 1017–1021. [CrossRef]
2. Whiffin, V.S.; van Paassen, L.A.; Harkes, M.P. Microbial Carbonate Precipitation as a Soil Improvement Technique. *Geomicrobiol. J.* **2007**, *24*, 1–7. [CrossRef]
3. Arp, G.; Hofmann, J.; Reitner, J. Microbial fabric formation in spring mounds ('microbialites') of alkaline salt lakes in the Badain Jaran Sand Sea. *Palaios* **1998**, *13*, 581–592. [CrossRef]
4. Phillips, A.J.; Gerlach, R.; Lauchnor, E.; Mitchell, A.C.; Cunningham, A.B.; Spangler, L. Engineered applications of ureolytic biomineralization: A review. *Biofouling* **2013**, *29*, 715–733. [CrossRef] [PubMed]

5. Perry, C.T. Biofilm-related calcification, sediment trapping and constructive micrite envelopes: A criterion for the recognition of ancient grass-bed environments. *Sedimentology* **1999**, *46*, 33–45. [CrossRef]
6. Benzerara, K.; Miot, J.; Morin, G.; Ona-Nguema, G.; Skouri-Panet, F.; Ferard, C. Significance, mechanisms and environmental implications of microbial biomineralization. *CR Geosci.* **2011**, *343*, 160–167. [CrossRef]
7. Wen, Z.F.; Zhong, J.H.; Li, Y.; Guo, Z.Q.; Gao, J.B.; Xu, X.L. Current study on genesis and formation conditions of stromatolites. *Geol. J. China Univ.* **2004**, *10*, 418–428.
8. Braissant, O.; Decho, A.W.; Przekop, K.M.; Gallagher, K.L.; Glunk, C.; Dupraz, C.; Visscher, P.T. Characteristics and turnover of exopolymeric substances in a hypersaline microbial mat. *FEMS Microbiol. Ecol.* **2009**, *67*, 293–307. [CrossRef] [PubMed]
9. Chen, L.; Shen, Y.H.; Xie, A.J.; Huang, B.; Jia, R.; Guo, R.Y.; Tang, W.Z. Bacteria-mediated synthesis of metal carbonate minerals with unusual morphologies and structures. *Cry. Growth Des.* **2009**, *9*, 743–754. [CrossRef]
10. Hammes, F.; Verstraete, W. Key roles of pH and calcium metabolism in microbial carbonate precipitation. *Rev. Environ. Sci. Technol.* **2002**, *1*, 3–7. [CrossRef]
11. Mobley, H.L.; Hausinger, R.P. Microbial ureases: Significance, regulation, and molecular characterization. *Microbiol. Rev.* **1989**, *53*, 85–108. [PubMed]
12. Fujita, Y.; Ferris, F.G.; Lawson, R.D.; Colwell, F.S.; Smith, R.W. Calcium carbonate precipitation by ureolytic subsurface bacteria. *Geomicrobiol. J.* **2000**, *17*, 305–318. [CrossRef]
13. Friedrich, B.; Magasanik, B. Urease of Klebsiella aerogenes: Control of its synthesis by glutamine synthetase. *J. Bacteriol.* **1977**, *131*, 446–452. [PubMed]
14. Kaltwasser, H.; Krämer, J.; Conger, W.R. Control of urease formation in certain aerobic bacteria. *Arch. Microbiol.* **1972**, *81*, 178–196. [CrossRef]
15. Bachmeier, K.L.; Williams, A.E.; Warmington, J.R.; Bang, S.S. Urease activity in microbiologically-induced calcite precipitation. *J. Biotechnol.* **2002**, *93*, 171–181. [CrossRef]
16. Tiano, P.; Biagiotti, L.; Mastromei, G. Bacterial bio-mediated calcite precipitation for monumental stones conservation: Methods of evaluation. *J. Microbiol. Methods* **1999**, *36*, 139–145. [CrossRef]
17. Stocks-Fischer, S.; Galinat, J.K.; Bang, S.S. Microbiological precipitation of $CaCO_3$. *Soil Biol. Biochem.* **1999**, *31*, 1563–1571. [CrossRef]
18. Spanos, N.; Koutsoukos, P.G. The transformation of vaterite to calcite: Effect of the conditions of the solutions in contact with the mineral phase. *J. Crys. Growth* **1998**, *191*, 783–790. [CrossRef]
19. Marvasi, M.; Visscher, P.T.; Martinez, L.C. Exopolymeric substances (EPS) from *Bacillus subtilis*: Polymers and genes encoding their synthesis. *FEMS Microbiol. Lett.* **2010**, *313*, 1–9. [CrossRef] [PubMed]
20. Buczynski, C.; Chafetz, H.S. Habit of bacterially induced precipitates of calcium carbonate and the influence of medium viscosity on mineralogy. *J. Sed. Res.* **1991**, *61*, 226–233. [CrossRef]
21. Le Metayer-Levrel, G.; Castanier, S.; Orial, G.; Loubiere, J.F.; Perthuisot, J.P. Applications of bacterial carbonatogenesis to the protection and regeneration of limestones in buildings and historic patrimony. *Sediment. Geol.* **1999**, *126*, 25–34. [CrossRef]
22. Miller, H. *Experiments in Molecular Genetics*; CSHL Press: Plainview, NY, USA, 1972.
23. Greenburg, A.E.; Clesceri, L.S.; Eaton, A.D. *Standard Methods for the Examination of Water and Wastewater*, 18th ed.; American Public Health Association: Washington, DC, USA, 1992.
24. Peaslee, D.E. Colorimetric determination of calcium in soil extracts. *Soil Sci.* **1964**, *97*, 248–251. [CrossRef]
25. Loeppert, R.H. *Methods of Soil Analysis—Part 3. Chemical Methods—SSSA Book Series No. 5*; SSSA: Madison, WI, USA, 1996.

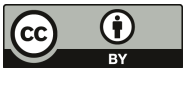

© 2018 by the authors. Licensee MDPI, Basel, Switzerland. This article is an open access article distributed under the terms and conditions of the Creative Commons Attribution (CC BY) license (http://creativecommons.org/licenses/by/4.0/).

crystals

MDPI

Article

Experimental Value of the Specific Surface Energy of the Cleavage {10.4} Calcite Rhombohedron in the Presence of Its Saturated Aqueous Solution

Emanuele Costa * and Dino Aquilano

Department of Earth Sciences, Università di Torino, Via Valperga Caluso 35, 10125 Torino, Italy; dino.aquilano@unito.it

* Correspondence: emanuele.costa@unito.it; Tel.: +39-347-2281511

Received: 26 April 2018; Accepted: 28 May 2018; Published: 30 May 2018

Abstract: In this study, we describe a method to obtain experimental values of the surface energy of calcite. A zenithal imaging device was used to acquire pictures of droplets of $CaCO_3$ saturated aqueous solution on the surface of a calcite crystal sample. Pictures were used to measure the contact angle between the droplets and the {10.4} calcite surfaces. The method is discussed along with its geometrical ground, as well as the theoretical foundation of the contact angle calculation. A comparison is made with the literature data; a good agreement is found between our experimental values and those obtained from the more recent ab initio calculations.

Keywords: calcite; contact angle; surface energy

1. Introduction

Measuring the surface energy of calcite is often obtained using methods involving the determination of the contact angle of various liquids in the system: crystal/liquid/air, but also in submerged systems using non-aqueous solvents. Evaluating the contact angle usually requires sophisticated mechanical and optical devices, to ensure perfect co-planarity of the calcite surface and the optical axis of the camera, the absence of parallax error during the image acquisition, and somewhat ability of the operator regarding the determination of the real angle formed between the calcite face and the droplet boundary at the contact interface [1–3]. The use of a simple experimental device for the collection of zenithal pictures of liquid droplets on mineral surfaces could allow to precisely evaluate both the diameter of a drop of known volume and its contact angle. The acquisition of pictures from a vertical perspective eliminates some problems encountered in traditional imaging of droplet profile, and the rapidity of the operation allows the capture of a great number of images, within a simple experiment run, thus improving the statistics of the measurements. Accordingly, it is worth remembering the reliability of a statistical method when dealing with a real crystal surface. Let us consider the {10.4} crystal surfaces of both a cleaved and an as-grown crystal. At a microscopic level, two different situations are found: the cleaved surface is populated by features of micrometric thickness which interrupt the flatness of the ideal (10.4) terraces, like macrosteps, while in the as-grown surfaces, the thickness of the growth steps decreases down to a nanometric level. As an example, we can observe SEM images of calcite cleavage surface or as-grown calcite surface (Figure 1).

This does not represent a negligible detail, since the contribution of surface steps to the interfacial energy appreciably depends on its height. Consequently, measurements made on a population of droplets settled on different sites of a given crystal surface better represent the interfacial energy value with respect to the one obtained from a single macroscopic drop. Finally, it should not be neglected that the corresponding calculated values of the interfacial energy are obtained by considering an ideal flat interface (i.e., the only (10.4) terraces, in our case).

When a liquid droplet (in a system solid/liquid/vapor) settles on a solid surface: (i) if the droplet is in mechanical and thermodynamic equilibrium with the substrate and the surrounding vapor phase; and (ii) if the specific adhesion energy between the solid surface and the droplet (β_{adh}) is higher than the specific energy (γ_{lv}) of the liquid–vapor interface, then the contact angle (θ) between the droplet and the surface is higher than 90°. This ensues from the coupling of the Young's (1) and Dupré's (1) laws [4–6] where we will define γ_{sv} as the specific energy of the solid-vapor interface, and γ_{sl} as the specific energy of the solid–liquid interface. The latter has been obtained through two independent ways:

$$\gamma_{lv} \cos\theta + \gamma_{sv} = \gamma_{sl} \quad (1)$$

$$\gamma_{lv} + \gamma_{sv} - \beta_{adh} = \gamma_{sl} \quad (2)$$

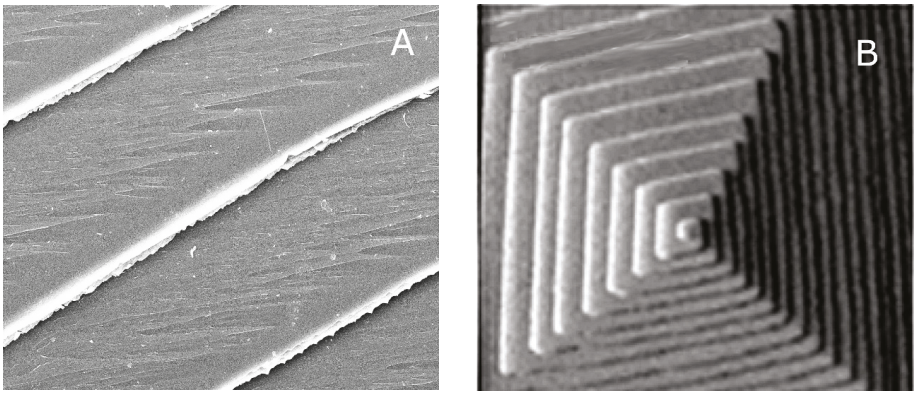

Figure 1. SEM images of calcite crystal surfaces showing features at different scales. (**A**) A sequence of thin and thick cleavage steps on a {10.4} face of a calcite crystal: the mean step spacing is close to 50 μm, while the mean height of thick steps is close to 1 μm. F.O.V. 100 μm (by courtesy of Dr. Linda Pastero, private communication); (**B**) A growth spiral on the {10.4} crystal surfaces of calcite showing monolayered steps (height = 0.3 nm) with mean steps spacing of 30 nm. F.O.V. 600 nm [6].

From Equations (1) and (2) and considering the constraint: $-1 \leq \cos\theta \leq 1$, it follows that the adhesion energy ranges between two limiting values: $0 \leq \beta_{adh} \leq 2\gamma_{lv}$. The minimum ($\beta_{adh} = 0$) corresponds to the situation in which the droplet does not wet the substrate (a water droplet on a hydrophobic surface, for instance). The maximum corresponds to the perfect wetting (the droplet spreads onto the substrate reaching the maximum of its contact area and, consequently, its minimum thickness). In any case, the β_{adh} value cannot exceed the value of the cohesion energy (K_l) of the liquid itself having recollected that $K_l = 2\gamma_{lv}$. It is worth to outline that the θ angle defined in (1) is the angle comprised between the vector representing the interfacial tension γ_{sv} (between the substrate and the vapor) and the vector representing the interfacial tension γ_{lv} (between the liquid droplet and the vapor); this is to avoid any confusion about the sign of the function $\cos\theta$. In other words, the higher the angle θ, the higher the wetting and, hence, the adhesion energy between the droplet and the substrate (Figure 2).

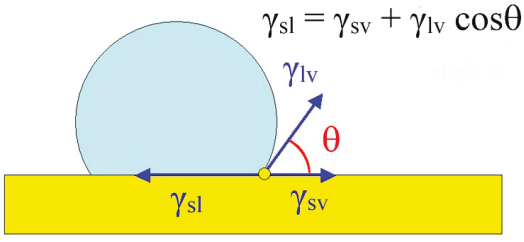

Figure 2. The relationship between the three interfacial tension acting on the boundaries between drop, surface and air (Young's formula).

2. Materials and Methods

2.1. Picture Acquisition

To calculate the contact angle θ, strictly related to β_{adh}, we put a single drop of liquid on a flat surface of the chosen material. The volume of the droplet is a priori constrained, using gas-chromatography syringe, that allows to put down droplets varying from 10 to 100 microliters in volume, with a precision of about half a microliter. The choice of so small volumes is due to the difficulty of obtaining flat and smooth surfaces of natural crystals, large enough to host macro-drops settling on them.

For practical use, a droplet of 20 µL of aqueous solution saturated at room temperature (about 295 K) with respect to calcite, colored with 0.5 ‰ methylene blue to better determine the drop borderline, was settled on a horizontal surface (for preliminary experiments cleaned glass surfaces and distilled water were used). The pictures were acquired with a very simple USB Celestron Handeld Microscope micro-camera, mounted at fixed focus height on a laboratory support, with a 20× magnification and a resolution of 640 × 480 pixels. The focus was preliminary adjusted to measure the field of view (on a picture of a graph paper sheet or a ruler, advantageous for checking deformations as well), and thus determining the relation between pixels' size and real length on the pictures, useful for the subsequent calculation of droplet diameter (Figure 3). With this equipment we saved pictures having 6 mm of F.O.V. spread on 640-pixel width, thus attaining a 10 µm resolution.

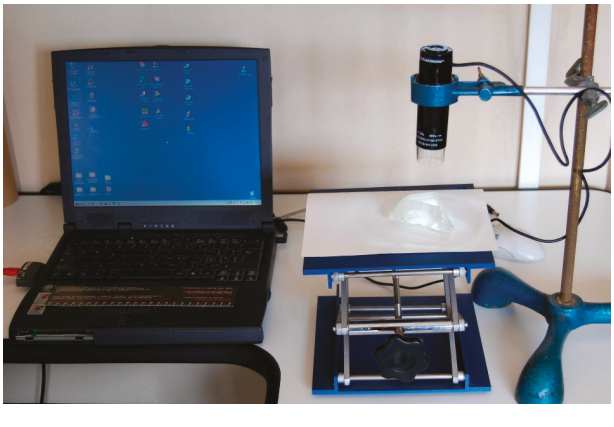

Figure 3. The simple device used to obtain a zenithal image of drops on horizontal surfaces. The handled microscope is suspended and stopped in a laboratory stand, at fixed height and fixed focus distance, previously checked. The lab screw jack is used as vertical translator stage and hosts in this picture a calcite crystal. A simple portable PC is enough to acquire the images via a USB connection.

Experiments on calcite were performed on a fresh cleavage {10.4} surface of a very pure calcite crystal. The fresh surfaces were equilibrated in air at about 296 K. The data reliability was improved by working with different droplets of the same volume, by measuring (for every drop) two different perpendicular diameters and using the averaged value for calculations. Drops of irregular shape were preliminary discarded. After each measurement, the crystal surface was washed with distilled water and dried with a gently air whisper, to avoid scratch of the surface and massive electrostatic charge generation. During two different experimental sessions, about 60 drops were photographed and measured.

2.2. Calculation of the Geometrical Parameters of the Droplets

The droplet shape should be approximately regarded as a spherical cap of diameter D, belonging to a sphere of radius R (Figure 4).

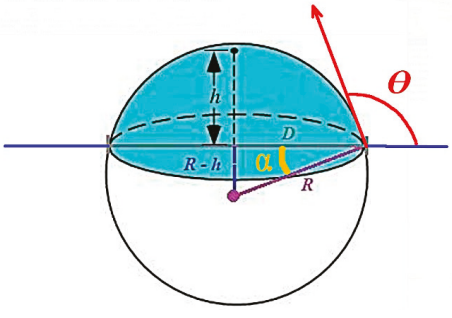

Figure 4. Droplet shape should be approximately regarded as a spherical cap of height h and diameter D, related to a sphere of radius R.

The diameter of the drop is easily obtained from a picture taken with the previously described device, having the sensor plane parallel to the solid surface (substrate, hereinafter), and the optical axis as close as possible to the symmetry axes of the droplets (in practice, with the drop in the center of the image sensor device).

To obtain θ from geometric consideration we need to obtain "h", the height of the drop spherical cap on the surface. From two measurable parameters (the droplet volume V, constrained at the beginning, and the related diameter D = 2r), one can calculate the height (h) of the spherical cup, through the simple relation:

$$\pi h^3 + 3\pi r^2 h + 6V = 0 \quad (3)$$

This third order equations can be solved through different analytical methods, but we used a quick one, by applying free software for drawing the resulting equation, and checking the intercept value of the corresponding curve with the abscissa axis. We used an online equation grapher (Equation Grapher, [7]). From r (measured) and h (calculated) values, one gets the curvature radius R of the generating sphere:

$$R = (r^2 + h^2)/2h \quad (4)$$

Thus, one can easily obtain the angle (α):

$$\alpha = \sin^{-1}[(R - h)/R] \quad (5)$$

Finally, the contact angle θ comes out, with the precision derived from the measuring chain:

$$\theta = \alpha + \pi/2 \quad (6)$$

On the other hand, the zenithal method cannot be used for liquid/solid surface coupling with a contact angle lower than 90°, because in this case, the circumference in the contact surface is smaller than that of the superjacent droplet; hence, the circumference of the contact boundary is hidden by the drop itself. Luckily, the case of contact angle lower than 90° is rare when mineral surfaces interact with water or similar liquids.

3. Results

3.1. Stability of the Droplet

We checked the mechanical stability of the droplets during the experiment. First of all, the real shape of a liquid droplet on a solid horizontal surface is not that of a perfect spherical cap, and is affected by some deformation. This, in turn, induces some variation of the contact angle that is in difficult to evaluate. Secondly, the evaporation should modify the initial volume of the droplet, and then the cap diameter D could decrease until equilibrium (saturation) is reached between the liquid and the saturated vapor phase. Performing the pictures in free air conditions, this equilibrium could not normally be reached, so the drop could undergo to complete evaporation. Experiments were performed to check the modification of the drop diameter with time. A single drop of colored distilled water was placed on a clean glass surface, and pictures of this drop were taken every minute, for a total of fifteen minutes, this time interval being considered adequate to take picture also in hostile laboratory environments. Figure 5 shows a reduced example of this sequence, from which one can argue that the strong adhesion between water and glass constrains the circumference of the drop to the fixed initial position, and the evaporation loss causes a volume reduction and convexity modification (as can be deduced by the reflected image of the lighting led on the drop surface) but nevertheless, the diameter of the spherical cap, which is the only parameter we really need to measure, is not affected at all.

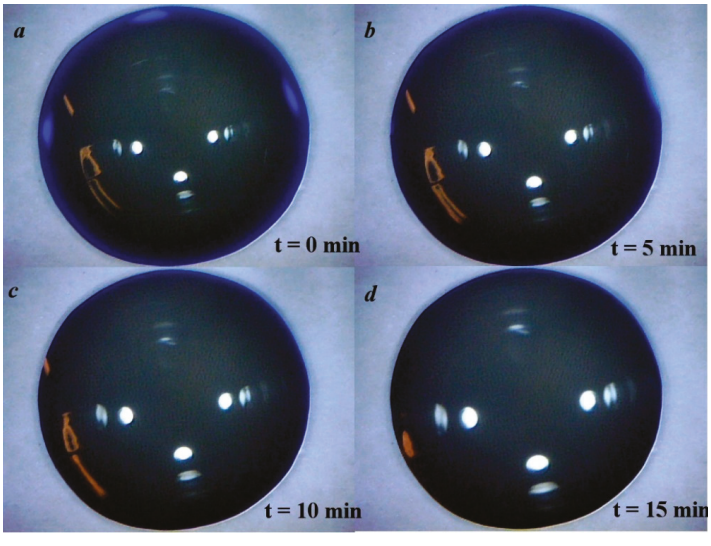

Figure 5. A spherical cap photographed at different time intervals (**a**–**d**), after its deposition on the substrate Although evaporation occurs during time, reducing the volume and curvature of the droplet (as it could be seen by the different position of the light reflexes on the drop surface), the diameter of it remain the same for a time-lapse sufficient to capture the image. All the pictures were acquired at different times on the same droplet with the same focus and field of view (reduced by cropping to approx. 6 mm).

3.2. From the Contact Angle to the Calcite/Solution Interface Energy

We performed (in different moments) two different runs of experiments on a calcite {10.4} cleaved surface. From the first experimental series (31 drops), an averaged radius of 2.85 mm was obtained, with a dispersion comprised between 2.70 and 2.95 mm, and a relative standard deviation of 3.2%. The resulting contact angle is $\theta_1 = 146.40^\circ$. From the second run (30 drops), an average radius of 2.97 mm was obtained, with dispersion ranging between 2.80 and 3.20 mm and a relative standard deviation of 3.5%. The resulting contact angle is $\theta_2 = 131^\circ$. From this, we obtain an average contact angle of 138.70°.

From the average contact angle we obtained at the triple interface: {10.4} cleaved calcite/saturated solution/air, one can calculate the interfacial energy (γ_{sl}) at the crystal-liquid boundary using the Young's Formula (1).

At 293 K, the surface energy of water in contact with its own vapor is γ_{lv} =72.7 erg/cm^2. When dealing with a calcite aqueous solution saturated at room temperature, it is reasonable to adopt this γ_{lv} value, as well, owing to the very low solubility of calcite in water [8]. Calculations showed that γ_{sv}, the surface energy of $\{10.4\}_{calcite}$ in vacuum at 0 K [9–13] ranges between 500 and 530 erg/cm^2. Recently, ab initio calculations showed that at T = 300 K, γ_{104} = 464 ± 18 erg/cm^2. Thus, here we assume this last more reliable γ_{104} value [13]. The contact angle we used is the averaged value from the two experimental sets, i.e., $<\theta> = 138.70^\circ$.

Replacing these values in the Young's formula we obtain the surface energy $calcite_{\{10.4\}}$/solution: $\gamma_{sl(10.4)}$ = 409.38 erg/cm^2.

Accordingly, the adhesion energy, coming from Dupré's condition (2), corresponds to 127.32 erg/cm^2. Then, we verified also that the limiting values (θ_1 and θ_2) of the contact angle give values of the adhesion energy compatible with the constraints of the Dupré's condition, i.e., β_{adh} (θ_1) = 120.39 and β_{adh} (θ_2) = 133.25 erg/cm^2. In both cases the adhesion energy of the liquid phase is lower than the cohesion energy of the droplet, $K_{droplet} = 2\gamma_{lv}$ = 145.4 erg/cm^2.

4. Discussion

The result is largely satisfactory, since the constraints imposed by the Dupré's condition to the adhesion energy are fulfilled. To the best of our knowledge, this is the first time that an experimental value of the interface energy between the cleavage 10.4 surface and its surrounding solution fits with the theoretical prediction, obtained by ab initio calculations of the crystal/vacuum interfacial energy.

Moreover, we would like to outline once more the reliability of the measurement method we adopted. As we detailed in the Introduction, a cleavage surface, even for the best cases like that represented by the one of $\{10.4\}_{calcite}$, does not coincide with an ideal crystallographic plane, but is populated by surface defects like steps, kinks and dislocation outcrops. Quality and density of these defects vary from site to site of the surface: accordingly, the higher the number of measurements on different surface sites, the higher the approach to the real physical meaning of the measured property.

Now, to have some more data for comparison, we will compare the value we just obtained with that coming out by using the empirical formula proposed by Neumann and reported by Spelt and Li [14]:

$$\cos\theta_\gamma = -1 + 2(\gamma_{sv}/\gamma_{lv})^{1/2} \exp\left[-\beta(\gamma_{lv} - \gamma_{sv})^2\right] \quad (7)$$

where θ_γ represents the contact angle measured following the Young method, while β is a constant which was found to be 1.247×10^{-4} (m^2/mJ)^2. This formula allows to determine the solid surface tension (γ_{sv}) from experimental (Young) contact angle and liquid surface tension (γ_{lv}).

When putting in Equation (4) the values of β, γ_{lv} and θ_γ, one obtains:

$$\ln(\gamma_{sv}) = 0.11735 + 2.494 \times 10^{-4}(72.7 - \gamma_{sv})^2 \quad (8)$$

which reduces to:

$$\ln(\gamma_{sv}) = 2.494 \times 10^{-4} (\gamma_{sv})^2 - 3.626 \times 10^{-2} \gamma_{sv} + 1.4355 \quad (9)$$

From the intersection of the logarithmic curve ($y = \ln\gamma_{sv}$) and the parabolic one (4c), one does find the value of $\gamma_{sv} = 218$ erg/cm^2 which is placed almost in the middle of the range of $\{10.4\}_{calcite}$ surface energy, as reported in the literature, were we can found largely dispersed values (ranging from 70 to 1500 erg cm^{-2}) [15]. Probably, this last value, $\gamma_{sv} = 218$ erg/cm^2, does not represent a realistic value for (10.4)/vacuum interface; because as a matter of fact, it is not reasonable to accept that the surface energy (at 0 K) of calcite (that is made by positive (2+) and negative (2−) electrical charges) could be slightly higher than that $\gamma(100)_{NaCl} = 161$ erg/cm^2 of a pure ionic crystal (made by positive (1+) and negative (1−) electrical charges), for faces exhibiting an analogue two-dimensional structure, as it comes out when comparing the {100}-NaCl and the {10.4}-$CaCO_3$ surfaces.

5. Conclusions

The method of zenithal imaging has some advantages and some disadvantages with respect to the classical method of lateral acquisition of the contact angle for liquid drops on a plane surface.

Advantages are the very simple experimental setup, easy-to-use apparatus, low costs, good precision in determining the geometrical parameters and quick acquisition of a large number of images to improve statistics. Disadvantages are the unusableness of the vertical acquisition when the contact angle is lower than 90°, and the necessity of a flat surface large enough to host drops of sufficient volume, a requirement that is not always easy to fulfil when dealing with natural samples.

We measured the surface energy $\gamma_{sl}{}^{(10.4)}$ of the calcite cleavage rhombohedron, in the presence of calcium carbonate saturated solution. The value we found through our method complies with the constraints imposed by the Dupré's formula.

In fact, from: (i) the well-known experimental value γ_{lv} of the surface energy between the solution and the vapor phase; (ii) γ_{sv}, the crystal-vapor interfacial energy, calculated at room temperature along with (iii) our experimental $\gamma_{sl(10.4)}$ value, a value has been obtained of ${}^{(10.4)}\beta_{adh}$, the adhesion energy between the crystal surface and the mother solution, which is compatible, for the first time, with the cohesion energy of the solution. The self-consistency of the results obtained by our method seem to be quite promising for further measurements on other crystal surfaces growing from solution.

Author Contributions: E.C. conceived and designed the experiments; E.C. performed the experiments; E.C. and D.A. analyzed the data; E.C. contributed reagents/materials/analysis tools; E.C. and D.A. wrote the paper.

Acknowledgments: The Authors wish to thank Linda Pastero and Marco Bruno (Dip. Scienze della Terra, Università di Torino) for their kind cooperation and suggestions.

Conflicts of Interest: The authors declare no conflict of interest.

References

1. Ferrari, M.; Liggieri, L.; Miller, R. *Drops and Bubbles in Contact with Solid Surfaces*; CRC Press: Boca Raton, FL, USA, 2013; 344p., ISBN 9781466575455.
2. Hartland, S. *Surface and Interface Tension*; CRC Press: Boca Raton, FL, USA, 2004; 1500p., ISBN 9780824750343.
3. Adams, N.K. The Chemical Structure of Solid Surfaces as Deduced from Contact Angles. In *Contact Angle, Wettability, and Adhesion*; Fowkes, F.E., Ed.; ACS Publications: Washington, DC, USA, 1964; pp. 52–56, ISBN 9780841200449. [CrossRef]
4. Young, T. An Essay on the Cohesion of Fluids Philos. *Trans. R. Soc. Lond.* **1805**, *95*, 65–87. [CrossRef]
5. Schrader, M.E. Young-Dupré Revisited. *Langmuir* **2002**, *11*, 3585–3589. [CrossRef]
6. De Yoreo, J.J.; Vekilov, P.G. Principles of Crystal Nucleation and Growth. *Rev. Mineral. Geochem.* **2003**, *54*, 57–93. [CrossRef]
7. Pierce, R. 'Equation Grapher'. Math Is Fun. 2017. Available online: http://www.mathsisfun.com/data/grapher-equation.html (accessed on 11 February 2018).

8. Haynes, W.M. *CRC Handbook of Chemistry and Physics*, 90th ed.; CRC Press, Taylor and Francis Group: Boca Raton, FL, USA, 2010; 2610p. [CrossRef]
9. Rohl, A.L.; Wright, K.; Gale, J.D. Evidence from surface phonons for the (2 × 1) reconstruction of the $(10\bar{1}4)$ surface of calcite from computer simulation. *Am. Mineral.* **2003**, *88*, 921–925. [CrossRef]
10. Bruno, M.; Aquilano, D.; Pastero, L.; Prencipe, M. Structures and Surface Energies of (100) and Octopolar (111) Faces of Halite (NaCl): An Ab initio Quantum-Mechanical and Thermodynamical Study. *Cryst. Growth Des.* **2008**, *8*, 2163–2170. [CrossRef]
11. Bruno, M.; Massaro, F.R.; Prencipe, M.; Aquilano, D. Surface reconstructions and relaxation effects in a centre-symmetrical crystal: The {00.1} form of calcite ($CaCO_3$). *CrystEngComm* **2010**, *12*, 3626–3633. [CrossRef]
12. Akiyama, T.; Nakamura, K.; Ito, T. Atomic and electronic structures of $CaCO_3$ surfaces. *Phys. Rev. B* **2010**, *84*, 085428. [CrossRef]
13. Bruno, M.; Massaro, F.R.; Pastero, L.; Costa, E.; Rubbo, M.; Prencipe, M.; Aquilano, D. New Estimates of the Free Energy of Calcite/Water Interfaces for Evaluating the Equilibrium Shape and Nucleation Mechanisms. *Cryst. Growth Des.* **2013**, *13*, 1170–1179. [CrossRef]
14. Spelt, J.K.; Li, D. The equation of state approach to interfacial tension. In *Applied Surface Thermodynamics*; Marcel Dekker: New York, NY, USA, 1996; pp. 239–293, ISBN 0-8247-9096-0.
15. Forbes, T.Z.; Radha, A.V.; Navrotsky, A. The energetics of nanophase calcite. *Geochim. Cosmochim. Acta* **2011**, *75*, 7893–7905. [CrossRef]

© 2018 by the authors. Licensee MDPI, Basel, Switzerland. This article is an open access article distributed under the terms and conditions of the Creative Commons Attribution (CC BY) license (http://creativecommons.org/licenses/by/4.0/).

crystals

MDPI

Article

Calcium Carbonate Polymorphs Growing in the Presence of Sericin: A New Composite Mimicking the Hierarchic Structure of Nacre

Linda Pastero [1,2,*] and Dino Aquilano [1]

[1] Department of Earth Sciences, University of Turin, Via Valperga Caluso 35, 10125 Torino, Italy; dino.aquilano@unito.it

[2] NIS—Nanostructured Interfaces and Surfaces, University of Turin, Via Quarello 15/A, 10135 Torino, Italy

* Correspondence: linda.pastero@unito.it; Tel.: +39-011-670-5155

Received: 28 May 2018; Accepted: 23 June 2018; Published: 26 June 2018

Abstract: Bioinspired self-assembled composite materials are appealing both for their industrial applications and importance in natural sciences, and represent a stimulating topic in the area of materials science, biology, and medicine. The function of the organic matrix has been studied from the biological, chemical, crystallographic, and engineering point of view. Little attention has been paid to the effect of one of the two main components of the organic matrix, the sericin fraction, on the growth morphology of calcium carbonate polymorphs. In the present work, we address this issue experimentally, emphasizing the morphological effects of sericin on calcite and aragonite crystals, and on the formation of a sericin-aragonite-calcite self-assembled composite with a hierarchic structure comparable to that of natural nacre.

Keywords: biomineralization; calcite; aragonite; sericin; nacre; CO_2; composite; hierarchic structure

1. Introduction

While the structural aspects of biomineralization have been widely studied through many crystallographic techniques, the mechanisms regulating the polymorphs selection or the crystal habit modification in biomineralization need further work, mainly for their crucial importance in the field of the functionalized inorganic-organic composite materials.

A critical challenge in biomineralization is the calcite/aragonite selection in mollusk and gastropod shells; in mollusks, the precipitation of these two $CaCO_3$ polymorphs is modulated in the same shell, the polymorph selection being functional to the structural properties of the mineralized layer. Among the strategies carried out to obtain the synthetic equivalents of nacre [1–4], it is worth remembering a recent one [5], where a synthetic composite very close to both hierarchy and chemical composition of natural nacre was obtained by a classical predesigned matrix directed mineralization method, realizing a chitosan matrix through a freezing-induced process [6,7]. Chitosan is converted to β-chitin by acetylation, and then the matrix is mineralized by flowing $Ca(HCO_3)_2$ in the presence of polyacrylic acid and magnesium. Finally, nacre is obtained by silk fibroin infiltration and hot-pressing of the mineralized matrix.

It is well known that the protein-polysaccharide organic matrix plays a crucial role in the mechanical properties of the mineralized material. Nacre is a robust natural composite made up of of tabular calcium carbonate crystals (95%) which are intimately associated with layers of an organic matrix (5%) that is mainly built of: (i) water-soluble aspartic acid-rich proteins, (ii) glycoproteins, (iii) insoluble highly ordered β-chitin fibers and (iv) Gly-Ala-rich protein hydrogels structurally comparable with silk-fibroin [6,8–17]. The brick-and-mortar structure of nacre reduces crack spreading inside the structure and confers to the nacre a toughness of increased magnitude in comparison with

the sole aragonite [18,19]. Moreover, the large prismatic calcite crystals in the outermost layers of the shell structure are functional to both wear and impact resistance.

Many papers deal with the effect of the shell proteins on calcium carbonate polymorphs stabilization. For example, it is known that chitin fibers act as a template for crystallization of calcite crystals oriented with c-axis perpendicular to the surface of the shell [13].

Each component of the organic matrix in biomineralization has a role in controlling the nucleation of the calcium carbonate polymorphs, their orientation, and morphology, either in the classical way or by means of precursors such as an amorphous carbonate phase (ACC) both in-vivo and in-vitro [15,20–22]. Macromolecules are unanimously considered to be responsible for the selection of the polymorph. As an example, sericin hydrogel contains acidic proteins controlling the morphology and the polymorph. Furthermore, sericin gel in nacre has been suggested as a promoter for aragonite nucleation instead of calcite [15,20,23], through the ability of the acidic functional groups of sericin in binding Ca^{2+} [24].

Proteins associated with calcium mineralization have common features: (i) richness in Ca-coordinating residues, (ii) presence of repetitive sequences, and (iii) common β-sheet secondary structure [8,25]. Some Authors proposed that the regular array of carboxylic groups in the β-sheet structure may promote the epitaxial growth of calcium carbonate in pearls and oyster shells [6,8].

Electron diffraction analysis of the protein/aragonite assembly was carried out by Weiner and coworkers [16,26]. Accordingly, Mann [8] proposed that, at the organic/inorganic interfaces, the cooperation of the electrostatic accumulation of ionic charge at the organic matrix surface by primary cation-binding, the stereochemical requirements and the structural correspondence, favor the nucleation of a biomineral phase. Further, Mann considered the " ... one-to-one geometrical matching between the functional groups of the matrix and the crystallographic lattice dimensions of a specific crystal face in the overlying mineral phase" as an epitaxy between the matrix surface and the crystallizing mineral. The idea of an aragonite matrix enriched in aspartic acid (Asp) residues, initially proposed by Weiner [27], was re-tabled by Mann as well. This polyanionic matrix should be sufficient to control nucleation, polymorphism, and morphology of crystals, while the protein sheet controls the orientation of the calcite primer. Adding soluble shell proteins, does promote the stabilization of aragonite (instead of calcite), while polyacidic proteins drive nucleation and growth of different polymorphs and morphologies. Following these considerations, Mann proposed that the local sequence of charged Asp-residues "could act as a structurally organized nucleation site by binding Ca ions in a configuration corresponding to the 001 plane of aragonite". This epitaxial hypothesis reads: when comparing the Ca-Ca distance in the 001 plane with the periodicity of the organic matrix, an acceptable matching along the [100] axes (4.96 and 4.7 Å respectively) is found. In contrast, a greater mismatch is observed along the [010] axes (7.97 and 6.9 Å respectively), but, along this direction, a good coincidence occurs over a sequence of seven Ca atoms (≅48 Å). It follows that the aminoacid sequence of Asp residues belonging to the matrix substrate, represents optimum binding sites for calcium, thus providing specific nucleation sites.

Recently, Chevalier et al. [25] demonstrated that the formation of the β-sheet structure does not fulfill the conditions required to precipitate ordered arrays of $CaCO_3$ polymorphs, and proved that no specific interaction between the organic and inorganic phases could be evidenced.

In summary, the macromolecules of the organic fraction control polymorphism, orientation, and morphology of carbonate phases in biominerals. Hydrogels interact with the precipitation of carbonate crystals because of (i) the presence of functional groups which may directly interact with reacting ions, (ii) the effect of nucleation sites, and (iii) the interaction between steps and faces with the functional groups. The protein content is less than 2%, but they determine the structural organization and the properties of the composite [7].

Until now, no focused attention has been paid to every possible reticular interface that can be generated when an organized soft matrix (template) promotes on itself the crystallization of an adsorbed hard phase (one out of the calcium carbonate polymorphs, in our case). This paper aims

at reducing this lack of information, and we will strike a blow in favor of the leading role of the template/adsorbate epitaxy. We will deal with the effects of increasing concentrations of sericin in carbonated aqueous solutions, in order to define: (i) the selection of the $CaCO_3$ polymorphs, (ii) the single crystal morphology of the grown polymorphs, and (iii) the interfacial relationships (if any) in the system aragonite/calcite/sericin. The morphological effect will be interpreted on the grounds of the lattice coincidences between sericin (SFLP, silk fibroin like protein in the tables), and calcium carbonate polymorphs. For the sake of simplicity, the fourth index (hk$\bar{i}$l) used in the rhombohedral system (calcite crystal) will be replaced in the text by a point: $\rightarrow$ (hk.l).

2. Materials and Methods

Silk sericin from Bombix moori was purchased from Sigma-Aldrich (Sigma-Aldrich, St. Louis, MO, USA). Calcium chloride, calcium carbonate, ammonium carbonate were analytical grade reagents from Sigma-Aldrich.

Ultrapure water (18 MΩ) was obtained by using an Elga (Veolia Elga LabWater, High Wycombe, UK) Purelab Flex3 ultrapure water system. A calcium carbonate supersaturated solution was obtained by bubbling CO_2 in a calcite/water suspension (0.5 g/L) at room temperature and pressure. The final concentration of the calcium carbonate solution was 5 mM; pH was slightly acidic (5.4). The starting value of the saturation index (SI) of the solution calculated with respect to calcite was −1.41, and −1.55 with respect to aragonite. After equilibration with the atmosphere, the supersaturation values were 0.21 and 0.06 respectively for calcite and aragonite.

Silk sericin cast gel (CG) was obtained following the procedure suggested by Teramoto and coworkers [28]: a solution 1% *w*/*w* of silk sericin was spread on a PP plate (2 mL/cm^2) and dried at 25 °C overnight. After drying, the gel was covered by a thin layer of calcium carbonate saturated solution. The carbon dioxide was allowed to equilibrate with the atmosphere all night long. Calcium carbonate nucleated on the cast gel surface.

In G experiments, calcium carbonate crystal growth was obtained by the slow diffusion of gases released by the thermal decomposition of ammonium carbonate [29,30]. Multiwell cell culture plates were chosen as reactors to ensure the same conditions for each experiment. Each well was filled with 5 mL $CaCl_2$ solution and a variable concentration of sericin to verify the effect of the impurity on the growth of calcium carbonates. One among the wells was filled with $(NH_4)_2CO_3$ saturated solution as a source of carbon dioxide. The multiwell plate was sealed to ensure the saturation of the inner atmosphere in CO_2. A well was filled with $CaCl_2$ solution and a Riedel-De Haën universal pH indicator solution, to monitor the pH value. A control well filled with a calcium chloride solution without sericin was maintained in every batch to separate the effect of sericin from that of the concentration of calcium and carbonate.

The concentration of calcium chloride ranged between 0.1 M and 0.001 M. The concentration of sericin ranged from 1% *w*/*w* to 0.001%.

B experiments were performed by adding sericin to the solution in a concentration ranging from 0.001% to 0.5%. CO_2 was allowed to equilibrate with the atmospheric pressure for two days. Calcium carbonate precipitated as a consequence.

All G, B, and cast gel experiments were performed at room temperature and pressure.

Saturation indexes SI expressed as the ratio of ionic activity product (IAP) to solubility product K_{sp} were calculated for the growth experiments from pure solution by using PHREEQC software (version 3.3.9) [31]. For B and cast gel experiments, the SI of the pure $CaCO_3$ solution equilibrated with the atmosphere was 0.21 with respect to calcite and 0.06 with respect to aragonite, experimentally confirmed by the precipitation of calcite and a few aragonite aggregates whose persistence in the system depends on the rate of the gas equilibration with the atmosphere. Furthermore, in G experiments at saturation with respect to ammonium carbonate in water, the calculations gave very high SI for both calcite and aragonite. SI ranged from 3.6 to 5.6 for calcite and from 3.4 to 5.4 for aragonite. Such high SI values result in both polymorphs being stable, even in

the absence of specific impurities, as experimentally demonstrated. The results of the calculation are reported in Table 1 and in Figure S1.

Table 1. Saturation indexes (SI) and ionic strength (I) of the pure solutions used for B, G and cast gel experiments.

Experiment	Solution	SI Aragonite	SI Calcite	I
B and cast gel	$CaCO_3$ 5 mM	0.06	0.21	1.176×10^{-2}
G	$CaCl_2$ 0.1 M	5.42	5.57	30.75
	$CaCl_2$ 0.01 M	4.41	4.56	29.97
	$CaCl_2$ 0.001 M	3.41	3.56	29.89

The evaluation of the supersaturation in G experiments has to be considered only qualitative. In fact, due to the very high ionic strength of the system, the Debye-Hückel model results were inadequate, and the calculation showed a break-down at 30 mol/kg_w < I < 46 mol/kg_w. The model is not useful for calculations about the fugacity of CO_2. For high ionic strength systems, the specific interaction approach to thermodynamic properties of aqueous solutions should be used [32–35], but this approach is not incorporated in PHREEQC. Moreover, the effect of the addition of sericin to the solution on the supersaturation values with respect to carbonates was disregarded because of the lack of thermodynamic data about sericin.

Polarized optical microscopy was carried out using a Zeiss Axiolab Pol microscope (Carl Zeiss AG, Oberkochen, Germany) equipped with a rotary stage and a JVC 3-CCD KY F55B camera with 750 lines of horizontal resolution and a 60 dB signal-to-noise ratio to capture images and videos.

μ-Raman measurements were performed using a high-resolution confocal μ-Raman system HR800 by Horiba Jobin Yvon equipped with two gratings (1800 and 600 grooves/mm), air-cooled CCD detector, and green polarized laser (solid state Nd, 532 nm, 250 mW). Edge filters (532 nm) and interferential filters complete the system.

SEM imaging was obtained using both a JSM IT300LV High Vacuum–Low Vacuum 10/650 Pa, 0.3–30 kV (JEOL USA Inc., Peabody, MA, USA) equipped with secondary electron (SE) and backscattered electron (BSE) detectors (typical experimental conditions: W filament, EHT 20 kV, working distance 5 mm) and a Zeiss SUPRA 40 (Carl Zeiss AG, Oberkochen, Germany) field emission scanning electron microscope (FE-SEM) based on the 3rd generation GEMINI® column (typical imaging conditions WD = 3 mm, aperture size = 30.00 μm, EHT = 5 kV).

AFM measurements were performed using a DME Igloo SPM microscope (DME, Herlev, Denmark) equipped with a DS95-50E scanner (scan volume 50 × 50 × 5 μm). Data were acquired using MikroMasch Ultrasharp NSC16/Si3N4 Cr-Au back-coated cantilevers with typical resonance frequency 190 kHz, force constant 45 N/m, tip radius lower than 35 nm, and full tip cone angle 40°. All measurements were performed in alternated contact mode.

3. Results and Discussion

From our experiments, we can describe many noticeable effects of sericin on the crystal growth morphology and polymorphs stability of calcium carbonate, the magnitude and significance of these effects depending on the concentration of sericin in solution. The polymorph selection and the morphological effect are closely related and can be emphasized by different experimental setups.

3.1. The Effect of Sericin on the Growth Morphology of Calcite and Aragonite

The effect of sericin as a crystal habit modifier has been studied mainly through the G experiments (see Section 2 for details). From G experiments we obtained both calcite and aragonite polymorphs in pure solution and in the presence of sericin. In fact, very high supersaturation values were reached at the interface between the solution and the surrounding atmosphere, due to the increasing exchange rate in correspondence of the interface. The supersaturation of the pure $CaCO_3$ solution obtained was evaluated using the PHREEQc [31] software (Table 1, Figure S1). The addition of sericin as an impurity into the system has a substantial effect on the nucleation frequency (modifying the supersaturation value and the viscosity of the medium), as well as on the morphology of both polymorphs.

At high supersaturation, aragonite polymorph occurs as aggregates of thin lamellae dominated by the {001} form. In the pure calcium carbonate solution, the aggregates show a very complex morphology, originating "rosetta-like" crystals (Figure 1a) composed by small aragonite platelets with morphology ruled by the {001} form and encompassed by the {010} and {110} forms (Figure 1c and inset). The "rosetta-like" morphology was already described in the literature by Gehrke [36], petals being built by the superposition of single aragonite crystals. Its appearance was ascribed to the sole effect of the supersaturation, as we can confirm.

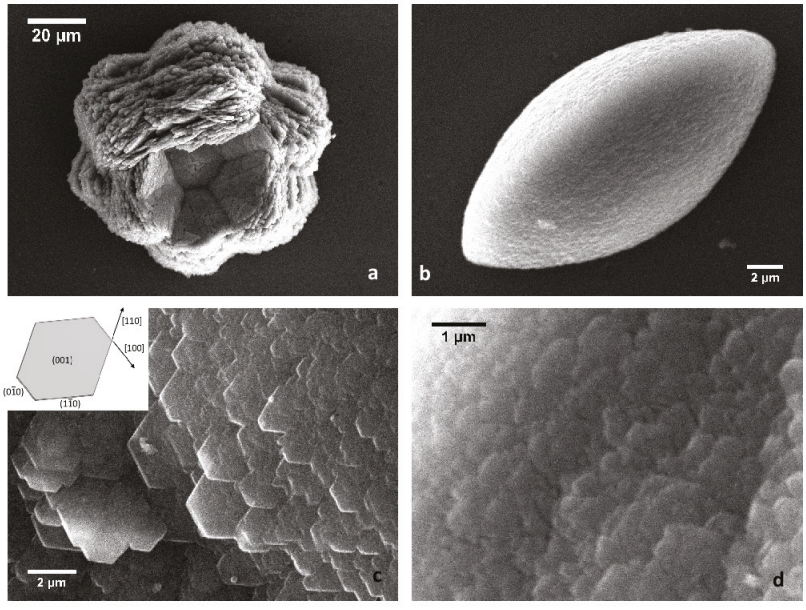

Figure 1. (**a**) "Rosetta-like" aggregate of aragonite grown in pure calcium carbonate solution and (**b**) in the presence of sericin (0.1%), in this case, the aggregate takes on the discoid morphology with smoother surfaces. (**c**) A detail of the aggregate from pure $CaCO_3$ solution, in the inset, the outline of the single crystal of aragonite forming the aggregate, and (**d**) detail of the aggregate grown in the presence of sericin.

In the presence of sericin, the size of the aggregates decreases, aragonite platelets' edges [110] and [100] become unstable and rounded, giving the single crystals an irregular behavior. The whole aspect of the "rosetta-like" aggregates is extremely modified by the presence of the impurity. At high concentrations of sericin, the aggregates take a discoid morphology with smoother surfaces, as shown in Figure 1b. Under quite a different pH and concentration conditions, Cheng and coworkers [24] obtained "rice-like" crystals of calcite, attributing the unusual morphology to the template effect of the

protein on the nucleation and growth of calcite. The simultaneous decrease in aggregates and single platelets size and the loss of stability of the edges of platelets ground the assumption of a synergic effect of sericin on both the supersaturation of the solution and the crystal morphology. The effect of sericin on aragonite morphology becomes evident when its concentration is approximately 0.05% *w*/*w*.

Calcite crystals also show a morphological change due to the presence of sericin as an impurity in solution. This originates: (i) in the stabilization of the {00.1}-pinacoid and the {11.0}-prism, and (ii) in the loss of stability of the $[\bar{4}41]$ and $[48\bar{1}]$ edges of the cleavage rhombohedron (Figure 2) which, in turn, produces the appearance of rough {10.4} surfaces. This effect may be recognized since the lower concentration of sericin and rises in magnitude, with the increasing concentration of the impurity.

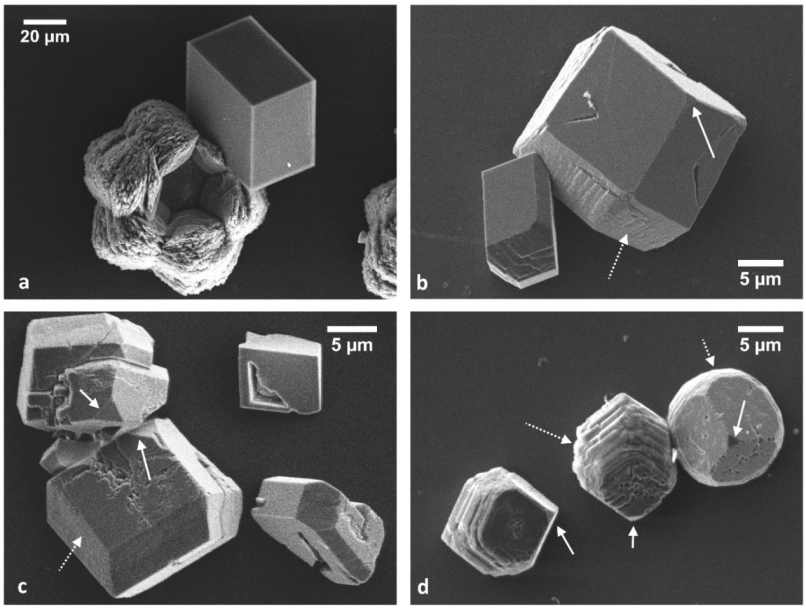

Figure 2. (**a**) calcite crystal and aragonite aggregate grown from pure calcium carbonate solution; (**b**) and (**c**) crystals of calcite grown in the presence of sericin (0.05% *w*/*w*), showing the incoming roughness of the cleavage rhombohedron and the appearance of the prism (dotted white arrows) and the pinacoid (solid white arrows). (**d**) The edges of the cleavage rhombohedron $[\bar{4}41]$ and $[48\bar{1}]$ are destabilized by the presence of sericin at higher concentration (0.1% *w*/*w*).

The staggering effect of sericin on calcite morphology is particularly significant when considering the growth morphology of prismatic calcite from *Pinna nobilis* shown by Marin in 2004 [37]. Removing the organic matrix from a *Pinna nobilis*' shell by using sodium hypochlorite, the authors obtained calcite crystals with well-developed {00.1} pinacoid and a prism (not indexed because of the lack of reference forms). Our crystals show small pinacoids and more developed prisms; even if the cleavage rhombohedron still dominates the morphology, the trend in morphological modification reflects the biological morphologies.

3.2. The Effect of Sericin on the Polymorph Selection

B and CG experiments are well suited to investigating the mechanism of growth of calcium carbonate spherulites and the role of the impurity in the selection of the polymorph. In general, the spherulitic aggregates take place since the early stages of growth, but only in the presence of

sericin and at the interface between solution and air. In Figure 3a,b, the spherulitic aggregates are characterized by the typical dark extinction cross when observed by polarized optical microscopy.

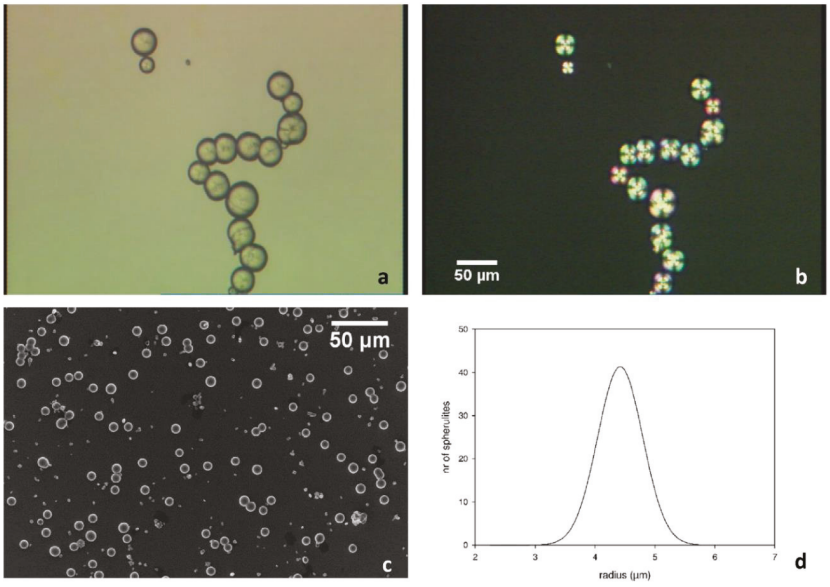

Figure 3. B experiment with 0.5% of sericin: spherulites are the prevailing morphology obtained, their nature of radial aggregates characterized by the typical dark extinction cross in polarized optical microscopy (**a**,**b**). The size distribution of the aggregates is quite uniform (**c**) and represented by a narrow Gaussian curve centered on 4.5 µm (**d**).

Calcium carbonate starts to grow as spherulitic polycrystalline aggregates of aragonite (as will be discussed in the following paragraphs). The size distribution is homogeneously scattered in a very narrow interval: as an example (see Figure 3c), in a B experiment in the presence of 0.5% of sericin, the radius of the aggregates is narrowly distributed around 4.5 µm (Figure 3d). The limited spread in size distribution of the spherulites may be related to two concurring factors: (i) the supersaturation value of the solution, depending on the concentration of calcium carbonate and sericin, and (ii) the nucleation of calcium carbonate on the external surfaces of CO_2 bubbles of selected size, that in turn depends on the pressure inside the vessel.

The presence of bubbles acting as nucleation centers for calcium carbonate is confirmed by the spherical holes at the center of the spherulites. In previous experiments carried out in pure water/carbonate solutions, gas bubbles nucleated heterogeneously onto solid substrates (glass slices, reactor walls) [38,39]. In the present case, bubbles nucleate preferentially at the solution/air interface, owing to the action of the sericin that modifies the ratio between the surface energies between gas and solution. The aggregates grow surrounding the bubbles toward the solution, forming "pearl-necklace" aggregates and single spherulites (Figure 3).

Figure 4a shows a section of two large and connected spherulites: the spherulite on the right is cut near the midpoint and shows the shape and size of the hollow center. The size of the cavity coincides with that of the gas bubble acting as a substrate (4.3 µm), and is close to those obtained by bubbling CO_2 in a calcium carbonate solution at room temperature and pressure by equilibrating the partial pressure of the CO_2 with the atmosphere [38]. Variable concentrations of sericin in solution modify the value of the specific surface energy between gas and solution and, accordingly, the size of the bubbles [39]. Spherulitic structures similar to those here described were already shown by Falini et al.

in 1996 [15], who associated the presence of sericin to the nucleation of the aragonite polymorph. In the paper by Cheng [24], the authors described the formation of "rice-like" and spherical aggregates in the presence of silk fibroin, the spherical ones being morphologically very similar to those obtained in this work, but made up of calcite crystals.

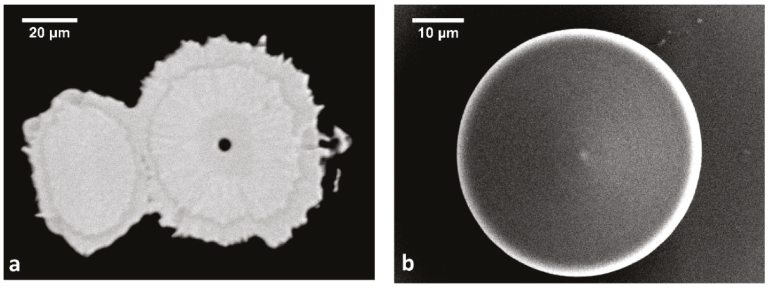

Figure 4. Sections of spherulites: (**a**) the center of the spherulite is a spherical cavity of about 4.3 µm of diameter. At the early stages of evolution, the spherulite grows by concentric layers around the cavity, as shown in (**b**). During the late stages of growth, the outermost layers become irregular (see (**a**)).

The spherulite grows by superposition of concentric shells of calcium carbonate (Figure 4b).

Experimentally, the final size of the spherulites is found to be dependent both on time left for the growth of the aggregates and on the concentration of the impurity. After 12 h of growth, the effect of the concentration of sericin on the size of the spherulites is definitely demonstrated. This means that, even if we did not evaluate the supersaturation of the solution in the presence of such organic impurities, it is reasonable to assume that this value strongly depends on the concentration of the sericin that hinders the nucleation rate, and consequently, increases the size of the spherulites.

At the SEM scale, the surface of the aragonite aggregates seems smooth and somewhat regular, and it is demonstrated to be formed by an aragonite-sericin composite by µ-Raman measurements. At the AFM scale (Figure 5), the aggregates were shown to be covered by nano-sized cobbles with poorly-defined geometries recalling the morphology of aragonite crystals obtained in G experiments (Figure 1d), with the edges rounded by the presence of sericin. Within this first grown layer, aragonite is intimately associated with sericin; in fact, both aragonite and sericin Raman fingerprints are detected.

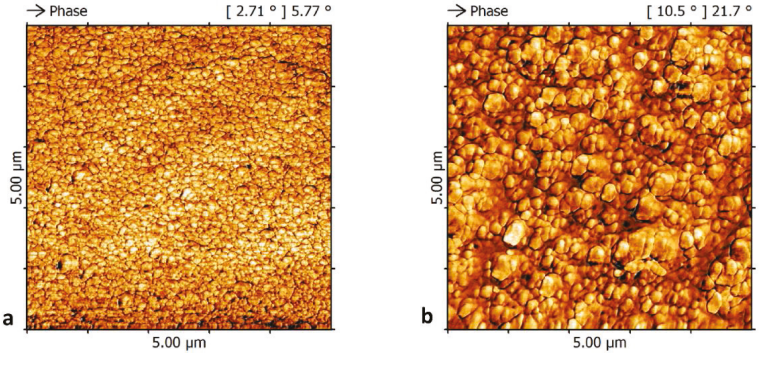

Figure 5. (**a**) AFM-Phase image of the surface of a spherulite grown in a solution containing 0.25% w/w of sericin, (**b**) AFM-Phase image of the surface of a spherulite grown in a solution containing 0.5% w/w of sericin.

The quality of the coverage, the mean size, and the dispersion of the size distribution of the cobbles on the surface of the aragonite aggregate depend on the concentration of the sericin in solution, as proven by the AFM measurements. This dependence is related to the effect of the impurity on the nucleation frequency of the crystals on the spherulites obtained in the most concentrated solution. In fact, in 0.25% w/w grown spherulites (Figure 5a), the cobbles cover the surface of the aggregate uniformly, while in 0.5% w/w grown spherulites (Figure 5b), the coverage is less uniform and the mean size of the cobbles is larger. This observation plays in favor of our early observation about the effect exerted by sericin on the supersaturation of the solution (in G experiments), i.e., at high concentration, sericin lowers the supersaturation even if the concentration of the calcium carbonate in solution is kept constant, thereby decreasing the nucleation rate and increasing the size of the crystals.

As the growth of the composite spherulite proceeds, aragonite aggregates are covered by a rough outer layer of trigonal crystals, as shown in Figure 6a. μ-Raman measurements confirm the presence of both polymorphs as concentric shells around the cavity left by the bubble and the presence of sericin. The signal of sericin is stronger in the inner parts of the aggregate, in correspondence with aragonite, and decreases toward the outer shells made of calcite (Figure 6e and Figure S2). The rough outer part is made by calcite growing with a spindle-like, columnar morphology developing along the radii of the spherulite (Figure 6b,c). This behavior leads to the formation of aggregates, as shown in Figures 6a and 7. However, a weak signal from sericin is detected in the calcite innermost layer of the layered structure. The signal of the sericin is wholly lost only in the very far part of the crystals, where the morphology tends to cure, originating calcite crystals with a complete morphology (Figure 7d).

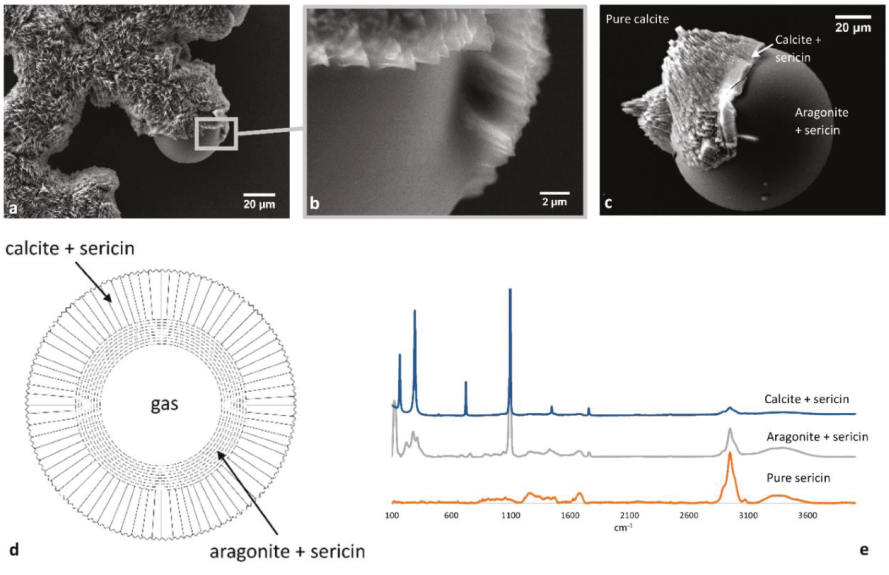

Figure 6. (**a**) a detail of a "pearl-necklace" aggregate of spherulites almost entirely covered by calcite, the trigonal symmetry being stunning evident; (**b**) detail of a spherulitic aggregate from (**a**), not yet wholly covered by columnar calcite crystals; (**c**) a spherulite partially covered by calcite. From μ-Raman measurements, the smoothest part results to be an aragonite-sericin composite, the first layer overgrown is composed by calcite and sericin and the farthest columnar layer by pure calcite (**d**); (**e**) μ-Raman spectra of the layers composing the final spherulite compared with the spectrum of pure sericin.

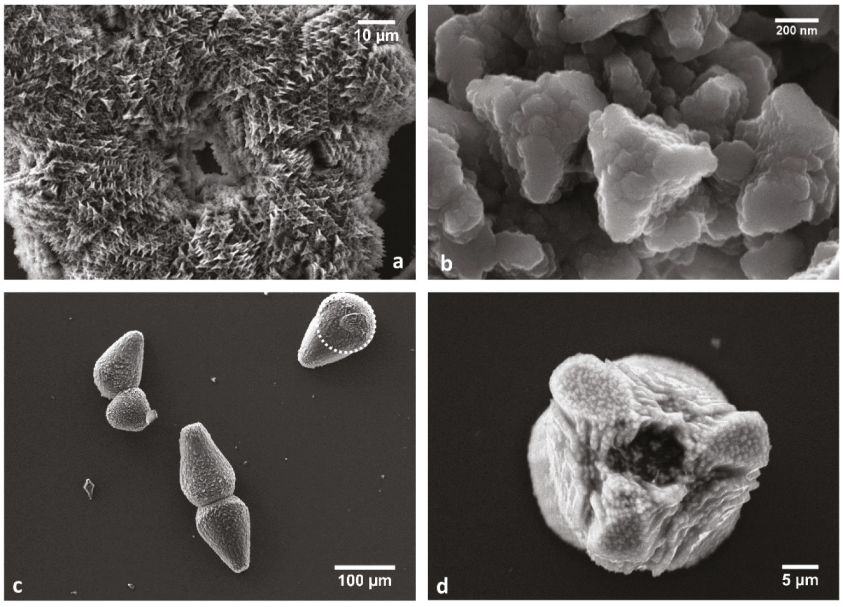

Figure 7. (**a**) Calcite aggregate completely masking the presence of spherulitic aragonite. The image outlines the trigonal symmetry of the crystals; (**b**) a detail of the skeletal calcite crystals growing from the surface of the spherulites; (**c**) when growing without hindrance, calcite gives to the aggregates a "pear-like" morphology. During the early stages of this overgrowth, the presence of the original spherulites is recognizable (dotted circle in the upper right aggregate); (**d**) the rounded shape of the original spherulite is partially masked by the overgrowth of calcite. Calcite skeletal crystals coalesce during growth, forming larger {10.4} surfaces.

The spindle-like columnar crystals are terminated toward the solution by irregular cleavage rhombohedra. In Figure 7a, the orientation of the three-fold axis of calcite toward the observer is clearly evident. At higher magnification, one can recognize skeletal calcite crystals with only the cleavage {10.4} rhombohedron stable surface, encompassed by unstable edges with mean orientation along the $[42\bar{1}]$ and [010] directions. The upper break-off of the crystal is represented by a bumpy {00.1} pinacoid which is macroscopically covered by cobbles, and the elongation of the crystal is due to the presence of an irregular, rounded, and strongly unstable {10.0} prism. This morphology represents the instability of the edges of the cleavage rhombohedron (from G experiments, see Figure 2).

The surface of the aggregate is rough (Figures 6 and 7), and if allowed to grow until the early layers are completely masked by the late ones and not confined, the spherulites take a "pear-like" morphology (Figure 7c), completely covered by calcite crystals with the very unusual morphology already described. The coalescence of many skeletal cleavage rhombohedra yields the formation of larger surfaces, as in Figure 7d. When spherulites are neighboring, during growth they can aggregate, forming the "pearl-necklace" morphologies shown in Figures 3 and 6.

Summing up, it has been shown for the first time what should be the fate of a quasi-stagnant and sericin doped Ca-carbonated aqueous solution that isothermally and spontaneously evolves around CO_2 bubbles from an initial saturation index towards the equilibrium. Ca-carbonate crystallizes at the interface bubble/solution in the form of aragonite during the early stages of growth and in the form of calcite at the end of the growth, the signal from sericin decreasing from the inner part toward the outermost layers, according to the scheme reported in Figure 6d. This behavior reminds one of the

crystallization sequence in mussels' shells, where an aragonite floor sets up in the inner part of the shell, intimately involved with the shell proteins, and followed by a thick layer of columnar calcite.

3.3. Lattice Coincidences between Aragonite (001) and Calcite (00.1) for Epi-Growth on Sericin (001)

As demonstrated in many previous papers, the 2D-epitaxial growth may be considered a common thread for the modification of a crystal growth habit and phase stabilization [40–44]. In the case of sericin and calcium carbonate polymorphs, we started from the considerations by Mann [8] about the matching of the Ca-Ca distances in the 001 plane of aragonite along the directions [010] and [100]. In detail, we remarked at first that: (i) a close matching occurs between the vectors $2 \times [100]_{Ar}$ = 9.922 Å and $2 \times [1/2\ 00]_{SFLP}$ = 9.5 Å, corresponding to a linear misfit of −4.4%, and (ii) a greater mismatch is observed between $[010]_{Ar}$ = 7.9672 Å and $[010]_{SFLP}$ = 6.9 Å, corresponding to a linear misfit of −15.4% that does not fulfill the epitaxy constraints. The linear misfits going in the same sense, the resulting misfit between the areas forming the 2D coincidence cell is dramatic. In fact, the coincidence cell of aragonite (001) has a multiplicity (2×), and the corresponding multiplicity of SFLP (001) is (1×), i.e., the areas of the coincidence cells are 79.05 $Å^2$ for aragonite and 65.55 $Å^2$ for sericin, respectively. Hence, the misfit of the two areas reaches the value of 20.59%, and accordingly, the associated probability of epitaxy is excluded.

According to the suggestion proposed in the Mann's paper, we found a coincidence lattice (Table 2 and 8b in Table 3) fulfilling the linear geometry conditions for epitaxy; however, the area of the corresponding 2D coincidence mesh is so high that it would occupy only the eleventh position in the ranking drawn in Table 3.

In the case of the coupling calcite/sericin, the unit cell of the host sericin substrate is the same as before, while the cell area for the form {001} of calcite is given by the scalar product [100] × [010] = 4.9896 × 4.9896 × cos30° = 21.5606 $Å^2$.

Moreover, we also tested the interface between $(00.1)_{Cc}/(001)_{SFLP}$ (Tables 4 and 5). It is worth outlining that the rotation angle indicates the angle between the vectors [100] of the two mutually rotated cells.

It is interesting to notice that, in the case of sericin on calcite, the surface lattice coincidences are not as good as in the case of sericin on aragonite, mainly due to the high angular misfit that lead to incremental errors in the coincidence areas.

In order to evaluate the hypothetical effect of sericin on the transition between aragonite in the inner part of the aggregate to calcite in the outermost layer, we checked the opportunity of good epitaxial agreement between calcite and aragonite. Given that the most developed form of aragonite in our spherulitic growth is represented by the (001) face, and that, experimentally, we found that calcite grows radially from the surface of the aragonite layer toward the solution with the three-fold axis almost perpendicular to the surface of the spherulite, we also checked the potential coincidences between the $(001)_{Ar}$ and the $(00.1)_{Cc}$ (Tables 6 and 7).

The coincidences between the $(001)_{Ar}$ and the $(00.1)_{Cc}$ are extraordinarily good, providing further proof of the control exerted by the substrate (aragonite) on the orientation of the guest phase (calcite).

Table 2. Comparison between host (sericin) and guest (aragonite) surface cells.

Host Substrate (SFLP) Form {001}	**Guest Crystal (Aragonite) Form {001}**
Unit cell (Å): [100] × [010] = 9.5 × 6.9 = 65.55 $Å^2$	Unit cell cell (Å): [100] × [010] = 4.9611 × 7.9672 = 39.526 $Å^2$

Table 3. 2D-coincidence cells at the interface (001)Ar/(001)SFLP.

2D-Coincidence Cells	Cell Vectors (Å)	Cell Vectors (Å)	Linear Misfit (Δ%)	Notes
(1a)	$-2 \times [1/2\ 00] = 9.5$	$-[110] = 9.3855$	−1.22	Rotation angle 55°
	$1/2[1\bar{6}0] = 21.238$	$[4\bar{1}0] = 21.384$	+0.69	Angular misfit: **2.63°**
Area (Å^2) and 2D-cell multiplicity	**196.65 (3×)**	**197.63 (5×)**	**+0.5**	Opposite linear misfits
(1b)	$2 \times [1/2\ 00] = 9.5$	$[110] = 9.3855$	−1.22	Rotation angle 58.5°
	$-1/2\ [160] = 21.238$	$[3\bar{2}0] = 21.804$	+2.66	Angular misfit: **2.12°**
Area (Å^2) and 2D-cell multiplicity	**196.65 (3×)**	**197.63 (5×)**	**+0.5**	Opposite linear misfits
(2)	$-[120] = 16.754$	$[1\bar{2}0] = 16.689$	−0.39	Rotation angle 52°
	$1/2\ [\bar{3}20] = 15.832$	$-[310] = 16.88$	+6.61	Angular misfit: **2.16°**
Area (Å^2) and 2D-cell multiplicity	**262.2 (4×)**	**276.682 (7×)**	**+5.52**	Opposite linear misfits
(3a)	$-[120] = 16.754$	$-[120] = 16.689$	−0.39	Rotation angle 20°
	$[2\bar{1}0] = 20.214$	$4 \times [100] = 19.844$	−1.86	Angular misfit: **2.71°**
Area (Å^2) and 2D-cell multiplicity	**327.75 (5×)**	**355.734 (9×)**	**−8.53**	Linear misfits in the same sense
(3b)	$[1\bar{2}0] = 16.754$	$[3\bar{1}0] = 16.882$	+0.76	Rotation angle 25°
	$[2\bar{1}0] = 20.214$	$4 \times [100] = 19.844$	+1.95	Angular misfit: **2.26°**
Area (Å^2) and 2D-cell multiplicity	**327.75 (5×)**	**355.734 (9×)**	**−8.53**	Linear misfits in the same sense
(4a)	$-[120] = 16.754$	$-[120] = 16.689$	−0.39	Rotation angle 17°
	$1/2\ [3\bar{6}0] = 25.131$	$2 \times [2\bar{1}0] = 25.45$	+1.27	Angular misfit: **0.56°**
Area (Å^2) and 2D-cell multiplicity	**393.30 (6×)**	**395.26 (10×)**	**+0.5**	Opposite linear misfits
(4b)	$-[120] = 16.754$	$-[120] = 16.689$	−0.39	Rotation angle 17°
	$1/2\ [1.\bar{1}0.0] = 34.825$	$[3\bar{4}0] = 35.1729$	+0.99	Angular misfit: **0.56°**
Area (Å^2) and 2D-cell multiplicity	**393.30 (6×)**	**395.26 (10×)**	**+0.5**	Opposite linear misfits
(4c)	$-[120] = 16.754$	$-[120] = 16.689$	−0.39	Rotation angle 17°
	$1/2[5\bar{2}0] = 24.732$	$5 \times [100] = 24.8055$	+0.297	
Area (Å^2) and 2D-cell multiplicity	**393.30 (6×)**	**395.26 (10×)**	**+0.5**	Opposite linear misfits
(4d)	$[1\bar{2}0] = 16.754$	$[310] = 16.882$	+0.75	Rotation angle **84°**
	$-1/2\ [360] = 25.131$	$2 \times [2\bar{1}0] = 25.45$	+1.27	Angular misfit: **0.25°**
Area (Å^2) and 2D-cell multiplicity	**393.30 (6×)**	**395.26 (10×)**	**+0.5**	Linear misfits in the same sense

Table 3. *Cont.*

2D-Coincidence Cells	Cell Vectors (Å)	Cell Vectors (Å)	Linear Misfit (Δ%)	Notes
(4e)	$[1\bar{2}0] = 16.754$	$[310] = 16.882$	+0.75	Rotation angle **85°**
	$-1/2\,[520] = 24.732$	$[1\bar{3}0] = 24.411$	−1.31	Angular misfit: **1.90°**
Area (Å^2) and 2D-cell multiplicity	**393.30 (6×)**	**395.26 (10×)**	**+0.5**	Opposite linear misfits
(5)	$[1\bar{2}0] = 16.754$	$[3\bar{1}0]$=16.882	+0.76	Rotation angle 27°
	$1/2\,[540] = 27.4682$	$-3 \times [110] = 28.1565$	+2.50	Angular misfit: **0.63°**
Area (Å^2) and 2D-cell multiplicity	**458.85 (7×)**	**474.312 (12×)**	**+3.37**	Linear misfits in the same sense
(6a)	$-1/2[360] = 25.131$	$-[130] = 24.411$	−2.95	Rotation angle 23°
	$-[2\bar{1}0] = 20.214$	$-\,4 \times [100] = 19.844$	−1.86	Angular misfit: **2.86°**
Area (Å^2) and 2D-cell multiplicity	**491.625 (7.5×)**	**474.312 (12×)**	**−3.65**	Linear misfits in the same sense
(6b)	$1/2\,[1\bar{8}0] = 28.006$	$3 \times [1\bar{1}0] = 28.156$	+0.54	Rotation angle 23°
	$[2\bar{1}0] = 20.214$	$4 \times [100] = 19.844$	−1.86	Angular misfit: **2.86°**
Area (Å^2) and 2D-cell multiplicity	**491.625 (7.5×)**	**474.312 (12×)**	**−3.65**	Linear misfits in the same sense
(7)	$1/2\,[3.\overline{10}.0] = 37.327$	$4 \times [1\bar{1}0] = 37.542$	+0.57	Rotation angle 10°
	$-[230] = 28.098$	$-3 \times [110] = 28.1565$	+0.21	Angular misfit: **nil**
Area (Å^2) and 2D-cell multiplicity	**950.475 (14.5×)**	**948.624 (24×)**	**−0.19**	Linear misfits in the same sense
(8a)	$2 \times [1/2\,00] = 9.5$	$2 \times [100] = 9.922$	+4.44	Rotation angle 0°
S. Mann coincidence cell	$[010] = 6.9$	$[010] = 7.9672$	+15.46	Angular misfit: **0°**
Area (Å^2) and 2D-cell multiplicity	**65.55 (1×)**	**79.052 (2×)**	***+20.6***	Linear misfits in the same sense
(8b)	$2 \times [1/2\,00] = 9.5$	$2 \times [100] = 9.922$	+4.44	Rotation angle 0°
S. Mann multiple cell	$7 \times [010] = 48.3$	$6 \times [010] = 47.83$	−1.03	Angular misfit: **0°**
Area (Å^2) and 2D-cell multiplicity	**458.85 (7×)**	**(12×)**	***+3.43***	Opposite linear misfits

Table 4. Comparison between host (sericin) and guest (calcite) surface cells.

Host Substrate (SFLP) Form {001}	Guest Crystal (Calcite) Form {001}
Unit cell: [100] × [010] = 65.55 Å^2	Unit cell: [100] × [010] = 21.5606 Å^2

Table 5. 2D-coincidence cells at the interface (00.1)Cc/(001)SFLP. (1a) and (1b) correspond to the same mutual position of the two lattices: this proves that both area and angular misfit play against the epitaxy.

2D-Coincidence Cells	Cell Vectors (Å)	Cell Vectors (Å)	Linear Misfit (Δ%)	Notes
(1a)	$3 \times [010] = 20.7$ $[100] = 9.5$	$4 \times [010] = 19.9584$ $[210] = 8.6422$	−3.72 −9.92	Rotation angle 0° Angular misfit: **0°**
Area (Å^2) and 2D-cell multiplicity	**196.65 (6×)**	**172.484 (8×)**	**−14.01**	Linear misfits in the same sense
(1b)	$3 \times [010] = 20.7$ $1/2\,[1\bar{2}0] = 8.376$	$4 \times [010] = 19.9584$ $[1\bar{1}0] = 8.6422$	−3.72 +3.18	Rotation angle 0° Angular misfit: **4.54°**
Area (Å^2) and 2D-cell multiplicity	**98.325 (3×)**	**86.2426 (4×)**	**−14.01**	Linear misfits in the same sense
	$-1/2\,[120] = 8.376$ $-[210] = 20.214$	$[1\bar{1}0] = 8.6422$ $-4 \times [010] = 19.9584$	+3.18 −1.28	Rotation angle 70° Angular misfit: **5.50°**
Area (Å^2) and 2D-cell multiplicity	**98.325 (3×)**	**86.2426 (4×)**	**−14.01**	Opposite linear misfits
(2a)	$1/2\,[120] = 8.376$ $[100] = 9.5$	$[120] = 8.6422$ $[210] = 8.6422$	+3.18 −9.92	Rotation angle 8° Angular misfit: **4.54°**
	65.55 (2×)	**64.682 (3×)**	**−1.34**	Opposite linear misfits
(2b)	$1/2\,[1\bar{2}0] = 8.376$ $[100] = 9.5$	$[210] = 8.6422$ $[120] = 8.6422$	+3.18 −9.92	Rotation angle 58° Angular misfit: **4.54°**
	65.55 (2×)	**64.682 (3×)**	**−1.34**	Opposite linear misfits
(2c)	$[1\bar{2}0] = 16.752$ $1/2\,[100] = 4.75$	$3 \times [100] = 14.9688$ $[010] = 4.9896$	**−11.91** +5.04	Rotation angle 90° Angular misfit: **4.54°**
	65.55 (2×)	**64.682 (3×)**	**−1.34**	Opposite linear misfits
(2d)	$-2 \times [010] = 13.8$ $1/2\,[100] = 4.75$	$[2\bar{1}0] = 13.2012$ $[110] = 4.9896$	−4.53 +5.04	Rotation angle 43° Angular misfit: **10.89°**
	65.55 (2×)	**64.682 (3×)**	**−1.34**	Opposite linear misfits
(2e)	$-2 \times [010] = 13.8$ $-1/2\,[100] = 4.75$	$[1\bar{2}0] = 13.2012$ $-[110] = 4.9896$	−4.53 +5.04	Rotation angle 19° Angular misfit: **10.89°**
	65.55 (2×)	**64.682 (3×)**	**−1.34**	Opposite linear misfits
(2f)	$-1/2\,[140] = 14.5946$ $1/2\,[100] = 4.75$	$3 \times [100] = 14.9688$ $[010] = 4.9896$	+2.564 +5.04	Rotation angle 82° Angular misfit: **11.006°**
	65.55 (2×)	**64.682 (3×)**	**−1.34**	Linear misfits in the same sense

Table 5. *Cont.*

2D-Coincidence Cells	Cell Vectors (Å)	Cell Vectors (Å)	Linear Misfit (Δ%)	Notes
(3)	$[1\bar{3}0] = 22.776$ $1/2\,[100] = 4.75$ **98.325 (3×)**	$[1\bar{4}0] = 22.865$ $[110] = 4.9896$ **107.803 (5×)**	+0.39 +5.04 **+9.64**	Rotation angle 35° Angular misfit: **5.54°** Linear misfits in the same sense
(4)	$1/2\,[300] = 14.25$ $-1/2\,[160] = 21.238$ **294.975 (9×)**	$[230] = 13.20$ $[3\bar{2}0] = 21.749$ **107.803 (13×)**	−7.94 +2.406 **−5.24**	**?** **?** Opposite linear misfits
(5a)	$1/2\,[1\bar{6}0] = 21.238$ $-[210] = 20.214$ **426.075 (13×)**	$[2\bar{3}0] = 21.749$ $-4 \times [110] = 19.9584$ **431.213 (20×)**	+2.406 −1.28 **+1.20**	Rotation angle 11° Very low angular misfit Opposite linear misfits
(5b)	$1/2\,[3\bar{4}0] = 19.839$ $-[130] = 22.776$ **426.075 (13×)**	$4 \times [100] = 19.9584$ $-[150] = 22.865$ **431.213 (20×)**	+0.612 +0.39 **+1.20**	Rotation angle 15° Very low angular misfit Linear misfits in the same sense
(5c)	$-1/2\,[160] = 21.238$ $[\bar{2}10] = 20.214$ **426.075 (13×)**	$[2\bar{3}0] = 21.749$ $-4 \times [110] = 19.9584$ **431.213 (20×)**	+2.406 −1.28 **+1.20**	Rotation angle 50° Very low angular misfit Opposite linear misfits

Table 6. Comparison between host (calcite) and guest (aragonite) surface cells.

Host Crystal (Calcite) Form {001}	Guest Crystal (Aragonite) Form {001}	Misfit (Δ%)
$[100] = [010] = 4.9896$ $\gamma = 120°$	$[100] = 4.9611$; $[010] = 7.9672$ $\gamma = 90°$	
$2 \times$ Unit cell: $[100] \times [010] \times \cos 30° = 43.121$	Unit cell: $[100] \times [010] = 4.9611 \times 7.9672 = 39.526$	**−9.096**

Table 7. 2D-coincidence cells at the interface (00.1)Cc/(001)Ar.

2D-Coincidence Cells	Cell Vectors (Å)	Cell Vectors (Å)	Linear Misfit (Δ%)	Notes
	[010] = 4.9896 [210] = 8.6422	[100] = 4.9611 −[010] = 7.9672	−0.574 −8.47	Rotation angle **90°**
Area (Å^2) and 2D-cell multiplicity	**43.121 (2×)**	**39.526 (1×)**	**−9.096**	Linear misfits in the same sense
	[1$\bar{1}$0] = 8.6422 −[120] = 8.6422	[1$\bar{1}$0] = 9.3855 −[110] = 9.3855	+8.60 +8.60	Rotation angle **0°**
Area (Å^2) and 2D-cell multiplicity	**64.681 (3×)**	**79.052 (2×)**	**+22.2**	Linear misfits in the same sense
	2 × [100] = 9.9792 2 × [110] = 9.9792	[1$\bar{1}$0] = 9.3855 2 × [100] = 9.9222	−6.325 −0.574	Rotation angle **30°**
Area (Å^2) and 2D-cell multiplicity	**86.242 (4×)**	**79.052 (2×)**	**−9.096**	Linear misfits in the same sense
	−[230] = 13.2012 2 × [1$\bar{1}$0] = 17.2844	−[210] = 12.725 [1$\bar{2}$0] = 16.6888	−3.74 −3.56	**(a)**Rotation angle **11°**
Area (Å^2) and 2D-cell multiplicity	**215.605 (10×)**	**197.63 (5×)**	**−9.096**	Linear misfits in the same sense
	[1$\bar{4}$0] = 22.8652 −[230] = 13.2012	−3 × [010] = 23.9016 −[210] = 12.725	+4.53 −3.74	**(b)**Rotation angle **11°**
Area (Å^2) and 2D-cell multiplicity	**237.165 (11×)**	**237.156 (6×)**	**+0.04**	Opposite linear misfits
	[320] = 13.2012 5×[010] = 24.948	[2$\bar{1}$0] = 12.725 2×[210] = 25.45	−3.74 +2.012	Rotation angle **52°**
Area (Å^2) and 2D-cell multiplicity	**323.4075 (15×)**	**316.208 (8×)**	**−2.28**	Opposite linear misfits
	−[350] = 21.7492 3 × [1$\bar{1}$0] = 25.9266	−[320] = 21.8040 [2$\bar{3}$0] = 25.8792	+0.252 −0.183	Rotation angle **8°**
Area (Å^2) and 2D-cell multiplicity	**517.452 (24×)**	**513.838 (13×)**	**−0.703**	Opposite linear misfits
	[2$\bar{3}$0] = 21.7492 3 × [210] = 25.9266	−[320] = 21.8040 [2$\bar{3}$0] = 25.8792	+0.252 −0.183	Rotation angle **66°**
Area (Å^2) and 2D-cell multiplicity	**517.452 (24×)**	**513.838 (13×)**	**−0.703**	Opposite linear misfits
	[3$\bar{2}$0] = 21.7492 2 × [320] = 26.402	−[320] = 21.8040 [2$\bar{3}$0] = 25.8792	+0.252 −2.022	Rotation angle **80°**
Area (Å^2) and 2D-cell multiplicity	**517.452 (24×)**	**513.838 (13×)**	**−0.703**	Opposite linear misfits

4. Conclusions

Two main effects due to the presence of sericin as an impurity in solution on the growth of calcium carbonate crystals have been experimentally confirmed: (i) a morphological effect on both calcite and aragonite, and (ii) a polymorph-stabilizer effect.

Concerning the first point, aragonite crystal morphologies have been compared in pure solution and in the presence of sericin. Even if the "rosetta-like" aggregates have already been described in the literature, the morphology of the single lamellae of aragonite building up the aggregates is modified by the presence of sericin. The lamellae are dominated by the flat {001} form, and encompassed by almost inexistent {110} and {100} forms. In the presence of sericin, the edges [110] and [010] of the single lamella lose their stability, becoming rounded and irregular. Moreover, the size of the lamellae decreases with the increase in sericin content, demonstrating the effect of sericin on both the supersaturation of the system and the interface energy between aragonite and the solution.

Concerning the calcite crystals, the {00.1}-pinacoid and the {11.0}-prism, usually unstable, are found. Calcite crystals still show the {10.4}-cleavage rhombohedron, but the stabilization of the new forms approaches the morphology to that of the biological prismatic calcite associated to nacre found in the literature. The morphological effect of sericin on calcite is undoubtedly driven by the kinetics of the growth process. In fact, the role of the impurity becomes more and more significant at low supersaturation values with respect to calcium carbonate when the rate of growth of the crystals is lower, and the competition between the kinetics of adsorption of the impurity and the kinetics of growth are comparable.

The effect of sericin on the growth morphology of both polymorphs can be explained in terms of lattice coincidences between the flat and continuous (001) layers of ordered sericin and the 2D-surface cells of both calcite {00.1} and aragonite {001}. This reticular property obviously only fulfills the necessary condition for the epitaxy to occur; however, it proves that the host/guest relation cannot be confined to the interaction between single molecules, being the result of the adhesion of two ordered entities.

The stabilization of aragonite during the early stages of precipitation, even if under moderate supersaturation conditions (that in pure solution bring to the precipitation of the sole rhombohedral calcite), is probably thanks to the good agreement between the surface lattice of aragonite and sericin.

In the presence of CO_2 equilibrating with the atmosphere, carbon dioxide in excess with respect to the atmosphere in the presence of sericin yields small bubbles inside the solution that act as preferential nucleation centers for calcium carbonate. The first layer of calcium carbonate, made by aragonite crystals intimately associated with sericin, grows on the external surface of the bubble. Then, lowering the supersaturation and decreasing the effect of the impurity that is found to be more concentrated in the inner part of the aggregate, calcite nucleates on the former substrate, oriented with the *c*-axis parallel to that of aragonite and with its {00.1} form epitaxially stabilized by the presence of the {001} form of aragonite. It is likely that the effect of sericin on the morphology of calcite could be considered partially responsible for the orientation and morphology of the calcite layer, because of its incomplete coverage; however, the epitaxial agreement between the two polymorphs is strong enough to rule the crystallization of calcite even at lower supersaturation.

Sericin is detectable in the aggregate by μ-Raman measurements and qualitatively decreases from the first mineralized layers in the core of the aggregate toward the external part of the spherulite. Moreover, the bubble encased in the growing calcium carbonate aggregate, segregates the CO_2, making it unavailable to the growing system and originating a confined slightly acid environment that, in turn, can be associated with the local concentration of sericin.

In this way, a three-phased poly-crystalline architecture made by calcium carbonate (in both aragonite and calcite forms) and sericin, radially distributed onto spherical surfaces, mimics the nacre structure. It is worth outlining that this complex object, ruled by three different epitaxies, spontaneously forms in the presence of a CO_2 bubble dipped into a quasi-stagnant aqueous solution

containing calcium carbonate and sericin. As the free CO_2 is ubiquitous near the living organisms, the association between sericin and CO_2 can partially explain the formation of nacre-like structures.

Supplementary Materials: The following are available online at at http://www.mdpi.com/2073-4352/8/7/263/s1, Figure S1: Saturation index (SI) of carbonates in G experiments varying the concentration of calcium chloride; Figure S2: (a) μ-Raman spectrum of the sunflower-like spherulitic aggregate showing the vibrational fingerprint of aragonite; (b) μ-Raman spectrum of calcite from G experiments; from (c) to (e) comparison among the μ-Raman spectra of the pure sericin, the inner and outer part of the spherulite, showing the sericin signal decreasing in intensity from the core toward the outermost part of the spherulite.

Author Contributions: Investigation, Methodology, Validation, Software, L.P.; Conceptualization, Writing-Review & Editing, L.P. and D.A.; Formal Analysis D.A.

Funding: This research received no external funding.

Acknowledgments: The Authors would like to thank Salvatore Guastella for FESEM imaging.

Conflicts of Interest: The authors declare no conflict of interest.

References

1. Finnemore, A.; Cunha, P.; Shean, T.; Vignolini, S.; Guldin, S.; Oyen, M.; Steiner, U. Biomimetic layer-by-layer assembly of artificial nacre. *Nat. Commun.* **2012**, *3*, 966. [CrossRef] [PubMed]
2. Liu, R.; Xu, X.; Cai, Y.; Cai, A.; Pan, H.; Tang, R.; Cho, K. Preparation of Calcite and Aragonite Complex Layer Materials Inspired from Biomineralization. *Cryst. Growth Des.* **2009**, *9*, 3095–3099. [CrossRef]
3. Das, P.; Malho, J.-M.; Rahimi, K.; Schacher, F.H.; Wang, B.; Demco, D.E.; Walther, A. Nacre-mimetics with synthetic nanoclays up to ultrahigh aspect ratios. *Nat. Commun.* **2015**, *6*, 5967. [CrossRef] [PubMed]
4. Zhu, B.; Jasinski, N.; Benitez, A.; Noack, M.; Park, D.; Goldmann, A.S.; Barner-Kowollik, C.; Walther, A. Hierarchical Nacre Mimetics with Synergistic Mechanical Properties by Control of Molecular Interactions in Self-Healing Polymers. *Angew. Chem. Int. Ed.* **2015**, *54*, 8653–8657. [CrossRef] [PubMed]
5. Mao, L.-B.; Gao, H.-L.; Yao, H.-B.; Liu, L.; Cölfen, H.; Liu, G.; Chen, S.-M.; Li, S.-K.; Yan, Y.-X.; Liu, Y.-Y.; et al. Synthetic nacre by predesigned matrix-directed mineralization. *Science* **2016**, *354*, 107–110. [CrossRef] [PubMed]
6. Weiner, S.; Addadi, L. Design strategies in mineralized biological materials. *J. Mater. Chem.* **1997**, *7*, 689–702. [CrossRef]
7. Belcher, A.M.; Wu, X.H.; Christensen, R.J.; Hansma, P.K.; Stucky, G.D.; Morse, D.E. Control of crystal phase switching and orientation by soluble mollusc-shell proteins. *Nature* **1996**, *381*, 56–58. [CrossRef]
8. Mann, S. Molecular recognition in biomineralization. *Nature* **1988**, *332*, 119–124. [CrossRef]
9. Falini, G.; Weiner, S.; Addadi, L. Chitin-Silk Fibroin Interactions: Relevance to Calcium Carbonate Formation in Invertebrates. *Calcif. Tissue Int.* **2003**, *72*, 548–554. [CrossRef] [PubMed]
10. Heinemann, F.; Launspach, M.; Gries, K.; Fritz, M. Gastropod nacre: Structure, properties and growth—Biological, chemical and physical basics. *Biophys. Chem.* **2011**, *153*, 126–153. [CrossRef] [PubMed]
11. Keene, E.C.; Evans, J.S.; Estroff, L.A. Matrix Interactions in Biomineralization: Aragonite Nucleation by an Intrinsically Disordered Nacre Polypeptide, n16N, Associated with a β-Chitin Substrate. *Cryst. Growth Des.* **2010**, *10*, 1383–1389. [CrossRef]
12. Mann, S. *Biomineralization: Principles and Concepts in Bioinorganic Materials Chemistry*; Oxford University Press: Oxford, UK, 2001; ISBN 9780198508823.
13. Al-Sawalmih, A.; Li, C.; Siegel, S.; Fabritius, H.; Yi, S.; Raabe, D.; Fratzl, P.; Paris, O. Microtexture and Chitin/Calcite Orientation Relationship in the Mineralized Exoskeleton of the American Lobster. *Adv. Funct. Mater.* **2008**, *18*, 3307–3314. [CrossRef]
14. Addadi, L.; Joester, D.; Nudelman, F.; Weiner, S. Mollusk Shell Formation: A Source of New Concepts for Understanding Biomineralization Processes. *Chem. Eur. J.* **2006**, *12*, 980–987. [CrossRef] [PubMed]
15. Falini, G.; Albeck, S.; Weiner, S.; Addadi, L. Control of Aragonite or Calcite Polymorphism by Mollusk Shell Macromolecules. *Source Sci. New Ser.* **1996**, *271*, 67–69. [CrossRef]
16. Weiner, S.; Traub, W.; Parker, S.B. Macromolecules in Mollusc Shells and Their Functions in Biomineralization [and Discussion]. *Philos. Trans. R. Soc. B Biol. Sci.* **1984**, *304*, 425–434. [CrossRef]

17. Levi-Kalisman, Y.; Falini, G.; Addadi, L.; Weiner, S. Structure of the Nacreous Organic Matrix of a Bivalve Mollusk Shell Examined in the Hydrated State Using Cryo-TEM. *J. Struct. Biol.* **2001**, *135*, 8–17. [CrossRef] [PubMed]
18. Bouville, F.; Maire, E.; Meille, S.; Van de Moortèle, B.; Stevenson, A.J.; Deville, S. Strong, tough and stiff bioinspired ceramics from brittle constituents. *Nat. Mater.* **2014**, *13*, 508–514. [CrossRef] [PubMed]
19. Niebel, T.P.; Bouville, F.; Kokkinis, D.; Studart, A.R. Role of the polymer phase in the mechanics of nacre-like composites. *J. Mech. Phys. Solids* **2016**, *96*, 133–146. [CrossRef]
20. Gotliv, B.-A.; Addadi, L.; Weiner, S. Mollusk Shell Acidic Proteins: In Search of Individual Functions. *ChemBioChem* **2003**, *4*, 522–529. [CrossRef] [PubMed]
21. Weiss, I.M.; Tuross, N.; Addadi, L.; Weiner, S. Mollusc larval shell formation: Amorphous calcium carbonate is a precursor phase for aragonite. *J. Exp. Zool.* **2002**, *293*, 478–491. [CrossRef] [PubMed]
22. Jin, W.; Jiang, S.; Pan, H.; Tang, R. Amorphous Phase Mediated Crystallization: Fundamentals of Biomineralization. *Crystals* **2018**, *8*, 48. [CrossRef]
23. Thompson, J.B.; Paloczi, G.T.; Kindt, J.H.; Michenfelder, M.; Smith, B.L.; Stucky, G.; Morse, D.E.; Hansma, P.K. Direct observation of the transition from calcite to aragonite growth as induced by abalone shell proteins. *Biophys. J.* **2000**, *79*, 3307–3312. [CrossRef]
24. Cheng, C.; Shao, Z.; Vollrath, F. Silk Fibroin-Regulated Crystallization of Calcium Carbonate. *Adv. Funct. Mater.* **2008**, *18*, 2172–2179. [CrossRef]
25. Chevalier, N.R.; Chevallard, C.; Goldmann, M.; Brezesinski, G.; Guenoun, P. $CaCO_3$ Mineralization under β-Sheet Forming Peptide Monolayers. *Cryst. Growth Des.* **2012**, *12*, 2299–2305. [CrossRef]
26. Weiner, S.; Talmon, Y.; Traub, W. Electron diffraction of mollusc shell organic matrices and their relationship to the mineral phase. *Int. J. Biol. Macromol.* **1983**, *5*, 325–328. [CrossRef]
27. Weiner, S.; Hood, L. Soluble protein of the organic matrix of mollusk shells: A potential template for shell formation. *Science* **1975**, *190*, 987–989. [CrossRef] [PubMed]
28. Ito, A.; Nakamura, S.; Aoki, H.; Akao, M.; Teraoka, K.; Tsutsumi, S.; Onuma, K.; Tateishi, T. Hydrothermal growth of carbonate-containing hydroxyapatite single crystals. *J. Cryst. Growth* **1996**, *163*, 311–317. [CrossRef]
29. Gómez-Morales, J.; Hernández-Hernández, Á.; Sazaki, G.; García-Ruiz, J.M. Nucleation and polymorphism of calcium carbonate by a vapor diffusion sitting drop crystallization technique. *Cryst. Growth Des.* **2010**, *10*, 963–969. [CrossRef]
30. Lakshminarayanan, R.; Kini, R.M.; Valiyaveettil, S. Investigation of the role of ansocalcin in the biomineralization in goose eggshell matrix. *Proc. Natl. Acad. Sci. USA* **2002**, *99*, 5155–5159. [CrossRef] [PubMed]
31. Parkhurst, D.L.; Appelo, C.A.J. Description of input and examples for PHREEQC version 3—A computer program for speciation, batch-reaction, one-dimensional transport, and inverse geochemical calculations: U.S. Geological Survey Techniques and Methods. In *U.S. Geological Survey Techniques and Methods, Book 6*; USGS: Reston, VA, USA, 2013; p. 497.
32. Bradley, D.J.; Pitzer, K.S. Thermodynamics of electrolytes. 12. Dielectric properties of water and Debye-Hückel parameters to 350 degree C and 1 kbar. *J. Phys. Chem.* **1979**, *83*, 1599–1603. [CrossRef]
33. Harvie, C.E.; Weare, J.H. The prediction of mineral solubilities in natural waters: The Na-K-Mg-Ca-Cl-SO_4-H_2O system from zero to high concentration at 25 °C. *Geochim. Cosmochim. Acta* **1980**, *44*, 981–997. [CrossRef]
34. Harvie, C.E.; Møller, N.; Weare, J.H. The prediction of mineral solubilities in natural waters: The Na-K-Mg-Ca-H-Cl-SO_4-OH-HCO_3-CO_3-CO_2-H_2O system to high ionic strengths at 25 °C. *Geochim. Cosmochim. Acta* **1984**, *48*, 723–751. [CrossRef]
35. Plummer, N.; Parkhurst, D.L.; Fleming, G.W.; Dunkle, S.A. *A Computer Program Incorporating Pitzer's Equations for Calculation of Geochemical Reactions in Brines*; Water-Resources Investigations Report 88-4153; U.S. Geological Survey: Reston, VA, USA, 1988.
36. Gehrke, N.; Cölfen, H.; Pinna, N.; Antonietti, M.; Nassif, N. Superstructures of calcium carbonate crystals by oriented attachment. *Cryst. Growth Des.* **2005**, *5*, 1317–1319. [CrossRef]
37. Marin, F.; Luquet, G. Molluscan shell proteins. *Comptes Rendus Palevol.* **2004**, *3*, 469–492. [CrossRef]
38. Aquilano, D.; Costa, E.; Genovese, A.; Roberto Massaro, F.; Pastero, L.; Rubbo, M. Hollow rhombohedral calcite crystals encompassing CO_2 microcavities nucleated in solution. *J. Cryst. Growth* **2003**, *247*, 516–522. [CrossRef]

39. Massaro, F.R.; Aquilano, D. Calcite bubbles. The control exerted on the bubble size by solubility and interfacial tension. *Eur. J. Miner.* **2007**, *19*, 339–344. [CrossRef]
40. Aquilano, D.; Pastero, L.; Bruno, M.; Rubbo, M. {1 0 0} and {1 1 1} forms of the NaCl crystals coexisting in growth from pure aqueous solution. *J. Cryst. Growth* **2009**, *311*. [CrossRef]
41. Pastero, L.; Massaro, F.R.; Aquilano, D. Experimental and theoretical morphology of single and twinned crystals of Li_2CO_3 (zabuyelite). *Cryst. Growth Des.* **2007**, *7*, 2749–2755. [CrossRef]
42. Aquilano, D.; Pastero, L. Anomalous mixed crystals: A peculiar case of adsorption/absorption. *Cryst. Res. Technol.* **2013**, *48*, 819–839. [CrossRef]
43. Pastero, L.; Giustetto, R.; Aquilano, D. Calcite passivation by gypsum: The role of the cooperative effect. *CrystEngComm* **2017**, *19*, 3649–3659. [CrossRef]
44. Pastero, L.; Aquilano, D.; Moret, M. Selective Adsorption/Absorption of Formamide in NaCl Crystals Growing from Solution. *Cryst. Growth Des.* **2012**, *12*, 2306–2314. [CrossRef]

© 2018 by the authors. Licensee MDPI, Basel, Switzerland. This article is an open access article distributed under the terms and conditions of the Creative Commons Attribution (CC BY) license (http://creativecommons.org/licenses/by/4.0/).

MDPI
St. Alban-Anlage 66
4052 Basel
Switzerland
Tel. +41 61 683 77 34
Fax +41 61 302 89 18
www.mdpi.com

Crystals Editorial Office
E-mail: crystals@mdpi.com
www.mdpi.com/journal/crystals

MDPI
St. Alban-Anlage 66
4052 Basel
Switzerland

Tel: +41 61 683 77 34
Fax: +41 61 302 89 18

www.mdpi.com

ISBN 978-3-03897-723-0